

**ANTHROPOMORPHIC PHANTOM DEVELOPMENTS FOR THE
CHARACTERIZATION AND EVALUATIONS OF MRI RF COILS**

by

Sossena Cherise Wood

Bachelor of Science in Electrical Engineering, University of Pittsburgh, 2011

Submitted to the Graduate Faculty of

Swanson School of Engineering in partial fulfillment

of the requirements for the degree of

Doctor of Philosophy

University of Pittsburgh

2018

UNIVERSITY OF PITTSBURGH
SWANSON SCHOOL OF ENGINEERING

This dissertation was presented

by

Sossena Wood

It was defended on

November 6, 2018

and approved by

George D. Stetten, M.D., Ph.D., Professor,

Department of Bioengineering

Howard Aizenstein, M.D., Ph.D., Professor of Psychiatry and Associate Professor,

Department of Bioengineering, and Clinical and Translational Science

John Brigham, Ph.D., Associate Professor,

Department of Civil Engineering and Bioengineering

Dissertation Director: Tamer S. Ibrahim, Ph.D., Associate Professor,

Departments of Bioengineering, Psychiatry and Radiology

ANTHROPOMORPHIC PHANTOM DEVELOPMENTS FOR THE CHARACTERIZATION AND EVALUATIONS OF MRI RF COILS

Sossena Wood, Ph.D.

University of Pittsburgh, 2018

Over the past few decades, Magnetic Resonance Imaging (MRI/MR) has proven to be one of the most resourceful diagnostic tools to non-invasively exam various parts of the human body. As MRI technology improved, research scanners were developed at greater field strengths to offer greater resolution and improved tissue contrast in comparison to clinical MR machines. In late 2017, the FDA approved the first clinical 7 Tesla (T) MR scanner, Siemens MAGNETOM Terra. The FDA's approval met the scientific demand for 7T MR imaging and ultra-high field (UHF) (≥ 7 Tesla) imaging's growing capability to detect human disease and tissue damage within the human body. While these machines offer promise, there are several issues experienced at higher field strengths that hinder its clinical feasibility. UHF MRI is presented with challenges such as 1) magnetic field (B_1^+) homogeneity, 2) increased global/local specific absorption rate (SAR) in biological tissue, and (3) addressing concerns regarding the unclear RF safety assurance due to temperature rise at UHF.

To address these challenges, the work of this dissertation develops tools to characterize RF coil designs for RF engineers. These tools are realized through hardware and other software methodologies for the evaluation of RF coil designs.

The results and the broad conclusion will support our long-term goal of achieving homogeneity and minimized RF power absorption at 7T *in-vivo* and further the UHF MRI community's understanding of 7T imaging. Thus, progress in this proposed work strengthens 7T's potential clinical feasibility and its ability to detect human disease and premature symptoms of brain damage.

TABLE OF CONTENTS

PREFACE	XXVII
DEDICATION	XXIX
1.0 INTRODUCTION	1
1.1 MOTIVATION	3
1.1.1 Challenges of UHF MRI Systems: Basic Phantoms.....	4
1.1.2 Challenges of UHF MRI Systems: RF Inhomogeneity and Elevated Specific Absorption Rate and Local Temperature Rise	5
1.2 SPECIFIC AIMS OF THIS DISSERTATION.....	6
1.3 OUTLINE OF THIS DISSERTATION	9
2.0 BACKGROUND.....	17
2.1 ELECTROMAGNETIC WAVES	18
2.2 MAGNETIC RESONANCE IMAGING.....	20
2.2.1 Macroscopic Magnetization and Atomic Model.....	20
2.2.2 Static Field (B_0).....	23
2.2.3 Radiofrequency Field (B_1)	24
2.2.4 Free Inductance Decay (FID).....	24
2.2.5 RF Pulse Design and Sequences.....	25
2.2.5.1 Types of Contrast Mechanisms in MR Imaging Protocols	25
2.2.6 B_1 Mapping	26
2.2.6.1 Saturated Turbo Flash (SatTFL).....	26

2.2.7	Thermal Heating in MRI.....	27
2.3	MRI SYSTEM AND MR INSTRUMENTATION.....	28
2.3.1	MR scanner.....	29
2.3.2	Gradient Coils	30
2.3.3	Computer System and Console.....	30
2.3.4	Radiofrequency Coils.....	30
2.3.4.1	History of UHF RF Coils	32
2.4	RADIOFREQUENCY SAFETY.....	33
2.5	MODELING ELECTROMAGNETIC FIELDS.....	36
2.5.1	Designing and Evaluating RF Coils.....	36
2.6	FINITE-DIFFERENCE TIME-DOMAIN.....	37
2.6.1	Background.....	37
2.6.2	Motivation for Choosing Finite-Difference Time-Domain	37
2.6.3	Formulation of Finite-Difference Time-Domain with Maxwell's Equations	38
2.6.3.1	Boundary Conditions.....	44
2.6.3.2	Stability Criterion	44
2.6.4	Formulation of Finite-Difference Time-Domain with Penne's Equations	44
2.6.4.1	Boundary Conditions.....	46
2.6.4.2	Stability Criterion	47
2.7	ANATOMICALLY DETAILED HEAD MODELS/ PHANTOMS	47
2.8	NONLINEAR ALGORITHMS FOR RF SHIMMING.....	49
3.0	DEVELOP AN ANTHROPOMORPHIC HETEROGENEOUS HEAD PHANTOM THAT IS EVALUATED AND CHARACTERIZED THROUGH EXPERIMENTAL MRI STUDIES AT 7T.....	51
3.1	INTRODUCTION	51

3.1.1	MRI Phantoms	52
3.1.2	Prior Work in Developing Electromagnetically-Equivalent Head-Phantoms	52
3.1.3	3D Printing a Tool for Physical Phantom Construction.....	54
3.2	MATERIALS AND METHODS.....	55
3.2.1	Images Acquired	57
3.2.2	Phantom Segmentation, Design and Fabrication.....	58
3.2.3	Physical Assembly	62
3.2.4	Preparation of the Phantom Tissue and Phantom Filling.....	63
3.2.5	Network Analyzer Measurements	67
3.2.6	7T MRI Experiments	70
3.3	RESULTS AND DISCUSSION.....	71
3.3.1	Results	71
3.3.1.1	Fabrication of Head Phantom.....	71
3.3.1.2	S-Matrix Simulation and Experimental Measurements of the Phantoms to the <i>In-Vivo</i> Volunteer	72
3.3.1.3	Verification of Congruent Slices to the <i>In-Vivo</i> Volunteer	72
3.3.1.4	Experimental Study of the Various Phantoms to the <i>In-Vivo</i> Volunteer.....	73
3.3.1.5	Magnetic field distributions and EPI testing of the various phantoms and the <i>in-vivo</i> volunteer.	74
3.3.2	Discussion.....	77
3.3.2.1	Fabrication of Head Phantom.....	77
3.3.2.2	S-Matrix Measurements of the Phantoms to the <i>In-Vivo</i> Volunteer.. ..	77
3.3.2.3	Magnetic Field Distributions of the Various Phantoms and the <i>In-Vivo</i> Volunteer	78
3.3.2.4	EPI testing of the various phantoms and the <i>in-vivo</i> volunteer	78

3.3.2.5	Future Phantom Applications.....	79
3.4	CONCLUSION.....	80
4.0	ELECTROMAGNETIC AND THERMAL CHARACTERIZATION OF THE ANTHROPOMORPHIC HETEROGENEOUS HEAD PHANTOM USING A TEM RESONATOR AT 3T AND 7T	81
4.1	INTRODUCTION	81
4.2	PART I-A: ELECTROMAGNETIC CHARACTERIZATION OF THE ANTHROPOMORPHIC HETEROGENEOUS HEAD PHANTOM USING A TEM RESONATOR AT 7T	84
4.2.1	Introduction	84
4.2.1.1	Current Studies Comparing Numerical and Experimental Electromagnetically-Equivalent Head-Phantoms	85
4.2.2	Materials and Methods	87
4.2.2.1	Numerical Studies.....	87
4.2.2.1.1	FDTD Simulations and Numerical Models at 7T.....	87
4.2.2.1.2	RF Coil and S-Matrix	88
4.2.2.1.3	FDTD Calculations of the B ₁ ⁺ Field	88
4.2.2.1.4	FDTD Calculations of the Electric Field Analysis	88
4.2.2.1.5	Phantom Generation and Fabrication	89
4.2.2.2	Experimental Studies.....	93
4.2.2.2.1	MR Instrumentation and Experimental Setup	93
4.2.2.2.2	Volunteer and Informed Consent.....	93
4.2.2.2.3	Experimental B ₁ ⁺ Field Mapping	94
4.2.3	Results and Discussion.....	94
4.2.3.1	Results.....	94
4.2.3.1.1	Numerical Scattering Parameters Measurements at 7T. ..	94
4.2.3.1.2	Numerical B ₁ ⁺ Field Mapping Measurements and Verifications of Experimental Measurements at 7T.....	96

4.2.3.1.3	Numerical Electric Field Distribution and Intensity Analysis at 7T.....	106
4.2.3.2	Discussion	112
4.2.3.2.1	Numerical Scattering Parameters Measurements at 7T.	112
4.2.3.2.2	Numerical B_1^+ Field Mapping Measurements and Verifications of Experimental Measurements at 7T.....	112
4.2.3.2.3	Numerical Electric Field Distribution and Intensity Analysis at 7T.	114
4.2.4	Summary	117
4.3	PART I-B: ELECTROMAGNETIC CHARACTERIZATION OF THE ANTHROPOMORPHIC HETEROGENEOUS HEAD PHANTOM USING A TEM RESONATOR AT 3T	118
4.3.1	Introduction	118
4.3.2	Materials and Methods	119
4.3.2.1	Numerical Studies	119
4.3.2.1.1	FDTD Simulations and Numerical Models at 3T.....	119
4.3.2.1.2	RF Coil and S-Matrix.	120
4.3.2.1.3	FDTD Calculations at 3T	120
4.3.2.1.4	Numerical Phantom Models.....	120
4.3.2.2	Experimental Studies.....	124
4.3.3	Results and Discussion	124
4.3.3.1	Results	124
4.3.3.1.1	Numerical Scattering Parameters Measurements at 3T.	124
4.3.3.1.2	Numerical B_1^+ Field Mapping Measurements at 3T.....	127
4.3.3.1.3	Numerical Electric Field Distribution and Intensity Analysis at 3T	134
4.3.3.2	Discussion	139
4.3.3.2.1	Numerical Scattering Parameters Measurements at 3T.	139

4.3.3.2.2	Numerical B_1^+ Field Mapping Measurements at 3T.....	140
4.3.3.2.3	Numerical Electric Field Distribution and Intensity Analysis at 3T.....	141
4.3.4	Summary.....	144
4.4	PART I-C: COMPARISON OF ELECTROMAGNETIC CHARACTERIZATION OF THE ANTHROPOMORPHIC HETEROGENEOUS HEAD PHANTOM USING A TEM RESONATOR AT 3T AND 7T.....	145
4.4.1	Introduction.....	145
4.4.2	Materials and Methods.....	146
4.4.3	Results.....	146
4.4.4	Discussion and Recommendations.....	146
4.4.4.1	Numerical Scattering Parameters Measurement Comparison at 3T and 7T.....	146
4.4.4.2	Numerical Analysis Comparison of B_1^+ Field Mapping at 3T and 7T.	148
4.4.4.3	Numerical Absolute Electric Field Analysis and Comparison at 3T and 7T.....	155
4.5	PART II: THERMAL AND SAR CHARACTERIZATION OF THE ANTHROPOMORPHIC HETEROGENEOUS HEAD PHANTOM USING A TEM RESONATOR AT 3T AND 7T.....	163
4.5.1	Introduction.....	163
4.5.2	Materials and Methods.....	166
4.5.2.1	Numerical Studies.....	166
4.5.2.1.1	Constitutive and Thermal Properties of Phantom Models at 3T and 7T.....	166
4.5.2.1.2	Numerical SAR Analysis at 3T and 7T.....	174
4.5.2.1.3	Numerical Temperature Calculations at 3T and 7T	175
4.5.2.1.3.1	Bioheat Equation and Boundary Conditions.....	175

4.5.2.1.3.2	Stability of Boundary Conditions and Steady-State Temperature Calculations.....	176
4.5.2.1.3.3	Temperature Elevation Calculations.....	178
4.5.3	Results and Discussion.....	178
4.5.3.1	Results.....	178
4.5.3.1.1	Numerical SAR Modeling and Analysis at 7T	178
4.5.3.1.2	Numerical Temperature Modeling and Analysis at 7T... ..	181
4.5.3.1.3	Numerical SAR Modeling and Analysis at 3T	183
4.5.3.1.4	Numerical Temperature Modeling and Analysis at 3T... ..	185
4.5.3.2	Discussion and Recommendation.....	188
4.5.3.2.1	Numerical SAR and Numerical Temperature Modeling at 7T	188
4.5.3.2.2	Numerical SAR and Numerical Temperature Modeling at 3T	191
4.5.3.2.3	Thermal Characterization Comparison of the Thermal Head Models at 3T and 7T	193
4.5.4	Summary.....	197
4.6	CONCLUSION.....	197
5.0	PRELIMINARY ELECTROMAGNETIC AND THERMAL CHARACTERIZATION OF THE ANTHROPOMORPHIC HETEROGENEOUS HEAD PHANTOM IN DIFFERENT 7T RF COILS.....	200
5.1	INTRODUCTION	200
5.2	MATERIALS AND METHODS.....	201
5.2.1	Experimental Studies of Electromagnetic and Thermal Characterization	201
5.2.1.1	Experimental Setup	201
5.2.1.1.1	MR Magnet and RF Experimental Setup.....	201
5.2.1.1.2	Experimental Network Analyzer	203

5.2.1.1.3	Neoptix™ Fiber Optic T ₁ Probes and Reflex™	203
5.2.1.1.4	Experimental RF Coils	204
5.2.1.1.4.1	Experimental 16ch–Tx/32ch-Rx TTT coil	206
5.2.1.1.4.2	Experimental 16-strut/4-port TEM Resonator.....	207
5.2.1.1.4.3	Experimental RAPID Biomed Coil.....	207
5.2.1.1.5	Experimental Phantoms	208
5.2.1.1.5.1	Experimental Anthropomorphic Heterogeneous Head Phantom Generation.....	208
5.2.1.1.5.2	Experimental Ambient Control Phantom.....	208
5.2.1.2	Experimental Bench Measurements using an Experimental Network Analyzer	209
5.2.1.3	Experimental B ₁ ⁺ Mapping Measurements in Each Experimental RF Coil.....	209
5.2.1.4	Experimental RF Heating Measurements Using the Experimental Anthropomorphic Heterogeneous Head Phantom Loaded within the TTT Coil at 7T (Preliminary Results).....	210
5.2.1.4.1	RF Heating Experiment Setup.....	210
5.2.1.4.2	Experimental RF Heating Measurements	212
5.2.2	Numerical Studies of Electromagnetic and Thermal Characterization..	213
5.2.2.1	RF Simulations	213
5.2.2.1.1	Numerical RF Coils.....	215
5.2.2.1.1.1	Numerical 16-strut/4-port TEM Resonator Model.	215
5.2.2.1.1.2	Numerical 16ch–Tx/32ch-Rx TTT Coil Model.....	215
5.2.2.1.1.3	Numerical RAPID Model	215
5.2.2.1.2	Numerical Electromagnetic Head Models	216
5.2.2.1.2.1	Numerical Segmented <i>In-Vivo</i> Human Head Model	216
5.2.2.1.2.2	Numerical Anthropomorphic Heterogeneous Head Phantom Model	216

5.2.2.1.3	FDTD Calculations of the B_1^+ Field and SAR.....	217
5.2.2.1.3.1	FDTD Calculations of the B_1^+ Field.....	217
5.2.2.1.3.2	FDTD Calculations of the SAR.....	218
5.2.2.2	Thermal Simulations.....	218
5.2.2.2.1	RF Coils.....	219
5.2.2.2.1.1	Numerical 16-strut/4-port TEM resonator Model ..	219
5.2.2.2.1.2	Numerical 16ch–Tx/32ch–Rx TTT coil model	219
5.2.2.2.1.3	Numerical RAPID Coil	219
5.2.2.2.2	Numerical Thermal Head Models	219
5.2.2.2.2.1	Numerical Segmented <i>In-Vivo</i> Human Head Model	220
5.2.2.2.2.2	Numerical Anthropomorphic Heterogeneous Head Phantom Model	220
5.2.2.2.2.3	Numerical Thermal Simulations Method	221
5.2.2.2.3	FDTD Calculations of Temperature Elevation	222
5.3	RESULTS.....	222
5.3.1	Validation of Conductive SLA Resin	222
5.3.2	Verification of Experimental Bench Measurements.....	224
5.3.1	Experimental B_1^+ Field Comparison Using the Experimental Anthropomorphic Heterogeneous Head Phantom Centered in Various Experimental RF Coils	226
5.3.2	Experimental RF Heating Using the Experimental Perfusionless Anthropomorphic Heterogeneous Head Phantom Loaded within the TTT Coil (Preliminary Results).....	230
5.3.2.1	Validation of Numerical Temperature Rise to Experimental Temperature Measurements	230
5.3.3	Numerical Studies of Electromagnetic and Thermal Characterization with the Anthropomorphic Heterogeneous Head Phantom using the TTT Coil..	232

5.3.3.1	Numerical RF Heating Comparison of the Perfusionless Anthropomorphic Heterogeneous Head Phantom to the Perfused Segmented <i>In-vivo</i> Human Head Model	234
5.4	DISCUSSION.....	235
5.5	CONCLUSION.....	239
6.0	CONCLUSIONS AND FUTURE WORK.....	241
6.1	SUMMARY AND FINDINGS.....	241
6.1.1	Development of an Anthropomorphic Heterogeneous Head Phantom to Evaluate and Characterize Experimental MRI Studies at 7T	241
6.1.2	Electromagnetic and Thermal Characterization of a Perfusionless Anthropomorphic Heterogeneous Head Phantom using the TEM Resonator at 3T and 7T MRI.....	242
6.1.3	Preliminary Electromagnetic and Thermal Performance Evaluation of the Perfusionless Anthropomorphic Heterogeneous Head Phantom using Various RF Coils at 7T MRI.....	244
6.2	FUTURE WORKS	245
APPENDIX A	247
	DEVELOPMENT AND MEASUREMENT OF MIMICKED BIOLOGICAL TISSUE PHANTOM RECIPES AT 7T	247
A.1	SUMMARY.....	247
A.2	DEVELOPING PHANTOMS FOR ELECTROMAGNETIC MEASUREMENTS.....	248
A.3	DEVELOPING PHANTOMS FOR THERMAL MEASUREMENTS USING AGAR	249
APPENDIX B	251
	ELECTROMAGNETIC CHARACTERIZATION OF THE VIRTUAL FAMILY DUKE MODEL AT 3T AND 7T.....	251
B.1	SUMMARY.....	251
B.2	ELECTROMAGNETIC PROPERTIES TO THE VIRTUAL FAMILY V1.0 DUKE MODEL	252
APPENDIX C	256

DESIGN, DEVELOP AND VALIDATE A NONLINEAR RF SHIMMING MRI OPTIMIZATION ALGORITHM AND GUI IN ORDER TO OPTIMIZE RF COIL PERFORMANCE AT 7T	256
C.1 INTRODUCTION	256
C.2 MATERIAL AND METHODS	257
C.2.1 Design and Development of an RF Shimming MRI Optimization Algorithm and Graphical User Interface	257
C.2.2 Verification of Various Nonlinear Algorithms using Experimental Studies	259
Experimental Verification	260
C.3 RESULTS AND DISCUSSION.....	260
C.3.1 Design of Graphical User Interface (GUI).....	260
C.3.2 Verification of Nonlinear Algorithm using Experimental Studies	263
C.4 CONCLUSION	264
BIBLIOGRAPHY	266

LIST OF TABLES

Table 2.1.	Regulations of IEC and FDA guidelines on SAR and RF heating in human experimental studies for volume and local transmit RF coils (64, 65)	34
Table 3.1.	Constitutive properties and densities of the classified tissues at 297.2 MHz.	65
Table 3.2.	Stability Parameters of Phantoms and the Volunteer for the EPI Stability Scans..	75
Table 4.1.	Constitutive Parameters of Phantom Materials at 297.20 MHz Derived from the Cited Literature (31, 98).	91
Table 4.2.	Detailed Mean B_1^+ Characteristics of Five Models through Numerical and Experimental Studies. A comparison of numerical and experimental B_1^+ characteristics highlighting the mean B_1^+ for 1W of input power ($\mu T/\sqrt{W}$) in three brain regions (all fillable compartments in the head phantom above and including the cerebellum), brain (excluding the Midbrain), and Midbrain).	102
Table 4.3.	Detailed Coefficient of Variation (CV) B_1^+ Field Values of Five Models through Numerical and Experimental Studies. A comparison of numerical and experimental B_1^+ field intensity characteristics highlighting the CV (standard deviation/ mean) in three brain regions (all fillable compartments in the head phantom above and including the cerebellum), brain (excluding the Midbrain), and Midbrain.	104
Table 4.4.	Percent Volume Change in the Absolute Electric Field Models Beyond the Percent Threshold at 7T. Calculations compared the percent of the volume change beyond the threshold of each phantom model in Figure 4.4.B-D to the segmented <i>in-vivo</i> human head model in Figure 4.4.A. The percentage volume change represents the deviation in accuracy from the segmented <i>in-vivo</i> human head model.	111
Table 4.5.	Constitutive Parameters of Phantom Materials at 128.00 MHz Derived from Cited Literature (31, 98).	122
Table 4.6.	Detailed Mean B_1^+ Characteristics of Five Models through Numerical Studies at 3T. A comparison of numerical B_1^+ characteristics highlighting the mean B_1^+ for 1W of input power ($\mu T/W$) in three regions of interest (all fillable compartments in the head phantom above and including the cerebellum), brain (excluding the Midbrain), and Midbrain).	130

Table 4.7.	Detailed CV B_1^+ Characteristics of Five Models through Numerical Studies at 3T. A comparison of numerical B_1^+ characteristics highlighting the coefficient of variation (std/ mean) in three brain regions (all fillable compartments in the head phantom above and including the cerebellum), brain (excluding the Midbrain), and Midbrain).	133
Table 4.8.	Percent Volume Change in the Absolute Electric Field Models Beyond the Percent Threshold at 3T. Calculations compare the percent volume change of each phantom model in Figure 4.11.B-D to the segmented <i>in-vivo</i> human head model in Figure 4.11.A. The percentage volume change represents the deviation in accuracy from the segmented <i>in-vivo</i> human head model.	138
Table 4.9.	Detailed Comparison of Mean B_1^+ Field Intensity Characteristics of Five Models through Numerical Studies at 3T and 7T. A comparison of numerical B_1^+ characteristics highlighting the mean B_1^+ field intensity for 1W of accepted power ($\mu T/W$) in three brain regions on interest (all fillable compartments in the head phantom above and including the cerebellum), brain (excluding the Midbrain), and Midbrain).	152
Table 4.10.	Detailed CV B_1^+ Characteristics of Five Models through Numerical Studies at 3T and 7T. A comparison of numerical B_1^+ characteristics highlighting the coefficient of variation (std/ mean) in three brain regions (all fillable compartments in the head phantom above and including the cerebellum), brain (excluding the Midbrain), and Midbrain).	154
Table 4.11.	Percent Volume Change in the Absolute Electric Field Models Beyond the Percent Threshold at 7T and 3T. Calculations compare the percent volume change of each phantom model in Figure 4.17.B-D and Figure 4.18.B-D to the segmented <i>in-vivo</i> human head model in Figure 4.17.A and Figure 4.18.A. The percentage volume change represents the deviation in accuracy from the segmented <i>in-vivo</i> human head model.	161
Table 4.12.	Segmented <i>In-Vivo</i> Human Head Model and Anthropomorphic Heterogeneous Head Phantom Model's Constitutive Properties (Permittivity, Conductivity) and Thermal Properties (Basal Metabolic Rate, Specific Heat, Blood Perfusion Coefficient, Thermal Conductivity) at 297.2MHz. Derived from the Cited Literature (31, 98, 159-164).	167
Table 4.13.	Segmented <i>In-Vivo</i> Head Model and Anthropomorphic Heterogeneous Head Phantom Model's Constitutive Properties (Permittivity, conductivity) and Thermal Properties (Basal Metabolic Rate, Specific Heat, Blood Perfusion Coefficient, Thermal Conductivity) at 128.0 MHz. Cited from the Literature (31, 98, 159-164)	171
Table 5.1.	Temperature Probe Locations within the Experimental Perfusionless Anthropomorphic Heterogeneous Head Phantom highlighting the location, tissue	

classification, and probe depth from the exterior locations in Figure 5.3.	211
Table C.3.1. Example of Filtered Results using ‘Fmincon’ Algorithm	264

LIST OF FIGURES

Figure 2.1.	The electromagnetic spectrum is indicating the ranges and applications of electromagnetics at a specified frequency. The frequency is either categorized as ionizing or non-ionizing radiation (33).	19
Figure 2.2.	Microscopic View of an Atomic Model: an atom and its nucleus aligned to the external magnetic field, B_0 .	21
Figure 2.3.	Macroscopic View of Atomic Model: an atom and its nucleus with an external magnetic field applied.	22
Figure 2.4.	Precession of an atom around the applied external magnetic field, B_0 , on a rectangular coordinate system.	23
Figure 2.5.	An example and visual representation of the conventional MR system and set-up with MR components (45).	28
Figure 2.6.	An illustration of the MRI scanner and its core MR instrumentation that includes its hardware and software (45).	29
Figure 2.7.	Yee space lattice (70) – The electric and magnetic field components in space. The E field components are represented by the blue arrows and placed in the middle of the Yee space and the H-components are represented by orange and placed in half steps on the center faces.	43
Figure 2.8.	Basic spherical and cylindrical MRI loading phantoms at General Electric Healthcare (80).	48
Figure 3.1.	A General Workflow to Design and Fabricate an Anthropomorphic Heterogeneous Head Phantom Using 3D Printing.	56
Figure 3.2.	Medical Data Acquisition and Segmentation. A 3T MRI scan with $1.0 \times 1.0 \times 1.0$ mm ³ resolution was segmented and divided into eight individual tissues. Each segmented tissue is listed with the corresponding tissue segmentation color within the tissue legend. The pictured MRI dataset and segmented tissues are shown in the	

	mid axial, coronal and sagittal views. Table 3.1 lists the physiological tissues that were used to classify the tissues in the legend.	59
Figure 3.3.	Phantom Design and Fabrication of Physical Phantom Model. Views of the shelled CAD files (A-C) which were developed in order to make volumetric cavities of the designated biological tissues that were segmented from a 3T MRI dataset. Views of the rapid prototype model (D) show the head phantom printed with stereolithography (SLA) resin. The physical head phantom dimensions are 304.8 mm tall, 254.0 mm long and 140.0 mm wide. The filling-ports are highlighted by arrows indicating the locations at which the fluids, resembling various tissue types, enter the phantom.	60
Figure 3.4.	Comparison of Phantoms to <i>In-Vivo</i> Volunteer using the Scattering Parameters of an RF Coil. S-Parameters for <i>in-vivo</i> volunteer and phantom models with center frequency is 297.2MHz with a span of 40.0 MHz.	69
Figure 3.5.	Comparison of the Magnetic Field Distribution Experimentally Mapped using a B_1 Map at 7T MRI in All Planes. Congruent slices of each phantom in comparison with the human volunteer are shown in all planar views. The color bar ranges from 0 to 48.9 μ T per 500V. The maximum B_1 intensity level is set by the highest pixel value among each of the phantoms and the volunteer.	73
Figure 3.6.	Comparison of Phantom to <i>in-vivo</i> Volunteer during an EPI Stability Scan at 7T MRI.	76
Figure 4.1.	View of the Phantoms and Healthy Volunteer Positioned in the TEM Resonator. A commercial spherical phantom of 170.00 mm diameter and the fabrication of the head phantom (18) (physical head phantom dimensions are 305.00 mm tall, 254.00 mm long and 140.00 mm wide) are shown in (A), and (D), respectively. The volunteer, based on which the phantom was designed, is shown in (G) along with the experimental setup in (H). The anthropomorphic head phantom is loaded inside of the TEM resonator as shown in the numerical model (E), and experimental setup (F). Similarly, the spherical water-doped phantom is loaded in the TEM resonator as shown in the numerical model (B) and the experimental setup (C).	85
Figure 4.2.	S-Parameters Measurements of Five Numerical Models Positioned in the 16-strut/4-port TEM Resonator at 7T. The frequency response is modeled for the segmented <i>in-vivo</i> human head model (A) and each phantom (B-E) model.	95
Figure 4.3.	B_1^+ Field Distributions of All Models using the 16-strut/4-port TEM Resonator at 7T. The B_1^+ field distribution of each numerical model is shown and compared to the model's experimental B_1^+ mapping measurements in the sagittal, axial, and coronal views (A-O). The numerical models are scaled to 1W input power supplied by the RF system. The color bar is scaled from 0 to the maximum numerical and experimental B_1^+ values.	98
Figure 4.4.	Numerical Absolute Electric Field Distribution in Four Models in the Axial View. The numerical absolute electric field is shown for each model in the head and upper	

shoulders to the 16-strut/4-port TEM resonator based on a scale to the highest peak in the midbrain region of the anthropomorphic homogeneous water-doped phantom.107

Figure 4.5. Numerical Absolute Electric Field Distribution in Four Models in Coronal and Sagittal View. The numerical absolute electric field is shown for each head model in the head and upper shoulders to the 16-strut/4-port TEM resonator based on a scale to the highest peak in the midbrain region of the anthropomorphic homogeneous water-doped head phantom. 108

Figure 4.6. Percent Change of Absolute Electric Fields Models. The percent change of each phantom model in Figure 4.4.B-D and Figure 4.5.B-D is compared to the segmented *in-vivo* human head model in Figure 4.4.A and Figure 4.5.A. The peak change values are shown by the yellow solid arrows and the images are scaled to a maximum of 150% based on the anthropomorphic homogeneous water-doped head phantom. The SLA resin material is removed to focus on the absolute electric field distribution in the fillable compartments. The overestimation of the absolute electric field distribution based on each phantom is shown in (A). The underestimation of the absolute electric field distribution based on each phantom is shown in (B). ... 109

Figure 4.7. Absolute Electric Field in Four Phantom/ Head Models at 297.2 MHz. A comparison is shown between the absolute electric field distribution in the segmented *in-vivo* human head model (A) to the absolute electric field distribution in the SLA resin in the anthropomorphic head models (B-D). 115

Figure 4.8. S-Parameters Measurements of Five Numerical Models Positioned in the 16-strut/4-port TEM Resonator at 3T. The frequency response is modeled for the segmented *in-vivo* human head model (A) and each phantom (B-E) model. A demo of the frequency response of one channel, S11, is shown 125

Figure 4.9. B_1^+ field Distributions within the 16-strut/4-port TEM Resonator at 3T. The B_1^+ field distribution is shown for each numerical model and compared to the model's corresponding numerical B_1^+ mapping measurements at 7T (Figure 4.3) in the sagittal, axial, and coronal views (A-O). The numerical models are scaled to 1-Watt (1W) input power supplied by the RF system. The color bar is scaled from 0 to the maximum numerical B_1^+ for 1W of input power values 128

Figure 4.10. Coronal View of Full B_1^+ field Distributions within the 16-strut/4-port TEM Resonator at 3T. The B_1^+ field distribution for each numerical model is shown and compared to the model's corresponding numerical B_1^+ mapping measurements at 7T (Figure 4.3) in the coronal views (A-O). The numerical models are scaled to 1W input power supplied by the RF system. The color bar is scaled from 0 to the maximum numerical B_1^+ values. 132

Figure 4.11. Numerical Absolute Electric Field Distribution in Four Models at 3T. The numerical absolute electric field is shown for each model in the head and upper shoulders to the 16-strut/4-port TEM resonator based on a scale to the highest peak in the lower

muscle region surrounding the lower brain region within the anthropomorphic head phantoms at 3T.....	135
Figure 4.12. Numerical Absolute Electric Field Distribution in Four Models in Coronal and Sagittal View at 3T. The numerical absolute electric field is shown for each model in the head and upper shoulders to the 16-strut/4-port TEM resonator based on a scale to the highest peak in the lower muscle region surrounding the lower brain region within the anthropomorphic head phantoms at 3T.	136
Figure 4.13. Percent Change of Absolute Electric Fields Anthropomorphic and Segmented <i>in-vivo</i> Human Head model at 3T. The percent change of each anthropomorphic phantom model in Figure 4.11 and Figure 4.12 is compared to the segmented <i>in-vivo</i> human head model in Figure 4.11.A and Figure 4.12.A. The images are scaled to a maximum of 150% based on the anthropomorphic water-doped head phantom. The SLA resin material is removed to focus on the absolute electric field distribution in the fillable compartments. The overestimation of the absolute electric field distribution based on each phantom is shown in (A). The underestimation of the absolute electric field distribution based on each phantom is shown in (B).	137
Figure 4.14. Absolute Electric Field in Four Phantom/ Head Models at 128.0 MHz. A comparison is shown between the absolute electric field distribution in the segmented <i>in-vivo</i> human head model (A) to the absolute electric field distribution in the SLA resin in the anthropomorphic head models (B-D).	142
Figure 4.15. S-Parameters Measurements of Five Numerical Models Loaded in the 16-strut/4-port TEM Resonator at 3T and 7T. The frequency response is modeled for the segmented <i>in-vivo</i> human head model (A) and each phantom (B-E) model. A demo of the frequency response of one channel, S11, is shown.	147
Figure 4.16. B_1^+ field Distributions within the 16-strut/4-port TEM Resonator at 3T and 7T. The B_1^+ field distribution for each numerical model is shown and compared to the model's numerical B_1^+ mapping measurements at 7T in the sagittal, axial, and coronal views (A-O). The numerical models are scaled to 1W accepted power supplied by the RF system. The color bar is scaled from 0 to the maximum numerical B_1^+ values.	149
Figure 4.17. Comparison of the Absolute Electric Field in Four Models for 1-Watt of Accepted Power at 7T and 3T. The numerical absolute electric field is shown for each model in the head to upper shoulders to the 16-strut/4-port TEM resonator based on a scale to the highest peak in the midbrain region of the anthropomorphic homogeneous water-doped head phantom model at 7T	157
Figure 4.18. Comparison of Absolute Electric Field in Four Models in the Coronal and Sagittal Views for 1-Watt of Accepted Power at 7T and 3T. The numerical absolute electric field is shown for each model in the head and upper shoulders to the 16-strut/4-port TEM resonator based on a scale to the highest peak in the midbrain region of the anthropomorphic homogeneous water-doped head phantom model at 7T.	158

Figure 4.19. Percent Change Comparison of Absolute Electric Fields in Four Models for 1-Watt of Accepted Power at 7T and 3T. The percent change of each phantom model in Figure 4.17.B-D and Figure 4.18.B-D is compared to the segmented <i>in-vivo</i> human head model in Figure 4.17.A and Figure 4.18.A. The images are scaled to a maximum of 190% based on the anthropomorphic water-doped head phantom model. The SLA resin material is removed to focus on the absolute electric field distribution in the fillable compartments. The overestimation of the absolute electric field distribution based on each phantom is shown in (A). The underestimation of the absolute electric field distribution based on each phantom is shown in (B).	159
Figure 4.20. Visual Representation of the Constitutive Parameters in Each Head Model at 297.2 MHz. The segmented <i>in-vivo</i> human head model's properties are A) Relative Permittivity, C.) Conductivity, and E.) Density. The anthropomorphic heterogeneous head phantom model's properties are B.) Relative Permittivity, D.) Conductivity, and F.) Density.	169
Figure 4.21. Visual Representation of the Thermal Parameters at 128.0 MHz and 297.2 MHz	170
Figure 4.22. Visual Representation of the Constitutive Parameters in Each Head Model at 128.0 MHz.	173
Figure 4.23. Steady-State in Segmented <i>In-Vivo</i> Human Head Model at 3T and 7T. The temperature in the A.) perfused segmented <i>in-vivo</i> human head model and B.) perfusionless Anthropomorphic Heterogeneous Head Phantom are shown upon reaching a steady-state	177
Figure 4.24. Numerical SAR Distribution in Two Numerical Thermal Head Models at 7T. The numerical SAR distribution per 1-Watt of Input Power is shown for each model loaded within the numerical 16-strut/4-port TEM resonator. The numerical SAR distribution is scaled from 0 to the highest peak SAR per 1-Watt of input power.	180
Figure 4.25. Temperature Elevation over time in the Numerical Perfusionless Anthropomorphic Model at 7T. The minimum to maximum temperature elevation is shown from steady-state (Figure 4.23.B) to a 10-minute thermal heating for a continuous FDA regulated average SAR of 3.2W/kg.	182
Figure 4.26. Temperature Elevation over time in the Perfused Semented In-Vivo Human Head Model at 7T. The minimum to maximum temperature elevation is shown from steady-state (Figure 4.23.A) to a 10-minute thermal heating for a continuous FDA regulated average SAR of 3.2W/kg.	182
Figure 4.27. Numerical SAR Distribution in Two Numerical Thermal Head Models at 3T. The numerical SAR distribution per 1-Watt of Input Power is shown for each model loaded within the numerical 16-strut/4-port TEM resonator. The numerical SAR	

distribution is scaled from 0 to the highest peak SAR per 1-Watt of input power.	184
Figure 4.28. Temperature Elevation over time in the Perfused Segmented <i>In-Vivo</i> Human Head Model at 3T. The minimum to maximum temperature elevation is shown from steady-state (Figure 4.23.A) to a 10-minute thermal heating for a continuous FDA regulated average SAR of 3.2W/kg.	186
Figure 4.29. Temperature Elevation over time in the Perfusionless Anthropomorphic Head Model at 3T. The minimum to maximum temperature elevation is shown from steady-state (Figure 4.23.B) to a 10-minute thermal heating for a continuous FDA regulated average SAR of 3.2W/kg.	187
Figure 4.30. Temperature Elevation in Each Thermal Model at 7T. The temperature measurements in each model per temperature location for a duration of 10-minutes.	191
Figure 4.31. Temperature Elevation in Each Thermal Model at 3T. The temperature measurements in each model per temperature location for a duration of 10-minutes.	193
Figure 4.32. Comparison of the Temperature Rise in Two Thermal Head Models at 3T and 7T. A.) Perfused Segmented <i>In-Vivo</i> Human Head Model and B.) Perfusionless Anthropomorphic Heterogeneous Head Phantom Model loaded within the numerical 16-strut/4-port TEM Resonator.	194
Figure 4.33. Comparison of Temperature Elevation Distribution in Each Thermal Model at 3T and 7T. The temperature elevation distributions are scaled from the minimum to the maximum temperature elevation from the ambient temperature.	196
Figure 5.1. Experimental RF Heating Setup. A) RF coil, Anthropomorphic Head Phantom, and ambient control phantom setup on the MR scanner, B) two Neoptix™ ReFlex™ boxes with capabilities to read eight fiber optic probes, and C) example of Neoptix™ T ₁ probes.	203
Figure 5.2. Dimensions and Placement of the Anthropomorphic Heterogeneous Head Phantom Positioned in Experimental Various 7T RF Coils.	205
Figure 5.3. Eight Temperature probe locations in the Experimental Perfusionless Anthropomorphic Heterogeneous Head Phantom (shown on SLA Resin) and the ambient control phantom.	210
Figure 5.4. Numerical Coil Description and FDTD Models of the Anthropomorphic Heterogeneous Head Phantom model loaded in the in-house developed RF Coils. The 16ch–Tx/32ch–Rx TTT Coil model with the A) Schematic of the TTT Coil (without the Receive Array) model and B) loaded Anthropomorphic Heterogeneous Head Phantom model. The 16-strut/4-port TEM Resonator with the C) Schematic of	

	the TEM Resonator (without the Receive Array) model and D) loaded Anthropomorphic Heterogeneous Head Phantom model.	214
Figure 5.5.	The SLA Resin by DSM Somos® is used to show the experimental anthropomorphic head phantom in (A), and the yellow arrows indicate the location of the probes. Various views of the numerical SAR model for the phantom are chosen to highlight local SAR points in (B). C.) The temperature rise of the SLA Resin that is indicated for 5.5 hours. The ambient temperature is captured in the last plot. D.) Temperature probe locations.	223
Figure 5.6.	Comparison of Experimental Anthropomorphic Heterogeneous Head Phantom loading using the Scattering Parameters of three Experimental RF Coils. The anthropomorphic heterogeneous head phantom loaded within A.) an experimental 16-strut/4-port TEM resonator, B.) an experimental 8-channel loop-based coil (similar to the RAPID commercial coil's design), and C.) an experimental 16ch–Tx/32ch-Rx TTT coil.	225
Figure 5.7.	Experimental B_1^+ Field Comparison of the Anthropomorphic Heterogeneous Head Phantom loaded in Each Experimental 7T RF Coil. Single slices are shown in all planar views. The magnitude was scaled to a maximum B_1^+ intensity of $0.80 \mu T \sqrt{W}$ for 1-Watt of input power.	227
Figure 5.8.	A representation of the Experimental Anthropomorphic Heterogeneous Head Phantom's Experimental B_1^+ profiles shown in all planar views. The distance is shown along the respective planar axis for the values of CV and mean B_1^+ field intensity (per slice measured in cm).	229
Figure 5.9.	RF Heating Validation Per Probe using the TTT coil and comparison to Numerical Temperature Rise at 7T. The perfusionless anthropomorphic heterogeneous head phantom loaded within the experimental TTT coil uses the first six probes in the RF heating experiment and show corresponding numerical results.	231
Figure 5.10.	Electromagnetic and Thermal Characterization of the Perfusionless Anthropomorphic Heterogeneous Head Phantom using the TTT coil. A.) Numerical B_1^+ Distribution and validated by the B.) Experimental B_1^+ Distribution for 1-Watt of Input Power. C.) Numerical SAR per a continuous mean B_1^+ intensity of $2 \mu T$ in the head phantom shown in the range 0 to the 8.00 W/kg.	233
Figure 5.11.	Numerical RF Heating Comparison of the Perfusionless Anthropomorphic Heterogeneous Head Phantom using the TTT coil at 7T. The temperature change is shown in both thermal models in six locations. These locations are the same locations as Figure 5.9.	234
Figure 5.12.	Numerical Comparison of the SAR, Permittivity and Absolute Electric Field Distribution in the Numerical Thermal Models within the Numerical TTT Coil. The numerical perfused segmented in-vivo human head model shows the A) SAR distribution in the region, B) permittivity in the region, C) the absolute electric field in the region, and the numerical perfusionless anthropomorphic heterogeneous head	

phantom model shows the D) SAR distribution in the region, E) permittivity in the region, F) the absolute electric field in the region.	235
Figure B.2.1. FDTD calculated S-Parameters of the Duke Head Model (A & C) and Segmented <i>In-Vivo</i> Human Head Phantom (B & D) at 7T and 3T, respectively, using the TEM Resonator.	253
Figure B.2.2. B_1^+ Field Distribution for 1-Watt of Input Power of the Duke Head Model (A & C) and Segmented <i>In-Vivo</i> Human Head Phantom (B & D) at 7T and 3T, respectively, using the TEM Resonator.	254
Figure B.2.3. SAR Distribution per continuous mean B_1^+ field intensity of 2 μ T of the Duke Head Model (A & C) and Segmented <i>In-Vivo</i> Human Head Phantom (B & D) at 7T and 3T, respectively, using the TEM Resonator.	255
Figure C.2.1. RF Shimming MR Optimization Tool GUI and Shimmed RF Fields. An RF shimming toolbox GUI A) is used to find the optimal performance of any load within an RF coil. Results of a single slice axial views of a B) initial, non-optimized, C) optimized, D) circularly localized, and E) irregularly localized RF fields of a human within a TTT coil.	258
Figure C.2.2. Main Tab. The main tab of the GUI offers several parameters for the user to select the tissue, geometry, model type, and plane of view.....	261
Figure C.2.3. Main Tab's Load Mask Subsection. The main tab of the GUI offers several parameters for the user to select the tissue, geometry, model type, and plane of view.	262
Figure C.2.4. Optimization Tab. Select optimization parameters for various excitation ports (channels) of the RF coil.	262
Figure C.2.5. Constraint Tab. Define optimization objective function to be minimizing the constraint	263

PREFACE

Firstly, I sincerely thank my research mentor and advisor, Dr. Tamer S. Ibrahim, for his guidance through my doctoral studies and journey as a researcher. Dr. Ibrahim mentored me through my undergraduate research and assisted in my transition from electrical engineering to bioengineering. Working within his laboratory during that time offered confidence in pursuing my doctoral degree. His assistance and guidance through my doctoral work greatly shaped my thinking into being an avid, young researcher. Throughout my studies, Dr. Ibrahim challenged my thinking in research and spoke in-depth regarding my passions and next career opportunities.

To my committee, thank you for your advice throughout the years. You all offered helpful research and career advice. Your diverse perspectives were beyond helpful.

I would like to acknowledge the National Institutes of Health for supporting most of my dissertation work and predoctoral experiences. I also thank the University of Pittsburgh's K. Leroy Irvis Fund, the National GEM Consortium, and the University of Pittsburgh's Provost Development Fund for providing resources throughout my predoctoral studies.

Finally, I would like to thank my colleagues for their support to complete my dissertation and predoctoral work. This work would not have been completed as swiftly nor as enjoyable without the assistance of my dearest colleagues: Narayanan Krishnamurthy, Yajuan Zhao, Jung-hwan Kim, Tales Santini, Nadim Farhat, Tiago Martins, Salem Alkhateeb, and Shailesh B. Raval. In addition, the work of Appendix C has thrived because of the assistance of young undergraduate

researchers like Yanpei Ai, Jacob Bartee, Minesok Koo, and Yutong Zhang. You all are amazing people that I enjoyed working with and would not even consider trading experiences with other colleagues.

DEDICATION

The beginning and end of this process — and all the steps in between — would not be possible without God. I have experienced a variety of emotions and my faith was tested and restored; but throughout it all, you have remained faithful.

I thank the famous singer, Sade Adu, for her creative melodies that inspired my productivity to complete my dissertation.

I dedicate the work of my dissertation to my family (Wood, Minor, Salley, Hendrix, and Reynolds). The journey to become the first doctoral student in our immediate family (that I can recall) has been an eye-opening experience that we all treasure. At the beginning of this journey, Dr. Edward E. Brown Jr., Associate Professor at the Rochester Institute of Technology, shared with me during a technical poster session to educate my family as I went through the doctoral process. I held that advice to heart. I have had incredible mentors who have taught my parents how to push me along in the process. My mom actively seeks my progress on writing and progression in the laboratory. I have Dean Stephanie G. Adams to thank for teaching my mom how to be such an encourager. Equally, I appreciate my father for being an incredible life coach and sounding board through the end of this process. At the last phase of this journey, I dedicate this piece of work to you – my family.

I dedicate this work to my guardian angels and family that have left this earth. I appreciate their guidance along the way. More importantly, I dedicate this work to my maternal grandmother

who was so excited, yet confused, as to why I would graduate from college and later decide to go back to college. She valued education and watched all 13 grandchildren complete a personal milestone that she had not – receive a high school diploma. Her love and support in all of my endeavors, as one of her many grandchildren, means so much!

I want to acknowledge those that have been an extended family and an incredible support system for me. I thank Dr. Marcus Huggans for the instrumental role that he has played in my academic career. You planted the seed of pursuing a doctorate and set me on a path that I could never have imagined. I thank you deeply for encouraging me to go forth with getting my degree. I am humbled by your humbleness and ability always to make time for me. This part of my journey would be nonexistent without your vision and encouragement. I thank the Pitt STRIVE staff and community for their support. I have been able to present at international conferences and enhance my network in my field and within the AGEP community. Thank you Mrs. Yetunde Sussan Olaore, for being the rock and force to Pitt STRIVE. I thank Dean Sylvanus Wosu for his mentorship through the pre-Ph.D. and my Ph.D. program. You believed in my abilities before I stepped through the door of the bioengineering department. I thank Dr. Harvey Borovetz for his academic and career guidance through the program. Anytime that I was timid and fell short of my beliefs in myself; you affirmed me and assured that I could and would surpass the challenge through your wise words. I thank Dr. Sanjeev Shroff for our conversations and the bioengineering department staff's support to various academic and career conferences. I thank the staff of the Pitt EXCEL program for their continued support after my years in my undergraduate program. Most of all thank you to Yvette Moore for her unconditional love, lending ear and nurturing support. You have been fertilizing soil and a gardener to a flower that I never knew was within me.

I dedicate the work of this dissertation to all of the middle and high school students and scholars that I worked with at the Funds for the Advancement of Minorities through Education (FAME) in Pittsburgh. You challenged my philosophical views on giving back to the community and allowed me to grow while mentoring and teaching you. I will forever cherish the time I spent with all of you. Thank you to the staff of FAME for providing opportunities for me to give back to the FAME and Greater Pittsburgh community and be an inspiration to the students. I want to specifically thank Mr. Darryl T. Wiley for always being there, Dr. Nichelle Nelson for being a great resource and support, and Ms. Donna Vaughn (Auntie) for always checking-in and challenging me.

I dedicate this work to my colleagues. You all have been an amazing group of inspirational individuals to work with and I simply could not have chosen a better group of people to spend my time. We work hard and laugh harder. I will truly miss my work days with you but I know that the bonds we built will be continual friendships that we will hold on to.

Lastly, I thank my mentors and extended family that I met through the National Society of Black Engineers ([NSBE](#)). You all challenged me to grow up and not just to be good but great. You opened my ears and added fuel to my internal light to be a beacon of hope for our communities. Specifically, I thank Virginia L. Booth Womack, Dean Stephanie G. Adams, and Dr. Karl W. Reid for their continued support during and after my time in office. My service to the organization and persona will forever be to exemplify our mission.

My written dedication hardly acknowledges all those that have been a tremendous support to me throughout my graduate years. In so many ways, I thank all of you!

1.0 INTRODUCTION

Magnetic Resonance Imaging (MRI/ MR) is a versatile, noninvasive medical imaging technique used to image human anatomy (1). Almost 45 years ago, the first MRI machine was implemented and developed by Paul Lauterbur (2) to image the human finger and since then, it has transformed the field of medical imaging to be more versatile in disease detection through the MR system's anatomical *in-vivo* analysis. Today medical imaging plays an important role in the early diagnosis of neurodegenerative diseases, organ damage, or diseases and other ailments within the human body. In comparison to other diagnostic medical imaging, MRI uses non-ionizing radiation, and government MR safety regulations to regulate its clinical machines. Over time, whole-body MRI systems of lower field strengths ($\leq 1.5T$) have become commercially and clinically available.

In recent decades, not only have ultra-high field (UHF) systems ($\geq 7T$) become commercially available (2) for researchers due to an increase in scientific demand, but also to explore UHF systems clinical feasibility in the study, detection, or treatment of diseases and various ailments within the human body. UHF MRI enhances the field of MRI and offers improved signal-to-noise ratio (SNR) (3), improved tissue contrast due to its magnetic susceptibility, greater chemical shift dispersion (4), and in some instances, a reduced scan time (with a use of higher acceleration) (1). These benefits significantly enhance the contrast in the visualization of human tissue, and at times may result in a quicker MR experience for the patient being imaged. However, these benefits are compromised by UHF MRI's challenges.

In this dissertation, all experimental imaging studies are performed on the Siemens 7T MAGNETOM® MRI scanner at the University of Pittsburgh. In 2007, this MR system was installed and at that time was one of less than ten 7T MRI scanners in the world. Since that time, several 7T MRI machines have been built to meet the scientific demand and popularity of 7T MRI. In 2015, Siemens announced the development of the first FDA approved 7T MRI scanner, MAGNETOM Terra (5), which was cleared in late 2017.

UHF MRI scanners are currently used only for research due to the challenges experienced at higher field strengths. For example, current clinical MR machines provide uniformity within the magnetic field under acceptable government regulations. The uniformity experienced in clinical MR machines allows radiofrequency (RF) engineers to only have to design receive coils since the scanners (3T and below) are equipped with a whole-body transmit coil. As the field strength increases, the electromagnetic fields become less uniform. Most UHF MRI scanners are not equipped with a whole-body transmit coil, like lower and high field MR machines; thus, it is essential to develop UHF RF instrumentation to address the challenges of UHF MRI.

The goals of this dissertation are to 1) design and fabricate a realistic anthropomorphic heterogeneous head phantom, and 2) develop and implement tools in order to characterize MRI RF coil instrumentations and designs using a) electromagnetic simulations and validation experiments, and b) temperature simulations and validation experiments. The studies are performed using *in-vivo* human heads and utilizing the newly developed anthropomorphic heterogeneous head phantom.

The context of Chapter 1.0 focuses on the motivation behind this dissertation and the objectives set in order to achieve the results of this dissertation work.

1.1 MOTIVATION

The benefits of UHF MRI systems to the MR community are attracting scientists, engineers, and clinicians to explore its challenges so that ultimately healthcare may improve. Various UHF neuroimaging studies (6, 7) indicate that the detection of the onset of various neurodegenerative diseases and superb visualization of neurological anatomy is through UHF MRI's spatial and temporal resolution. For example, researchers in a schizophrenic study can visualize structures of the hippocampus in schizophrenic patients (8). The visualization of the dentate granule cells in the hippocampus are not visible in 3T images. Recent findings (9) show that researchers have been able to visualize amyloid plaques within the brain in Alzheimer disease patients due to the spatial resolution of 7T. These studies and others are supportive examples of the difference in structural visualization at 7T that 3T does not offer.

However, RF inhomogeneity and elevated RF power deposition, quantified by specific absorption rate (SAR), (5) are known challenges to the use of UHF MRI systems. These challenges limit UHF MRI systems from being fully utilized. To explore feasible solutions to these challenges, MR safety protocols and multi-transmission methods (i.e. RF shimming) and minimized SAR techniques must be further researched for their more clinical applications. Realistic phantoms (10-14) will lead to more accurate solutions; however, the current MR community uses basic phantoms in its current MR protocol. Improved RF shimming and minimized SAR techniques of various works (2, 15-17) have the potential to minimize inhomogeneity of the RF field further and reach achievable SAR absorption in various coils. *The proposed work within this dissertation is therefore significant because our results show promise in being a solution to enhancing the safety of 7T MRI and aiding the MR community with*

applications designed to improve the early detection and prevention of human diseases or organ damage.

As an outcome of this dissertation, we expect that the utilization of the realistic phantom would be a valuable resource in enhancing MR safety and the homogeneity of the magnetic field distribution within UHF systems. Resources that improve the RF homogeneity at 7T can improve the SNR and be one of the factors to improving the visibility of human anatomy. Ultimately, higher SNR yields better tissue contrast, which is more visible in smaller voxels, than 3T offers. The improved SNR will enhance the visibility (3) of the structural anatomy of the human head that will then improve applications to areas such as neurological disease detection and evaluation. As a result, this dissertation is expected to aid in improving the clinical feasibility of 7T and other UHF MRI systems.

1.1.1 Challenges of UHF MRI Systems: Basic Phantoms

The design and evaluation of MRI anthropomorphic head phantoms is one approach to improve the challenges of UHF MRI machines for continuous evaluation of its clinical potential. MRI phantoms are used to analyze, evaluate, and calibrate the MRI machine and its instrumentation before conducting tests on humans. Commercially available phantoms (such as spherical or cylindrical phantoms) are appropriate for analysis and evaluation of lower field MRI machines and their instrumentation since the wavelength of the RF signal that propagates into human tissue is long. At higher magnetic field strengths, accurate anatomical phantoms are needed because the wavelength of an RF signal propagating through any tissue becomes smaller than the electric size of the human head. The RF wavelength affects the homogeneity of the magnetic field and the

construction of the current distribution that determines the behavior of the specific absorption rate (SAR) (1).

Recent findings show how researchers and engineers use anatomical phantoms in numerical and experimental studies to help investigate the behavior of the interaction of RF pulses and biological tissue(s) at higher electromagnetic frequencies. The most recent findings of a physical, realistic, multi-tissue anthropomorphic human head phantom for MRI only and ultra-high field MRI are by Graedel *et al.* (14) and the RF Research Facility (15, 18). These findings (14, 15, 18) build on the development of previous realistic phantoms (19-23), and these findings have comparable results of the designed phantom's simulations and experiments. Before these findings, the CHEMA (24) phantom was the most anthropomorphic phantom because of its shape and single compartment representative of averaged dielectric properties of all tissues in the human head at 7T.

To our knowledge, recent findings of realistic phantoms (14, 22) do not make phantom MR comparisons to the MR images from which the phantom evolved. Our recent work (18) is the only work that we are aware of that makes such comparisons.

1.1.2 Challenges of UHF MRI Systems: RF Inhomogeneity and Elevated Specific Absorption Rate and Local Temperature Rise

The challenges with UHF MRI are 1) the inhomogeneity in the magnetic (RF/B₁) field and 2) elevated specific absorption rate (SAR) and local temperature rise. There are two leading causes of these challenges: 1) the wavelength shortens, and 2) the skin depth decreases. In UHF MRI systems as the static field (B₀) increases at various frequencies, the wavelength of the RF field

within biological tissues shortens (approximately 11-13 cm at 7T) and becomes comparable to the size of the body itself (4, 16). The RF field becomes more reliant on its interaction with biological tissues. At higher frequencies, the electrical size of the head is much larger than its electrical size at lower field strengths. The RF field must travel through multiple wavelengths to travel the entire human anatomy at UHF compared to lower field strengths (1-4, 17, 25). At UHF systems, the penetration of the RF field into tissue significantly decreases, and the tissue is more conductive (26, 27). Thus, an inhomogeneous RF field distribution exists and achieving uniformity becomes more challenging (2). Inhomogeneous RF fields affect the tissue contrast in UHF systems, which impedes the ability of the researcher to identify biological tissues and anatomical structures properly. It is essential to note that inhomogeneous RF fields are not harmful; however, electric fields (inhomogeneous or homogeneous) that exceed SAR regulations are harmful. As the RF power absorption elevates in UHF MRI systems, it becomes a safety concern (28, 29). It is essential to minimize the SAR values equivalent to or below the government's (IEC/ FDA) regulated SAR criteria. Researchers identified that achieving a more uniform RF distribution is mutually exclusive to achieving minimal SAR and temperature rising at UHF systems (13, 30). As the technology of UHF MRI evolves, hardware must be developed to overcome these challenges so that the benefits and applications of UHF MRI may improve healthcare.

1.2 SPECIFIC AIMS OF THIS DISSERTATION

The **main goal of this dissertation** is to develop and provide resources as solutions through hardware and software to further the research that is focused on increasing the chances of UHF

MRI's clinical use and mastering the understanding of its limitations. The **specific aims** of this dissertation are:

Aim 1: Develop an Anthropomorphic Heterogeneous Human Head Phantom that is Evaluated and Characterized through Experimental MRI Studies at 7T. Hypothesis: Researchers in the MR community that use an anthropomorphic heterogeneous human head phantom instead of a basic spherical phantom will find it easier to evaluate RF head coils.

1. Design an anthropomorphic heterogeneous human head phantom from an MR dataset.
2. Construct a computer-aided design (CAD) model that yields a physical model of an anthropomorphic heterogeneous human head phantom with a total of eight tissue compartments, specifically six refillable and two non-refillable compartments.
3. Model and measure electromagnetically equivalent biological tissue properties (i.e., conductivity, permittivity, spin-lattice (T1) relaxation times) at 7T for the head phantom.
4. Test the designed phantom with an RF head coil by performing experimental studies of the designed head phantom and other basic phantom.

Aim 2: Evaluate the Performance and Characterization of the Anthropomorphic Heterogeneous Human Head Phantom using Several RF Coils through Simulation and Experimental Studies at 7T. Hypothesis: Researchers in the MR community that are equipped with an anthropomorphic heterogeneous human head phantom during experimental scans are able to accurately characterize the performance of RF coils when compared to using basic or homogeneous phantoms.

1. Use Finite-Difference Time-Domain (FDTD) EM and thermal modeling to evaluate the anthropomorphic heterogeneous human head phantom model, segmented *in-vivo* human head model, anthropomorphic water-doped homogeneous head phantom model, anthropomorphic brain-doped homogeneous head phantom model, and a commercial homogeneous water-doped spherical within two RF coils.
2. Evaluate the EM characterization (i.e., S-matrices, B_1^+ distribution, B_1^+ efficiency, local and global SAR, relative absorbed power efficiency) of the anthropomorphic heterogeneous human head phantom to the various head and phantom models positioned within the transverse electromagnetic (TEM) Resonator at 3T and 7T.
3. Evaluate the thermal characterization of the perfusionless anthropomorphic heterogeneous human head phantom to the perfused segmented *in-vivo* human head model through thermal heating methods using numerical and experimental studies at 3T and 7T.
4. Evaluate the EM performance of various RF coils through an experimental study by comparing and analyzing an anthropomorphic heterogeneous human head phantom and *in-vivo* human subject centered within various RF coils at 7T.

At the completion of this dissertation, it is expected that the combination of results collected from the specific aims will further advance the UHF MRI community's understanding of 7T imaging. To date, the inhomogeneity of the magnetic field and elevation of local/average SAR are major challenges that compromise the advantages of 7T over (1.5T/3T) clinical MRI machines. The results of specific aims 1 and 2 will be shared as resources to the MR community

and other communities that desire to understand the interaction of human biological tissue and electromagnetic waves at higher frequencies. Progress in this proposed work will allow the UHF MR community to have improved resources to enhance their ability to study, detect, or evaluate human diseases.

1.3 OUTLINE OF THIS DISSERTATION

A chapter-by-chapter review of this dissertation is provided in this section. In addition, peer-reviewed publications and any other peer-reviewed work are listed under the respective chapter from which the work evolved. The work of this dissertation was supported by the National Institutes of Health (NIH) through grants to myself and the RF Research Facility lab's Principal Investigator, Tamer S. Ibrahim, PhD, (NIH's Ruth L. Kirschstein F31 award F31EB019872, NIH's R01MH111265, R01EB009848, and R01NS062065) and the University of Pittsburgh's Provost Development Fund Doctoral Fellowship award.

Chapter 1.0 the purpose, significance, and motivation of this PhD dissertation. This chapter describes both the benefits and challenges of UHF MRI as it relates to this dissertation. Lastly, the overview of the dissertation by chapter is listed along with works that were produced as a result of the work conducted during the PhD study.

Chapter 2.0 offers an in-depth review of the relevant literature and terminology of UHF MRI which provides the background and foundation of this dissertation. The chapter overviews basic electromagnetic theory and MR physics and RF safety about MRI. The current literature and work relating to anthropomorphic phantoms are highlighted to share the history of these phantoms, their application and the difference that our work will have in this focus area. A review

of the history of RF coils at UHF is provided. The application of numerical methods such as the FDTD method are described, and its application in computational electromagnetics and thermal heating using Penne's bioheat equation are reviewed. Thermal heating methods are described including thermal simulations and validation using thermal probe measurements within the designed head phantom. Lastly, this chapter reviews and analyzes the use of nonlinear algorithms as a technique to design novel RF excitation pulses by mitigating the RF inhomogeneity while managing reduced SAR and power.

Chapter 3.0 highlights a detailed explanation of the development of the eight-compartment anthropomorphic heterogeneous human head phantom developed in our lab. The robustness of the head phantom's design was measured by its performance of its numerical analysis in relation to its experimental study. Comparisons of the head phantom to the studies of the volunteer's head, from which the phantom was designed, were conducted. The head phantom was also used for B_1 mapping, SAR analysis, and echo planar imaging (EPI) stability to explore its application further. The following peer-reviewed journal articles and conferences papers were a result of the work in this chapter:

- **Wood, S.**, Krishnamurthy, N., Santini, T., Raval, S. B., Farhat, N., Holmes, J. and Ibrahim T. S., "Design and Fabrication of a Realistic Anthropomorphic Heterogeneous Head Phantom for Various Electromagnetic Applications," PloS ONE, 12(8), August 2017.
- **Wood, S.**, Krishnamurthy N., Zhao, Y., Raval, S., Zhao, T., Holmes, J.A. and Ibrahim, T.S., "Anatomically Detailed Human Head Phantom for MR Testing Purposes," In Proc. of the 22nd International Society of Magnetic Resonance in Medicine Annual Meeting, Milan, Italy; 2014, May 10-16.

- **Wood, S., Krishnamurthy N., Zhao, Y., Zhao, T., Raval, S., Holmes, J.A. and Ibrahim, T.S.,** “Anatomically Detailed Human Head Phantom,” in The 2nd Pittsburgh Imaging Community Retreat - Bench to Bedside MRI, Pittsburgh, PA October 2013.

Chapter 4.0 takes a further exploration of the designed phantom described in Chapter 3.0 interaction of the electromagnetic fields. A transverse electromagnetic (TEM) resonator is used to generate electromagnetic fields in the designed phantom at 3T and 7T. The assessment of the fields at various field strengths are made through S-parameters, B_1 mapping, SAR analysis, and temperature rise to highlight the importance of having a designed head phantom. The following peer-reviewed journal articles and conferences papers are/will be a result of the work in this chapter:

- **Wood, S., Santini, T., Krishnamurthy N., Martins, T., and Ibrahim, T.S.,** “A Comprehensive Evaluation of an Advanced MRI Anthropomorphic Head Phantom, NMR Biomedicine, NMR Biomedicine, In Revision.
- **Wood, S., Santini, T., Krishnamurthy,N., Martins, T., Ibrahim, T.S.,** “Comparison of Electric and B_1^+ Fields for Heterogeneous and Homogeneous Anthropomorphic Phantoms and Anatomical Models: Numerical Simulations and Experimental Findings,” In Proc. of the 26th International Society of Magnetic Resonance in Medicine Annual Meeting, Paris, France; 2018, June 16-21.
- **Wood, S., Krishnamurthy, N., Santini, T., Raval, S., and Ibrahim, T. S.,** “Evaluation of an Anthropomorphic Phantom with *In-Vivo* Using Quantitative MRI,” In Proc. of the 25th International Society of Magnetic Resonance in Medicine Annual Meeting, Honolulu, Hawaii, USA; 2017, April 21-27.

Chapter 5.0 reviews the evaluation of the characterization and performance of the anthropomorphic heterogeneous human head phantom using various UHF RF coils or arrays through numerical and experimental studies. Evaluation and characterization of the anthropomorphic heterogeneous human head phantom are conducted through specified evaluation criteria — scattering parameters (S-Matrix), B_1 mapping, SAR, and temperature assessment. A demo is shown of the S-Matrices of the designed phantom positioned in various RF coils.

An assessment was made of the temperature rise within the designed head phantom described in Chapter 3.0 using the in-house developed Tic-Tac-Toe (TTT) coil. The experimental temperature analysis was validated by the numerical temperature studies of the anthropomorphic heterogeneous human head phantom and the segmented *in-vivo* human head within the TTT coil.

- **Wood, S.**, Santini, T., Farhat, N., Martins, T., Krishnamurthy, N., Ibrahim, T.S., “ B_1^+ and Temperature Analysis in Two UHF RF Coils”, In Proc. of the 26th International Society of Magnetic Resonance in Medicine Annual Meeting, Paris, France; 2018, June 16-21.
- **Wood, S.**, Martins, T., Santini, T., Ibrahim, T.S., “An electrically conductive SLA resin used for the Design of Anthropomorphic Phantoms,” In Proc. of the 26th International Society of Magnetic Resonance in Medicine Annual Meeting, Paris, France; 2018, June 16-21.

Chapter 6.0 is a summary of the results of this dissertation and future work proposed by the author that is extended as recommendations to the UHF MR community. In this chapter, the contributions of this dissertation are elaborated and specifically address the MR community as to how these developed resources can be used in the exploration for the benefits and overcoming the challenges to making UHF MRI clinical.

Appendix C reviews the development of the mimicked biological tissues outlined in Table 3.1. There are two methods used in this dissertation to develop the mimicked biological tissues. One method is used to capture electromagnetic measurements and the other method is used to capture thermal measurements. These methods are described in greater detail in this appendix chapter.

Appendix A reviews the electromagnetic measurements in Virtual Family v1.0 (31) Duke model. Since Duke is referenced in Chapters 3.0-5.0, it is necessary to provide the electromagnetic measurements of this model. Additional electromagnetic models and their electromagnetic characterization are shown to demonstrate the impact of the constitutive parameter beyond the results presented in Section 4.2.

Appendix C reviews the development of a nonlinear algorithm that develops novel RF pulses for various RF coils at 7T. Validation of the RF shimming toolbox was shown through experimental studies and previous works from the University of Pittsburgh's RF Research Facility. The following peer-reviewed journal articles and conferences papers were a result of the work in this exploratory aim:

- Santini, T., Zhao, Y., **Wood, S.**, Kim, J., Farhat, N., Krishnamurthy, N., Zhao, T., Ibrahim, T.S., "Experimental and numerical evaluations of simultaneously excitable Eigenmodes in a 20-channel transmit RF array for 7 Tesla human MRI", In Proc. of the 26th International Society of Magnetic Resonance in Medicine Annual Meeting, Paris, France; 2018, June 16-21.
- Santini, T., **Wood, S.**, Krishnamurthy, N., Zhang, Y., Farhat, N., Vinjamuri, N., Koo, M., Aizenstein, H., Ibrahim, T.S., "New optimization strategies for RF

shimming at UHF MRI”, In Proc. of the 26th International Society of Magnetic Resonance in Medicine Annual Meeting, Paris, France; 2018, June 16-21.

- Santini, T., Kim, J., **Wood, S.**, Krishnamurthy N., Raval, S., and Ibrahim, TS, “A new RF coil for foot and ankle imaging at 7T MRI”, In Proc. of the 25th International Society of Magnetic Resonance in Medicine Annual Meeting, Honolulu, Hawaii, USA; 2017, April 21-27.
- Raval, S., Santini, T., **Wood, S.**, Krishnamurthy, N., Ibrahim, TS., “*In-vivo* (8x4) 32-ch Tx-only Body Array for UHF MR”, In Proc. of the 25th International Society of Magnetic Resonance in Medicine Annual Meeting, Honolulu, Hawaii, USA; 2017, April 21-27.
- Santini, T., Krishnamurthy, N., **Wood, S.**, Raval, S., Zhao, Y., Fischetti, A., Koo, M., Aizenstein, H., and Ibrahim, TS., “A 64-channel Double-Octagon Tx Head Coil for 7T Imaging”, In Proc. of the 25th International Society of Magnetic Resonance in Medicine Annual Meeting, Honolulu, Hawaii, USA; 2017, April 21-27.
- Ibrahim, T. S., Santini, T., Raval, S., Krishnamurthy, N., **Wood, S.**, Kim, J., Zhao, Y., Wu, X., Yacoub, E., Aizenstein, H., Zhao, T., “Towards Homogeneous 7T Neuro Imaging: Findings and Comparisons between 7T TTT and NOVA RF Coil Systems”, In Proc. of the 25th International Society of Magnetic Resonance in Medicine Annual Meeting, Honolulu, Hawaii, USA; 2017, April 21-27.
- Raval, S. B., Zhao, T., Smith, D., Britton, C., Krishnamurthy, N., Santini, T, **Wood, S**, Ibrahim, TS., and Gorantla, V. “Ultra-high resolution non-contrast imaging for chronic rejection monitoring and procedural planning in reconstructive

transplantation,” 26th International Congress of the Transplantation Society. Hong Kong, China; 2016, August.

- Zhao, Y., Krishnamurthy, N., **Wood, S.**, Zhao, T., Raval, S. B., and Ibrahim, TS., “3D Eigenmodes Optimizations for 3D Imaging at 7T”, In Proc. of the 23rd International Society of Magnetic Resonance in Medicine Annual Meeting, Toronto, Canada, 2015, May 30- June 5.
- Raval, S. B., Zhao, T., Krishnamurthy, N., Zhao, Y., **Wood, S.**, Bae, KT., and Ibrahim, TS., “Initial Results: Ultra-High Field 32-ch Tx Body Array with Bright Centers,” in Proc. of the 23rd International Society of Magnetic Resonance in Medicine Annual Meeting, Toronto, Canada, 2015, May 30- June 5.
- Krishnamurthy, N., Zhao, Y., Raval, S. B., Kim, J., **Wood, S.**, Santini, T., Zhao, T., and Ibrahim, TS., “7T Multi-slab Whole-Head Homogenous and Low SAR T2 Acquisitions with Limited RF Power Amplifiers Capabilities,” In Proc. of the 23rd International Society of Magnetic Resonance in Medicine Annual Meeting, Toronto, Canada, 2015, May 30- June 5.
- Krishnamurthy, N., Zhao, Y., Zhao, T., Raval, S., **Wood, S.**, Santini, T., Kim, J., and Ibrahim, TS., “Homogeneous and Low SAR Acquisitions at 7T”, in The 3rd Pittsburgh Imaging Community Retreat - Bench to Bedside MRI, Pittsburgh, PA, USA, 2014 October.
- Krishnamurthy, N., **Wood, S.**, Kim, J., Zhao, Y., Raval, S. B., Zhao, T., Ibrahim, TS., “Transmit Array Performance across Subjects at 7T MRI: Simulations and Experiments,” The International Society for Magnetic Resonance in Medicine 22nd Annual Meeting Competition; Milan, Italy, 2014 May 10-16;.

- Ibrahim, TS., **Wood, S.**, Zhao, Y., “Coils, RF Shimming & SAR” Sunrise Educational Course: Nuts& Bolts of Advanced Imaging. The 23rd International Society of Magnetic Resonance in Medicine Annual Meeting, Toronto, Canada, 2015, May. http://www.ismrm.org/15/program_files/S09a.htm.
 - Ibrahim, TS., Zhao, Y., **Wood, S.**, “Break-Out Groups to Work on Exercises on Reconstruction or Parallel Transmission” Sunrise Educational Course: Nuts & Bolts of Advanced Imaging. The 22nd International Society of Magnetic Resonance in Medicine Annual Meeting, Milan, Italy, 2014, May. http://www.ismrm.org/14/program_files/S10c.htm.
- Zhao, Y., Krishnamurthy, N., **Wood, S.**, Zhao, T., and Ibrahim, TS., “Simultaneous Excitation of Distinct Electromagnetic Modes using a Tx Array,” in Proc. of The 21st International Society of Magnetic Resonance in Medicine Annual Meeting, Salt Lake City Utah, 2013, April.

2.0 BACKGROUND

This chapter provides the reader with the proper context to understand the work within this dissertation. First, the history of MRI is covered to demonstrate the evolution of MR clinical and research applications. Over the last few decades, the field of MR has evolved; and before delving into its complexity, it is important to review the basic theory of electromagnetics (Section 2.1) and basic physics of MRI (Sections 2.2.1 to 2.2.4). MRI is an excellent diagnostic tool for human imaging and to ensure RF safety; it is regulated by government standards and guidelines. The importance of RF safety is further elaborated in Section 2.4 to support Section 1.1.2 that presents quantifying high SAR values as one of the challenges of UHF MRI.

It is critical to abide by the regulated procedures and guidelines for MR safety and patient scans. However, numerical modeling is an assessment tool to verify and validate experimental studies for MRI and RF coil developments. Thus, the remainder of this chapter overviews some tools that are used to perform RF safety through hardware and software developments. Finite-difference time-domain (FDTD), a numerical method used for validation of electromagnetic and thermal applications, is reviewed by highlighting the background, motivation, and formulation of FDTD. Thermal heating assesses the RF heating in MR applications. The various methods to assess thermal heating and methods of thermal heating validation are covered. FDTD studies often

require patient-specific modeling or phantoms, and Section 2.7 covers the use of anthropomorphic models within MRI. Lastly, the use and theory of and nonlinear algorithms in MRI is reviewed as a tool for producing uniform RF fields that meet RF safety guidelines.

2.1 ELECTROMAGNETIC WAVES

Electromagnetic waves are electrical charges with an applied magnitude of the applied force through a given medium. Basic physics emphasizes that two charges create a field or force between each other. These fields are known to be either the electric field or the magnetic field. When both the electric and magnetic field of a given charge are in oscillation, the electromagnetic (EM) wave is generated. The EM wave oscillates at the resonant frequency through a given medium until dissipated by a medium or redirected by an alternate force (32).

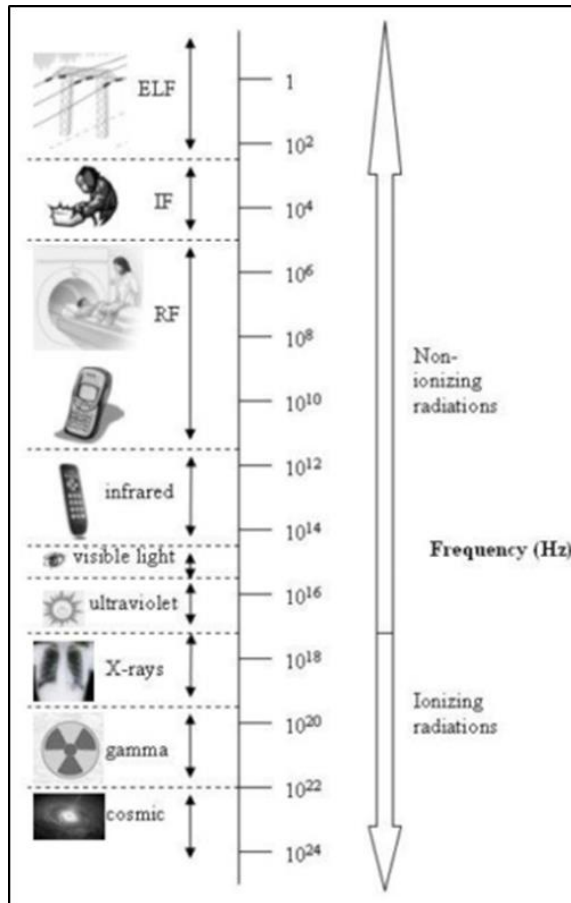


Figure 2.1. The electromagnetic spectrum is indicating the ranges and applications of electromagnetics at a specified frequency. The frequency is either categorized as ionizing or non-ionizing radiation (33).

Electromagnetic theory can span across a variety of different applications in focus areas such as radar, remote sensing, transmission lines, microwave devices, X-Rays, ultraviolet radiation, MRI and several other applications. While the electromagnetic spectrum has range spans from 1 to 10^{24} Hz, this chapter and dissertation will only focus on the application of non-ionizing radiation - being MRI.

2.2 MAGNETIC RESONANCE IMAGING

The first Magnetic Resonance Imaging (MRI) system developed in 1973 by Lauterbur (2) transformed the field of medical imaging to be more versatile in disease detection through the system's anatomical *in-vivo* analysis. Over time, whole-body MRI systems of lower field strengths ($\leq 1.5\text{T}$) have become commercially and clinically available. In recent decades, ultra-high field (UHF) systems ($\geq 7\text{T}$) have become available in the marketplace (2) for researchers to explore the clinical feasibility of UHF MRI's capacity to diagnose, study, or detect diseases and various ailments. UHF MRI enhances the field of MRI and offers improved signal-to-noise resolution (SNR), improved contrast-to-noise resolution (CNR) due to magnetic susceptibility, a greater chemical shift dispersion (29), and reduced scan time (with the use of higher acceleration). These benefits impact the overall quality of the image, enhance the contrast in the visualization of the tissue, and may result in a quicker experience for an imaged patient. In order for researchers and scientists to improve the MR community, the RF hardware instrumentation, compatible software, and MR safety protocols must be improved for UHF MRI systems to meet clinical standards.

The basic elements of MRI are covered in the subsections below.

2.2.1 Macroscopic Magnetization and Atomic Model

All variations of medical imaging can manipulate atoms within biological tissue. While some imaging modalities observe the atom's radioactivity, MRI focuses on the charge and moments of the atom. Every atom has a charge, a spin, and an angular momentum. In NMR and MRI, nuclei with an odd number of protons and neutrons are imaged. ^1H , ^{13}C , ^{19}F , ^{31}P , and ^{23}Na are some of

the most prevalent nuclei in biological systems and proteins with detectable signals. The nucleus charges and its moment are shown in Figure 2.2.

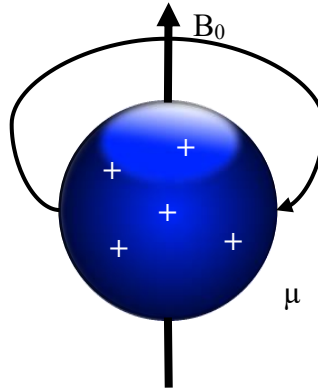


Figure 2.2. Microscopic View of an Atomic Model: an atom and its nucleus aligned to the external magnetic field, B_0 .

Assume there is a positive charge on the nucleus as shown in Figure 2.2. The angular moment of the atom is

$$\mu = \gamma B_0 \quad (2.1)$$

where μ (A/m^2) is the magnetic moment, B_0 is the applied external magnetic field, and γ (MHz/T) is the gyromagnetic constant given by

$$\gamma = \frac{\gamma}{2\pi} \quad (2.2)$$

The atom does not have a net magnetic field because the microscopic fields cancel each other out. Therefore, once an external magnetic field is applied, the atom in Figure 2.1 has a net magnetic field. In MRI, B_0 is the applied external magnetic field along the z-direction.

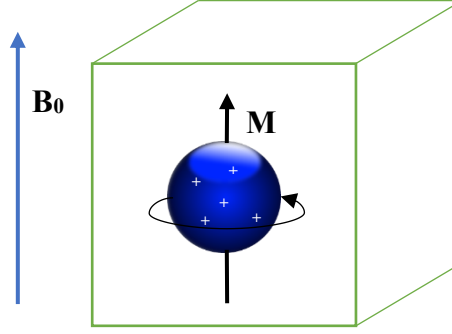


Figure 2.3. Macroscopic View of Atomic Model: an atom and its nucleus with an external magnetic field applied.

Figure 2.3 represents the macroscopic view of an atom within a voxel of tissue where an external magnetic field, \mathbf{B}_0 , is applied. Mathematically, the magnitude of the magnetic moment of μ is a sum of moments shown as

$$\vec{\mathbf{M}} = \sum_{n=1}^{N_i} \mu_n \quad (2.3)$$

where \mathbf{M} represents the magnitude of the moment of the atom, μ is the magnetic moment, N_i is the total number of moments, and n is the index for the moments. When \mathbf{M} is parallel to the external magnetic field, \mathbf{B}_0 , \mathbf{M} reaches equilibrium, \mathbf{M}_0 . Mathematically, the magnitude of \mathbf{M}_0 at equilibrium is shown as

$$\vec{\mathbf{M}}_0 = \frac{B_0 \gamma^2 \hbar^2}{4kT} P_D \quad (2.4)$$

where k is the Boltzham constant, T is the temperature, P_D is proton density.

In MRI, \mathbf{M} is a function of time (1). As time increases the magnetic moment precesses until it reaches its equilibrium state once parallel to \mathbf{B}_0 . During the time of precession, the magnetic moment experiences an external magnetic field, \mathbf{B}_0 , applied perpendicularly to experience a torque, also known as the angular momentum, \mathbf{J} .

$$\frac{d\mathbf{J}(t)}{dt} = \mathbf{M}(t) \times \mathbf{B}(t) \quad (2.5)$$

where $\mathbf{J}(t)$ is the angular momentum varying with time, $\mathbf{M}(t)$ is the magnetic moment varying with time, and $\mathbf{B}(t)$ is the magnetic field varying with time.

The atom precesses at the Larmor frequency, ω (MHz) written as: $\omega = \gamma B_0$

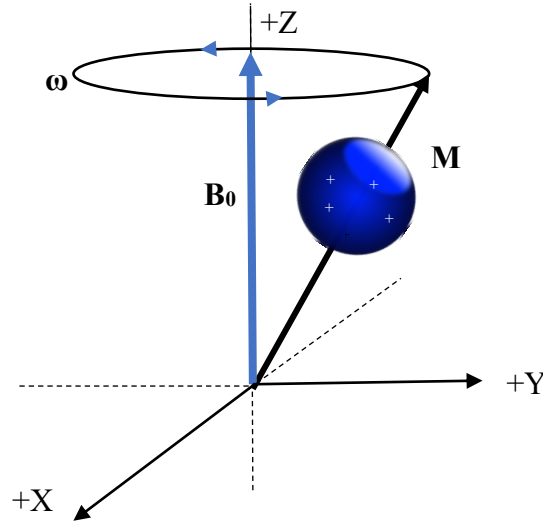


Figure 2.4. Precession of an atom around the applied external magnetic field, B_0 , on a rectangular coordinate system.

2.2.2 Static Field (B_0)

In a given medium, the direction and spin of the nuclei are randomly arranged. The random direction and individual force of each nuclei can result in an minimal or net force magnitude. MRI systems utilize an external and static magnetic force, B_0 , that is applied to the nuclei of all media in the +z-direction (34). Thus, the magnitude and direction of B_0 is given mathematically as:

$$\vec{B}_0 = B_0 \hat{a}_z \quad (2.6)$$

where B_0 is the magnitude of the static magnetic field and \hat{a}_z is the unit vector in the +z-direction.

Commercial MRI and low field systems have operational frequencies of 0.5T, 1.5T, and 3.0T. High field (HF) MRI systems operate at operational frequencies of 4.0T. UHF systems operate at operational frequencies of 7.0 T, 8.0 T, 9.4 T, and 11 T and are primarily research systems. These classifications of categorized field strengths have evolved as higher field strengths become clinical.

2.2.3 Radiofrequency Field (B_1)

The transmission of the RF field, B_1 , is transmitted into a patient or load via an RF coil (35). The origin of the RF pulse is in the transverse (x-y) plane view, and it is tuned to the resonant frequency. At a given point in time (t), the \vec{B}_1 is represented as a complex magnetic field on a rectangular coordinate system as

$$\vec{B}_1(t) = A(t)e^{i\theta} \quad (2.7)$$

where B_1 (μ T) is the magnitude of the RF field represented as a complex number, A is the amplitude at a given point in time, and θ (rad) is the phase at a given point in time.

2.2.4 Free Inductance Decay (FID)

Free inductance decay (FID) is the emitted, detectable NMR signal that is produced from an RF pulse forcing the net magnetization to precess around the static field. An FID is detectable as long as an RF pulse is applied and there is a non-zero component in the longitudinal magnetization (M_{xy}) direction. An ideal FID is produced from a 90° RF pulse, but truly any RF pulse with any flip angle produces some detectable FID. The FID that is produced provides an oscillating voltage for receiving in an RF coil. MR researchers and developers use a simple FID for multiple instances

such as characterizing an RF coil (i.e., tuning, amplitude, phase, etc.) and optimization of MR sequences. The FID sequence is used in this dissertation to perform RF heating in the anthropomorphic heterogeneous head phantom.

2.2.5 RF Pulse Design and Sequences

The formation of an RF pulse is covered in subsections 2.2.3 and 2.2.4. By placing an RF current through an RF coil, the magnitude of the magnetization vector \mathbf{M} is controlled. The nuclei are excited by the representation of any magnitude of the \mathbf{B}_1 field and adjusts the system to no longer be in equilibrium.

The nuclei precess along the +z-direction until the system reaches equilibrium. The MR image is generated from Mo precessing around \mathbf{B}_1 . An RF pulse sequence combines RF pulses and gradient pulses to obtain the desired MR image. The combination of RF pulses and gradient pulses is dependent on the desired tissue contrast.

MR sequences are the result of an echo signal detected that followed RF pulses over a time interval known as the echo time (TE). MR sequences are categorized as spin echo or gradient echo sequences (30). The difference between these two RF sequences is the use of RF pulses with low flip angles, which are produced by gradients.

2.2.5.1 Types of Contrast Mechanisms in MR Imaging Protocols

The concepts presented in previous sections revealed that transverse magnetization $\mathbf{M}_{xy}(t)$ generate the MR signal. To observe contrast in the tissues, the value and signal of $\mathbf{M}_{xy}(t)$ must vary for each tissue. Generating various tissue contrast is controlled by the tissue properties and the RF

pulse sequence parameters and can be categorized as proton density weighted, T1-weighted, and T2-weighted.

2.2.6 B₁ Mapping

B₁ mapping is a technique used to quantify the homogeneity of the RF distribution within an RF coil in an MR environment. B₁ mapping is a method used to analyze the RF field distribution and RF homogeneity in the designated field of view (FOV). There are a variety of B₁ mapping methods (36, 37) that are used to analyze the RF field in two-dimensional (2D) and three-dimensional (3D) views. Ultimately, researchers are determined to use a relatively quick acquisition time sequence with low SAR. At ultrahigh field (UHF), fewer B₁ methods can be used because of the challenges with SAR at higher fields. To avoid these challenges at UHF, some studies (38) prefer SatTFL as the preferred B₁ methodology because SatTFL uses minimal SAR and has a quicker acquisition time in comparison to other B₁ methods. Thus, in this dissertation our B₁ mapping technique is SatTFL.

2.2.6.1 Saturated Turbo Flash (SatTFL)

SatTFL is a B₁ mapping technique that uses ultrafast GRE sequences with six different flip angles. The results are fitted to the cosine function and post-processing is performed to generate the final B₁ map.

2.2.7 Thermal Heating in MRI

Thermal heating (sometimes called RF heating) in MRI is a technique used to capture the variation of temperature or electrical fields within a load inside an RF coil. The technique is used to validate and ensure that RF safety is considered in all experiments according to the necessary SAR and temperature-rise guidelines. There are several temperature mapping techniques used by researchers to determine the change in temperature. These methods include MR thermometry (capturing the phase before, during and after a heating experiment (39, 40)), using fiber thermal-optic probes (14, 39, 41, 42), and computational electromagnetic simulations that generate SAR and thermal maps. Recently, using numerical simulations to generate SAR maps has become more popular by researchers in the MRI field (40). However, increased and high SAR is not the concern for RF safety, it is the temperature increase and rise in the imaged load that is an RF safety concern.

Proton resonance frequency (PRF) MR thermometry (43) is a well-known method in MRI to visualize the temperature elevation; however, it is not widely used in ultrahigh field applications due to limited human studies at the time and challenges with inhomogeneous electric fields. Although PRF MR thermometry is not used for *in-vivo* human studies at UHF scanners, there are experimental UHF studies (44) that utilize phase mapping by constructing the phase difference between the baseline GRE phase map and post-RF-heating phase map.

2.3 MRI SYSTEM AND MR INSTRUMENTATION

There are many components that allow an MR scanner to successfully operate. The MR scanner is one of many components within the MR system. Most commercial and research scanners have a similar MR room setup to the configuration in Figure 2.5.

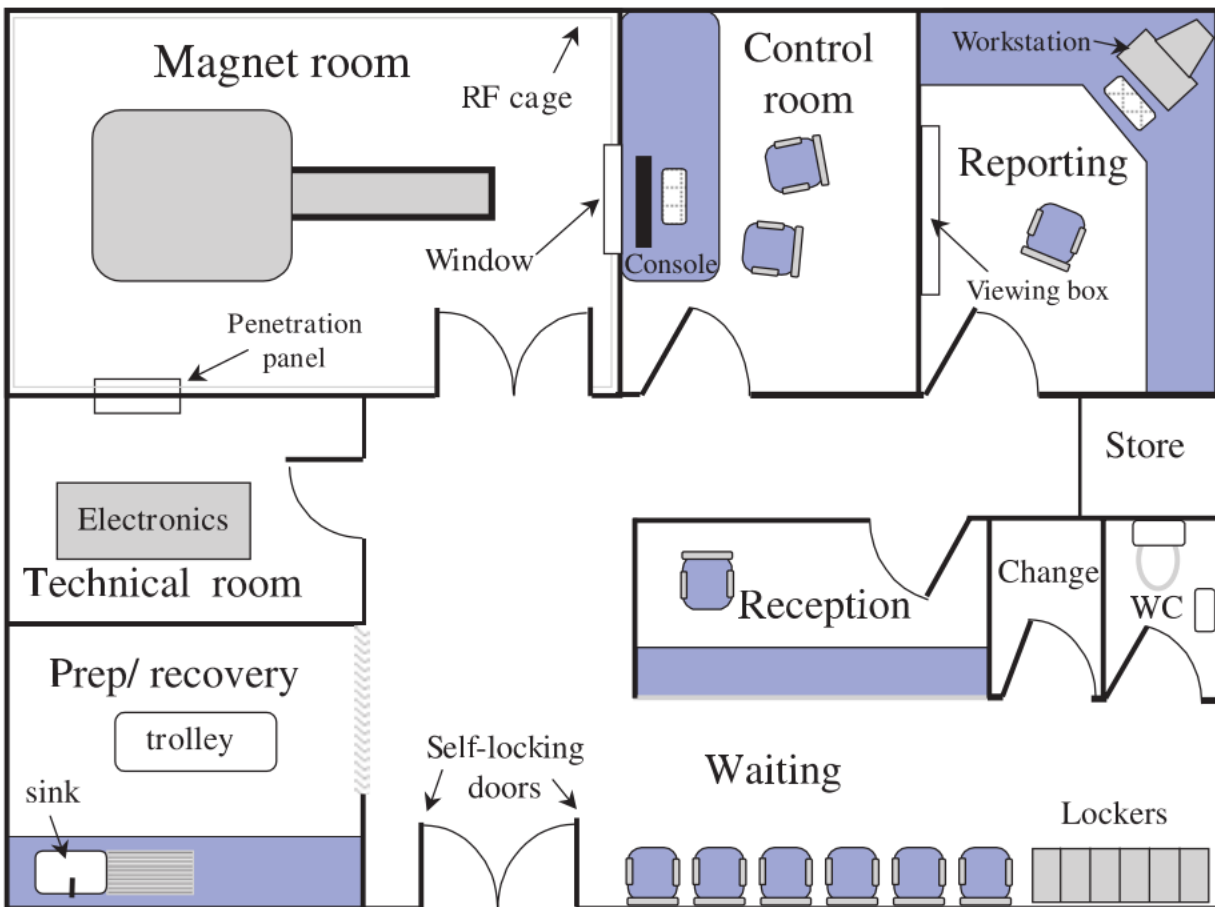


Figure 2.5. An example and visual representation of the conventional MR system and set-up with MR components (45).

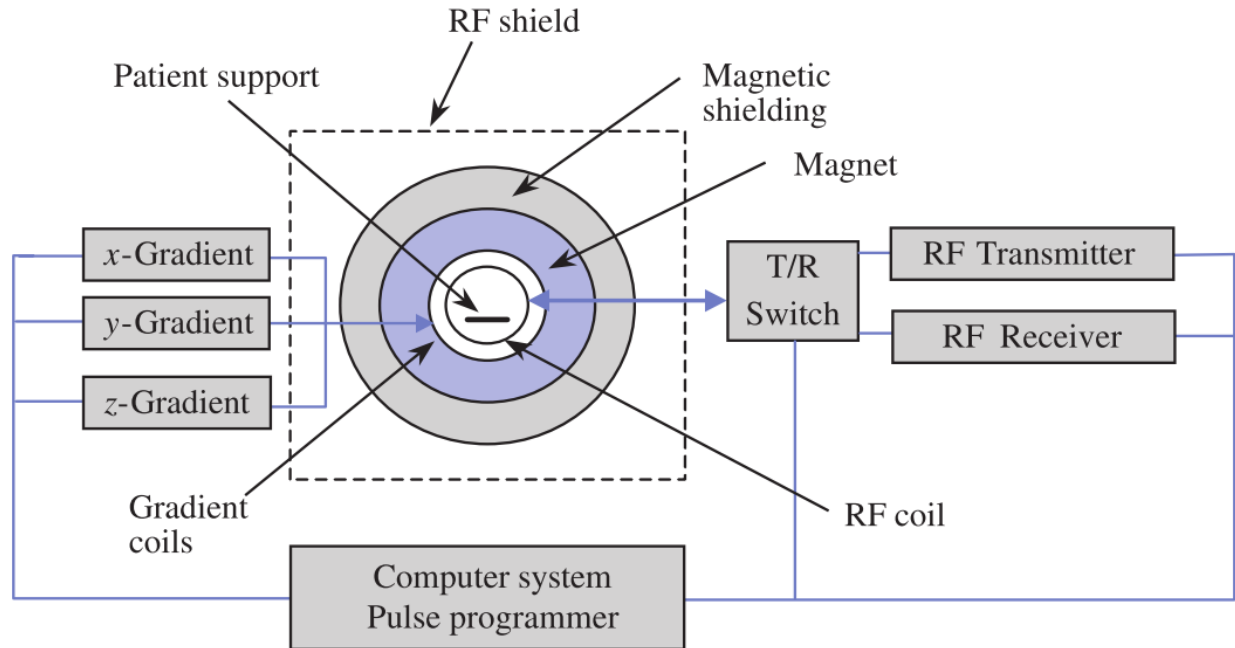


Figure 2.6. An illustration of the MRI scanner and its core MR instrumentation that includes its hardware and software (45).

The MR scanner requires the main magnet, RF shielding, gradient coils, magnet shielding, patient table, RF coil, T/R switch, RF transmitter, RF receiver, and the computer or console. The control room in an MR system holds the hardware that drives components of the MR system.

2.3.1 MR scanner

The MR scanner is a superconducting magnet at low- to UHF systems and housed inside of a scanner room. Figure 2.6 illustrates the instrumentation and equipment that is required to operate an MR scanner. MR scanners can operate as an open or closed bore. Closed bore scanners are used more for clinical high field MR systems and research UHF MR systems. Superconducting magnets need liquid helium to operate. The magnet experiences a ramp up performed by technical

MR field experts to allow the magnetic field strength of the magnet to be reached. Various devices are connected to the scanner to monitor the helium levels to avoid quenching. Quenching occurs when the superconductivity of the magnet is lost, the field becomes close to zero, and large amounts of helium are released as gas.

2.3.2 Gradient Coils

The RF field produces the B_1 field from the RF transmitter and the gradient coil. The gradient coil is a set of three individual magnets. The gradient coil dictates the location in all Cartesian directions and frequency of the imaged load. The gradient coils surround the bore of the MR scanner. Gradient coils are responsible for the spatial encoding within an MR sequence. The gradients produce the loud knocking when activated during a scan; thus, patients must protect their hearing during scans to prevent any ear damage.

2.3.3 Computer System and Console

The MR system is controlled and operated through the console shown in Figure 2.6. in this dissertation, the console uses Siemens' syngo.via MR VB17A operated through Microsoft Windows XP platform installed on the operating workstation.

2.3.4 Radiofrequency Coils

Radiofrequency (RF) coils are hardware devices (antennas) used in MRI to transmit, receive, or transmit and receive the RF signal by the resonating proton of interest to the Larmor frequency in

order to acquire an MR dataset (46-48). The RF coils' function is known and can respectively be labeled as transmit (TX) coil, receive (RX) coil, or transmit/ receive (TX/ RX) coil. To achieve maximum signal and an adequate MR image, RF coil designers tune the coils to the Larmor frequency (ω) or operational frequency of the magnet and match the coil equivalent or very close to 50Ω . The magnitude of the Larmor frequency can be found by scaling the gyromagnetic ratio (γ) by the magnetic field strength of the MRI, $\omega = \gamma B_0$. At 7 Tesla, the Larmor or operational frequency is 297.2 MHz. Also, the impedance of the RF coil must match the impedance of the receiver.

A multi-turn solenoid was the first RF coil and was developed for NMR experiments (49, 50). RF coils are often referred to as RF resonators. The resonant frequency is expressed as a function of

$$f = \frac{1}{2\pi\sqrt{LC}} \quad (2.8)$$

where f (Hz) is the resonant frequency, L (H) is the inductance, and C (F) is the capacitance of the coil. When a coil is designed, not only are its inductance and capacitance values of importance but also the RF coils geometry is critical and dependent on the desired application. RF coils can be categorized as surface coils or volume coils (51). Ackerman *et al.* (52) developed the first surface coil in 1980. Its advantage and benefit was its high sensitivity and in localized regions. Therefore, surface coils are preferred for applications that require high magnetization on the surface of the imaged volume. They are widely used for spectroscopy and great to image small animals such as mice. In human imaging, surface coils are ideal for imaging surfaces and the exteriors of the desired volume.

Biot-Savart's law determines the sensitivity in the design of the surface coil. The principle of Biot-Savart is the larger the region of interest (ROI), the deeper the signal may penetrate through

a given medium (48). However, an increased in the signals penetration in a given volume will increase noise. Thus, surface coils are designed by developing a coil that yields a desired penetration to the media.

Through the last few decades, RF coil design became more complex for high field strength applications. As the field strength of MR magnets increased volume coils that varied in geometry became a necessity to image throughout an entire volume. Similar to the design of surface coils, the design of volume coils applies the theory of sensitivity to decrease the noise of the MR image. Multiple loops are designed close together to combine the transmit field magnitude and decrease noise. Volume coils are used for transmission and obtaining homogeneity in a given volume.

Hayes *et al.* (53) developed the first birdcage resonator in 1984 while working within the General Electric (GE) Research and Development Center. The birdcage resonator is a popular commercial coil and coil design used in many commercial coils for clinical MR systems at 1.5T and 3T due to its ability to provide highly uniform circularly polarized (CP) magnetic fields at these fields strengths. Double tuned coils were later developed using the birdcage theory to have the coil resonate to two protons. Roschmann (54) later introduced the transmission line resonator.

2.3.4.1 History of UHF RF Coils

In the early 2000s, researchers began to explore the possibilities of MRI beyond 4T. Many research facilities began to develop their own RF coils for purely MR research testing and evaluation (55-61). Initially, birdcage and TEM coils were the popular UHF MR coil designs and their variants would later follow. Vaughan *et al.* (62) built on the developments of Roschmann's transmission line resonator (54) to produce the TEM resonator with 16 transmission line resonators within a resonant cavity. TEM resonators are characterized by improved homogeneity, higher Q

factor, multiple frequencies of operations, and not very significant dropping in SNR. The TEM volume design was later constructed and used at UHF for body, head, and extremities.

The goal of RF coil designers at UHF has always been to develop coils that take advantage of the benefits and minimize the challenges of UHF MRI. At UHF, there is no body coil to transmit the RF field. Thus, RF coil designers and simple RLC circuits are not useful because the EM fields are nonlinear. RF coil designers design separate transmit and receive coils or a combined transmit and receive coil for the desired physiological region.

In various chapters of this dissertation, namely Chapters 3.0 to 5.0, RF coils developed in our laboratory are verified and compared to commercial RF coils applied at 7T for UHF brain imaging.

2.4 RADIOFREQUENCY SAFETY

Patient safety is a priority for researchers and clinicians in all human medical imaging systems. In MRI, each successful scan is motivated by a common goal to minimize risk to the patient. MRI safety is categorized into several focus areas; yet, those safety regulations most relevant to this dissertation work are thermal heating and MRI artifacts(63).

As expressed, tissue heating is a concern in MRI and is a bioeffect of RF absorption. SAR assesses the safety of RF exposure to the biological tissue. Mathematically, SAR is given by the following:

$$SAR = \frac{\sigma |\overline{E}|^2}{\rho} \quad (2.9)$$

where σ is the conductivity of the tissue (S/m), ρ is the mass density of the tissue (kg/m³), and E is the electric field (V/m). SAR is computed for any 1g or 10gm of tissue. Numerical studies predict SAR and MR scanners monitor SAR during experimental MR scans. The SAR is monitored by the predicted electric field per patient, the RF pulse of the MR sequence, and the patient's characteristics such as weight and height (since the patient's exact constitutive parameters are not readily known. It is vital to accurately determine the patient's weight and height to allow the scanner to perform safe SAR predictions throughout the MR protocol that are within safety guidelines. The US Food and Drug Administration (FDA) and International Electrotechnical Commission (IEC) regulate guidelines for RF exposure to humans in the United States and Europe, respectively. The SAR limits regulated by the scanner are calculated over time Table 2.1 shows the guidelines of these federal agencies.

Table 2.1. Regulations of IEC and FDA guidelines on SAR and RF heating in human experimental studies for volume and local transmit RF coils (64, 65)

Limit	Volume Transmit Coils		Local Transmit Coils	
	Whole-Body Average	Head Average	Head, Trunk Local	Extremities Local
IEC (6-minute average time)				
Normal (all patients)	2 W/kg (0.5°C)	3.2 W/kg	10 W/kg	20 W/kg
First level (supervised)	4 W/kg (1°C)	3.2 W/kg	20 W/kg	40 W/kg
Second level (IRB approval)	> 4 W/kg (>1°C)	>3.2 W/kg	>20 W/kg	>40 W/kg
Localized heating limit	39°C in 10 g	38°C in 10 g	--	40°C in 10 g
FDA	4 W/kg for	3.2 W/kg for	8 W/kg in 1g	12 W/kg in 1g
	15 min	10 min	for 10 min	for 5 min

SAR is an indicator of the magnitude of the temperature rising in a given voxel of tissue and can be computed based on its dependence on bioheat equations.

Because the SAR value is patient dependent, it is a tremendous challenge to predict patient-specific SAR. Electric fields become heterogeneous at 3T, and the electric field's inhomogeneity increases with stronger field strengths. While MRI machines calculate the patient SAR during the scan, the value computed is inaccurate. The work of Bottomley demonstrates that in a 3T experimental study, there was a difference in the value of the thermal SAR and the SAR provided by the scanner(66). The thermal SAR was much lower than the scanner SAR. The manufacturers of the MRI system made the value much higher so that various clinical studies are considered safe. However, this presents an issue to researchers studying the effect of implanted devices in MRI systems where the exact SAR value is desired (67).

SAR is monitored within several MR safety applications. In this dissertation, the SAR calculations are explicitly focused on its calculations within commercial or in-house developed RF coils and inside the human head that is loaded within the coil. SAR is a useful tool to measure the thermal heating within the imaged load. Thermal heating can occur within an RF coil from the coupling of EM fields, physiological tissue thermal parameters, and patient factors such as tattoos and implants. Patients are screened to ensure that they are MR compatible. RF coils are assessed using SAR and thermal heating through various experimental validations such as measurements with fiber optic probes, MR thermometry, comparison to B_1^+ maps, and measurement of SAR (68).

2.5 MODELING ELECTROMAGNETIC FIELDS

Decades ago, modeling electromagnetic fields was a technique used to understand the phenomena of what was occurring between the induced currents in the load from an RF coil and the reception of RF fields in the receive antenna. The application of modeling electromagnetic fields has grown broadly and become a useful technique.

Today, researchers model electromagnetic fields in more applications than when MRI was initially developed. The technique is used to evaluate RF coils, RF safety, optimizing sequences, and parallel reception.

2.5.1 Designing and Evaluating RF Coils

At lower field strengths the RF coil and load have significantly smaller electrical sizes in comparison to the RF wavelength. It is easier to perform circuit analysis using Kirchhoff's law and Biot-Savart law at lower field strengths. However, at higher field strengths, modeling electromagnetic fields is a critical process in the analysis and performance of designing the RF coil. The magnetic field can no longer be calculated using Biot-Savart at higher field strengths. Instead, Maxwell's equations with applied boundary conditions must be used to figure out what the magnetic field distributions within the coil are respective to a load.

Modeling the electromagnetic fields allows the researcher to understand how the design of the coil works. The resonant modes generated by the electrical currents are modeled. The magnetic fields from each of these resonant modes are modeled. It is also important to note how the RF field distributions interact with the load, the quantified SAR, and SNR. All of these features are important characteristics of the RF coil.

2.6 FINITE-DIFFERENCE TIME-DOMAIN

2.6.1 Background

Numerical modeling is a prevalent technique used to solve unknown equations in various electromagnetics applications. MRI researchers use numerical modeling to determine the parameters required in the experimental setup before MRI scans and to assist in the design of MR instrumentation. The electromagnetic fields are accurate in determining the RF coil design and configuration (69) and RF safety analysis of an MR experiment. Finite-difference time-domain (FDTD), finite element method (FEM), the method of moments (MM), or various hybrid techniques are some of the more popular numerical methods used today.

In 1966, Kane Yee introduced the numerical method, FDTD (70). FDTD solves the solutions to time and space-dependent Maxwell equations. FDTD is a full-wave model used to predict the electromagnetic fields of a single system RF coil and load (71) or design the MR instrumentation. The technique uses a discretized version of Maxwell's equations in the time domain for a given number of iterations of time and space. FDTD uses the central finite-difference approximation to discretize the second order Maxwell's equations. In this dissertation, FDTD is applied to a 3-dimensional space for a single system RF coil and various loads.

2.6.2 Motivation for Choosing Finite-Difference Time-Domain

FDTD is used because of its ability to calculate a greater quantity of unknown parameters in a volume or surface while utilizing less memory in comparison to other numerical methods. As the electric and magnetic fields are computed for each time step, the field arrays are updated for each

iteration, and the memory is conserved by replacing the current time step values with the previous time step values. Other numerical methods that are commonly used such as the finite element method (FEM) and the method of moments (MM) do not have this capability. FEM and MM require the solutions to the matrix equations to be given, but FDTD does not have this requirement (28).

An in-house FDTD code (71), which was developed in our lab, is used to perform the numerical calculations needed to solve the number of unknowns regarding the electric and magnetic fields in the system. The code uses a combination of C programming language and MATLAB (The MathWorks, Inc., Natick, MA, USA) to model an array of the dielectric properties, the RF coil, the load, electric field, and magnetic fields at a given frequency. The RF coil and the load models one system like other works (13, 72). This system is defined as the computational grid of the model. The FDTD code is set to the resonant frequency of 297.2 MHz (7T) or 128 MHz (3T) in this dissertation. To ensure that the proper frequency is applied to the system, the Discrete Fourier Transform (DFT) is applied at each time step within the system. Formulation of the FDTD method is shown below for two equations used in this dissertation: Maxwell's Equations (Subsection 2.6.3) and Penne's Bioheat Transfer Equation (Subsection 2.6.4).

2.6.3 Formulation of Finite-Difference Time-Domain with Maxwell's Equations

Maxwell's equations (73) are linear, non-dispersive, and isotropic and are written below:

$$\nabla \times \vec{E} = -\frac{\partial \vec{B}}{\partial t} - \sigma_m \vec{H} \quad (2.10)$$

$$\nabla \times \vec{H} = \frac{\partial \vec{D}}{\partial t} + \vec{J} \quad (2.11)$$

$$\nabla \cdot \vec{D} = \rho_e \quad (2.12)$$

$$\nabla \cdot \vec{B} = \rho_m \quad (2.13)$$

where equations (2.10) to (2.13) are a function of space and time. While the magnitude of the magnetic field \vec{B} and the electric field \vec{D} in a linear, nondispersive, and isotropic material are defined as:

$$\vec{B} = \mu \vec{H} \quad (2.14)$$

$$\vec{D} = \epsilon \vec{E} \quad (2.15)$$

where the variables in equations (2.10) to (2.15) are defined as with their respective units:

\vec{B} - Magnetic Flux Density [Webers/ meters²],

\vec{E} - Electric Field [Volts/ meter],

\vec{H} - Magnetic Field [Amperes/ meter],

\vec{D} - Electric Flux Density [Coulombs/ meter²],

\vec{J} - Electric Current Density [Amperes/ meters²],

σ – Electric conductivity [Siemens/ meter],

ϵ – Electric Permittivity [Farads/ meter],

μ - Magnetic Permeability [Henrys/ meter],

ρ_e - Electric Charge Density [Coulombs/ meter³]

ρ_m - Magnetic Charge Density [Weber/ meter³].

To derive the FDTD equation for a lossy medium, Maxwell's equations are needed in 3D.

The difference equation is appropriately centered so that \vec{E} and \vec{H} fields are offset in time and space. Assuming that the equation is sourceless, the equations derived from Faraday's law and Ampere's law are seen below.

Assuming all $\frac{\partial}{\partial t} \frac{\partial}{\partial t}$ are finite, then FDTD must solve for \mathbf{H}_x , \mathbf{H}_y , \mathbf{H}_z , \mathbf{E}_x , \mathbf{E}_y , and \mathbf{E}_z .

Expansion of (2.10) in the rectangular coordinate system yields matrices in the form of

$$\nabla \times \vec{E} = \begin{pmatrix} \vec{a}_x & \vec{a}_y & \vec{a}_z \\ \frac{\partial}{\partial x} & \frac{\partial}{\partial y} & \frac{\partial}{\partial z} \\ E_x & E_y & E_z \end{pmatrix} \quad \text{and} \quad \nabla \times \vec{H} = \begin{pmatrix} \vec{a}_x & \vec{a}_y & \vec{a}_z \\ \frac{\partial}{\partial x} & \frac{\partial}{\partial y} & \frac{\partial}{\partial z} \\ H_x & H_y & H_z \end{pmatrix}$$

Expansion of the vector components of each matrix of the curl operators of (2.10) and (2.11) yield six coupled scalar equations. The matrix $(\nabla \times \vec{H})$ is separated in each direction in the rectangular coordinate system for \vec{H} .

In the x-direction:

$$\hat{a}_x: \mu \frac{\partial H_x}{\partial t} = \frac{\partial E_z}{\partial z} - \frac{\partial E_y}{\partial y} - \sigma_m H_x \quad (2.16)$$

In the y-direction:

$$\hat{a}_y: \mu \frac{\partial H_y}{\partial t} = \frac{\partial E_z}{\partial x} - \frac{\partial E_x}{\partial z} - \sigma_m H_y \quad (2.17)$$

In the z-direction:

$$\hat{a}_z: \mu \frac{\partial H_z}{\partial t} = \frac{\partial E_x}{\partial y} - \frac{\partial E_y}{\partial x} - \sigma_m H_z \quad (2.18)$$

The matrix $(\nabla \times \vec{E})$ is separated in each direction in the rectangular coordinate system for \vec{E} .

$$\text{In the x-direction:} \quad \hat{a}_x: \epsilon \frac{\partial E_x}{\partial t} = \frac{\partial H_z}{\partial y} - \frac{\partial H_y}{\partial z} - \sigma_e E_x \quad (2.19)$$

$$\text{In the y-direction:} \quad \hat{a}_y: \epsilon \frac{\partial E_y}{\partial t} = \frac{\partial H_x}{\partial z} - \frac{\partial H_z}{\partial x} - \sigma_e E_y \quad (2.20)$$

$$\text{In the z-direction:} \quad \hat{a}_z: \epsilon \frac{\partial E_z}{\partial t} = \frac{\partial H_y}{\partial x} - \frac{\partial H_x}{\partial y} - \sigma_e E_z \quad (2.21)$$

Equations (2.16) to (2.21) are scalar equations and are discretized using Yee's notation. A point in space represents $(x_i, y_i, z_i) = (i, j, k)$ and a function representative of both time and space

takes the form $F(x_i, y_i, z_i, t_n) = F^n(i, j, k)$. The function and vector \vec{F} is a component of a vector where $\vec{F} = (F_x, F_y, F_z)$. The discretized scalar equations yield

$$\begin{aligned} H_x(x_i, y_i, z_i, t_n) &= H_x^n(i, j, k); & H_y(x_i, y_i, z_i, t_n) &= H_y^n(i, j, k); & H_z(x_i, y_i, z_i, t_n) &= H_z^n(i, j, k); \\ E_x(x_i, y_i, z_i, t_n) &= E_x^n(i, j, k); & E_y(x_i, y_i, z_i, t_n) &= E_y^n(i, j, k); & E_z(x_i, y_i, z_i, t_n) &= E_z^n(i, j, k); \\ \sigma_m \rightarrow \sigma_m(x_i, y_i, z_i) &= \sigma_m(i, j, k); & \sigma_e \rightarrow \sigma_e(x_i, y_i, z_i) &= \sigma_e(i, j, k); & \varepsilon_r \rightarrow \varepsilon_r(x_i, y_i, z_i) &= \varepsilon_r(i, j, k); \end{aligned}$$

The space-time elements discretized formulas of finite difference have superscripts and subscripts for every element to distinct space and time. The subscript “i” corresponds to the spatial step in the + x-direction; the subscript “j” corresponds to the spatial step in the + y-direction; a, and subscript “k” corresponds to the spatial step in the + z-direction. The spatial step size is determined by the resolution of the selected image. The superscript “n” corresponds to the time step.

According to Yee’s (70) algorithm and theory, it is important to remember that the \vec{E} field and \vec{H} field should be staggered in space, but not time. By applying the central difference theorem, the discretized equations (2.16) to (2.21) have perfectly conducting boundary conditions and yield In the x-direction:

$$\begin{aligned} \widehat{a_x}: E_x^{n+1}\left(i + \frac{1}{2}, j, k\right) &= \left(\frac{2\varepsilon - \sigma_e \Delta t}{2\varepsilon + \sigma_e \Delta t}\right) E_x^{n+1}\left(i + \frac{1}{2}, j, k\right) + \left[\frac{2\Delta t}{2\varepsilon + \sigma_e \Delta t}\right] \left\{ \frac{1}{\Delta y} \left[H_z^{n+\frac{1}{2}}\left(i + \frac{1}{2}, j + \frac{1}{2}, k\right) - \right. \right. \\ &\quad \left. \left. H_z^{n+\frac{1}{2}}\left(i + \frac{1}{2}, j - \frac{1}{2}, k\right) \right] - \frac{1}{\Delta z} \left[H_y^{n+\frac{1}{2}}\left(i + \frac{1}{2}, j, k + \frac{1}{2}\right) - H_y^{n+\frac{1}{2}}\left(i + \frac{1}{2}, j, k - \frac{1}{2}\right) \right] \right\} \end{aligned} \quad (2.22)$$

In the y-direction:

$$\begin{aligned} \widehat{a_y}: E_y^{n+1}\left(i, j + \frac{1}{2}, k\right) &= \left(\frac{2\varepsilon - \sigma_e \Delta t}{2\varepsilon + \sigma_e \Delta t}\right) E_y^{n+1}\left(i, j + \frac{1}{2}, k\right) + \left[\frac{2\Delta t}{2\varepsilon + \sigma_e \Delta t}\right] \left\{ \frac{1}{\Delta z} \left[H_x^{n+\frac{1}{2}}\left(i + \frac{1}{2}, j, k + \frac{1}{2}\right) - \right. \right. \\ &\quad \left. \left. H_x^{n+\frac{1}{2}}\left(i + \frac{1}{2}, j, k - \frac{1}{2}\right) \right] - \frac{1}{\Delta x} \left[H_z^{n+\frac{1}{2}}\left(i + \frac{1}{2}, j + \frac{1}{2}, k\right) - H_z^{n+\frac{1}{2}}\left(i - \frac{1}{2}, j + \frac{1}{2}, k\right) \right] \right\} \end{aligned} \quad (2.23)$$

In the z-direction:

$$\widehat{a}_z: E_z^{n+1}\left(i, j, k + \frac{1}{2}\right) = \left(\frac{2\varepsilon - \sigma_e \Delta t}{2\varepsilon + \sigma_e \Delta t}\right) E_y^{n+1}\left(i, j, k + \frac{1}{2}\right) + \left[\frac{2\Delta t}{2\varepsilon + \sigma_e \Delta t}\right] \left\{ \frac{1}{\Delta x} \left[H_y^{n+\frac{1}{2}}\left(i + \frac{1}{2}, j, k + \frac{1}{2}\right) - H_y^{n+\frac{1}{2}}\left(i, j - \frac{1}{2}, k + \frac{1}{2}\right) \right] - \frac{1}{\Delta y} \left[H_x^{n+\frac{1}{2}}\left(i + \frac{1}{2}, j + \frac{1}{2}, k\right) - H_x^{n+\frac{1}{2}}\left(i, j - \frac{1}{2}, k + \frac{1}{2}\right) \right] \right\} \quad (2.24)$$

In the x-direction:

$$\widehat{a}_x: H_x^{n+\frac{1}{2}}\left(i, j + \frac{1}{2}, k + \frac{1}{2}\right) = \left(\frac{2\mu - \sigma_m \Delta t}{2\mu + \sigma_m \Delta t}\right) H_x^{n-\frac{1}{2}}\left(i, j + \frac{1}{2}, k + \frac{1}{2}\right) + \left[\frac{2\Delta t}{2\mu + \sigma_m \Delta t}\right] \left\{ \frac{1}{\Delta z} \left[E_y^n\left(i, j + \frac{1}{2}, k + 1\right) - E_y^n\left(i, j + \frac{1}{2}, k\right) \right] - \frac{1}{\Delta y} \left[E_z^n\left(i, j + 1, k + \frac{1}{2}\right) - E_z^n\left(i, j, k + \frac{1}{2}\right) \right] \right\} \quad (2.25)$$

In the y-direction:

$$\widehat{a}_y: H_y^{n+\frac{1}{2}}\left(i + \frac{1}{2}, j, k + \frac{1}{2}\right) = \left(\frac{2\mu - \sigma_m \Delta t}{2\mu + \sigma_m \Delta t}\right) H_y^{n-\frac{1}{2}}\left(i + \frac{1}{2}, j, k + \frac{1}{2}\right) + \left[\frac{2\Delta t}{2\mu + \sigma_m \Delta t}\right] \left\{ \frac{1}{\Delta x} \left[E_y^n\left(i + 1, j, k + \frac{1}{2}\right) - E_y^n\left(i, j, k + \frac{1}{2}\right) \right] - \frac{1}{\Delta z} \left[E_x^n\left(i + \frac{1}{2}, j, k + 1\right) - E_x^n\left(i + \frac{1}{2}, j, k\right) \right] \right\} \quad (2.26)$$

In the z-direction:

$$\widehat{a}_z: H_z^{n+\frac{1}{2}}\left(i + \frac{1}{2}, j + \frac{1}{2}, k\right) = \left(\frac{2\mu - \sigma_m \Delta t}{2\mu + \sigma_m \Delta t}\right) H_y^{n-\frac{1}{2}}\left(i + \frac{1}{2}, j + \frac{1}{2}, k\right) + \left[\frac{2\Delta t}{2\mu + \sigma_m \Delta t}\right] \left\{ \frac{1}{\Delta y} \left[E_x^n\left(i + 1, j + \frac{1}{2}, k\right) - E_x^n\left(i, j, k + \frac{1}{2}\right) \right] - \frac{1}{\Delta x} \left[E_y^n\left(i + 1, j + \frac{1}{2}, k\right) - E_y^n\left(i, j + \frac{1}{2}, k\right) \right] \right\} \quad (2.27)$$

where μ , σ_e , and σ_m are material parameters.

Yee's algorithm is used to compute the electric and magnetic fields concerning time and space while using the coupled Maxwell curl equations. Thus, the \vec{E} field should be surrounded by 4 \vec{H}

field and vice versa. The \vec{E} and \vec{H} field are a function of time, which demonstrates a ‘leapfrog’ effect as shown in Figure 2.7.

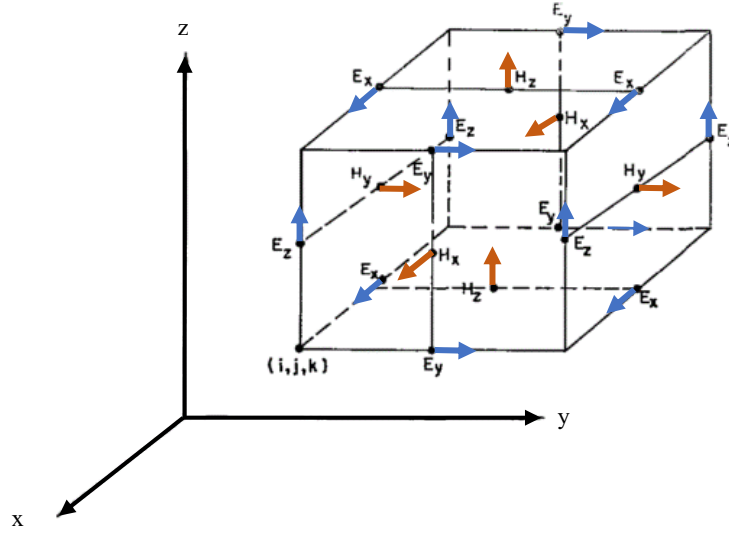


Figure 2.7. Yee space lattice (70) – The electric and magnetic field components in space. The \vec{E} field components are represented by the blue arrows and placed in the middle of the Yee space and the H-components are represented by orange and placed in half steps on the center faces.

At a given space and time, all \vec{E} field components are computed and stored in memory while using the previous stored \vec{H} data.

Next, the \vec{H} field in that given space are computed and stored in memory using the previously stored \vec{E} . It would continue to compute the next \vec{E} with the recently computed \vec{H} . Once the final time step is reached, the cycle would end.

The equations are central-difference of second-order accuracy. The equations are then converted to a discrete point in the grid and discrete point in time so that the algorithm can be developed and MATLAB friendly.

2.6.3.1 Boundary Conditions

Boundary conditions are needed to create a finite domain for the computer to be able to run Yee's algorithm. Having perfectly matching boundary conditions ensure that the tangential components of the electric field and the normal component of the magnetic field vanish. Creating a finite domain is important because it is impossible to calculate the equations for an infinite time. Thus, the values are made finite so that the equation is solvable.

2.6.3.2 Stability Criterion

There are properties of linear time-invariant systems, in which stability is required. The given grid must have space elements such that the electric field does not increase dramatically. Thus, the dimensions of x, y, and z are equal. Also, the rectangular dimension of the lattice space must be an incremental fraction of the wavelength. To have a rigorous stability criterion,

$$\sqrt{(\Delta x)^2 + (\Delta y)^2 + (\Delta z)^2} > c\Delta t = \sqrt{\frac{1}{\epsilon\mu}}\Delta t \quad (2.28)$$

where c is the light's velocity. If c_{\max} is the maximum of the light's velocity (2.28) becomes

$$\sqrt{(\Delta x)^2 + (\Delta y)^2 + (\Delta z)^2} > c_{\max}\Delta t \quad (2.29)$$

Chapters 4.0 to 5.0 of this dissertation discusses how the FDTD method is used to assist MRI experimental studies.

2.6.4 Formulation of Finite-Difference Time-Domain with Penne's Equations

Penne's bioheat transfer equation (74) is written below:

$$\rho c_p \frac{dT}{dt} = \nabla \cdot (k\nabla T) + A_0 - B(T - T_b) + \rho SAR \quad (2.30)$$

where C_p (J/kg °C) denotes the specific heat (the amount of heat per unit mass required to raise the temperature by one degree Celsius), K (J/m s °C) denotes the thermal conductivity (the property of a material that indicates its ability to conduct heat), A_0 (J/m³ s) denotes the basal metabolic rate (the minimum calorific requirement needed to sustain life in a resting individual), and B (J/m³ s °C) denotes the blood perfusion coefficient. The initial body temperature T_b was set to 37°C for the perfused segmented *in-vivo* human head model and 18.00°C for all phantoms models.

A point in space represents $(x_i, y_i, z_i) = (i, j, k)$ and a function representative of both time and space takes the form $T(x_i, y_i, z_i, t_n) = T^n(i, j, k)$. The spatial steps in the discretized bioheat equation are represented as:

$$\Delta x = \Delta y = \Delta z = \Delta \quad (2.31)$$

The bioheat equation (2.30) are central-difference of second-order accuracy. The equation (2.30) is converted to a discrete point in the grid and discrete point in time as shown through the equations below:

$$\begin{aligned} \nabla^2 T(i, j, k) &= \frac{\partial T(i, j, k)}{\partial x^2} + \frac{\partial T(i, j, k)}{\partial y^2} + \frac{\partial T(i, j, k)}{\partial z^2} \\ &= \frac{1}{\Delta^2} [T(i+1, j, k) + T(i-1, j, k) + T(i, j+1, k) + T(i, j-1, k) + \\ &\quad T(i, j, k+1) + T(i, j, k-1) - 6T(i, j, k)] \end{aligned} \quad (2.32)$$

By applying equation (2.32) into equation (2.30), the equation now yields the following equation:

$$\begin{aligned} \rho(i, j, k) \times c(i, j, k) \frac{T^{n+1}(i, j, k) - T^n(i, j, k)}{\Delta t} &= \\ &= \frac{K(i, j, k)}{\Delta^2} [T^n(i+1, j, k) + T^n(i-1, j, k) + T^n(i, j+1, k) + T^n(i, j-1, k) + \\ &\quad T^n(i, j, k+1) + T^n(i, j, k-1) - 6T^n(i, j, k) + A_0(i, j, k) \\ &\quad - B(i, j, k) \times (T^n(i, j, k) - T_b) + p(i, j, k) \times SAR(i, j, k)] \end{aligned} \quad (2.33)$$

To solve $T^{n+1}(i, j, k)$, equation (2.34) is transformed to yield the following equation:

$$\begin{aligned}
T^{n+1}(i, j, k) = & \left[1 - \frac{6K(i, j, k)\Delta t}{\rho(i, j, k)C_p(i, j, k)(\Delta)^2} - \frac{B(i, j, k)\Delta t}{\rho(i, j, k) \times C_p(i, j, k)} \right] T^n(i, j, k) \\
& + \frac{\Delta t K(i, j, k)}{\rho(i, j, k) \times C_p(i, j, k)(\Delta)^2} [T^n(i+1, j, k) + T^n(i-1, j, k) + T^n(i, j+1, k) \\
& + T^n(i, j-1, k) + T^n(i, j, k+1) + T^n(i, j, k-1)] \\
& + \frac{\Delta t}{\rho(i, j, k) \times C_p(i, j, k)} [A_0(i, j, k) + B(i, j, k)T_b + p(i, j, k) \times \text{SAR}(i, j, k)]
\end{aligned} \tag{2.34}$$

2.6.4.1 Boundary Conditions

As mentioned in Section 2.6.3.1, boundary conditions are set to make the bioheat differential equation solvable. When performing numerical temperature studies, the three mechanisms of heat transfer are considered being convection, conduction, and radiation. For our application. The boundary conditions applied to the bioheat equation listed in (2.35) is:

$$k \frac{dT}{dn}(x, y, z) = -H_a(T_{x,y,z} - T_a) \tag{2.35}$$

where H_a is the convection transfer coefficient that is valued at $20 \text{ J/m}^2 \text{ s } ^\circ\text{C}$ (75). T_a is the ambient temperature and has a value of 18°C from an averaged ambient temperature inside of the bore throughout the calendar year at our research facility.

To obtain the minimum boundary along x-direction, equation (2.36) is discretized as

$$K(i_{\min} + 1, j, k) \times \frac{T(i_{\min}, j, k) - T(i_{\min} + 1, j, k)}{\Delta x} = -H_a T(i_{\min}, j, k) + T_a H_a \tag{2.36}$$

Equations (2.33) and (2.31), $T(i_{\min}, j, k)$ is written as:

$$T(i_{\min}, j, k) = \frac{K(i_{\min} + 1, j, k) \times T(i_{\min} + 1, j, k)}{K(i_{\min} + 1, j, k) + H_a \Delta} + \frac{T_a H_a \Delta}{K(i_{\min} + 1, j, k) + H_a \Delta} \tag{2.37}$$

All directions of the boundary conditions are represented in equations (2.38) to (2.42) and are presented below:

$$T(i_{\max}, j, k) = \frac{K(i_{\max}-1, j, k) \times T(i_{\max}-1, j, k)}{K(i_{\max}-1, j, k) + H_a \Delta} + \frac{T_a H_a \Delta}{K(i_{\max}-1, j, k) + H_a \Delta} \quad (2.38)$$

$$T(i, j_{\min}, k) = \frac{K(i, j_{\min}+1, k) \times T(i, j_{\min}+1, k)}{K(i, j_{\min}+1, k) + H_a \Delta} + \frac{T_a H_a \Delta}{K(i, j_{\min}+1, k) + H_a \Delta} \quad (2.39)$$

$$T(i, j_{\max}, k) = \frac{K(i, j_{\min}-1, k) \times T(i, j_{\min}-1, k)}{K(i, j_{\min}-1, k) + H_a \Delta} + \frac{T_a H_a \Delta}{K(i, j_{\min}-1, k) + H_a \Delta} \quad (2.40)$$

$$T(i, j, k_{\min}) = \frac{K(i, j, k_{\min}+1) \times T(i, j, k_{\min}+1)}{K(i, j, k_{\min}+1) + H_a \Delta} + \frac{T_a H_a \Delta}{K(i, j, k_{\min}+1) + H_a \Delta} \quad (2.41)$$

$$T(i, j, k_{\max}) = \frac{K(i, j, k_{\max}-1) \times T(i, j, k_{\max}-1)}{K(i, j, k_{\max}-1) + H_a \Delta} + \frac{T_a H_a \Delta}{K(i, j, k_{\max}-1) + H_a \Delta} \quad (2.42)$$

2.6.4.2 Stability Criterion

Numerical stability is a necessity to ensure equation (2.30) is solvable. Thus, the time step Δt is used to satisfy equation (2.43) (76)

$$\Delta t \leq \frac{2\rho C_p \Delta^2}{12K + b\Delta^2} \quad (2.43)$$

The value of the time step is set by the air.

2.7 ANATOMICALLY DETAILED HEAD MODELS/ PHANTOMS

The use of anthropomorphic phantoms was necessary as early as the 1960's to assess the safety of ionized imaging techniques (77, 78) and as time progressed researchers realized the need to have imaging phantoms for other imaging modalities. Recent findings show how researchers and engineers use anatomical phantoms in numerical and experimental studies to help investigate the behavior of the interaction of RF pulses and biological tissue(s) at higher electromagnetic frequencies. The most recent findings of a physical, realistic, multi-tissue anthropomorphic human head phantom for MRI only and ultra-high field MRI is by Graedel (14). This work builds on the

development of previous realistic phantoms (14, 22, 79) and has comparable simulations and experiments. Before these works, the CHEMA (24) phantom was the most anthropomorphic phantom by its shape and single compartment representative of averaged dielectric properties of all tissues in the human head at 7T. Previous works (79) and most commercial whole-body scanners provide a one compartment cylindrical or a spherical phantom that may be filled with water or a soluble solution as shown in Figure 2.8. It should be noted that these works (14, 22, 79) did not have comparable simulations to the *in-vivo* high field and ultra-high field human experiments because these studies chose not to incorporate *in-vivo* comparison. It can be concluded that the path forward to understanding the challenges of ultra-high field MRI are to further the research of most recent works (14).



Figure 2.8. Basic spherical and cylindrical MRI loading phantoms at General Electric Healthcare (80).

The development of a physical multi-compartment head phantom with more than four compartments, to-date, is not known. Therefore, the proposed eight compartment head phantom

and our preliminary work (9) presents an expansion in the research and development of MR safety protocol and phantom head design. Unlike most realistic phantoms, the proposed work is segmented and prototyped from the T1-weighted MR images of a volunteer, and the final phantom will be compared to the same volunteer. Other realistic phantoms do not make phantom MR comparisons to the MR images on which the phantom evolved. The initial prototype used liquids instead of gels to represent the desired compartments' electromagnetic properties. The benefit of using liquids over gels is that the project is more versatile. However, the gels were used for the thermal studies in Chapters 3.0 and 5.0.

However, the uniqueness in the design of the head phantom of this dissertation is that the phantom has eight (22) chambers that include more compartments of the human head than previous work (14) and are comparable to the volunteer from which the phantom was modeled. This novel design is far more relative to the real-life applications of the interaction of the RF fields and the human head than what one or four tissue phantoms do.

2.8 NONLINEAR ALGORITHMS FOR RF SHIMMING

Linear and nonlinear problems use numerical analysis to solve an equation for a set of unknown variables. Nonlinear problems are either unconstrained or constrained. In this dissertation, nonlinearly constrained algorithms are used in Appendix C (on page 256) to optimize the inhomogeneity in the magnetic field and minimize the SAR. The number of unknowns to the problem is large with several variables that can be altered. Thus, it is easier to solve the problem by constraining it to a set of problems that can be solved.

Typical nonlinear constrained problems are of the form

$$\begin{aligned} &\text{minimize} && f(\mathbf{x}) \\ &\text{subject to} && h_i(\mathbf{x}) = 0, \quad i = 1, 2, \dots, m \\ & && g_j(\mathbf{x}) \leq 0, \quad j = 1, 2, \dots, r \\ & && \mathbf{x} \in S \end{aligned} \tag{2.44}$$

\mathbf{X} is an n -dimensional of unknown variables (i.e. $\mathbf{x} = (x_1, x_2, x_3 \dots x_n)$) and \mathbf{f} , \mathbf{h}_i and \mathbf{g}_j are real-valued functions of the n -dimensional \mathbf{x} variables. The function $\mathbf{f}(\mathbf{x})$ is the objective function and other equations are the functional constraints. A solution in \mathbf{x} that satisfies the constraints is said to be feasible.

The goal of the minimization optimization is to find a local minimum. If the functional constraints are active, then the local minimum is found in the domain of \mathbf{x} .

In this dissertation, the objective function is defined by the user in the parallel transmission RF toolbox (Appendix C on page 256) to minimize the magnetic field while constraining the SAR and power. The function chooses a mathematical operation to alter the total magnetic field in the selected region of interest where the magnitude of each voxel of tissue is based on the RF excitations of active sources in the RF coil. The constraints are set by the user to constrain the magnitude of the selected voxels of tissues. The object function and constraints are written as functions in MATLAB.

There are a variety of nonlinear algorithms that are chosen based on the criteria of the problem. In this dissertation, MATLAB's library of nonlinear algorithms is used to optimize the magnetic fields and minimize the SAR.

3.0 DEVELOP AN ANTHROPOMORPHIC HETEROGENEOUS HEAD PHANTOM THAT IS EVALUATED AND CHARACTERIZED THROUGH EXPERIMENTAL MRI STUDIES AT 7T

The work within this chapter was published and featured as a first author in PLoS One on 14th August 2017.

3.1 INTRODUCTION

Phantoms are numerical and/or physical models that represent the characteristics of some specified human anatomy (81-84). Phantoms are an inexpensive approach to testing several electromagnetic applications, specifically various medical diagnostic imaging tools and wireless communication applications (83, 85, 86). Recent studies demonstrate how researchers use anthropomorphic phantoms in numerical and experimental studies as one of the many resources that help investigate

the behavior of the interactions of electromagnetic (EM) fields and biological tissue(s) at varying electromagnetic frequencies (39). While electromagnetic numerical modeling has been the greatest resource to understand and analyze the interaction of electromagnetic fields and biological tissue(s) (13, 71, 87-90), in the last few years, experimental phantoms are increasingly becoming a useful resource in conjunction with EM modeling (14, 85).

The design of physical phantoms has evolved over the years to verify the mimicry of a real patient or customer environment with the electromagnetic device in order to minimize the error in modeling the physical experiment. While the evolution and usage of physical phantoms is endless in electromagnetic applications, in this chapter, we will narrow our focus on how to develop and test a physical and realistic head phantom using magnetic resonance imaging (MRI/MR). We recommend a method to design and fabricate a physical anthropomorphic heterogeneous head phantom using 3D printing technology.

3.1.1 MRI Phantoms

MRI phantoms are used to analyze, evaluate, and calibrate the MRI system and its instrumentation prior to conducting tests on humans. MRI phantoms also allow researchers to understand the phenomena of the interaction of electromagnetic waves and biological tissues most especially at high field strengths where these interactions are difficult to measure and to interpret (72, 87).

3.1.2 Prior Work in Developing Electromagnetically-Equivalent Head-Phantoms

Most designed and commercial phantoms are typically homogenous, simple in shape, and containing homogenous liquid. Today, most commercial whole-body MRI scanners provide a

one-compartment spherical phantom filled with saline water. While studies supported by MR companies find homogeneous commercial phantoms to offer an acceptable quality assurance (QA) to test the MRI system, anthropomorphic shaped phantoms are typically needed to go beyond QA such as mimicking a human experiment. Furthermore, while commercially available homogeneous phantoms are suitable resources for analysis and evaluation of lower field MRI systems, they are not typically viable for characterizing the electromagnetic-biological interactions at higher field strengths. At higher field strengths, the electromagnetic fields produced by MRI radiofrequency (RF) antennas become much more dependent on their interactions with biological tissues due to the higher operational frequency and consequently, the RF wavelength is shortened (91).

In the early 2000s, studies (20, 24, 92) designed and used electromagnetic anthropomorphic homogeneous head phantoms. An anthropomorphic homogeneous head phantom, Specific Anthropomorphic Mannequin (SAM) (92), is a commonly used head phantom in many wireless communication application studies. The CHEMA (24) phantom and SAM were the most common physical anthropomorphic homogeneous phantoms used to quantify a real-life comparison of RF absorption. Safety protocols and standards of various electromagnetic committees within professional societies have approved physical homogeneous phantoms. Nonetheless, there is a need to research the feasibility of designing more anthropomorphic heterogeneous phantoms for applications that require accurate specific absorption rate (SAR) testing, analysis of the interaction of RF fields and biological tissue(s), and direct comparisons with *in-vivo* studies. IEEE Standards Association's (IEEE-SA) standards and recommendations of IEEE SA - 1528-2013 (92) recommends the criteria for the design of an anthropomorphic head phantom. Although study (92) states that heterogeneous head models are difficult to construct, studies (14, 15, 86) indicate the feasibility of constructing an anthropomorphic heterogeneous head phantom and build on the

development of previous realistic heterogeneous phantoms (19, 22, 23, 93, 94). The results of studies (14, 15, 86) support the finding (92) that heterogeneous phantoms are more accurate. Thus, various electromagnetic applications/ safety protocols/ standards will benefit from 1) describing the methodology of developing and 2) validating the results associated with, anthropomorphic heterogeneous head phantoms that can be tailored to a specific research lab and/ or an industry application.

Although to our knowledge the findings from Graedel *et al.* (14) is the most comparable to this proposed work, the comparison of an anthropomorphic heterogeneous phantom to human head on which the phantom was prototyped does not exist. To further research the comparison mentioned above, this chapter shares the findings of such a comparison with an increased number of compartments filled with biologically equivalent electromagnetic liquids. While the findings of studies (14, 24, 86) are helpful, there is a critical need to further develop anthropomorphic heterogeneous head phantoms so that researchers make realistic findings in various electromagnetic medical applications at varying frequencies.

3.1.3 3D Printing a Tool for Physical Phantom Construction

3D printing is becoming an attractive tool within the fields of medicine, science and engineering in a variety of applications. Specifically, within the bioengineering field, 3D bioprinting is commonly used in tissue and organ engineering (94); and in the construction of bioprinted organs and anthropomorphic phantoms (95) of the human anatomy. Various imaging modalities (X-Ray, CT, MRI, etc.) can be incorporated to examine human anatomy and help in producing a physical model of the imaged tissue. Computer-aided design (CAD) software can also be used to accurately

reproduce the imaged tissues from a file that contains the surface meshes and contours of the imaged tissues.

In this chapter, we propose a methodology that develops a realistic anthropomorphic heterogeneous head and upper shoulder phantom through 3D printing that will be used as an application to various electromagnetic applications. The methodology is successfully evaluated on a Siemens MAGNETOM® (Erlangen, Germany) 7T whole-body scanner with the head phantom centered within an RF head coil and compared to other phantoms and the *in-vivo* volunteer from which it evolved. In addition, this chapter highlights a methodology to evaluate the performance of the designed phantom through numerical and experimental studies performing specific electromagnetic applications — scattering parameters (S-Matrix), B_1 mapping and EPI applications. An anthropomorphic heterogeneous head phantom results are compared to a spherical and anthropomorphic homogeneous head phantom filled with water and a soluble, mimicked brain solution.

3.2 MATERIALS AND METHODS

The design of the anthropomorphic heterogeneous head phantom follows a workflow shown in Figure 3.1. The workflow is intended to be used for designing an anthropomorphic heterogeneous phantom of any physiological representation. This section outlines each step within the general workflow.

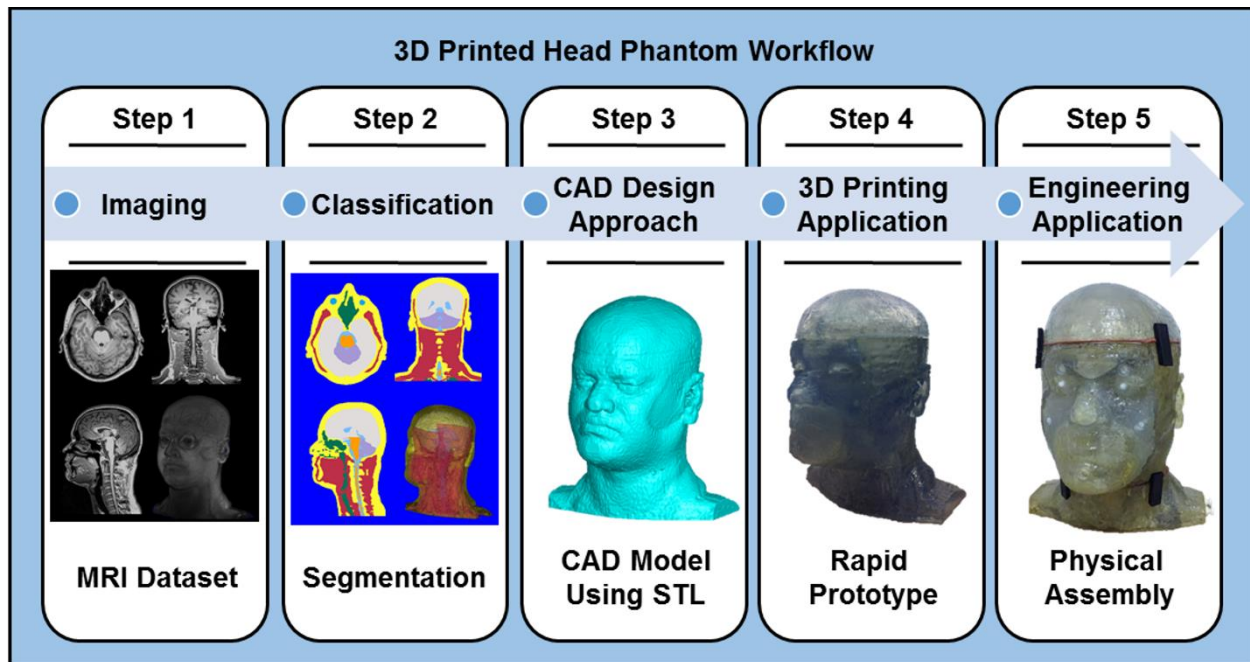


Figure 3.1. A General Workflow to Design and Fabricate an Anthropomorphic Heterogeneous Head Phantom Using 3D Printing.

Step 1. Acquiring 3D images of the human head. The physical phantom’s application and functionality determines the choice of using a single or a combination of imaging modalities (i.e. MRI, CT, X-Ray, etc.)

Step 2. Segmentation. Segmentation – a design approach used to classify tissues within the imaged dataset – requires the developer to have the guidance of an expert in physiology or a physiological atlas in order to properly classify the tissues. Software that offers automatic segmentation algorithms should be used through most of the segmentation process. To obtain a geometric mesh of the classified tissues, the segmented data should be in a proper format that is compatible with CAD software and 3D printing software.

Step 3. Modifying the design of the phantom for suitable 3D printing. Specifications of 3D printing such as type and resolution should be considered during the design process to achieve a rapid prototype with limited errors.

Step 4. Analyzing 3D printing techniques. Issues regarding the 3D printing technology that is most suitable for the phantom should be considered. These include cost, material durability, compatibility of the material with the phantom's application, and material printing resolution. Table 3.1 within study (96) provides a helpful summary of various 3D printers and each 3D printing materials' corresponding characteristics.

Step 5. Physical assembly of the head model. Adequate steps for facilitating the design and assembly in the CAD software can minimize the extensive manual assembly efforts of the physical phantom.

The following represents the developmental steps for developing our anthropomorphic heterogeneous human head phantom.

3.2.1 Images Acquired

An MR dataset is acquired using 3D magnetization-prepared rapid gradient-echo (MPRAGE) sequence because of its ability to offer excellent structural contrast in order to appropriately segment various tissue (93, 97, 98). The MR images were acquired from a healthy adult, male, human volunteer using a Siemens MAGNETOM TIM Trio® 3T whole-body scanner (Erlangen, Germany) at University of Pittsburgh Medical Center. The images are isotropic, T1-weighted with the following parameters: FOV: 320 x 320 mm²; TE: 2.62 ms; TR: 2110 ms; TI: 1100 ms; FA: 8°; BW: 200 Hz/pixel; Resolution: 1.0 x 1.0 x 1.0 mm³).

3.2.2 Phantom Segmentation, Design and Fabrication

An eight-tissue compartment head phantom was segmented and developed from the 3T MRI dataset as shown in Figure 3.2. To obtain an anatomically detailed human head model, tissues were labeled and automatically segmented using iSeg (ZMT Zurich MedTech AG, Zurich, Switzerland) segmentation software. To achieve accurate labeling, a human head atlas (97) was used to properly classify the tissues and segment the dataset as shown in Figure 3.2. The head phantom compartments consist of eight grouped classified tissues namely: brain, brainstem, eyes, air cavities, cerebellum, cerebrospinal fluid (CSF), muscle, and the remainder volume being a combination of the fat, bone, and skin. The classification of the tissues was distinguished by relatively similar constitutive parameters and the ability to fabricate the model. We combined, for instance, the white matter, grey matter and the CSF—in the vicinity of the grey and white matter—and classified the grouped tissue as “brain”. Similarly, we used the same logic for the “eye”, which is a combination of the physiological tissues known as the lens, vitreous humor, cornea and sclera. Once classified, the tissues were exported from iSeg as surface mesh objects in STereoLithography (STL) format and voxel matrices in MATLAB (mat) format.

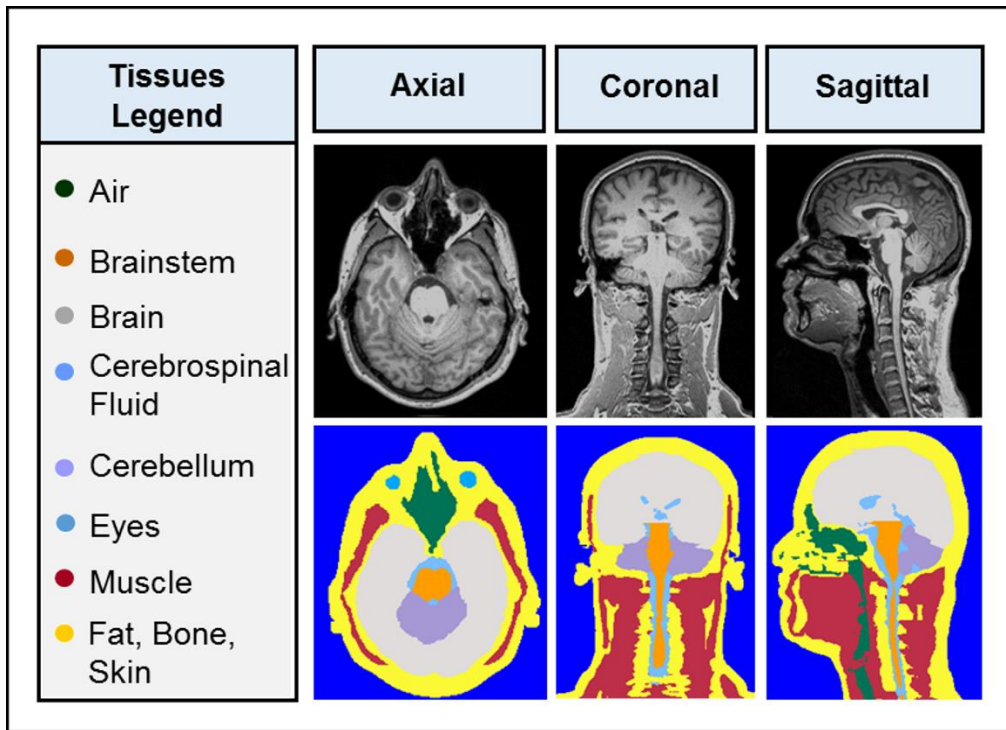


Figure 3.2. Medical Data Acquisition and Segmentation. A 3T MRI scan with $1.0 \times 1.0 \times 1.0 \text{ mm}^3$ resolution was segmented and divided into eight individual tissues. Each segmented tissue is listed with the corresponding tissue segmentation color within the tissue legend. The pictured MRI dataset and segmented tissues are shown in the mid axial, coronal and sagittal views. Table 3.1 lists the physiological tissues that were used to classify the tissues in the legend.

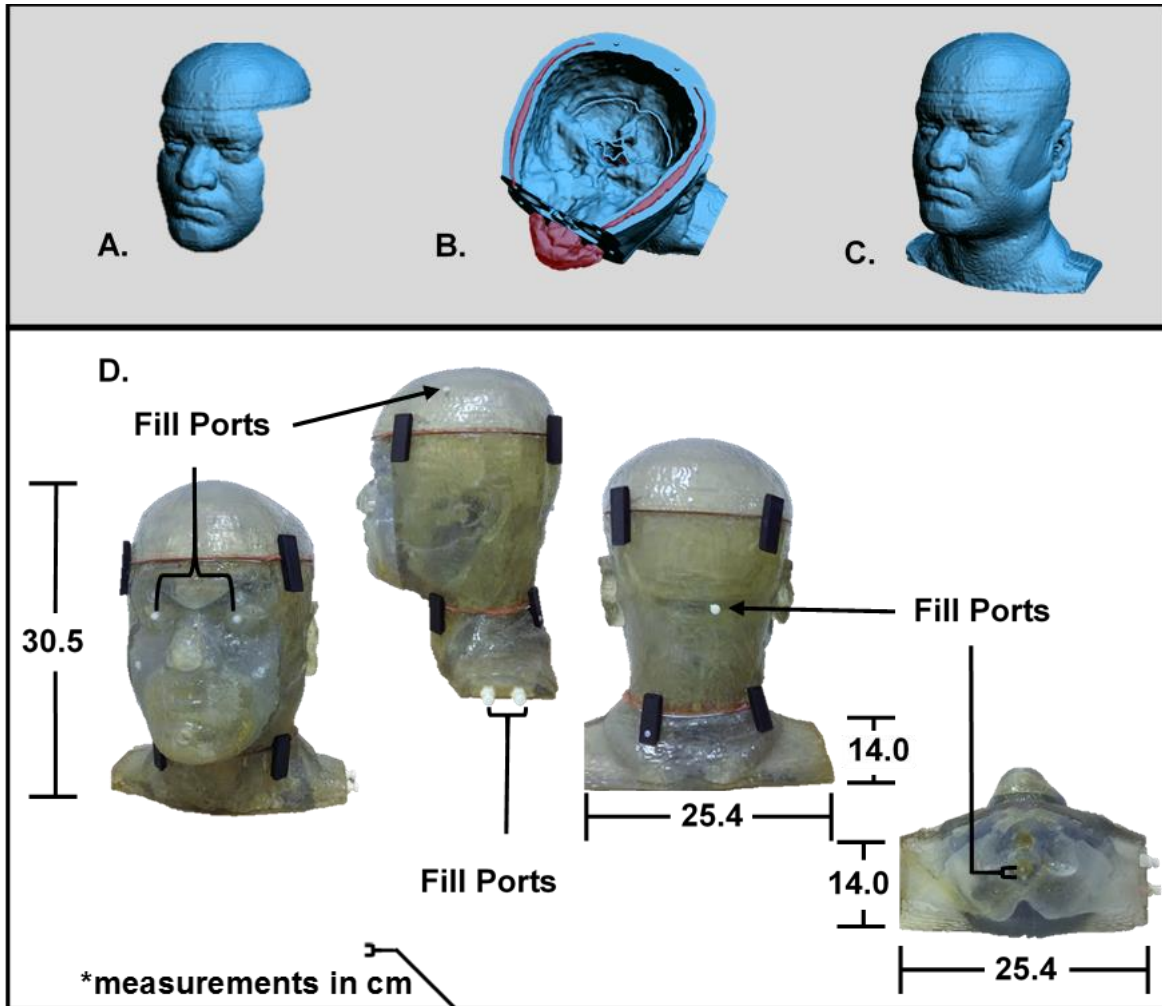


Figure 3.3. Phantom Design and Fabrication of Physical Phantom Model. Views of the shelled CAD files (A-C) which were developed in order to make volumetric cavities of the designated biological tissues that were segmented from a 3T MRI dataset. Views of the rapid prototype model (D) show the head phantom printed with stereolithography (SLA) resin. The physical head phantom dimensions are 304.8 mm tall, 254.0 mm long and 140.0 mm wide. The filling-ports are highlighted by arrows indicating the locations at which the fluids, resembling various tissue types, enter the phantom.

Using 3D CAD software (Geomagic Studios 2012 (Geomagic, Morrisville, North Carolina)), each compartment was designed to reserve the mixture of the desired tissue over time

as seen in Figure 3.3A– Figure 3.3C. The wall thickness of each tissue compartment and the molding compartment - combination of fat, bone and skin - were rendered and later printed using stereolithography (SLA) resin (DSM Somos® WaterShed® XC 11122 (Elgin, Illinois)) with the 3D Systems Viper™ si2 3D printer (3D Systems, Valencia, California). Six compartments are refillable with fluid through chambers that were positioned within each of the designated tissue compartments. The other two compartments are the molding compartment and the air cavities.

The cured SLA resin material is hydrophobic and durable to external and internal pressures. Among all of the 3D printing materials available, the DSM Somos® WaterShed® XC 11122 best fits the need to preserve the liquid with time. We tried polycarbonate material in the fabrication of a single-compartment, anthropomorphic homogeneous head phantom. The polycarbonate material is not hydrophobic, and it is porous. With time, the liquid evaporated from the inside and crystalized on the exterior of the model. This material, however, was useful for the study (15) that utilized ABS material and a waterproof spray coating or other studies that used agar to mimic the biological tissues. In contrast, an application of waterproof spray coating is unnecessary with the SLA material used in this study.

The physical head phantom model was designed and printed in five separate parts in order to manually remove the inner structural supports that come out with 3D printing. Leaving the structural supports inside of the model is undesired because it causes artifacts and bubbles within each tissue compartment leading to less accurate approximation of the electromagnetic fields produced in biological tissues.

3.2.3 Physical Assembly

Once the model was 3D printed, manual mechanics were applied to each printed part. After the structural inserts were removed, each part was manually smoothed by sanding in areas where the printed parts do not mesh well. Using a combination of sandpaper and the Dremel tool (Robert Bosch Tool Corporation, Mt. Prospect, Illinois) is typically necessary. The overall print time of the phantom took almost a week in hours.

To make the physical model fully airtight, various engineering designs were considered and the final phantom design incorporated epoxy adhesive, plastic latches, nylon screws and threads, and rubber foam. A well-designed CAD model and plentiful resources can reduce manual construction. Various sealants were researched for their electromagnetic compatibility as well as MR signal. Materials with metallic components were avoided. An epoxy adhesive (DP100 Plus Clear, 3M™ Scotch-Weld™, St. Paul, Minnesota) was applied to various halves to bind the physical 3D printed model parts together. Epoxy adhesive was only used on parts that would not be reopened. For parts that required reentry, the silicone rubber was applied as a sealant and then doubled on contacting surfaces to act as a rubber gasket. Latches were strategically mounted on the physical phantom model to apply pressure to the foam as sealant, which prevents the filling liquids from leaking at these junctions.

The filling ports were manually designed based on the CAD model and the ease of filling the designated liquid per compartment. Each refillable liquid has at least two ports: one for filling, while the other for releasing air bubbles that may accumulate during the filling process.

3.2.4 Preparation of the Phantom Tissue and Phantom Filling

In this study, the tissues in Table 3.1 were classified as biological tissues that are grouped together based on the location and constitutive parameters of the tissue. These groups were chosen to represent tissues of the phantom without running into the complications of having an overly detailed and ineffective design with diminished structural integrity. While the physical model is realistic, some assumptions were made to match the constitutive properties of the human tissues listed by Gabriel *et al.* (98). These values are based on calculations of the constitutive parameters while being a function of the physiological tissues density that make up each group. The air cavities are representative of the nasal cavities, sinuses and esophagus. The brain tissue composes of the gray matter, white matter, blood vessels in the brain, Dura and the CSF in between and surrounding the brain. The brainstem is representative of the pons, medulla oblongata and the spinal cord. The constitutive parameters of the brainstem tissue match those of the spinal cord listed in (98). The internal CSF is representative of the actual CSF inside of the ventricles and lateral horns—lateral gray columns of the spinal cord—and the CSF that surrounds the exterior of the spinal cord. The cerebellum is representative of the actual cerebellum. The eye tissue is a composition of the vitreous humor, cornea, eye sclera, nerves and the blood vessels within the eye. The muscle is representative of the continuity of muscle and tendons in the head (including the tongue), neck and upper shoulders. The bone is representative of the bone, cartilage, bone marrow and bone cortical throughout the head, neck and upper shoulders. Since the bone possesses relatively lower values in terms of conductivity and permittivity and the fat is a discontinuous tissue with similar electromagnetic characteristics, the phantom combines both the bone, fat, and skin (not considered in this study) into one tissue. This combined tissue is physically and electromagnetically representative of the SLA resin material due to each corresponding low

loss/permittivity (with the exception of the skin). The skin was too thin to be properly segmented and 3D printed into a separate tissue for filling.

Table 3.1. Constitutive properties and densities of the classified tissues at 297.2 MHz.





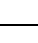


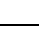














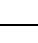




Phantom Tissue Classification	General Biological Tissue Classification	Conductivity (S/m)	Relative Permittivity	Density (kg/m ³)	Tissue Representation in Model
Air	Sinuses, Esophagus	0.00	1.00	1.25	    
Brain (WM/GM)	White Matter, Gray Matter, External CSF, Dura	0.55	51.98	1040.00	  
Brainstem	Pons, Medulla Oblongata, Spinal Cord	0.42	36.97	1039.00	 
Cerebellum	Cerebellum	0.97	59.86	1040.00	 
Cerebrospinal Fluid (CSF)	Internal CSF near lateral horns and around the spinal cord	2.22	72.80	1007.00	 
Eyes	Cornea, Vitreous Humor, Eyes Sclera	0.92	56.46	1020.07	 
Muscle	Tendons, Tongue, Muscle	0.77	58.24	1049.78	 
Fat/ Bone/ Skin (3D SLA Material)	Fat, Cortical Bone, Cartilage, Skin Dry	0.11	2.79	1120.00	    
Fat	Fat	0.04	5.64	916.00	

Table 3.1 (Continued)

Bone	Cortical Bone	0.08	13.45	1990.00	
Skin	Skin Dry	0.64	49.93	1100.00	
Water-Doped	Homogeneous Phantom Solution with Saline	0.46	79.00	1000.00	

Legend:

- ▲ Segmented *In-Vivo* Human Head Model ◆ Heterogeneous Head Model ✦ Spherical (Water-Doped) Model
- ◆ Homogeneous (Water-Doped) Head Model ♦ Homogeneous (Brain-Doped) Head Model

Table 3.1 provide values that were achieved by calculations using studies (93, 98). The conductivity (σ) and permittivity (ϵ_r) volumes were developed by in-house mixtures of distilled water, sodium chloride (NaCl), and/or denatured ethanol (C₂H₆O) at room temperature (elaborated in Appendix A on page 247). The in-house mixture must have a relatively low viscosity while remaining soluble; thus, the selected chemicals are used for a relatively inexpensive in-house mixture. The constitutive parameters of each tissue shown in Table 3.1 (98) were measured using a dielectric probe (SPEAG DAK (AG SPE, Zurich, Switzerland)) with measurements calibrated between a spectrum window of 295 MHz and 300 MHz. Distilled water was chosen as a base for the solution within the six compartments. Various studies (98, 99) demonstrate that the permittivity value of water decreases as concentrations of solvents with lower permittivity values are mixed into the solution. NaCl was used to control the conductivity (100) and C₂H₆O was used to adjust the permittivity of the developed solution. Various concentrations of NaCl and C₂H₆O were used to match the values that are listed in (98). Using the dielectric probe, the values reported in Table 3.1 were measured several times ($n=10$, $\sigma=0.01$) to ensure stability over time. The prepared liquids with constitutive parameters shown in Table 3.1 were used to fill the phantom.

3.2.5 Network Analyzer Measurements

Workbench analysis of the three phantoms and an *in-vivo* volunteer centered in an RF coil were measured with a network analyzer (Agilent E5602A, Keysight Technologies, Santa Rosa, California). Scattering parameters indicate to an RF engineer how well tuned a coil is to the present load and the measurements of transmission and reflection per channel. Using the scattering parameters, each phantom and the volunteer were characterized through the reflection coefficient

(S11) of one representative channel and therefore the input impedance of an in-house built RF volume coil (a 16-strut transverse electromagnetic (TEM) resonator) (62, 101).

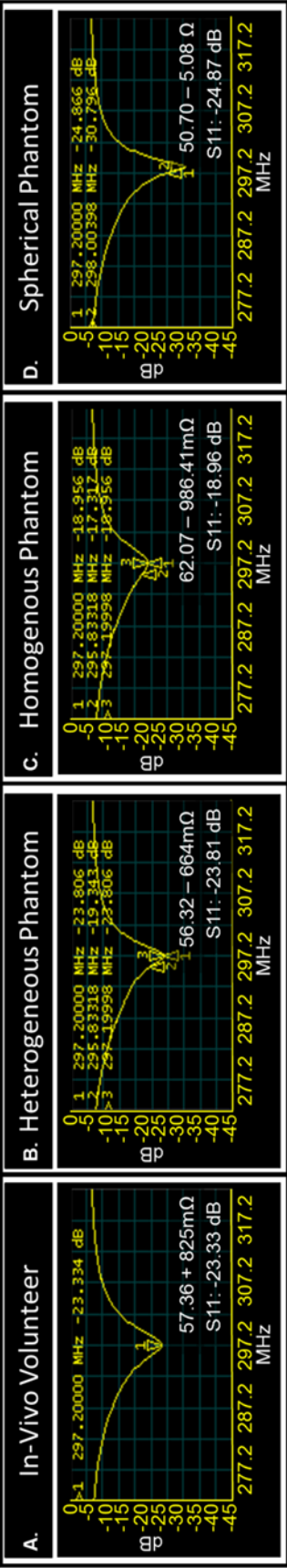


Figure 3.4. Comparison of Phantoms to *In-Vivo* Volunteer using the Scattering Parameters of an RF Coil. S-Parameters for *in-vivo* volunteer and phantom models with center frequency is 297.2MHz with a span of 40.0 MHz.

3.2.6 7T MRI Experiments

Experimental B_1 mapping of the anthropomorphic heterogeneous head phantom, anthropomorphic homogeneous head phantom, spherical phantom and the *in-vivo* volunteer (with signed consent form approved by the Institutional Review Board at the University of Pittsburgh) within the TEM coil were acquired using Siemens MAGNETOM® 7T whole-body scanner (Erlangen, Germany). The volunteer has given a written informed consent (as outlined by PLoS ONE consent form) to publish the details in this manuscript and dissertation. The anthropomorphic homogeneous head phantom (the designed phantom) and the spherical phantom were filled with a solution that has conductivity = 0.41 S/m and relative dielectric constant = 79. The *in-vivo* study was performed by acquiring images with the head centered within the TEM coil. The sequence used for B_1 mapping was SAT TurboFLASH with the following parameters: Pulse: rectangular RF pulse of 1ms at 500V; FOV: 64 x 64 mm²; TE: 1.16 ms; TR: 2000 ms; FA: 6°; BW: 1502 Hz/pixel; and Resolution: 3.1 x 3.1 x 2.0 mm³.

The stability of the head phantom and *in-vivo* volunteer were measured using similar stability QA protocols methods used at lower field strengths (102). The RF shielding in this particular TEM resonator produces ghosting effects and is very distorted; thus, another commercially available RF head coil was used to properly evaluate echo planar imaging (EPI) stability scans. Experimental 2D EPI images of the anthropomorphic heterogeneous phantom and the *in-vivo* volunteer were acquired by centering the head phantom and the volunteer within the 8-channel RAPID coil (Rapid Biomedical, Wurzburg, Germany). The sequence for EPI acquisition used the following parameters: FOV: 148 x 148 mm²; TE: 20 ms; TR: 2500 ms; FA: 65°; BW:

1778 Hz/pixel; Acquisitions: 10; Slices: 86; Scan Plane: Axial; and Resolution: 1.5 x 1.5 x 1.5 mm³. QA data was analyzed quantitatively through fBIRN (NA-MIC, Bethesda, MD, USA) and Matlab (The MathWorks Inc., Natick, MA, USA). In this work, we monitored the stability through the signal-to-ghosting ratio (SGR) and fluctuation indicated by Friedman and Glover (103, 104) in one comparative slice for 9 acquisitions (similar to typical fMRI analysis, the first acquisition was removed from the analysis). The SGR is computed using eq. (2) in Simmons (105) and Weisskoff (102) and the fluctuation using eq. (5) in Simmons (105) is applied.

3.3 RESULTS AND DISCUSSION

3.3.1 Results

3.3.1.1 Fabrication of Head Phantom

The phantom was successfully fabricated as shown in Figure 3.3D which demonstrates the feasibility of using 3D printing technology to develop an anthropomorphic heterogeneous head phantom. The in-house mixtures were made with low viscosity and it requires no more than an hour to fill the entire phantom with limited air bubbles. Emptying the phantom is much quicker; however, there are multiple methods to empty the phantom. Both ports must be open and the liquid can be poured out or suctioned out based on preference.

3.3.1.2 S-Matrix Simulation and Experimental Measurements of the Phantoms to the *In-Vivo* Volunteer

The scattering parameters of each phantom were successfully measured and shown in Figure 3.4. The reflection coefficients and load of each phantom (Figure 3.4A to C) and *in-vivo* volunteer (Figure 3.4D) at 297.2 MHz are listed respectively: -23.33 dB, -18.96 dB, and -24.87 dB. The resonant frequency of 297.2 MHz is indicated by marker 1.

Figure 3.4B to D represent the shift in resonance of the heterogeneous phantom, in comparison to the *in-vivo* volunteer through markers 2 and 3. The homogeneous head phantom shifts (0.1 MHz) to the left and the spherical phantom (0.8 MHz) shifts to the right. The bench measurements indicate that the heterogeneous head phantom is most similar in bench measurements to the *in-vivo* volunteer.

3.3.1.3 Verification of Congruent Slices to the *In-Vivo* Volunteer

The experimental B_1 mapping statistics and distributions of both head phantoms, spherical phantom and the *in-vivo* volunteer are captured for one axial, coronal and sagittal slice at a comparable location in the volunteer, spherical phantom and the two head phantoms Figure 3.5.

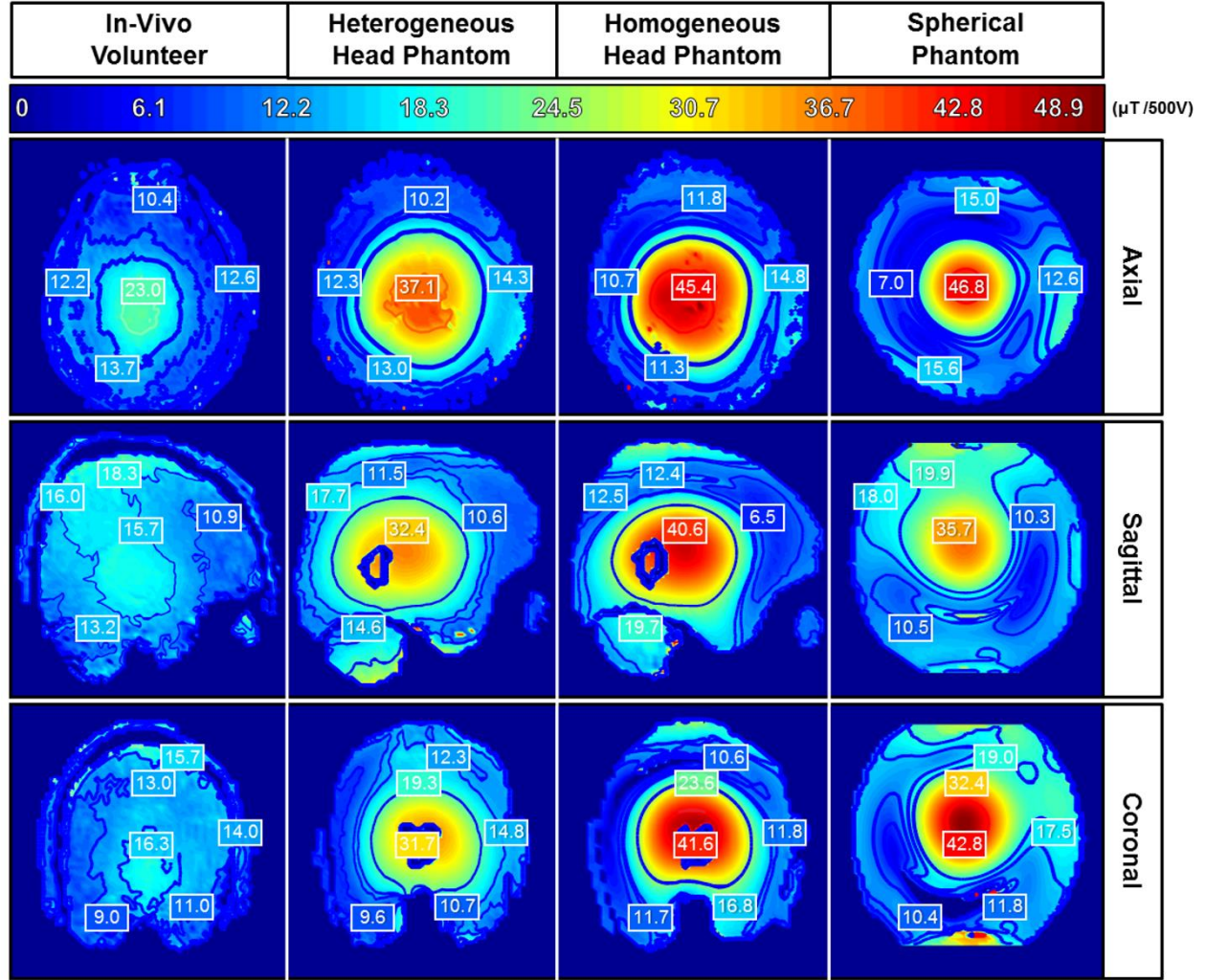


Figure 3.5. Comparison of the Magnetic Field Distribution Experimentally Mapped using a B_1 Map at 7T MRI in All Planes. Congruent slices of each phantom in comparison with the human volunteer are shown in all planar views. The color bar ranges from 0 to $48.9\mu\text{T}$ per 500V. The maximum B_1 intensity level is set by the highest pixel value among each of the phantoms and the volunteer.

3.3.1.4 Experimental Study of the Various Phantoms to the *In-Vivo* Volunteer

The results shown in Figure 3.5 represent a preliminary evaluation of the electromagnetic behavior of the three phantoms and the *in-vivo* volunteer. Each B_1 map is computed by $B_1 = \frac{\theta}{\gamma t}$, where θ is the flip angle, γ is the gyromagnetic ratio at 42.58 MHz/T, B_1 is the RF field (at 7T or 297 MHz)

and t is the pulse width. The corresponding values for each pixel indicate the field strength required to make the B_1 at that pixel perpendicular to the magnetic field strength (B_0). The B_1 was acquired and scaled to a voltage of 500V for a rectangular pulse duration of 1ms. The scaling per 500V of the B_1 is due to power limits. The scanner is limited to produce 8kW of power from the power amplifier after power losses from the cables and other electronic components; thus, the maximum voltage delivered through the power amplifier is 500V. Qualitative/quantitative analysis were conducted along congruent slices of each phantom in comparison with the human volunteer. The contours span the same range in terms of values.

When compared to the other two phantoms, the anthropomorphic heterogeneous head phantom possesses the most comparable B_1 field distribution to the *in-vivo* volunteer. The other phantoms have a higher magnetic intensity per volt when compared to the anthropomorphic heterogeneous head phantom and the human volunteer.

3.3.1.5 Magnetic field distributions and EPI testing of the various phantoms and the *in-vivo* volunteer.

The results shown in Figure 3.6 represent an evaluation of EPI stability scans of all the anthropomorphic phantom, spherical phantom, and the volunteer. The stability parameters such as the signal-to-ghosting ratio (SGR), fluctuation, and stability are shown in Table 3.2.

Table 3.2. Stability Parameters of Phantoms and the Volunteer for the EPI Stability Scans.

Stability Parameter	Head Phantom	Volunteer
SGR	423.8	47.1
SNR	1097.9	276.6
Fluctuation (%)	0.05	4.16

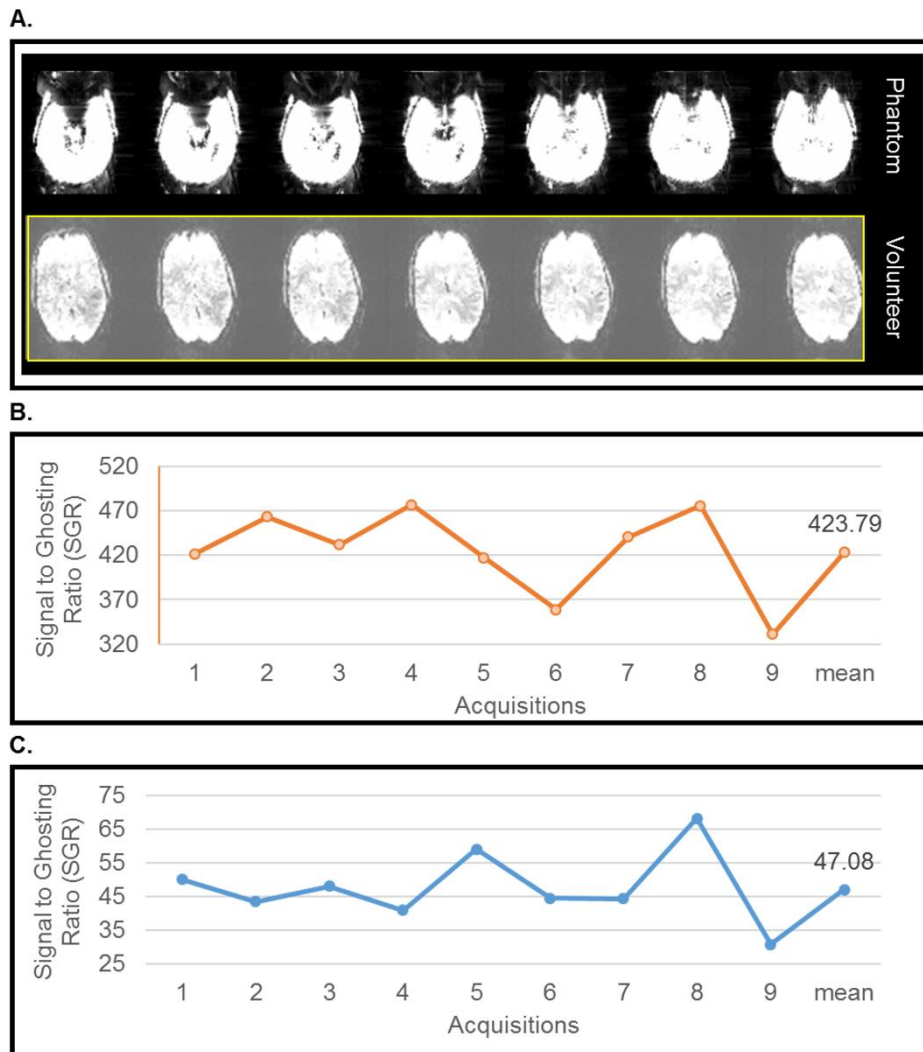


Figure 3.6. Comparison of Phantom to *in-vivo* Volunteer during an EPI Stability Scan at 7T MRI.

3.3.2 Discussion

This chapter aims to address the challenges associated with phantom design and fabrication and offers a methodology to design, fabricate and evaluate the development of a realistic anthropomorphic heterogeneous head phantom for various electromagnetic applications. The design and construction of the head phantom differs from homogeneous (24, 106, 107) phantoms and recent anthropomorphic heterogeneous (19, 20, 22, 23, 86) phantoms as it is more comparable to a volunteer from whom it was developed. The design is one solution to the challenge of making a heterogeneous physical phantom.

3.3.2.1 Fabrication of Head Phantom

The fabrication of the designed head phantom required adequate resources in technology and funding. We determined to voxelize and print the phantom at a higher printing resolution. It was determined that smoothening the CAD models as an automated process was not desired since it would remove the detail of the phantom and lessen the accuracy of the electromagnetic comparison to the volunteer. Thus, the physical assembly of the phantom took a few months to complete and requires extensive planning.

3.3.2.2 S-Matrix Measurements of the Phantoms to the *In-Vivo* Volunteer

The bench analysis demonstrates that the anthropomorphic phantom is capable of being a usable tool for RF engineers to conduct loading analysis for RF coil developments. From the current measurements, the anthropomorphic phantom appeared more realistic than the spherical phantom in comparison to the transmission and reflection coefficients of the volunteer. However, this chapter and dissertation is not intended to provide a full analysis to the respective S-matrices.

3.3.2.3 Magnetic Field Distributions of the Various Phantoms and the *In-Vivo* Volunteer

The B_1 field distribution for each phantom and the volunteer does not have uniform distribution in any planar view. The B_1 maps highlight the phenomena of a shorter RF wavelength at higher field strengths (3, 91, 108, 109). The B_1 mapping results demonstrate that the anthropomorphic heterogeneous head phantom is the most realistic phantom to mimic and model the *in-vivo* volunteer. While our anthropomorphic heterogeneous head phantom does not offer full accuracy in its comparison of the electromagnetic fields to the *in-vivo* volunteer, it is considerably more comparable than the spherical, anthropomorphic homogenous head phantom or other fabricated heterogeneous phantom studies (14, 86). The magnetic field distribution of the spherical homogenous phantom is most comparable to the anthropomorphic homogenous head phantom. The B_1 intensity values are higher in the phantoms due to having differing constitutive parameters for the skin tissue resulting in higher RF penetration and therefore higher B_1 values. That being said, the heterogeneous phantom is the most comparable to the *in-vivo* volunteer in terms B_1 distribution and intensity. As noted, while the anthropomorphic homogeneous head phantom has the same molding and contours as the anthropomorphic heterogeneous head phantom, it uses the same constitutive parameters as the spherical phantom. More evaluations need to be conducted in order to determine how the phantom's anatomy and the thickness of the compartment shells affect the electromagnetic field distributions.

3.3.2.4 EPI testing of the various phantoms and the *in-vivo* volunteer

Short acquisitions are usually carried out to demonstrate stability testing. We have compared the stability parameters in Table 3.2 of the anthropomorphic heterogeneous head phantom and the volunteer. As expected, the fluctuation indicates that the phantom's signal is stable compared to the volunteer. The difference between the mean SGR of the head phantom and volunteer are about

112%. Because the phantom does not offer comparable bold contrast to the volunteer, the signal intensity is much higher in the phantom.

Although, we achieved success segmenting, designing and fabricating the phantom, the phantom design presents limitations to some electromagnetic applications. The representation of the fat, bone and skin as one tissue is a limitation. Due to this limitation, the particular tissue will have an artificially lower SAR. In various telecommunications applications, the SAR is observed to be the highest in the ear for adult models. The electromagnetic properties of the physiological skin and ear are more conductive than the SLA resin material. The exact comparison and measurement of this limitation can be evaluated in future investigations.

3.3.2.5 Future Phantom Applications

Our study has the potential to span and benefit many EM applications prior to any device's interaction with a patient/ human. While numerical EM modeling is still a helpful resource for various EM applications, our study indicates that there is a benefit to further developing physical phantoms to study the interaction of EM waves and biological tissue in the real experimental environment.

There is an opportunity to evolve this study further to assess the benefit of using a realistic physical phantom in MR applications. There are a variety of MR applications that would benefit from using a physical phantom. Perhaps, the most beneficial applications are those that involve a true assessment of RF safety. Future studies using the designed phantom will include MR thermometry, RF coil design, and implanted devices.

As previously mentioned, SAM is a commonly used head phantom in many wireless communication application studies. Many studies (85, 110-112) use the SAM phantom along with

a hand phantom to evaluate the emitted RF signals of a wireless RF antenna (i.e. a cell phone, Bluetooth device, Google glasses, etc.) and the SAR within the tissue in relation to government regulated standards for health concerns. From the results of our study and other studies (14, 15, 86), we recommend utilizing heterogeneous phantoms to conduct RF testing.

Although we designed the phantom for MR purposes, the design and fabrication of the phantom can be used for various EM applications.

3.4 CONCLUSION

In conclusion, an anthropomorphic heterogeneous head phantom based on *in-vivo* MR dataset was developed, tested and compared to a human head. The hypothesis in Specific Aim 1 was proven accurate in determining that using an anthropomorphic heterogeneous human head phantom was easier and more accurate to evaluate the RF head coil instead of the basic spherical phantom.

4.0 ELECTROMAGNETIC AND THERMAL CHARACTERIZATION OF THE ANTHROPOMORPHIC HETEROGENEOUS HEAD PHANTOM USING A TEM RESONATOR AT 3T AND 7T

Part I-A of this chapter is currently under review for journal publication as a first author.

4.1 INTRODUCTION

The purpose of this chapter is to evaluate and compare the performance of a six-compartment, 3D-printed anthropomorphic heterogeneous head phantom (fabricated in Chapter 3.0) to an *in-vivo* volunteer's human head in a real MR environment and through EM and thermal simulations. The designed phantom (15, 18, 113) is evaluated for EM and thermal characterization of this phantom using a TEM resonator tuned and matched to two field strengths, 3T (~ 128 MHz) and 7T (~300 MHz).

The work of Chapter 3.0 supports the findings of studies (14, 24, 86) that anthropomorphic-shaped and, furthermore, heterogeneous phantoms are most helpful for several EM characterization. While exploring these findings at 7T, there is a critical need to develop anthropomorphic heterogeneous head phantoms further so that researchers make realistic findings

in various EM medical applications at varying frequencies. To-date, 3T is the current gold standard for high-resolution clinical MR imaging. In 1991, the first 3T clinical scanner was produced and in 1999 the Food and Drug Administration (FDA) approved the first 3T whole-body MR scanner. The FDA recently approved (114) the first whole-body 7T MR clinical scanner — 18 years after 3T’s approval. Now, there is a stronger need for MR researchers to make a comparison at both field strengths to prove 7T’s clinical value beyond research. This chapter aims to make this comparison through an RF homogeneity assessment and MR safety evaluations. The results are shown in three-tiered sections organized within Part I (Sections 4.2-4.4) and Part II (Section 4.5) of this chapter.

Part I of this chapter highlights the EM characterization by performing specific EM measurements and calculations of S-Matrix, B_1^+ fields, and electric fields at both field strengths in Part I-A and Part I-B and comparing the results in Part I-C (Section 4.4). The EM characterization was conducted through numerical and experimental studies at 7T (Section 4.2) and only numerical studies at 3T (Section 4.3). Five numerical phantom models (Subsections 4.2.2.1.1 and 4.3.2.1.1) were developed, simulated, and validated with the same positioning within the TEM resonator (shown in Figure 4.1.B and Figure 4.1.E). The constitutive and thermal properties of each model are presented in Subsections 4.2.2.1.5, 4.3.2.1.4, and 4.5.2.1.1 at both field strengths. EM characterization assessments and comparisons are organized within the chapter as follows:

- 1) The numerical scattering parameters at 7T (Subsection 4.2.3.1.1) and 3T (Subsection 4.3.3.1.1) are compared in Subsection 4.4.4.1.
- 2) The B_1^+ fields at 7T (Subsection 4.2.3.1.2) and 3T (Subsection 4.3.3.1.2) are compared in Subsection 4.4.4.2.

- 3) The electric fields at 7T (Subsection 4.2.3.1.3) and 3T (Subsection 4.3.3.1.3) are compared in Subsection 4.4.4.3.

Part II of this chapter highlights each model's thermal characterization by performing and comparing the specific thermal measurements and calculations of SAR, and RF heating at both field strengths. The thermal characterization was performed on two thermal models being the 1) perfused segmented *in-vivo* human head model and 2) the perfusionless anthropomorphic heterogeneous head phantom. The assessments were evaluated using the same TEM resonator and model positioning as Part I. Part II highlights the thermal characterization conducted through numerical studies at 7T and 3T. The thermal characterization assessments and comparisons are organized within the chapter as follows:

- 1) The numerical SAR simulations at 7T (Subsection 4.5.3.1.1) and 3T (Subsection 4.5.3.1.3) are compared in the discussion (Subsection 4.5.3.2).
- 2) The numerical thermal simulations at 7T (Subsection 4.5.3.1.2) and 3T (Subsection 4.5.3.1.4) are compared in the discussion (Subsection 4.5.3.2).

The entire chapter provides a robust evaluation and comparison of the need and benefits of using an anthropomorphic heterogeneous phantom at 3T and 7T. Recommendations from the results and discussion are summarized in the summary of this chapter (Section 4.6).

4.2 PART I-A: ELECTROMAGNETIC CHARACTERIZATION OF THE ANTHROPOMORPHIC HETEROGENEOUS HEAD PHANTOM USING A TEM RESONATOR AT 7T

4.2.1 Introduction

MR researchers use phantoms for a wide range of MR applications such as improving the design and performance of radiofrequency (RF) coils and MR instrumentation, evaluating MR safety, optimizing MR sequences, and assessing the interaction between biological tissue and electromagnetic (EM) waves (48). Characterization of MR instrumentation using numerical and experimental phantoms is critical at higher field strengths since the EM wavelength shortens with increased operational frequency and becomes smaller than the tissue's size (2, 25). For example, the RF field must propagate further electrical distances to cover the entire human head at ultrahigh field (UHF) strengths when compared to lower field strengths (25, 26, 75, 115-117). The wavelength for proton imaging is ~11-13 cm at 7T, and the human head length in the anterior to posterior (AP) direction is ~18-22 cm. At UHF frequencies (~300 MHz and higher), the penetration of the RF field into tissue significantly decreases (23, 108) than at lower field strengths. Hence, inhomogeneous RF field distributions exist which causes a wide variety of performance and safety issues. Experimental phantoms (similar to that shown in Figure 4.1.A and Figure 2.8 (82, 118, 119)) could be more resourceful in high and UHF systems; yet, current experimental phantom studies (14, 24, 120) and are not necessarily representative of human studies.

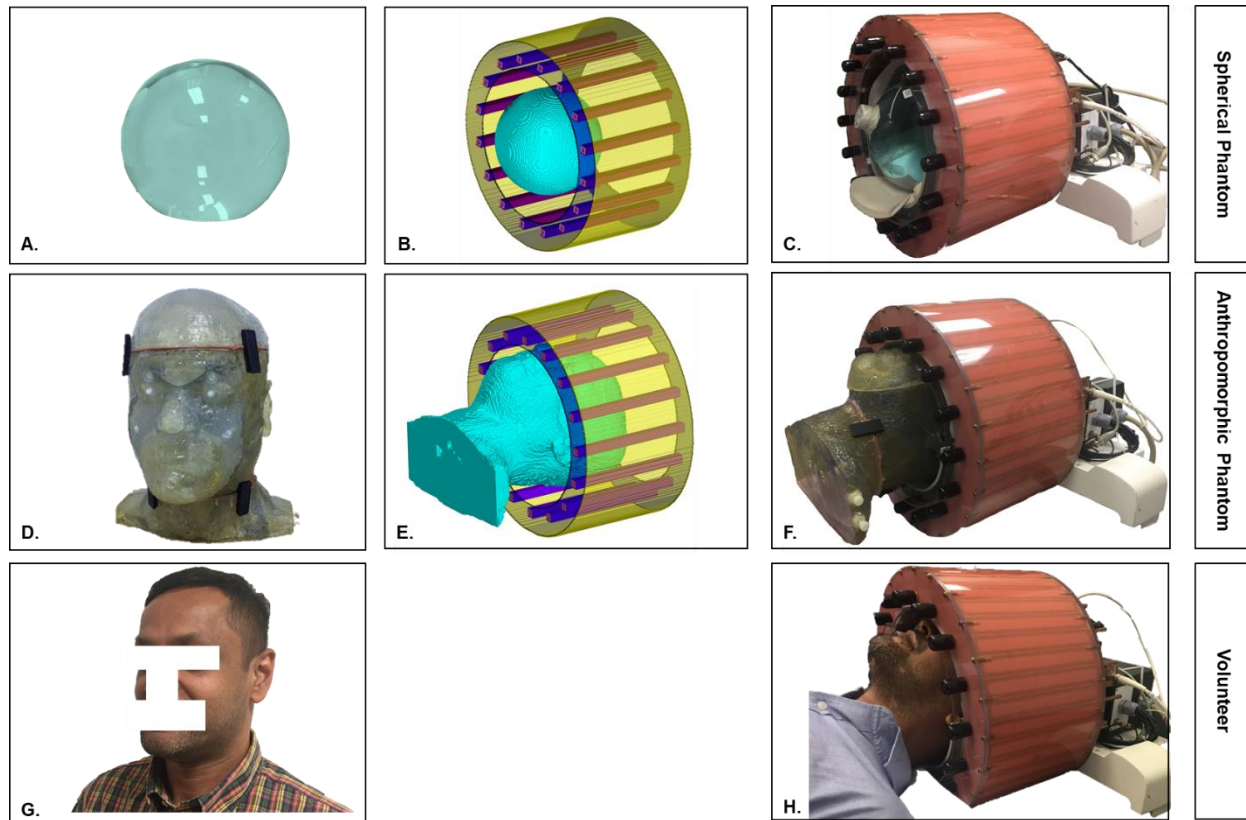


Figure 4.1. View of the Phantoms and Healthy Volunteer Positioned in the TEM Resonator. A commercial spherical phantom of 170.00 mm diameter and the fabrication of the head phantom (18) (physical head phantom dimensions are 305.00 mm tall, 254.00 mm long and 140.00 mm wide) are shown in (A), and (D), respectively. The volunteer, based on which the phantom was designed, is shown in (G) along with the experimental setup in (H). The anthropomorphic head phantom is loaded inside of the TEM resonator as shown in the numerical model (E), and experimental setup (F). Similarly, the spherical water-doped phantom is loaded in the TEM resonator as shown in the numerical model (B) and the experimental setup (C).

4.2.1.1 Current Studies Comparing Numerical and Experimental Electromagnetically-Equivalent Head-Phantoms

Numerical modeling is a necessary technique used to validate experimental MR studies (12, 13), as it measures the RF field distribution, potentially minimizing safety concerns in patient MR studies through quantifying the specific absorption rate (SAR) and the temperature rise in tissue(s).

In recent studies (12, 13, 121), MR researchers successfully compared numerical EM modeling to corresponding experimental studies to evaluate the performance and characterization of various RF coils using a numerical and physical, spherical phantom or a numerical, anthropomorphic head phantom. While few studies (122) measured SAR in patients through MR thermometry techniques, the bulk of the RF studies in MRI (71, 123-128) have relied heavily on numerical modeling to be an accurate predictive indicator of what occurs electromagnetically during MRI *in-vivo* studies. Recent studies (14, 22, 89, 129) have used physical, anthropomorphic phantoms to perform quantitative EM measurements by evaluating the temperature, magnetic susceptibility, and permittivity. Shmueli *et al.* (22) found the magnetic susceptibility of the anthropomorphic heterogeneous phantom comparable to a healthy human volunteer. As of today, there is limited information as to which extent physical anthropomorphic heterogeneous head phantoms are electromagnetically comparable to what subjects' experience during an MRI session.

The importance of the interaction of the biological tissue and electromagnetic field at increasing frequencies projects understanding of EM fields and MR safety. This section of the chapter views the electromagnetic field at 7T using the anthropomorphic head phantom with a 16-strut/4-port TEM resonator. The purpose of this Part I is to evaluate and compare the performance of a six-compartment, 3D-printed anthropomorphic heterogeneous head phantom to a volunteer's human head in a real MR environment. The designed phantom (15, 18, 113) is evaluated through numerical and experimental studies performing specific EM measurements and calculations of S-Matrix, B_1^+ and electric fields. Prior works have used the finite-difference time-domain (FDTD) (69, 70, 130, 131) method to yield a realistic approximation of the electromagnetic interactions between the subject and the RF coil in an MR environment. This work provides numerical and experimental electromagnetic comparisons between a spherical phantom, anthropomorphic head

phantom filled with homogeneous media, anthropomorphic heterogeneous head phantom, and *in-vivo*.

4.2.2 Materials and Methods

4.2.2.1 Numerical Studies

4.2.2.1.1 *FDTD Simulations and Numerical Models at 7T*

Using the FDTD method (70), a validated in-house numerical simulation software (13, 59, 71, 101, 132), with an accurate transmission line model for the excitation mechanism, generates output time-domain and frequency domain data. The software utilizes an isotropic spatial resolution of $\sim 1.59 \text{ mm}^3$ and temporal resolution of $\sim 3.00 \text{ ps}$. The output data is read by MATLAB (The MathWorks, Inc., Natick, MA, USA) in order to produce the electric and magnetic fields and the scattering parameters (S-parameters).

A first-order differentiated Gaussian pulse was used to excite the coil and load. The pulse has a 5.8 ns period that ran for 100,000-time steps, which was enough time to yield a stable steady state time domain solution.

Before generating the EM fields, the numerical system is properly tuned and matched to 297.20 MHz (7T) using the Virtual Family v1.0 (31) Duke head to shoulder model. Five numerical models are used in this particular study namely: 1) a 10-tissue segmented *in-vivo* head model (252*252*287 Yee-cells in the respective x, y, and z-direction), 2) an anthropomorphic heterogeneous head phantom (252*252*287 Yee-cells), 3-4) anthropomorphic homogeneous water-doped and brain-doped head phantom (252*252*287 Yee-cells), 5) a basic (diameter =

170.00 mm) spherical water-doped phantom (252*252*231 Yee-cells). The numerical models (shown in Figure 4.1.B and 4.1.E) are positioned within the RF coil similar to experiments (shown in Figure 4.1.C, 4.1.F, and 4.1.H).

4.2.2.1.2 RF Coil and S-Matrix

16-strut/4-port TEM resonator (62) is utilized as the RF coil. The computational domain of all head models includes the anatomy of the entire head, neck, and shoulders. The coil is driven in the circularly polarized (CP) mode by combining all four channels to be driven in quadrature. The S-matrix and load impedance of each model are shown in Figure 4.2 with a frequency span of 100.0 MHz within the center frequency of 297.2 MHz. This coil is 228.6 mm long and has an outer diameter of 355.6 mm and an inner diameter of 279.4 mm diameter.

4.2.2.1.3 FDTD Calculations of the B_1^+ Field

The B_1^+ field intensity per volt (V) is obtained using the simulated input pulse amplitude, which is determined by the Fast Fourier transform (FFT) of the Gaussian pulse in the time domain at ~297.2 MHz. The B_1^+ field is scaled to 1 Watt (W) of input power that is equivalent to applying 10.0 V as an input peak voltage. The B_1^+ field is analyzed by capturing the mean B_1^+ field intensity and the coefficient of variation (CV) within each model. The mean B_1^+ field intensity is determined by the mean in the Region of Interest (ROI), and the CV is determined by the quotient of the standard deviation in the ROI and the mean in the ROI. Our study uses three ROIs being all fillable compartments in the head phantom 1) above and including the cerebellum, 2) brain (excluding the Midbrain), and 3) Midbrain.

4.2.2.1.4 FDTD Calculations of the Electric Field Analysis

The numerical absolute electric field is computed for all models using the following equation:

$$E_{(i,j,k)} = \sqrt{(E_{x(i,j,k)}^2 + E_{y(i,j,k)}^2 + E_{z(i,j,k)}^2)} \quad (4.1)$$

where i, j, k are the indices in a 3D Cartesian coordinate system (m) and E (V/m) is the electric field (direct output from the FDTD code). Comparison of each phantom's absolute electric field is made to the respective values of the segmented *in-vivo* human head model. For all head models, the numerical absolute electric field is shown for fillable compartments from the entire head to shoulders to visualize peak values within the tissue.

4.2.2.1.5 Phantom Generation and Fabrication

A physical, anthropomorphic heterogeneous head phantom (18) (shown in Figure 4.1.D) was built to accurately access the interaction of EM waves and biological tissues in an MR environment. The constructed phantom comprises of eight different classified tissue types with corresponding constitutive parameters as described in Table 4.1. The tissues are grouped and averaged based on physiological tissues nearby in the region with similar constitutive parameters. The tissues that are representative of various phantom models are labeled according to the legend in Table 4.1. The classified tissues were made in-house using distilled water as a base and varying concentrations of sodium chloride (NaCl), and denatured ethanol (C₂H₆O) at room temperature to achieve the desired permittivity and conductivity in Table 4.1. C₂H₆O was used due to its low viscosity and ease in refilling the phantom during its prototype state with minimal artifacts. The in-house tissue mixtures were verified with a dielectric probe SPEAG DAK (AG SPE, Zurich, Switzerland)

calibrated at 297.2 MHz. The stereolithography (SLA) resin (DSM Somos® WaterShed® XC 11122 (Elgin, Illinois)) material is representative of the combination of the fat, bone, and skin. It's constitutive parameters are close to the weighted average of these tissues combined (7T: conductivity = 0.17 S/m, relative dielectric constant = 16.17, and density = 1223.49).

The designed phantom has six-compartments that are filled with various homogeneous and heterogeneous solutions. The homogeneous solution is either the water-doped solution (7T: conductivity = 0.46 S/m and relative dielectric constant = 79.00) or the brain-doped solution (7T: conductivity = 0.55 S/m and relative dielectric constant = 51.98) as described in Table 4.1. The heterogeneous solution comprises of various tissue-mimicking shown in Table 4.1. A commercial spherical phantom (shown in Figure 4.1A), 170.00 mm in diameter, is water-doped.

Table 4.1. Constitutive Parameters of Phantom Materials at 297.20 MHz Derived from the Cited Literature (31, 98).


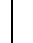


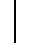


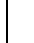

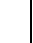











Phantom Tissue Classification	General Biological Tissue Classification	Conductivity (S/m)	Relative Permittivity	Density (kg/m ³)	Wavelength (m)	Skin Depth (m)	Tissue Representation in Model
Air	Sinuses, Esophagus	0.00	1.00	1.25	1.01	N/A	    
Brain (WM/GM)	White Matter, Gray Matter, External CSF, Dura	0.55	51.98	1040.00	0.07	0.13	  
Brainstem	Pons, Medulla Oblongata, Spinal Cord, Midbrain	0.42	36.97	1039.00	0.15	0.09	 
Cerebellum	Cerebellum	0.97	59.86	1040.00	0.12	0.05	 
Cerebrospinal Fluid (CSF)	Internal CSF near lateral horns and around spinal cord	2.22	72.80	1007.00	0.09	0.03	 
Eyes	Cornea, Vitreous Humor, Eyes Sclera	0.92	56.46	1020.07	0.11	0.04	 
Muscle	Tendons, Tongue, Muscle	0.77	58.24	1049.78	0.12	0.06	    
Fat/ Bone/ Skin (3D SLA Material)	Fat, Cortical Bone, Cartilage, Skin Dry	0.11	2.79	1120.00	0.56	0.09	

Table 4.1 (Continued)

Fat	Fat	0.04	5.64	916.00	0.42	0.33	▲
Bone	Cortical Bone	0.08	13.45	1990.00	0.27	0.24	▲
Skin	Skin Dry	0.64	49.93	1100.00	0.13	0.06	▲
Water-Doped	Homogeneous Phantom Solution with Saline	0.46	79.00	1000.00	0.27	0.04	◆ ✦ ✦

Legend:	▲ Segmented <i>In-Vivo</i> Human Head Model	◆ Heterogeneous Head Model	✦ Spherical (Water-Doped) Model
	◆ Homogeneous (Water-Doped) Head Model	◆ Homogeneous (Brain-Doped) Head Model	

The constitutive parameters of each classified phantom/ segmented tissue in the respective model are the conductivity (σ), permittivity (ϵ_r), density (ρ), wavelength (λ), and skin depth (δ). The key legend indicates which tissue is represented in the various models. The phantom tissue classification is based on the assumption that averaged tissue classification is comparable to the percentage of the biological tissue in the Virtual Family v1.0 Duke head model.

4.2.2.2 Experimental Studies

4.2.2.2.1 *MR Instrumentation and Experimental Setup*

All MR images are acquired using a Siemens MAGNETOM® (Siemens Healthcare, Erlangen, Germany) 7T whole-body scanner that has a 60-cm horizontal patient bore and is used in the combined mode to connect to the 16-strut/4-port TEM resonator. The MR computer system uses Siemens' syngo.via MR VB17A through Microsoft Windows XP platform. The 16-strut/4-port TEM resonator (13, 62) with a centered and fixed 14ch receive (133) is connected to the single mode transmission of the scanner. A 4-way Wilkinson power splitter together with phase shifters provides the quadrature excitation to transmit power to the coil's four excitation ports, where each channel of the 16-strut/4-port TEM resonator has a similar amplitude of the signal, and the phases alter in 90° increments in the clockwise direction. The 16-strut/4-port TEM resonator was constructed using an acrylic cylinder with coil dimensions outer diameter of 355.6 mm, an inner diameter of 279.4 mm, and 228.6 mm long. A thin copper shield was placed inside the acrylic and the top ring. The rods of the TEM resonator have a diameter of 6.77 mm. Similar to the simulation, the 16 elements are separated equally 22.5° apart around the cavity between two circular rings.

4.2.2.2.2 *Volunteer and Informed Consent*

One healthy human volunteer MR scan was performed (with a signed informed consent form approved by local Institutional Review Board) by acquiring B_1^+ field maps with the head resting within the TEM resonator. The volunteer has, also, given written informed consent to publish the details of this study in this dissertation.

4.2.2.2.3 *Experimental B_1^+ Field Mapping*

Each phantom and the volunteer are positioned in the TEM resonator (shown in Figure 4.1.C, 4.1.F, and 4.1.H) to acquire experimental 3D B_1^+ field maps using the saturated TurboFLASH (SatTFL) (38) MR sequence normalized to 1ms rectangular RF pulse per 500.0V. The MR protocol image parameters are: input peak voltage = 300V; FOV = 64 x 64 mm², TE = 1.16 ms, TR = 2000 ms, FA = 6°, BW = 1502 Hz/pixel, resolution = 3.13 x 3.13 x 2.00 mm³. The SatTFL output is fit into a cosine function and normalized for 1-Watt input power. The B_1^+ field for 1-Watt input power is computed by scaling the B_1^+ field map per 500.0 V in the designated ROI. To compute region-specific information and eliminate the noise of the SLA resin, masks for each phantom were segmented using ITK-SNAP (134) software.

4.2.3 Results and Discussion

4.2.3.1 Results

4.2.3.1.1 *Numerical Scattering Parameters Measurements at 7T.*

Numerical results show the calculated frequency response (S11) and Smith chart for one representative port of the TEM resonator loaded with the numerical segmented *in-vivo* human head model (Figure 4.2.A) and each phantom model (Figure 4.2.B-E) at 297.2 MHz. The S-matrix and load impedance values for all other ports are also included in (Figure 4.2). Note that the simulated coil is originally tuned and matched to the Virtual Family v1.0 Duke head model and is not retuned for any of the different models utilized in this work.

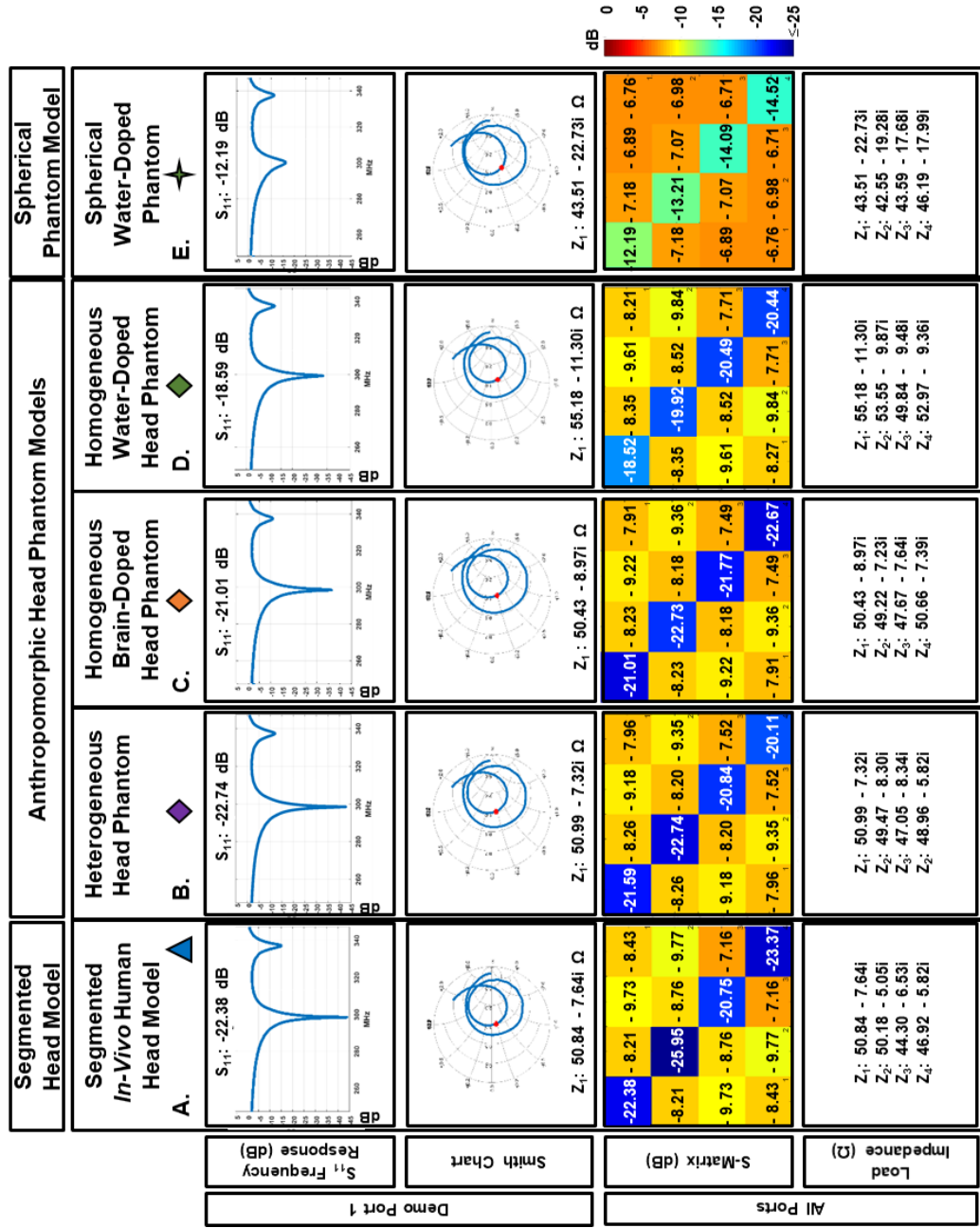


Figure 4.2. S-Parameters Measurements of Five Numerical Models Positioned in the 16-strut/4-port TEM Resonator at 7T. The frequency response is modeled for the segmented in-vivo human head model (A) and each phantom (B-E) model.

A demo of the frequency response of one channel, S11, is shown in Figure 4.2 for a span of 100 MHz from 297.2 MHz and 5.0 dB for a span of 5.0 dB to -45.0 dB. The S11 is shown in magnitude log (top) and the Smith chart (second from top) and reflects the voltage and current in the frequency domain in the chosen port's transmission line. The reflection coefficient to reach port and coupling between channels is shown in the S-matrix (second from bottom). The load impedance of each port is shown (bottom) for each model.

Port 1's load impedance with the segmented *in-vivo* human head model (Figure 4.2.A) is $50.84 - 7.64 \Omega$ (baseline). An evaluation of the percentage change in the value of the reflection coefficient was performed in all five models. For port 1, the percentage change from the segmented *in-vivo* human head model is calculated as follows: spherical water-doped phantom (45.53%), anthropomorphic homogeneous water-doped head phantom (16.93%), anthropomorphic homogeneous brain-doped head phantom (6.12%), and the anthropomorphic heterogeneous head phantom (1.61%). While these values hold true for port 1, the average of all channels is as follows: spherical water-doped phantom (41.58%), anthropomorphic homogeneous water-doped head phantom (14.06%), anthropomorphic heterogeneous head phantom (7.74%), and anthropomorphic homogeneous brain-doped head phantom (4.63%).

4.2.3.1.2 Numerical B_1^+ Field Mapping Measurements and Verifications of Experimental Measurements at 7T.

Figure 4.3.A-O show the numerical and verified experimental measurements of the B_1^+ field maps for 1) each phantom and 2) the segmented *in-vivo* human head model and the *in-vivo* volunteer for matching axial, sagittal and coronal slice locations. The positions of the spherical phantom slices are chosen to match that associated with the head phantoms, the segmented *in-vivo* human head

model, and the *in-vivo* volunteer. All numerical B_1^+ field maps are scaled to the same magnitude scale (0 to $1.33 \mu\text{T}/\sqrt{W}$), and all experimental B_1^+ field maps are scaled to the same magnitude scale (0 to $1.20 \mu\text{T}/\sqrt{W}$). The loss experienced by the coil plugs, splitters, cables and coil components total to a value of 10%. The experimental B_1^+ field maps are scaled for 1W of input RF power. The B_1^+ field maps are masked to all fillable compartments in the head phantom, the segmented *in-vivo* human head model and the *in-vivo* volunteer in order to eliminate the B_1^+ field in the SLA resin, which produces low MR signal.

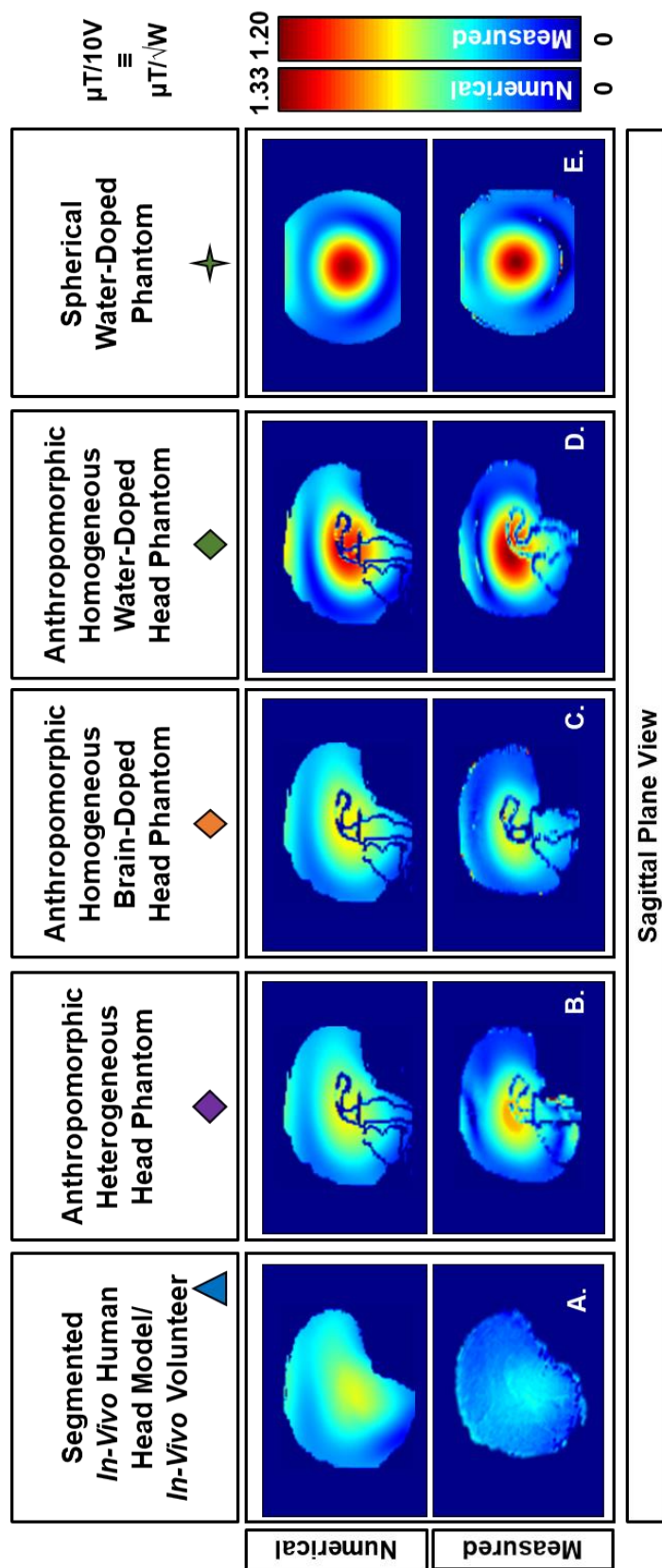


Figure 4.3. B_1^+ Field Distributions of All Models using the 16-strut/4-port TEM Resonator at 7T. The B_1^+ field distribution of each numerical model is shown and compared to the model's experimental B_1^+ mapping measurements in the sagittal, axial, and coronal views (A-O). The numerical models are scaled to 1W input power supplied by the RF system. The color bar is scaled from 0 to the maximum numerical and experimental B_1^+ values.

Figure 4.3 (Continued)

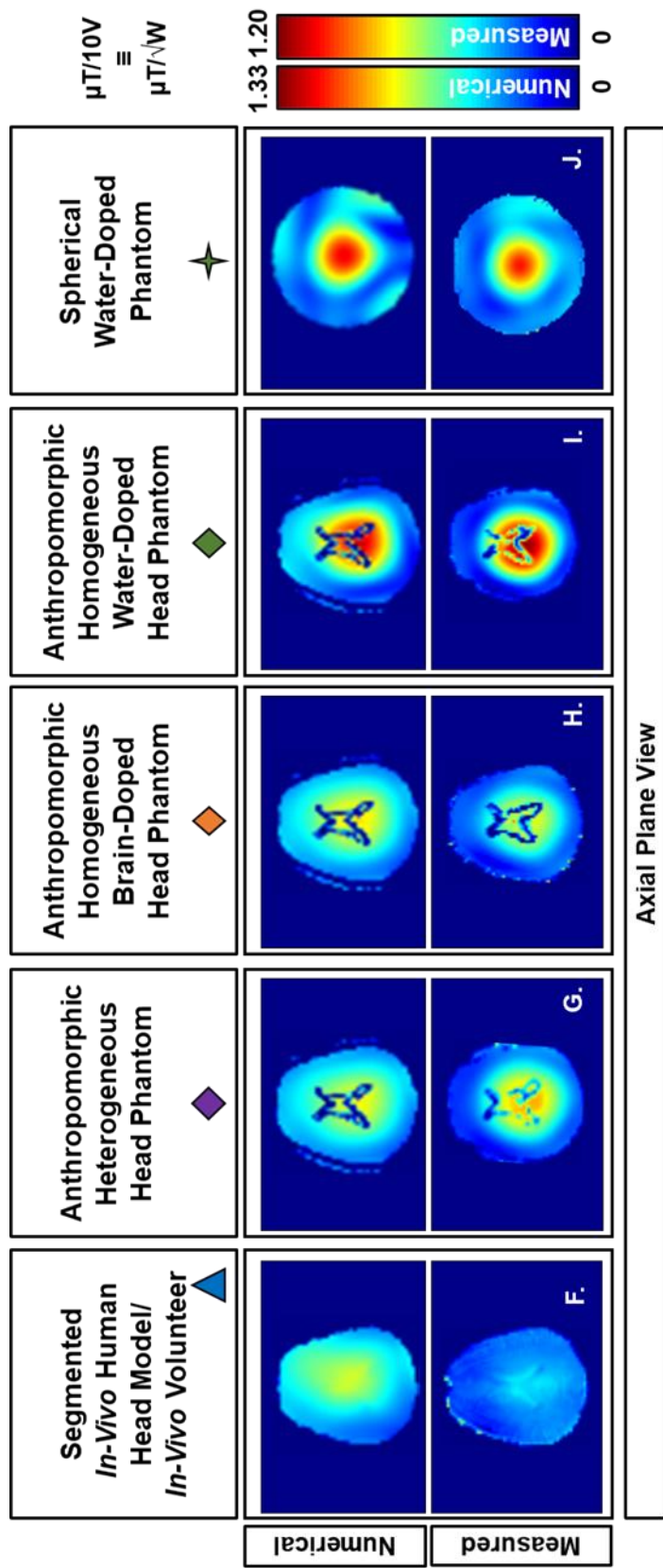


Figure 4.3 (Continued)

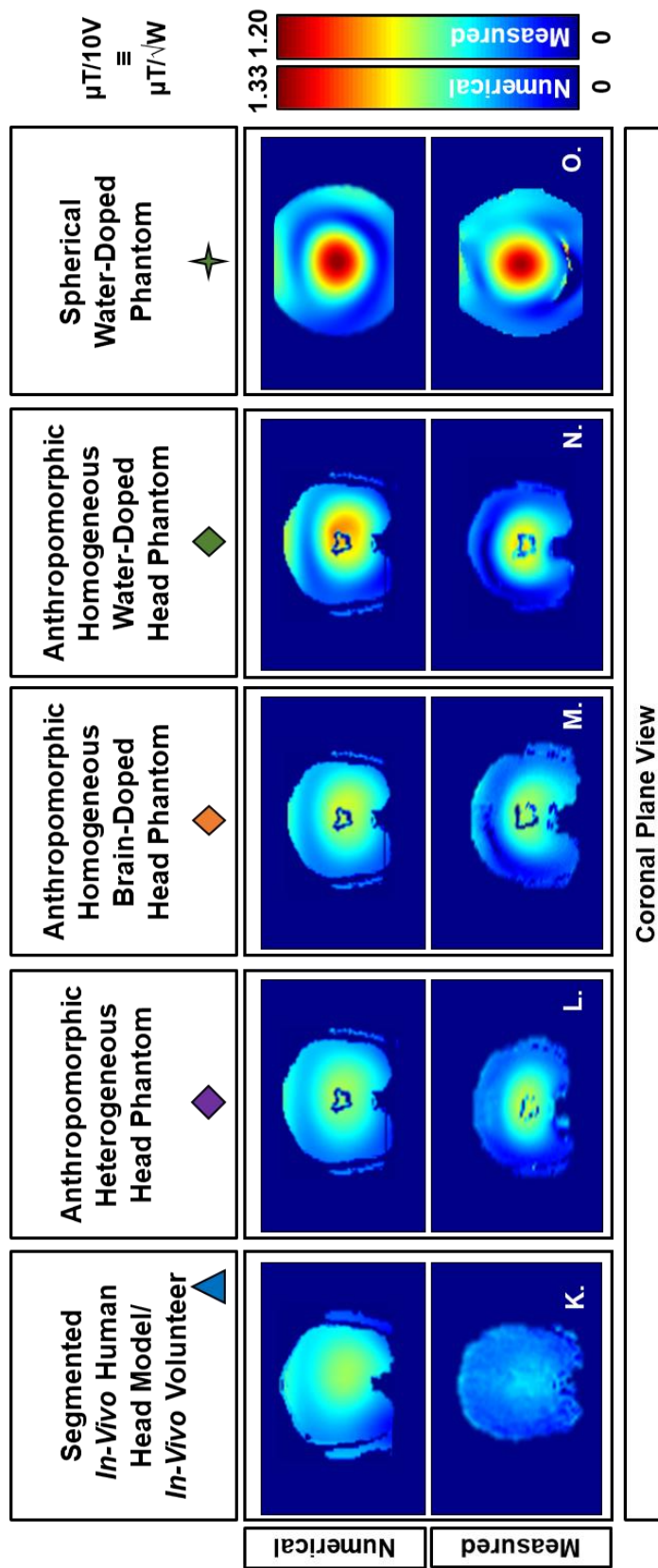


Table 4.2 highlights the numerical and experimental the B_1^+ field statistics for each phantom and the *in-vivo* volunteer in three different brain regions for each head phantom and the *in-vivo* volunteer. The mean B_1^+ field intensity is highest in the Midbrain region given that the TEM resonator is driven in quadrature for all five models. A general observation (Figure 4.3) for this specific coil on all the different loads, the quadrature excitation produces the highest B_1^+ field intensity in the middle region of the phantoms/models/*in-vivo*, but the B_1^+ field intensity considerably drops in the periphery in a semi-radial pattern away from the load's center. Upon excluding the Midbrain region for the anthropomorphic homogeneous water-doped head phantom and the full spherical water-doped phantom, Table 4.2 illustrates that the quantitative average B_1^+ field intensity values of various anthropomorphic head phantoms are comparable to that of the segmented *in-vivo* human head model and the *in-vivo* volunteer.

Table 4.2. Detailed Mean B_1^+ Characteristics of Five Models through Numerical and Experimental Studies. A comparison of numerical and experimental B_1^+ characteristics highlighting the mean B_1^+ for 1W of input power ($\mu T/\sqrt{W}$) in three brain regions (all fillable compartments in the head phantom above and including the cerebellum), brain (excluding the Midbrain), and Midbrain).

Selected Regions of Interest in All Models	Head Models								Basic Phantom Model	
	Segmented <i>In-Vivo</i> Human Head Model/ <i>In-Vivo</i> Volunteer ▲		Anthropomorphic Heterogeneous Phantom Model ◆		Anthropomorphic Homogeneous (Brain-Doped) Phantom Model ◆		Anthropomorphic Homogeneous (Water-Doped) Phantom Model ◆		Spherical (Water-Doped) Phantom Model ★	
	Num.	Exp.	Num.	Exp.	Num.	Exp.	Num.	Exp.	Num.	Exp.
All Fillable Compartments in Head Phantom Above & Including the Cerebellum	0.468	0.290	0.471	0.335	0.479	0.332	0.474	0.364	0.497	0.345
Brain (excluding the Midbrain)	0.470	0.293	0.473	0.339	0.480	0.332	0.473	0.370	--	--
Midbrain	0.682	0.363	0.647	0.406	0.710	0.444	0.862	0.569	--	--

Table 4.3 tabulates a comparison of the numerical and experimental CV of the B_1^+ field distributions of three brain regions for each head phantom and the *in-vivo* volunteer. In all models, the B_1^+ field map is most uniform in the Midbrain region (smaller in volume). Figure 4.3 qualitatively demonstrates that the anthropomorphic heterogeneous phantom's B_1^+ distribution is most comparable to the *in-vivo* volunteer and segmented *in-vivo* human head model. Table 4.3, however, illustrates that the quantitative CV values of the B_1^+ field distribution of the anthropomorphic heterogeneous phantom and the anthropomorphic homogeneous brain-doped head phantom are comparable to that of the segmented *in-vivo* human head model and the *in-vivo* volunteer. A similarity in CV values is observed for the anthropomorphic homogeneous water-doped head phantom and the spherical water-doped phantom.

Table 4.3. Detailed Coefficient of Variation (CV) B_1^+ Field Values of Five Models through Numerical and Experimental Studies. A comparison of numerical and experimental B_1^+ field intensity characteristics highlighting the CV (standard deviation/ mean) in three brain regions (all fillable compartments in the head phantom above and including the cerebellum), brain (excluding the Midbrain), and Midbrain.

Selected Regions of Interest in All Models	Head Models						Basic Phantom Model	
	Segmented <i>In-Vivo</i> Human Head Model/ <i>In-Vivo</i> Volunteer		Anthropomorphic Heterogeneous Phantom Model		Anthropomorphic Homogeneous (Brain-Doped) Phantom Model		Anthropomorphic Homogeneous (Water-Doped) Phantom Model	
	Num.	Exp.	Num.	Exp.	Num.	Exp.	Num.	Exp.
All Fillable Compartments in Head Phantom Above & Including the Cerebellum	0.287	0.245	0.276	0.436	0.303	0.356	0.469	0.460
Brain (excluding the Midbrain)	0.268	0.225	0.267	0.424	0.296	0.358	--	--

Table 4.3 (Continued)

Midbrain	0.156	0.154	0.181	0.275	0.131	0.145	0.193	0.215	--	--
----------	-------	-------	-------	-------	-------	-------	-------	-------	----	----

4.2.3.1.3 *Numerical Electric Field Distribution and Intensity Analysis at 7T.*

Figure 4.4 and Figure 4.5 shows the absolute electric field in all phantom and segmented *in-vivo* human head models scaled from a minimum of 0 V/m to the maximum absolute electric field among all models being the anthropomorphic homogeneous water-doped phantom model. In each anthropomorphic head phantom model, the resin material has a higher absolute electric field than the segmented *in-vivo* human head model (baseline). When excluding the SLA resin regions (fat/bone/skin), the anthropomorphic water-doped head phantom model is highest among other head phantom models with a peak absolute electric field value positioned at 3.00 cm above the ventricles. Figure 4.6 indicates the percent change in each anthropomorphic head phantom model's absolute electric field distribution/intensity in comparison to that of the segmented *in-vivo* human head model. The overestimation and underestimation of the absolute electric field are shown to visualize physiological regions where the absolute electric field is most or least overestimation or underestimated. Table 4.4 shows the calculations to Figure 4.6 for specified threshold values. The calculations highlight the deviation in the accuracy of the absolute electric field within each anthropomorphic phantom model in comparison to the segmented *in-vivo* human head model. The calculations demonstrate that the anthropomorphic head phantom models generally predict the global absolute electric field well. However, the anthropomorphic heterogeneous head phantom model provides a better maximum deviation in the accuracy of the absolute electric field in the baseline model, which is supported by Table 4.4 demonstration of thresholds to a 50% and higher percentage change.

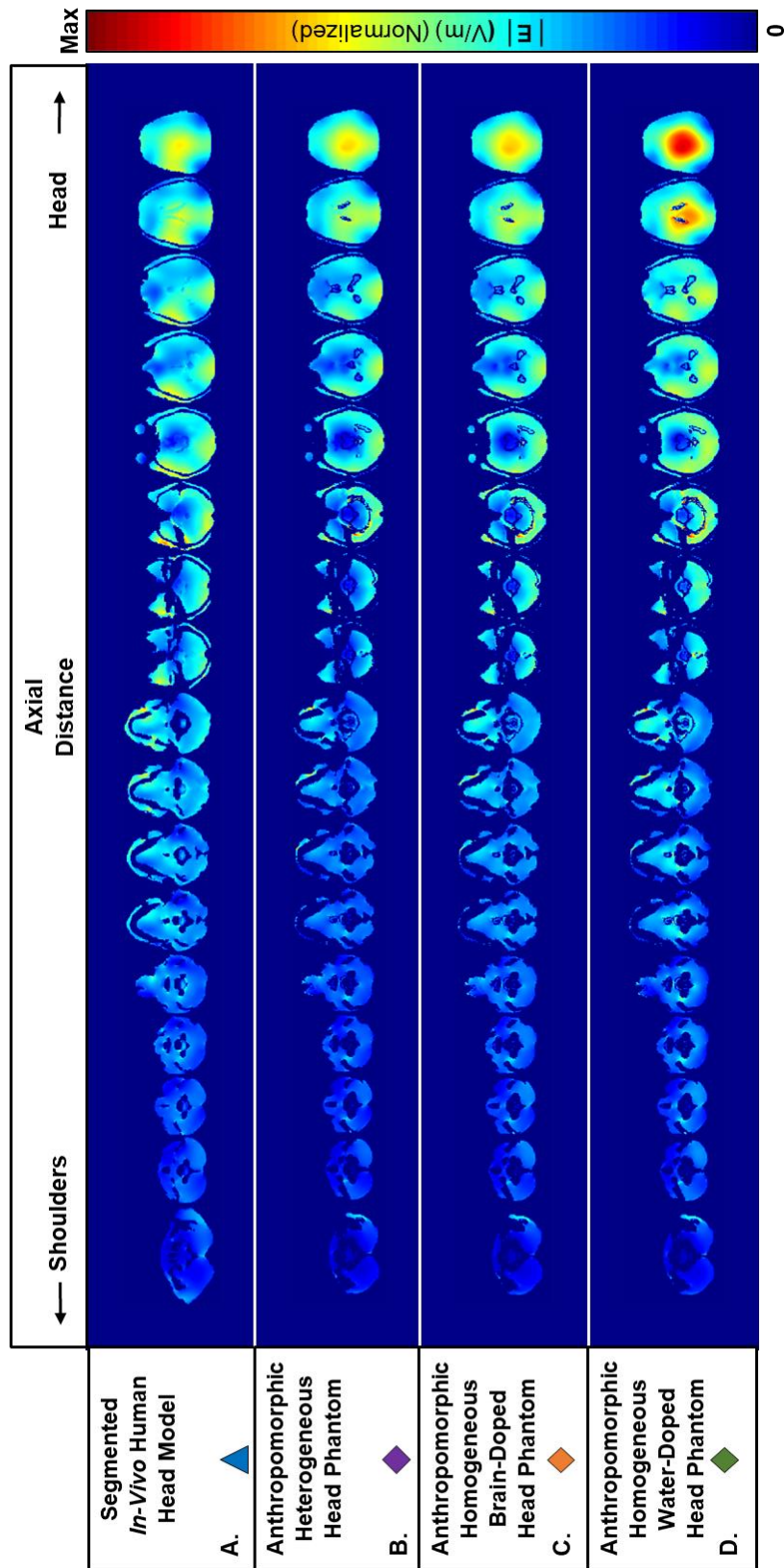


Figure 4.4. Numerical Absolute Electric Field Distribution in Four Models in the Axial View. The numerical absolute electric field is shown for each model in the head and upper shoulders to the 16-strut/4-port TEM resonator based on a scale to the highest peak in the midbrain region of the anthropomorphic homogeneous water-doped phantom.

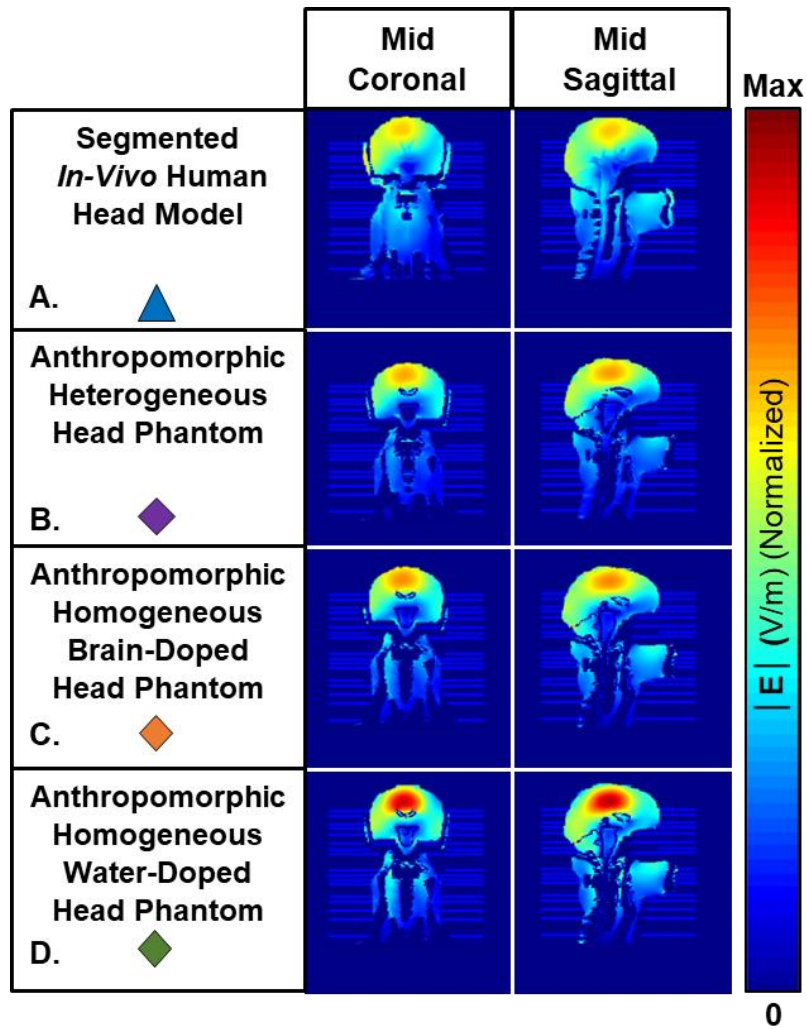


Figure 4.5. Numerical Absolute Electric Field Distribution in Four Models in Coronal and Sagittal View. The numerical absolute electric field is shown for each head model in the head and upper shoulders to the 16-strut/4-port TEM resonator based on a scale to the highest peak in the midbrain region of the anthropomorphic homogeneous water-doped head phantom.

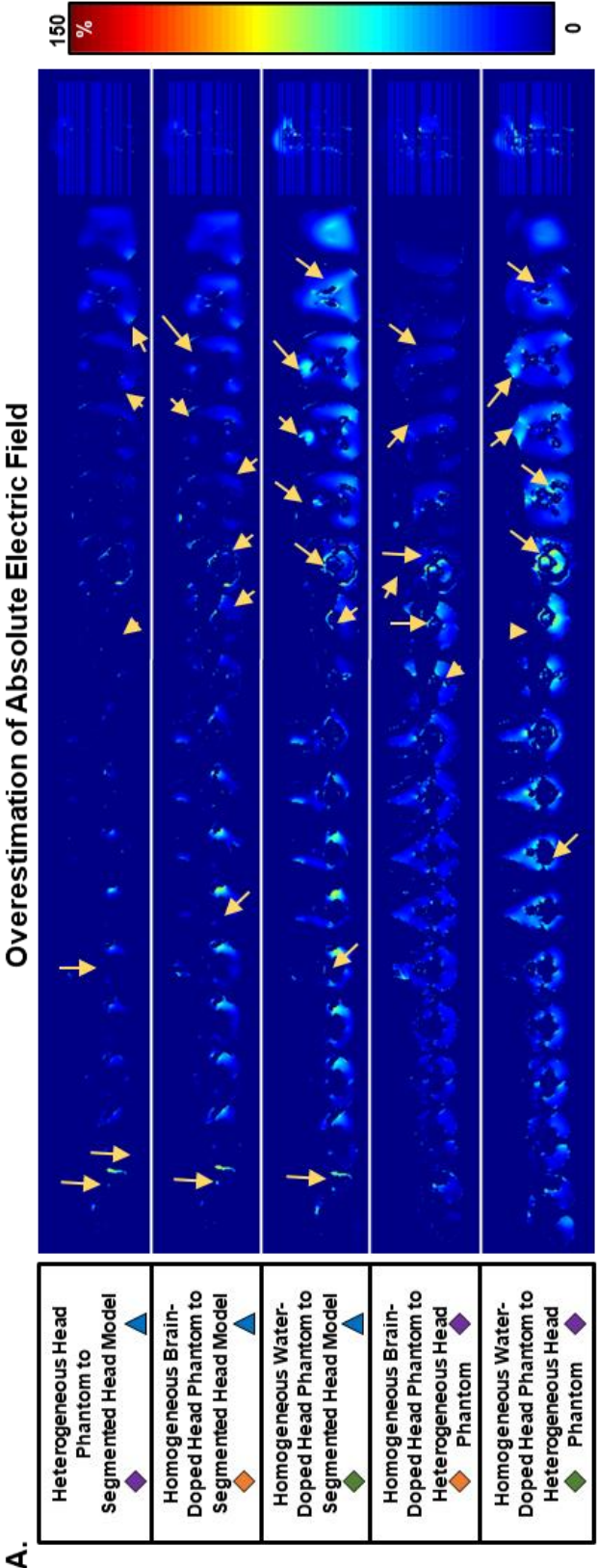


Figure 4.6. Percent Change of Absolute Electric Fields Models. The percent change of each phantom model in Figure 4.4.B-D and Figure 4.5.B-D is compared to the segmented *in-vivo* human head model in Figure 4.4.A and Figure 4.5.A. The peak change values are shown by the yellow solid arrows and the images are scaled to a maximum of 150% based on the anthropomorphic homogeneous water-doped head phantom. The SLA resin material is removed to focus on the absolute electric field distribution in the fillable compartments. The overestimation of the absolute electric field distribution based on each phantom is shown in (A). The underestimation of the absolute electric field distribution based on each phantom is shown in (B).

Figure 4.6 (Continued)

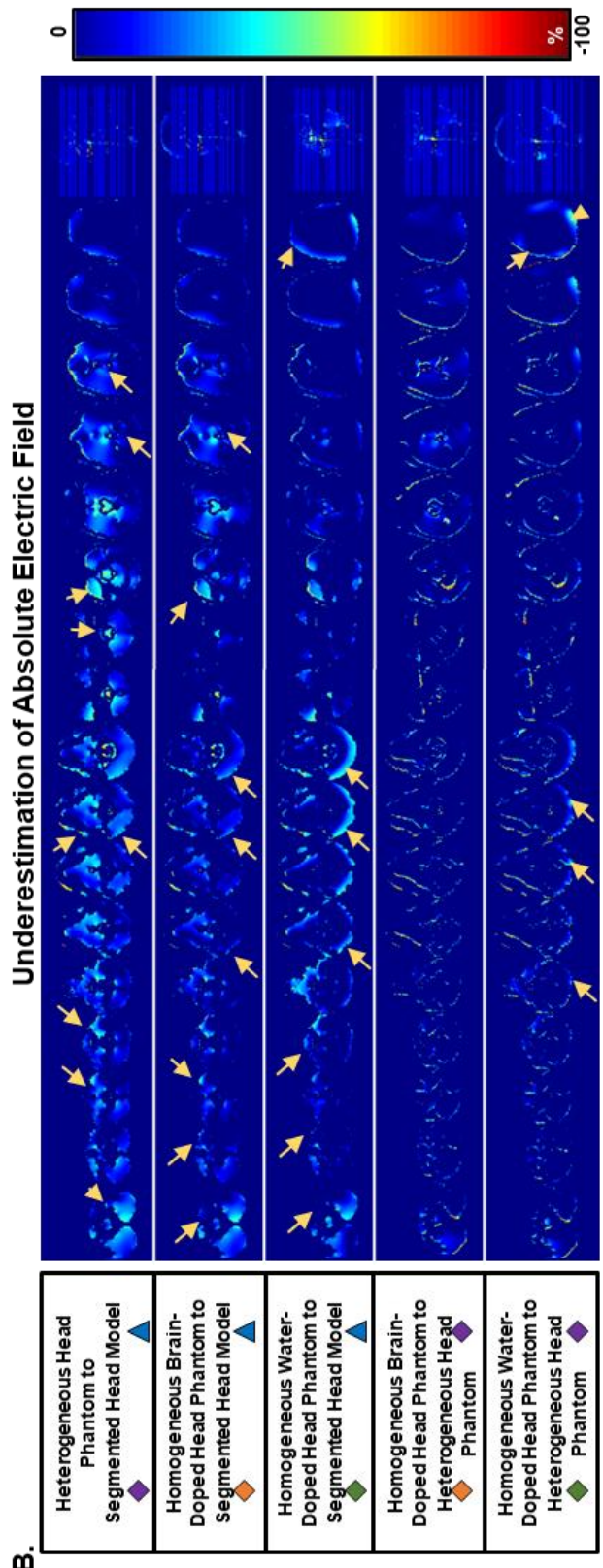








Table 4.4. Percent Volume Change in the Absolute Electric Field Models Beyond the Percent Threshold at 7T. Calculations compared the percent of the volume change beyond the threshold of each phantom model in Figure 4.4.B-D to the segmented *in-vivo* human head model in Figure 4.4.A. The percentage volume change represents the deviation in accuracy from the segmented *in-vivo* human head model.

Head/ Phantom Model	Threshold			
	25	50	75	100
Heterogeneous Head Phantom  to  Segmented Head Model	9.65%	0.88%	0.11%	0.00%
Homogeneous Brain-Doped Head Phantom  to  Segmented Head Model	7.36%	1.04%	0.29%	0.04%
Homogeneous Water-Doped Head Phantom  to  Segmented Head Model	19.80%	2.17%	0.57%	0.09%

4.2.3.2 Discussion

4.2.3.2.1 *Numerical Scattering Parameters Measurements at 7T.*

While the following results could be coil (TEM resonator) or field strength (7T) specific, Figure 4.2 indicates that the spherical water-doped phantom (**Error! Reference source not found..E**) does not have similar loading effects to either the anthropomorphic head phantoms (Figure 4.2.B-D) or the segmented *in-vivo* human head model (Figure 4.2.A). The numerically calculated S-parameters shown in Figure 4.2 indicate that the coil load impedance and reflection coefficients are mostly comparable to the segmented *in-vivo* human head model with anthropomorphic heterogeneous head phantom (7.74% difference), anthropomorphic homogeneous brain-doped head phantom (4.63% difference) than with the anthropomorphic homogeneous water-doped head phantom (14.06% difference) and spherical water-doped phantom (41.58% difference).

It is most advantageous to assess the RF loading of the coil via S-matrix and frequency response using an anthropomorphic head phantom filled with appropriate conductive media (homogeneous or heterogeneous) instead of a homogeneous spherical water-doped phantom.

4.2.3.2.2 *Numerical B_1^+ Field Mapping Measurements and Verifications of Experimental Measurements at 7T.*

Figure 4.3 compares B_1^+ field distributions of the various phantoms to the segmented *in-vivo* human head model/*in-vivo*. Figure 4.3 demonstrates that the spherical water-doped phantom is not comparable to the *in-vivo* volunteer and that the anthropomorphic heterogeneous and homogeneous brain-doped head phantoms are better comparisons to the *in-vivo* volunteer. A previous work (23) has shown similar RF characteristics indicating that the RF travels a further

electrical distance in water-doped phantoms because the RF wavelength is shorter (dielectric constant is 50% higher than the homogeneous brain-doped and heterogeneous models as shown in Table 4.1). Among the anthropomorphic head phantoms, the results of Figure 4.3 and Table 4.2 to 4.3 indicate that anthropomorphic homogeneous brain-doped head phantom and anthropomorphic heterogeneous head phantom provide the most comparable magnetic field behavior to that associated with the *in-vivo* volunteer and the segmented *in-vivo* human head model. This finding indicates that the B_1^+ field distribution is generally more sensitive to the load's geometry and physical dimensions at 7T.

Table 4.3 shows a robust comparison of the anthropomorphic head phantom models to the segmented *in-vivo* human head model / *in-vivo* volunteer numerically and experimentally in select brain regions. While the B_1^+ field can be analyzed in each selected region, the cerebellum was not chosen because the B_1^+ field intensity is too low for this coil and the comparison is not meaningful. Figure 4.3 visually demonstrates the difference in the center brightness of the various loads, specifically the Midbrain region. The quantitative B_1^+ field intensity values indicate that in the Midbrain, the anthropomorphic homogeneous water-doped head phantom model is very different (50.5%) from the *in-vivo* volunteer. From a B_1^+ perspective, the anthropomorphic homogeneous brain-doped head phantom model is similar to the anthropomorphic heterogeneous head phantom model.

Figure 4.3.A, 4.3.F, and 4.3.K illustrate that the change in the B_1^+ field distribution of the numerical model and experimental *in-vivo* measurements are due to the segmented *in-vivo* human head model being an assumption of the volunteer's anatomy. Similarly, Zhang *et al.* (135) observed that the comparison of the Virtual Family v1.0 Duke model to *in-vivo* differed slightly due to pathological changes in the human anatomy of Duke and the human subject. Although the

segmented *in-vivo* human head model and *in-vivo* B_1^+ field slightly vary in our study, it is much more imperative to notice the precise matching of the physical dimensions of the segmented *in-vivo* human head model and the *in-vivo* volunteer.

In summary, the results show that an RF coil designer can use either an anthropomorphic heterogeneous or homogeneous brain-doped head phantoms for accurate magnetic field comparisons to that obtained *in-vivo*.

4.2.3.2.3 Numerical Electric Field Distribution and Intensity Analysis at 7T.

One method to monitor MR safety is to measure temperature rise during MR scans. Numerical modeling, however, is the most utilized resource for predicting MR safety in a real MR environment, and EM numerical modeling was the only available resource to assess the MR safety of each phantom model in this study.

SAR is directly proportional to the electric field squared; thus, an elevation in the electric field intensity can be harmful if temperature rise occurs and exceeds safety limits. It is difficult to directly assess SAR and/or electric field dependence; a high SAR value does not directly indicate high electric field because SAR is scaled by the conductivity as well. Our study assesses the absolute electric field distribution in various loads, and Figure 4.4, Figure 4.5, and Table 4.4 is an illustration of each absolute electric field distribution with respect to the four phantom/head models.

The anthropomorphic homogeneous water-doped head phantom model has the highest absolute electric field intensities within the fillable compartments. Even more, all anthropomorphic head models have the highest absolute electric field distribution in the SLA resin material. Since the goal of this study is not to compare the absolute electric field in the SLA resin, the absolute electric field distribution is only shown in the fillable regions of the four phantom/

head models. However, the SLA resin material was strategically chosen to represent the combination of fat, bone, and skin that is similar to the weighted averaged of these tissues. As a result, the SLA resin material represents the electric field behavior of the fat and bone well. The fat and bone tissues are low conductive media, and the absolute electric field is much higher in these tissues in comparison to the skin. While it is ideal to use a conductive resin that is representative of the skin, the skin is too thin to accurately 3D print currently and its relatively high conductivity is difficult to achieve in a resin material.

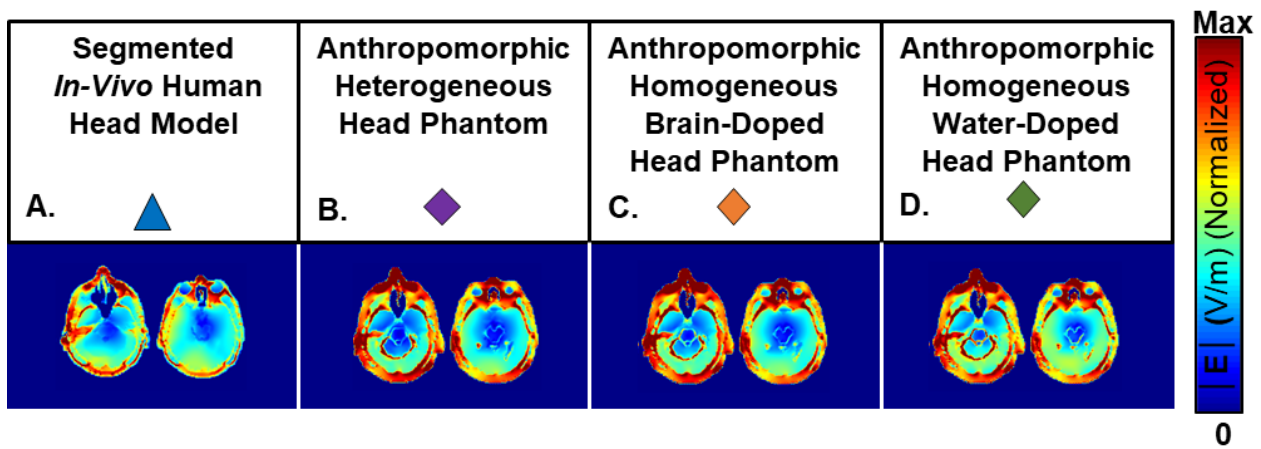


Figure 4.7. Absolute Electric Field in Four Phantom/ Head Models at 297.2 MHz. A comparison is shown between the absolute electric field distribution in the segmented *in-vivo* human head model (A) to the absolute electric field distribution in the SLA resin in the anthropomorphic head models (B-D).

The segmented *in-vivo* human head model (Figure 4.4.A) represents how the electric field is relatively low in the skin and increases in value as the EM wave propagates through the bone and fat. The designed phantom utilizes a resin material with conductivity = 0.11 S/m, which is similar to the averaged conductivity (0.17 S/m) of the fat, bone, and skin. Although the conductivity and permittivity of media in the phantom’s fillable compartments are altered due the presence of the SLA resin, this phantom offers similarities of what occurs at the boundaries of air

cavities and physiological tissue in human anatomy. The designed anthropomorphic head phantom model (Figure 4.7.B-D) offers a realistic mimicry to the segmented *in-vivo* human head model specifically for the electric field interactions within the nasal cavities, ear canal, and eyes. The absolute electric field is highest in these areas because the conductivity value is relatively low. As a result, the comparison of Figure 4.4 and Figure 4.5 are most essential for MR safety applications.

Figure 4.4 and Figure 4.5 shows that the absolute electric field distribution in the anthropomorphic head phantom models are more comparable to the segmented *in-vivo* human head model as opposed to the spherical water-doped phantom model. While the anthropomorphic head phantom models are most comparable to the segmented *in-vivo* human head model, Figure 4.5 and Table 4.4 further highlight that there are subtle differences in the absolute electric field distributions and emphasizes that the anthropomorphic heterogeneous head model offers a better indication in the accuracy of the peak absolute electric field intensities of the segmented *in-vivo* human head model.

While the anthropomorphic homogeneous brain-doped head phantom is sufficient to predict the B_1^+ field distribution and S-matrix obtained *in-vivo*, more differences are noted in the absolute electric field distribution when compared to the anthropomorphic heterogeneous head phantom. These differences are most apparent in the designed anthropomorphic head phantom's brain region, the cerebellum, and the muscle as indicated by the yellow arrows in Figure 4.6.A. Of all head phantoms, the anthropomorphic homogeneous water-doped head phantom model offers the highest differences from the segmented *in-vivo* human head model. Notice in Figure 4.4, the absolute electric field in the anthropomorphic homogeneous water-doped head phantom model is higher in the fillable regions because the dielectric constant primarily in the brain region is 50% higher than the other models.

An overestimation of the absolute electric field may lead to high SAR and increased temperature rise. Nevertheless, both anthropomorphic homogeneous phantom models overestimate the electric field of the segmented *in-vivo* human head model; however, brain-doped media would be a better choice over water-doped media because a lower dielectric constant offers a more comparable absolute electric field. Overall, the anthropomorphic heterogeneous head phantom and its model overestimates/underestimates the electric field the least.

4.2.4 Summary

Using parameters such as the B_1^+ and the absolute electric field distributions/intensities and S-parameters, a quantitative analysis was performed to compare the *in-vivo* volunteer to 1) the designed anthropomorphic head phantom with different various media contents in its compartments and 2) the spherical water-doped phantom. In summary, our findings indicate that the designed anthropomorphic phantom is a highly useful tool for RF coil evaluation and testing. The S-parameters and B_1^+ field distributions/intensities are comparable to that associated with the *in-vivo* volunteer or the segmented *in-vivo* human head model when the anthropomorphic head phantom and its models are filled with homogenous brain-doped or heterogeneous solutions. However, when comparing the absolute electric field distribution/intensity, the anthropomorphic heterogeneous head phantom is most comparable to the segmented *in-vivo* human head model by having the smallest deviation in accuracy of the absolute electric field intensities. The results also indicate that accurate numerical modeling is still an effective and efficient predictive resource for an EM analysis as shown in Figure 4.3.

While previous RF safety studies (136) conclude that using a physical spherical phantom to approximate an *in-vivo* experiment is a good approximation of the electric field and SAR, our

study is a pilot to indicate the need for further exploration of the designed anthropomorphic head phantom as a more accurate comparison (specifically at 7T) to *in-vivo* studies. Future work will be explored to see if the anthropomorphic head phantom is essential at different field strengths (3T is shown in Part I-B) and with different RF coils (shown in Chapter 5.0).

4.3 PART I-B: ELECTROMAGNETIC CHARACTERIZATION OF THE ANTHROPOMORPHIC HETEROGENEOUS HEAD PHANTOM USING A TEM RESONATOR AT 3T

4.3.1 Introduction

This section presents the same study and methodology as Part I-A (Section 4.2) but is performed at 3T. As the science of 7T MRI advances, 3T will be compared as 7T's closest MR competitor as it relates to technology and standards. 7T will need to undergo robust RF technical developments and MR safety to have a true chance of being an operable and desirable clinical human MR machine — just as 3T did nearly two decades ago. Part I-A (Section 4.2) demonstrates that using an experimental anthropomorphic heterogeneous head phantom and its numerical model is advantageous and comparable to an *in-vivo* volunteer for the TEM Resonator at 7T. Part I-B aims to observe numerically if the anthropomorphic heterogeneous head phantom model is also advantageous and comparable to the segmented *in-vivo* human head model at 3T.

It is known that inhomogeneous RF field distributions exist at 7T and cause a wide variety of performance and safety issues. The wavelength for proton imaging is ~26-28 cm at 3T (25), and the human head length in the anterior to posterior (AP) direction is ~18-22 cm. At HF

frequencies (~ 128 MHz to less than ~ 297 MHz), the penetration of the RF field into tissue does not decrease as quick as ultrahigh field strengths. The challenges of 3T are similar yet different than the challenges of 7T. At 3T, there are challenges in areas such as the susceptibility, chemical shift, pulse sequences and RF inhomogeneity in larger body regions like the torso. Since 3T is known to have a more homogeneous RF field distribution than 7T, experimental phantoms (similar to that shown in Figure 4.1.A (82, 118, 119) and Figure 2.8) have been the gold standard. Various works (137-139) used anthropomorphic head phantoms at 3T to address some of its challenges and limitations such as chemical shift (137), validation of segmentation to replicate *in-vivo* T1 signal intensity (139), and the SNR degradation within a receive coil (138). However, our designed experimental anthropomorphic head phantom may appear to be most resourceful when analyzing RF safety and addressing the other challenges at 3T beyond what works (137-139) covered. Thus, Part I-B addresses the need of using the anthropomorphic heterogeneous head phantom model at 3T through performing the methods of Part I-A numerically at 3T.

4.3.2 Materials and Methods

4.3.2.1 Numerical Studies

4.3.2.1.1 FDTD Simulations and Numerical Models at 3T

A similar method to Subsection 4.2.2.1.1 is used to produce the electric and magnetic fields and the scattering parameters (S-parameters). The software utilizes the same isotropic spatial and temporal resolution to Subsection 4.2.2.1.1. A first-order differentiated Gaussian pulse (5.8 ns period and 150,000-time steps) was used to excite the RF coil and various loads.

Before generating the EM fields, the TEM resonator is properly tuned and matched to 128.0 MHz (3T) by loading the Virtual Family v1.0 Duke head to shoulder model with its respective constitutive parameters at this operational frequency. The same five numerical models (used in Subsection 4.2.2.1.1) were simulated at 3T with the identical positioning within the TEM resonator (shown in Figure 4.1.B and 4.1.E) and to have its corresponding constitutive properties shown in Table 4.5.

4.3.2.1.2 *RF Coil and S-Matrix.*

16-strut/4-port TEM resonator (62) is utilized as the RF coil and tuned and matched to 128.0 MHz. The computational domain and coil dimensions are the same as 7T. The coil is also driven in quadrature. The S-matrix and load impedance of each phantom and head model are shown in Figure 4.8 with a frequency span of 100.0 MHz within the center frequency of 128.0 MHz.

4.3.2.1.3 *FDTD Calculations at 3T*

The FDTD calculations were computed using the same methods as shown in Subsections 4.2.2.1.3 and 4.2.2.1.4 at 128.0 MHz. Methods to compute and analyze the EM fields are as follows: 1) calculate the B_1^+ field referenced in Subsection 4.2.2.1.3 and 2) calculate the absolute electric field referenced in Subsection 4.2.2.1.4.

4.3.2.1.4 *Numerical Phantom Models*

A physical, anthropomorphic heterogeneous head phantom (18) (shown in Figure 4.1.D) was built as described in Subsection 4.2.2.1.5 and only the numerical models are used in this study. The tissues were labeled according to the respective phantom models in the legend of Table 4.5. The stereolithography (SLA) resin (DSM Somos® WaterShed® XC 11122 (Elgin, Illinois)) material is representative of the combination of the fat, bone, and skin and its constitutive parameters are

close to the weighted average of these tissues combined (3T: conductivity = 0.18 S/m, relative dielectric constant = 25.94, and density = 1223.49).

In this study, the anthropomorphic head phantom has six-compartments that are filled with various homogeneous and heterogeneous solutions. The homogeneous solution is either the water-doped solution (3T: conductivity = 0.51 S/m and relative dielectric constant = 76.56) or the brain-doped solution (3T: conductivity = 0.47 S/m and relative dielectric constant = 63.80) as described in Table 4.5. A commercial spherical phantom (shown in Figure 4.1.A), 170 mm in diameter, is water-doped with the homogeneous solution at 3T.

Table 4.5. Constitutive Parameters of Phantom Materials at 128.00 MHz Derived from Cited Literature (31, 98).























Phantom Tissue Classification	General Biological Tissue Classification	Conductivity (S/m)	Relative Permittivity	Density (kg/m ³)	Wavelength (m)	Skin Depth (m)	Tissue Representation in Model
Air	Sinuses, Esophagus	0.00	1.00	1.25	2.34	N/A	    
Brain (WM/GM)	White Matter, Gray Matter, External CSF, Dura	0.47	63.80	1040.00	0.27	0.10	  
Brainstem	Pons, Medulla Oblongata, Spinal Cord, Midbrain	0.35	44.07	1039.00	0.32	0.12	 
Cerebellum	Cerebellum	0.83	79.74	1040.00	0.22	0.07	 
Cerebrospinal Fluid (CSF)	Internal CSF near lateral horns and around spinal cord	2.14	84.04	1007.00	0.17	0.03	 
Eyes	Cornea, Vitreous Humor, Eyes Sclera	1.30	67.71	1020.07	0.21	0.05	 
Muscle	Tendons, Tongue, Muscle	0.72	63.50	1049.78	0.24	0.07	 
Fat/ Bone/ Skin (3D SLA Material)	Fat, Cortical Bone, Cartilage, Skin Dry	0.00	4.56	1120.00	--	0.09	   

Table 4.5 (Continued)

Fat	Fat	0.04	5.92	916.00	0.89	0.38	▲
Bone	Cortical Bone	0.07	14.72	1990.00	0.58	0.32	▲
Skin	Skin Dry	0.52	65.44	1100.00	0.26	0.09	▲
Water-Doped	Homogeneous Phantom Solution with Saline	0.51	76.56	1000.00	--	--	◆ ✦ ✧

Legend: ▲ Segmented *In-Vivo* Human Head Model ◆ Heterogeneous Head Model ✦ Spherical (Water-Doped) Model
 ◆ Homogeneous (Water-Doped) Head Model ✧ Homogeneous (Brain-Doped) Head Model

The constitutive parameters of each classified phantom/ segmented tissue in the respective model are the conductivity (σ), permittivity (ϵ_r), density (ρ), wavelength (λ), and skin depth (δ). The key legend indicates which tissue is represented in the various models. The phantom tissue classification is based on the assumption that averaged tissue classification is comparable to the percentage of the biological tissue in the Virtual Family v1.0 Duke head model at 128.0 MHz.

4.3.2.2 Experimental Studies

Experimental studies were not performed at 3T due to limited resources.

4.3.3 Results and Discussion

4.3.3.1 Results

4.3.3.1.1 Numerical Scattering Parameters Measurements at 3T.

Numerical results show the calculated frequency response (S11) and Smith chart for one representative port of the TEM resonator loaded with the numerical segmented *in-vivo* human head model (Figure 4.8.A) and each phantom model (Figure 4.8.B-E) at 128.0 MHz. The simulated coil is tuned and matched once to the Virtual Family v1.0 Duke head model at 128.0 MHz (as done in Subsection 4.2.3.1.1) and was not re-tuned for any of the different models/ loads. As a demo, using the same single port (Port 1) on the 16-strut/4-port TEM resonator for both frequencies, each model's numerical S11 is assessed for its frequency response, Smith chart, S-Matrix, and load impedance.

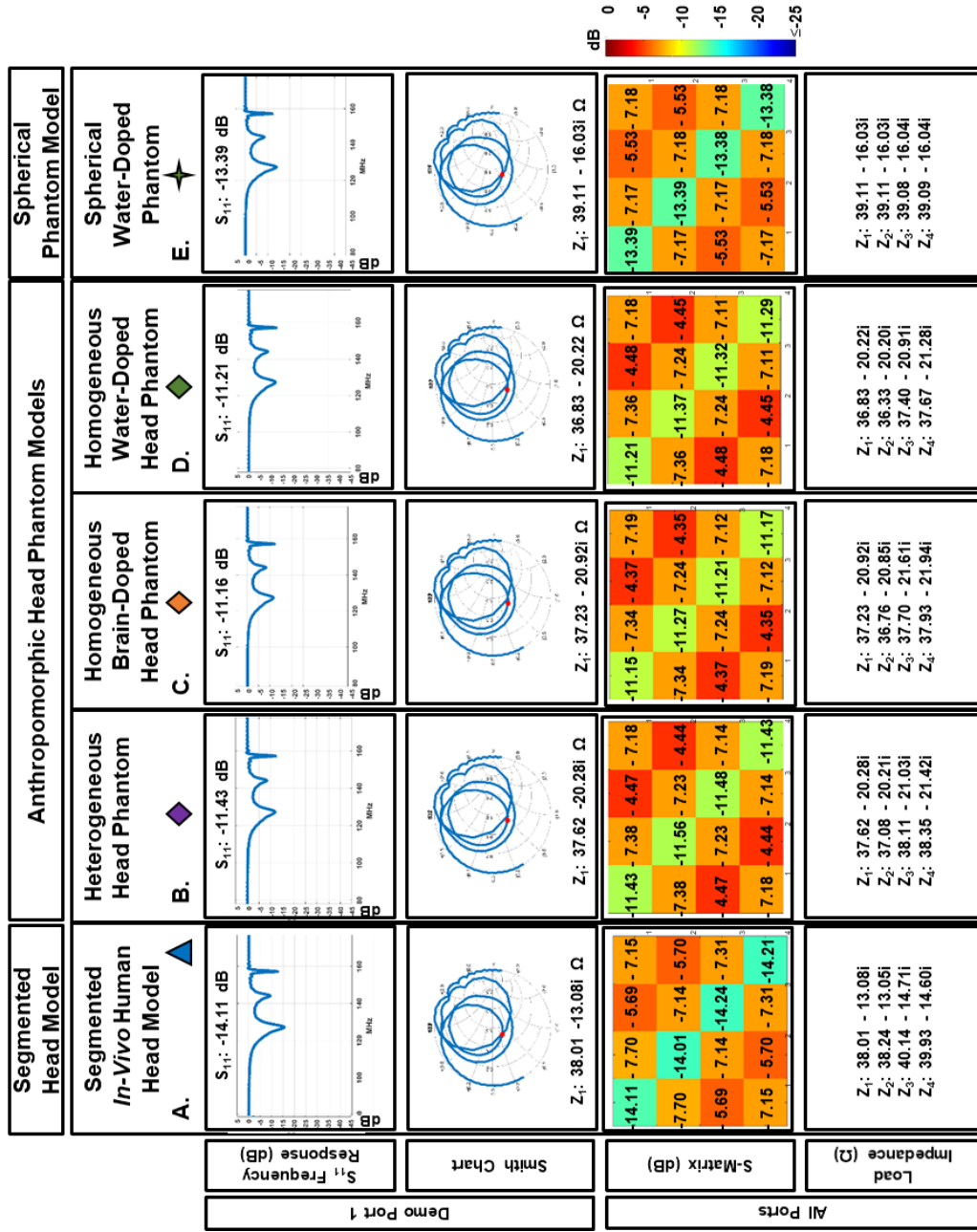


Figure 4.8. S-Parameters Measurements of Five Numerical Models Positioned in the 16-strut/4-port TEM Resonator at 3T. The frequency response is modeled for the segmented *in-vivo* human head model (A) and each phantom (B-E) model. A demo of the frequency response of one channel,

The S11 frequency response and Smith chart is shown in Figure 4.8 for all five models loaded within a 16-strut/4-port TEM resonator at 128.0 MHz. Despite the media content, the S11 frequency responses were relatively similar for all four phantom models. The anthropomorphic head phantom models were valued at an amplitude of ~11 dB; the spherical water-doped phantom model had an amplitude of -13.39 dB; and the segmented *in-vivo* human head model had an amplitude of -14.11 dB.

Port 1's load impedance with the segmented *in-vivo* human head model (Figure 4.2A) is $38.01 - 13.08 \Omega$ (baseline). An evaluation of the percentage change in the value of the reflection coefficient was performed in all five models. For Port 1, the percentage change from the segmented *in-vivo* human head model is calculated as follows: anthropomorphic homogeneous brain-doped head phantom model (20.90%), anthropomorphic homogeneous water-doped head phantom model (20.60%), anthropomorphic heterogeneous head phantom model (18.90%), and spherical water-doped phantom model (13.16%). While these values hold true for Port 1, the average percent change of all channels is as follows: anthropomorphic homogeneous brain-doped head phantom model (20.80%), anthropomorphic homogeneous water-doped head phantom model (20.10%), the anthropomorphic heterogeneous head phantom model (18.90%), and spherical water-doped phantom model (13.31%).

The S-Matrix indicates that all phantom models load similarly regardless of the port and the phantom's media and geometry at 3T. It is difficult to distinguish the phantom model type by referring only to the S-Matrix. The load impedance of the spherical water-doped phantom model is in closest agreement to the segmented *in-vivo* human head model's S-Matrix measurements and load impedance values. In the case of the anthropomorphic head phantom models, the load impedance values are relatively similar per port regardless of the media inside of the

anthropomorphic head phantom model. The S-Matrix measurement of the coupling between ports for the segmented *in-vivo* human head model is in close agreement with the coupling of the other various phantom models.

4.3.3.1.2 *Numerical B_1^+ Field Mapping Measurements at 3T*

Figure 4.9 shows the numerical B_1^+ field measurements to each phantom and the segmented *in-vivo* human head model at 3T with corresponding planar view and slices to Figure 4.3 at 7T. All numerical B_1^+ field maps are scaled to the maximum magnitude scale of the five models (0 to $1.60\mu\text{T}/\sqrt{W}$). The B_1^+ field maps are masked to all fillable compartments to exclude the B_1^+ field within the SLA resin, which produces low MR signal.

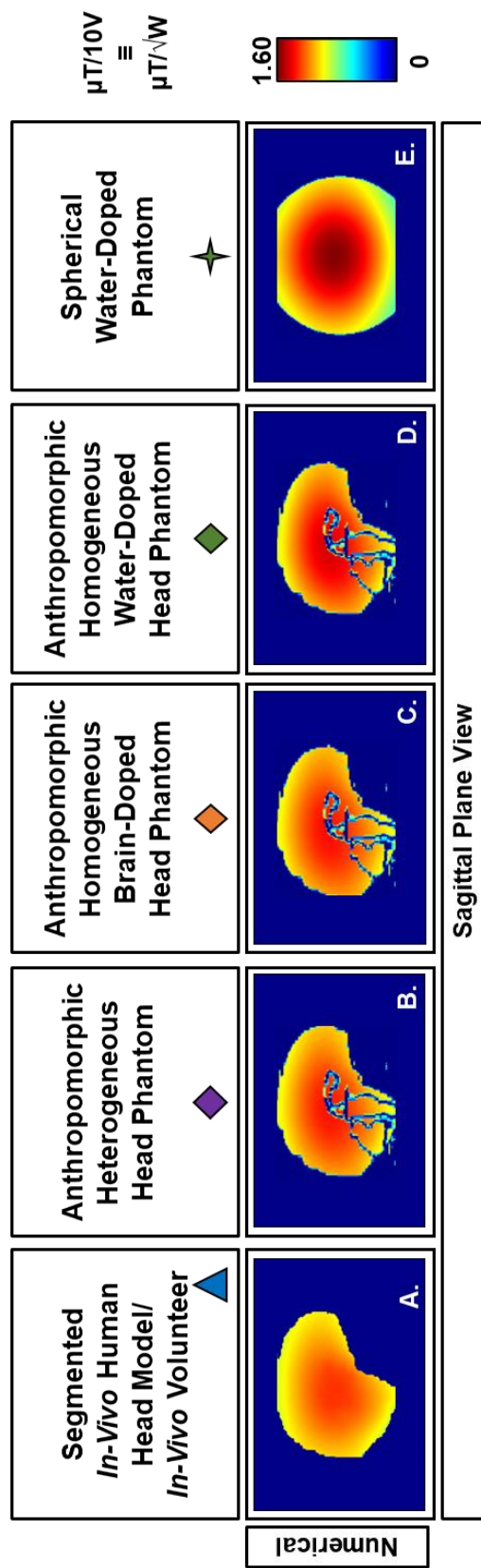


Figure 4.9. B_1^+ field Distributions within the 16-strut/4-port TEM Resonator at 3T. The B_1^+ field distribution is shown for each numerical model and compared to the model's corresponding numerical B_1^+ mapping measurements at 7T (Figure 4.3) in the sagittal, axial, and coronal views (A-O). The numerical models are scaled to 1-Watt (1W) input power supplied by the RF system. The color bar is scaled from 0 to the maximum numerical B_1^+ for 1W of input power values

Figure 4.9 (Continued)

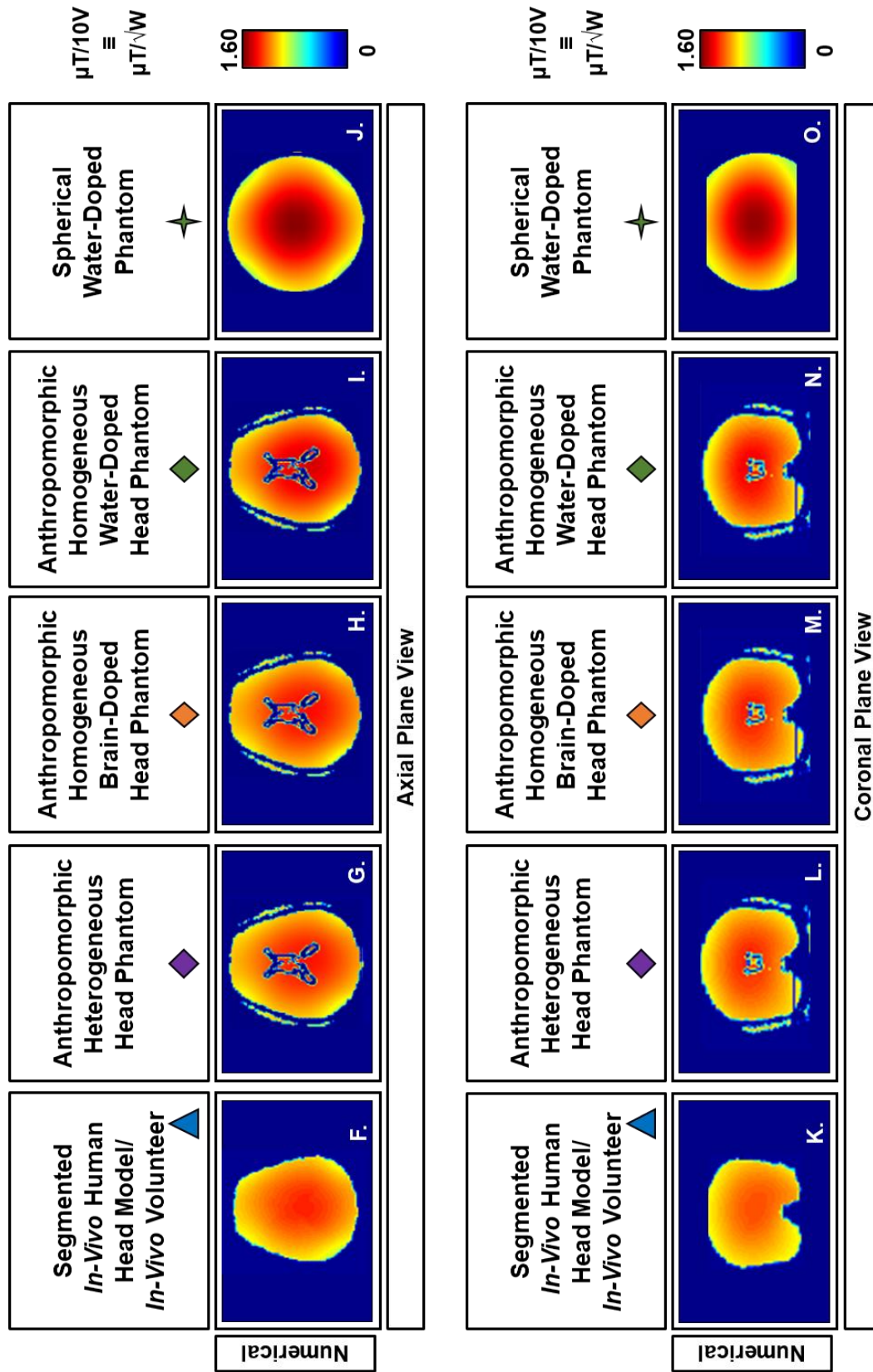


Table 4.6. Detailed Mean B_1^+ Characteristics of Five Models through Numerical Studies at 3T. A comparison of numerical B_1^+ characteristics highlighting the mean B_1^+ for 1W of input power ($\mu T/\sqrt{W}$) in three regions of interest (all fillable compartments in the head phantom above and including the cerebellum), brain (excluding the Midbrain), and Midbrain).





Selected Regions of Interest in All Models	Head Models				Basic Phantom Model
	 Segmented In-Vivo Human Head Model/ In-Vivo Volunteer	 Anthropomorphic Heterogeneous Phantom Model	 Anthropomorphic Homogeneous (Brain-Doped) Phantom Model	 Anthropomorphic Homogeneous (Water-Doped) Phantom Model	
All Fillable Compartments in Head Phantom Above & Including the Cerebellum	1.092	1.146	1.157	1.181	1.148
Brain (excluding the Midbrain)	1.100	1.152	1.163	1.188	--
Midbrain	1.235	1.223	1.226	1.273	--

Table 4.6 highlights the numerical mean B_1^+ field intensity evaluation parameters for each phantom model and the segmented model in three different brain regions. The mean B_1^+ is highest within the midbrain region given that the TEM resonator is driven in quadrature for all five numerical models. Figure 4.9 demonstrates the B_1^+ field maps are very homogeneous at 3T despite the changes in the media used to fill the phantom or the phantom's geometry. Figure 4.9 illustrates the phantoms with the SLA resin. The phantom and segmented *in-vivo* human head models become less homogeneous below the brain ROI compared to a more uniform field throughout the brain as shown in Figure 4.10.

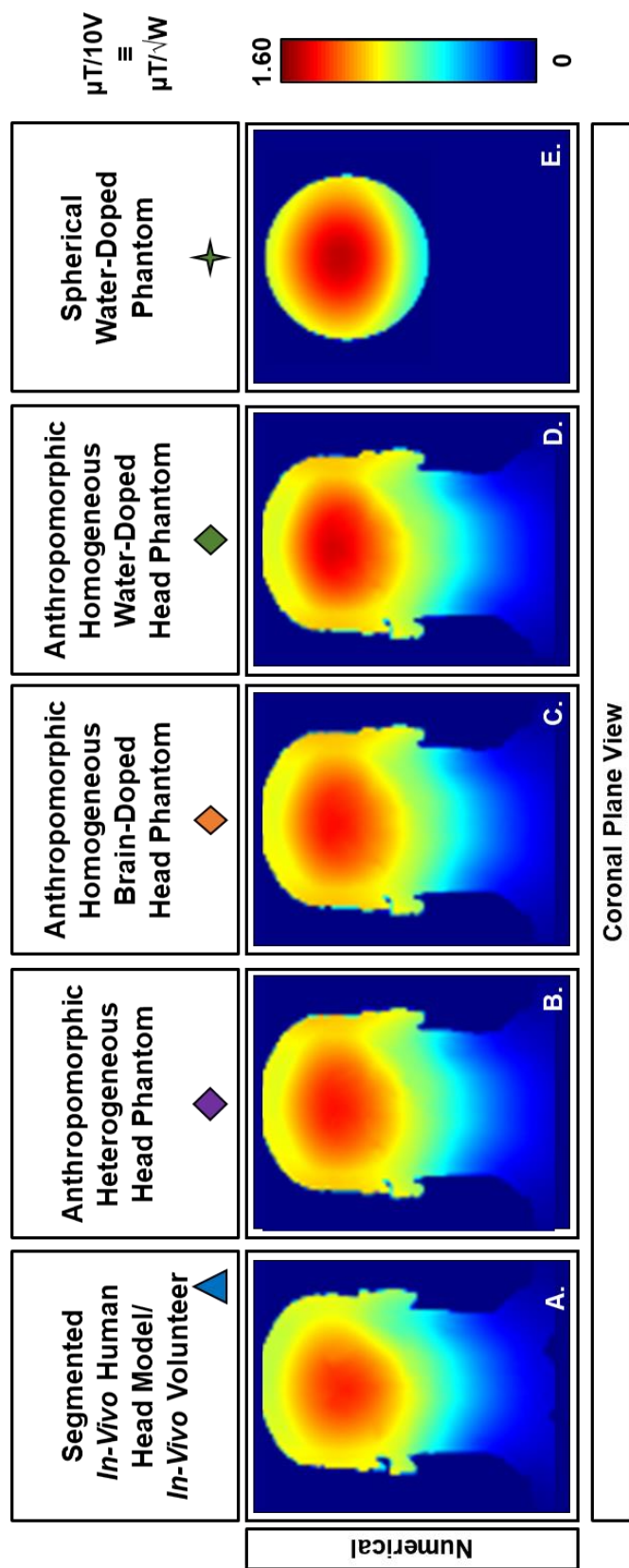


Figure 4.10. Coronal View of Full B_1^+ field Distributions within the 16-strut/4-port TEM Resonator at 3T. The B_1^+ field distribution for each numerical model is shown and compared to the model's corresponding numerical B_1^+ mapping measurements at 7T (Figure 4.3) in the coronal views (A-O). The numerical models are scaled to 1W input power supplied by the RF system. The color bar is scaled from 0 to the maximum numerical B_1^+ values.

Table 4.7. Detailed CV B_1^+ Characteristics of Five Models through Numerical Studies at 3T. A comparison of numerical B_1^+ characteristics highlighting the coefficient of variation (std/ mean) in three brain regions (all fillable compartments in the head phantom above and including the cerebellum), brain (excluding the Midbrain), and Midbrain).



Selected Regions of Interest in All Models	Head Models				Basic Phantom Model
	Segmented <i>In-Vivo</i> Human Model/  <i>In-Vivo</i> Volunteer	 Anthropomorphic Heterogeneous Phantom Model	 Anthropomorphic Homogeneous (Brain-Doped) Phantom Model	 Anthropomorphic Homogeneous (Water-Doped) Phantom Model	
All Fillable Compartments in Head Phantom Above & Including the Cerebellum	0.101	0.087	0.087	0.104	0.155
Brain (excluding the Midbrain)	0.090	0.083	0.083	0.100	--
Midbrain	0.041	0.047	0.049	0.055	--

Table 4.7 highlights the numerical CV of the B_1^+ field distributions of three brain regions for each phantom head model. In all models, the B_1^+ field map is most uniform in the Midbrain region (smaller in volume) since the coil was driven in quadrature mode. Table 4.7, however, indicates that the anthropomorphic head model's various ROIs are quantitatively homogeneous. In comparison to all models, the anthropomorphic head models are most homogeneous and comparative to the segmented *in-vivo* human head model. The spherical water-doped phantom is not as homogeneous as the anthropomorphic head phantom models as proven quantitatively through Table 4.7. In the other regions, the anthropomorphic heterogeneous and homogeneous brain-doped head phantom models are most similar in the three ROIs to the segmented *in-vivo* human head model. The phantom models filled with the water's constitutive parameter have a small divergence from the segmented *in-vivo* human head model, but it is not significant. For the fillable compartment ROI, the water-doped phantom models are ~0.003 to 0.05 CV units higher than the segmented *in-vivo* human head model.

4.3.3.1.3 Numerical Electric Field Distribution and Intensity Analysis at 3T

Figure 4.11 and Figure 4.12 shows the absolute electric field in all phantom models and the segmented *in-vivo* human head model scaled from a minimum of 0 V/m to the maximum absolute electric field among all models. In each anthropomorphic head phantom model, the resin material has a higher absolute electric field than the segmented *in-vivo* human head model (baseline). When excluding the SLA resin regions (fat/bone/skin), the anthropomorphic head phantom models have the highest peak electric field value among the four numerical models with the peak positioned in the periphery of the lower muscle region surrounding the lower brain region. Note the absolute field is shown only in the models most comparative to the segmented *in-vivo* human head model.

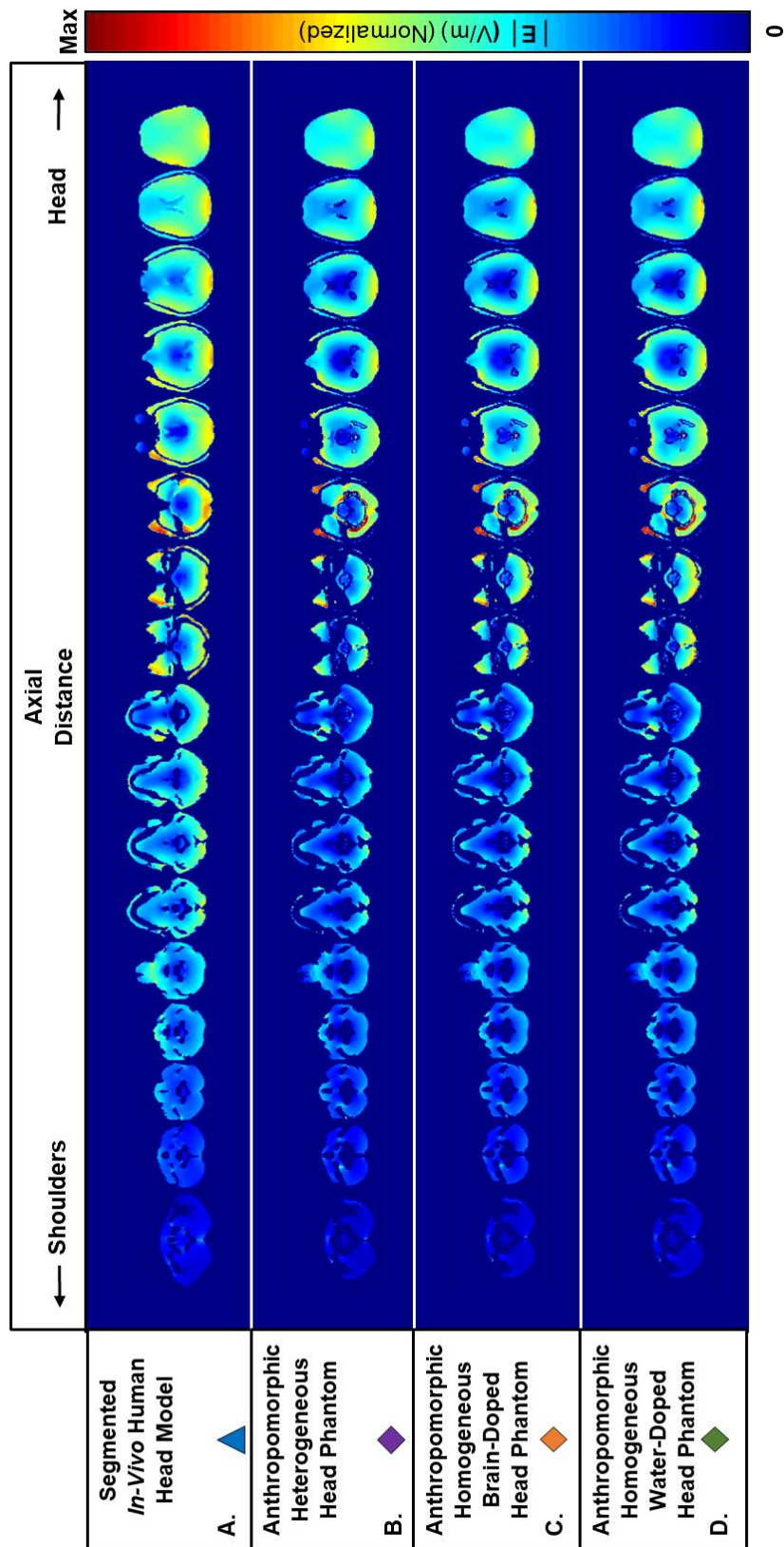


Figure 4.11. Numerical Absolute Electric Field Distribution in Four Models at 3T. The numerical absolute electric field is shown for each model in the head and upper shoulders to the 16-strut/4-port TEM resonator based on a scale to the highest peak in the lower muscle region surrounding the lower brain region within the anthropomorphic head phantoms at 3T.

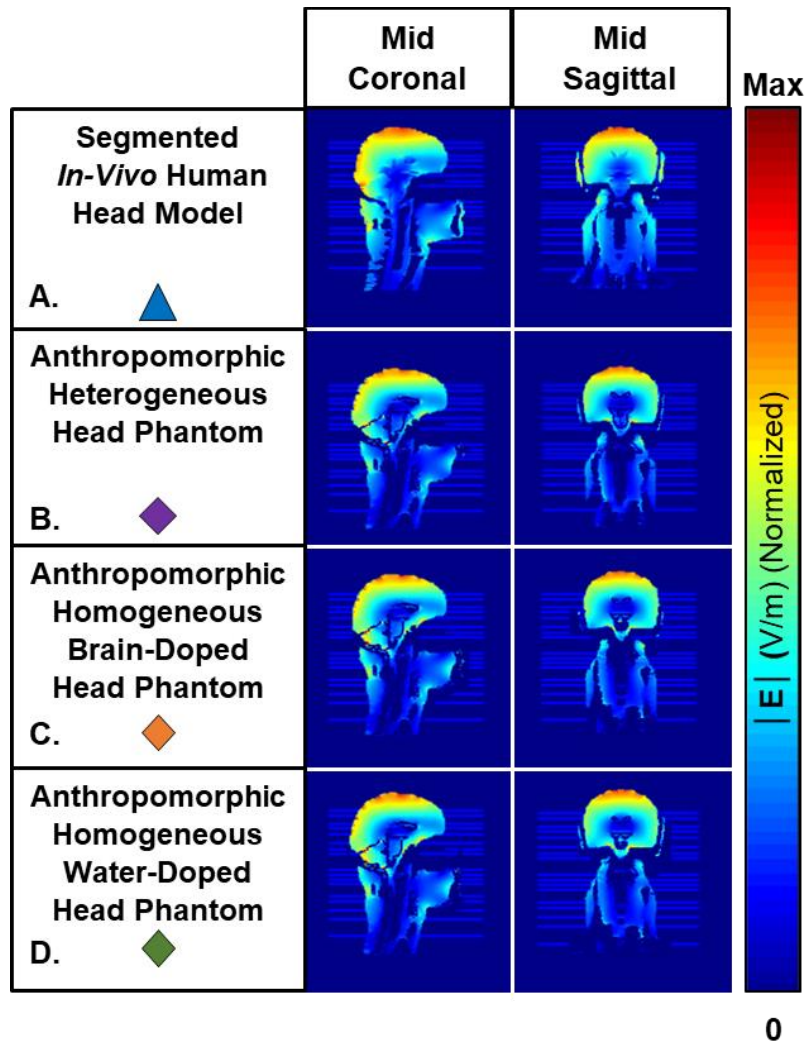


Figure 4.12. Numerical Absolute Electric Field Distribution in Four Models in Coronal and Sagittal View at 3T. The numerical absolute electric field is shown for each model in the head and upper shoulders to the 16-strut/4-port TEM resonator based on a scale to the highest peak in the lower muscle region surrounding the lower brain region within the anthropomorphic head phantoms at 3T.

Figure 4.12. indicates the percent change in each phantom model's electric field distribution/intensity in comparison to that of the segmented *in-vivo* human head model. The overestimation and underestimation of the electric field are shown to visualize the physiological regions where the electric field is most or least overestimated or underestimated. Figure 4.13 shows the percent volume change calculations for the specified threshold percentages.

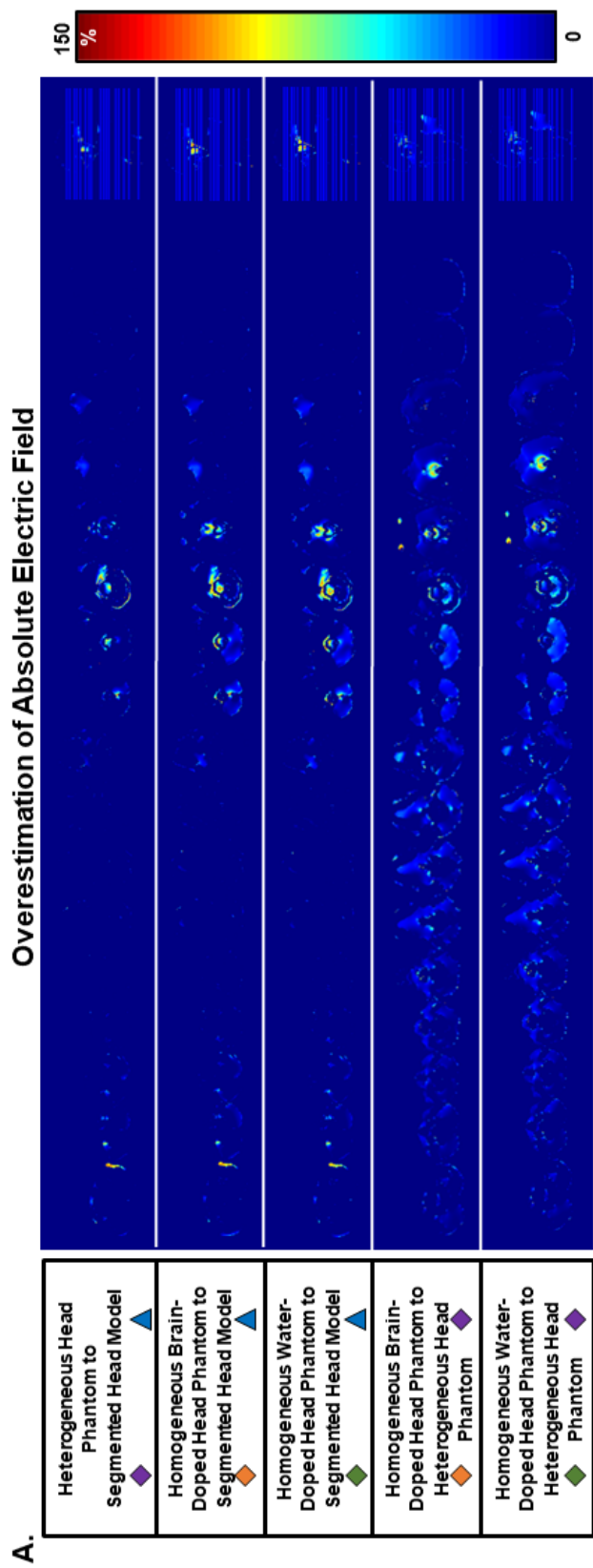


Figure 4.13. Percent Change of Absolute Electric Fields Anthropomorphic and Segmented *in-vivo* Human Head model at 3T. The percent change of each anthropomorphic phantom model in Figure 4.11 and Figure 4.12 is compared to the segmented *in-vivo* human head model in Figure 4.11.A and Figure 4.12.A. The images are scaled to a maximum of 150% based on the anthropomorphic water-doped head phantom. The SLA resin material is removed to focus on the absolute electric field distribution in the fillable compartments. The overestimation of the absolute electric field distribution based on each phantom is shown in (A). The underestimation of the absolute electric field distribution based on each phantom is shown in (B).

Table 4.8. Percent Volume Change in the Absolute Electric Field Models Beyond the Percent Threshold at 3T. Calculations compare the percent volume change of each phantom model in Figure 4.11.B-D to the segmented *in-vivo* human head model in Figure 4.11.A. The percentage volume change represents the deviation in accuracy from the segmented *in-vivo* human head model.







Head/ Phantom Model	Threshold			
	25	50	75	100
Heterogeneous Head Phantom  to  Segmented Head Model	19.31%	2.78%	0.49%	0.15%
Homogeneous Brain-Doped Head Phantom  to  Segmented Head Model	16.89%	2.54%	0.74%	0.36%
Homogeneous Water-Doped Head Phantom  to  Segmented Head Model	16.49%	2.82%	0.85%	0.46%

Table 4.8 is organized to show the comparison of phantom models in rows and the threshold percentages in columns. The comparisons highlight the percent volume change in the electric field within each anthropomorphic head phantom model and the deviation of accuracy (or error) from segmented *in-vivo* human head model. The threshold percentages range from 25% to 100% in intervals of 25%. A threshold percentage indicates the volume of absolute electric field intensities in the model comparison that are above the threshold percentage. The calculations demonstrate that the anthropomorphic head phantom models generally predict the global absolute electric field well. The anthropomorphic head phantom models have a high absolute electric field in the SLA resin due to the conductivity being close to air. However, the anthropomorphic heterogeneous head phantom model provides a better maximum deviation in the accuracy of the absolute electric field from the baseline model and shows the least amount of volume change with a significant error, which is supported by demonstration where significant error is defined as beyond the 100% threshold and volume change.

4.3.3.2 Discussion

4.3.3.2.1 Numerical Scattering Parameters Measurements at 3T

While the following results could be coil (TEM resonator) or field strength (3T) specific, Figure 4.8 indicates that all phantom models (Figure 4.8.B-E) have similar loading effects to the segmented *in-vivo* human head model (Figure 4.8.A). The numerically calculated S-parameters shown in Figure 4.8 indicate that the coil load impedance and reflection coefficients are mostly comparable to the segmented *in-vivo* human head model with the anthropomorphic heterogeneous head phantom model (18.9% difference) than with the anthropomorphic homogeneous water-doped head phantom model (20.1% difference), the anthropomorphic homogeneous brain-doped

head phantom model (20.8% difference), and spherical water-doped phantom model (13.3% difference).

While the reflection coefficients are relatively comparable, the spherical water-doped phantom is most similar to the segmented *in-vivo* human head model but not by much of a difference is observed otherwise. Thus, it is most advantageous to assess the RF loading of the coil via S-matrix and frequency response using an anthropomorphic head phantom model filled with appropriate conductive media (homogeneous or heterogeneous) or the spherical water-doped phantom at 128.0 MHz.

4.3.3.2.2 Numerical B_1^+ Field Mapping Measurements at 3T

Figure 4.9 compares B_1^+ field distributions of the various phantoms to the segmented *in-vivo* human head model. Figure 4.9 demonstrates that the anthropomorphic head phantom models are better comparisons to the segmented *in-vivo* human head model than the spherical water-doped phantom model. Among the anthropomorphic head phantom models, the results of Figure 4.9, Figure 4.10, Table 4.6, and Table 4.7 indicate that any anthropomorphic head phantom model provides comparable magnetic field behavior to that associated with the segmented *in-vivo* human head model. This finding indicates that the B_1^+ field distribution is generally more sensitive to the load's geometry and physical dimensions than media at 3T.

Table 4.7 shows a robust comparison of the anthropomorphic head phantom models to the segmented *in-vivo* human head model numerically in select brain regions to assess B_1^+ homogeneity. Figure 4.9 visually demonstrates that there is not much difference in the B_1^+ distribution in the various loads. The quantitative B_1^+ field intensity values indicate that the Midbrain is the most homogeneous brain region within each head model.

In summary, the results show that an RF coil designer can use any phantom models for accurate magnetic field comparisons to that obtained in a segmented *in-vivo* human head model and likely *in-vivo*. If physiological region-specific head measurements are desired, the anthropomorphic (heterogeneous or homogeneous) head phantom models are most suitable.

4.3.3.2.3 *Numerical Electric Field Distribution and Intensity Analysis at 3T.*

Numerical modeling is the most utilized resource for predicting MR safety in a real MR environment, and EM numerical modeling is a resource to assess the MR safety of each phantom model in this study.

Part I-A states that SAR is directly proportional to the electric field squared; thus, an elevation in the electric field intensity can be harmful if temperature rise occurs and exceeds safety limits. Our study assesses the absolute electric field distribution in various loads, and Figure 4.11 and Figure 4.12 are an illustration of each absolute electric field distribution concerning the four phantom/head models.

The absolute electric field is highest in the periphery of the lower muscle region surrounding, the lower brain region within the anthropomorphic head phantoms at 3T. When considering all compartments in the phantom, all anthropomorphic head models have the highest absolute electric field distribution in the SLA resin material. As a result, the SLA resin material represents the electric field behavior of the fat and bone well. The fat and bone tissues are low conductive media, and the absolute electric field is much higher in these tissues in comparison to the skin. As mentioned in Subsection 4.2.3.2.3 in Part I-A, using a conductive resin that is representative of skin is ideal; however, the skin is too thin to accurately 3D print, and its relatively high conductivity is difficult to achieve in a resin material.

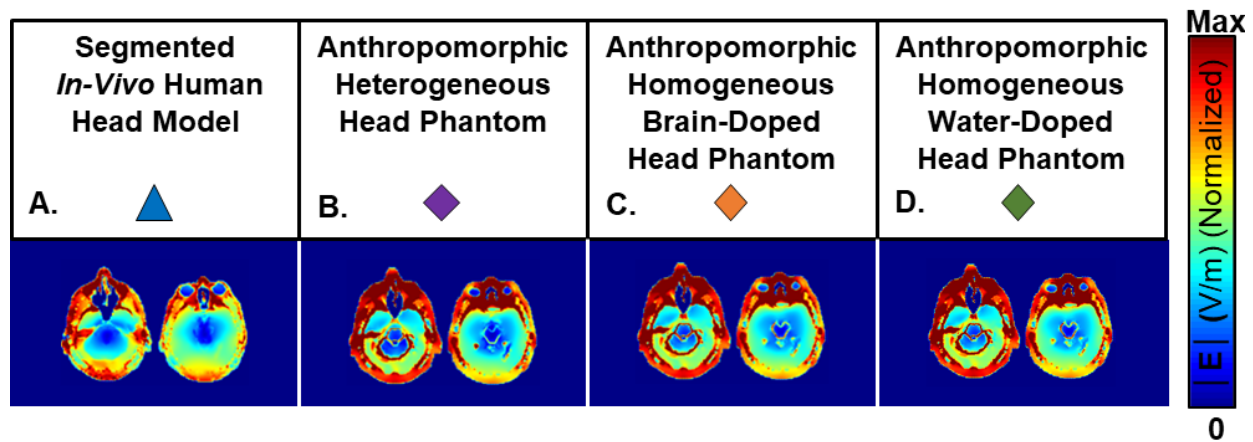


Figure 4.14. Absolute Electric Field in Four Phantom/ Head Models at 128.0 MHz. A comparison is shown between the absolute electric field distribution in the segmented *in-vivo* human head model (A) to the absolute electric field distribution in the SLA resin in the anthropomorphic head models (B-D).

The segmented *in-vivo* human head model (Figure 4.14.A) represents how the electric field is relatively low in the skin and increases in value as the EM wave propagates through the bone and fat. The designed anthropomorphic head phantom model utilizes a resin material with conductivity = 0.006 S/m, which is not as comparable to the averaged conductivity (0.18 S/m) of the fat, bone, and skin. Although the conductivity and permittivity of media in the anthropomorphic head phantom's fillable compartments are altered due the presence of the resin, this phantom offers similarities of what occurs at the boundaries of air cavities and physiological tissue in human anatomy. The designed anthropomorphic head phantom model (A) represents how the electric field is relatively low in the skin and increases in value as the EM wave propagates through the bone and fat. The designed anthropomorphic head phantom model utilizes a resin material with conductivity = 0.006 S/m, which is not comparable to the averaged conductivity (0.18 S/m) of the fat, bone, and skin. Although the conductivity and permittivity of media in the anthropomorphic head phantom's fillable compartments are altered due the presence of the resin, this phantom offers similarities of what occurs at the boundaries of air cavities and physiological

tissue in human anatomy. The designed anthropomorphic head phantom model (Figure 4.14.B-D) offers a realistic mimicry to the segmented *in-vivo* human head model specifically for the electric field interactions within the nasal cavities, ear canal, posterior mid-cerebellum, and eyes. The absolute electric field is highest in these areas because the permittivity value is relatively low. As a result, the comparison of Figure 4.11 and Figure 4.12 are most essential for MR safety applications.

Figure 4.12 shows that the absolute electric field distribution in the anthropomorphic head phantom models are most comparable to the segmented *in-vivo* human head model as opposed to the spherical water-doped phantom model. While the anthropomorphic head phantom models are most comparable to the segmented *in-vivo* human head model, Figure 4.11 and Figure 4.12 further highlights that there are subtle differences in the absolute electric field distributions and emphasizes that the anthropomorphic heterogeneous head phantom model offers a better indication in the accuracy of the peak absolute electric field intensities of the segmented *in-vivo* human head model .

While any featured phantom is sufficient to predict the B_1^+ field distribution and S-matrix to the segmented *in-vivo* human head model, more differences are noted in the absolute electric field distribution in the anthropomorphic head phantom models when compared to the anthropomorphic heterogeneous head phantom model. These differences are most apparent in the designed anthropomorphic head phantom's classified tissues being the cerebrospinal fluid, eyes, and the muscle. Of all head phantom models, the anthropomorphic homogeneous water-doped head phantom model offers the larger deviation in peak absolute electric field intensities from the segmented *in-vivo* human head model. Notice in Figure 4.11 and Figure 4.12, the absolute electric field in this phantom is the least high in the fillable regions.

An overestimation of the absolute electric field may lead to high SAR and increased temperature rise. Nevertheless, both anthropomorphic homogeneous head phantoms underestimate the absolute electric field of the segmented *in-vivo* human head model; however, brain-doped media would be a better choice over water-doped media because a lower dielectric constant offers a more comparable absolute electric field to *in-vivo*. Overall, the anthropomorphic heterogeneous head phantom overestimates/underestimates more accurately the absolute electric field of the segmented *in-vivo* human head model because it produces the least amount of volume change with a significant error from the absolute electric field intensity of the segmented *in-vivo* human head model.

4.3.4 Summary

Using parameters such as the B_1^+ and the absolute electric field distributions/intensities and S-parameters, a quantitative analysis was performed to compare the segmented *in-vivo* human head model to any phantom model with different various media contents in its compartments and geometry shapes at 3T. In summary, our findings indicate that based on the numerical results the designed anthropomorphic head phantom would be a highly useful tool for RF coil evaluation and testing at 3T. The S-parameters and B_1^+ field distributions/intensities are comparable to that associated with the segmented *in-vivo* human head model when using any anthropomorphic head phantom model or spherical water-doped phantom model. However, when comparing the absolute electric field distribution/intensity, the anthropomorphic heterogeneous head phantom is most comparable to the segmented *in-vivo* human head model by determining its accuracy absolute electric field intensities. The results also indicate that accurate numerical modeling is still an

effective and efficient predictive resource for an EM analysis. Future work will be explored to see if the study can be validated through experiments at 3T.

4.4 PART I-C: COMPARISON OF ELECTROMAGNETIC CHARACTERIZATION OF THE ANTHROPOMORPHIC HETEROGENEOUS HEAD PHANTOM USING A TEM RESONATOR AT 3T AND 7T

4.4.1 Introduction

This section compares the numerical electromagnetic characterization of the anthropomorphic head phantom models shown in Part I-A (Section 4.2) and Part I-B (Section 4.3). Part I-A and I-B revealed that the designed anthropomorphic head phantom is a highly useful tool for RF coil evaluation and testing at 3T and 7T. Part I-A showed that the anthropomorphic heterogeneous head phantom was the most comparable to the *in-vivo* volunteer when assessing the B_1^+ and electric field distributions/ intensities. Although the B_1^+ distribution is very homogeneous at 3T, the electric field distribution is not. The results of Part I-B indicate that the designed anthropomorphic head phantom model is most useful assessing the electric field at 3T. In order to adequately observe the differences and similarities of Part I-A and Part I-B, the electromagnetic characterization shown in this section considers the loss and uses 1-Watt of accepted power instead of 1-Watt of input power.

4.4.2 Materials and Methods

The methods are the same from Part I-A (4.2.2) and Part I-B (4.3.2).

4.4.3 Results

The results were presented in Part I-A (4.2.3.1) and Part I-B (4.3.3.1) of this chapter. For the comparison, the field distributions are shown in the discussion for 1-Watt of input power.

4.4.4 Discussion and Recommendations

4.4.4.1 Numerical Scattering Parameters Measurement Comparison at 3T and 7T.

Figure 4.15 highlights the loading effects in all models loaded within the 16-strut/4-port TEM resonator at both field strengths. As a demo, using the same single port (Port 1) on the 16-strut/4-port TEM resonator for both frequencies, each model's numerical S11 is assessed for the frequency response.

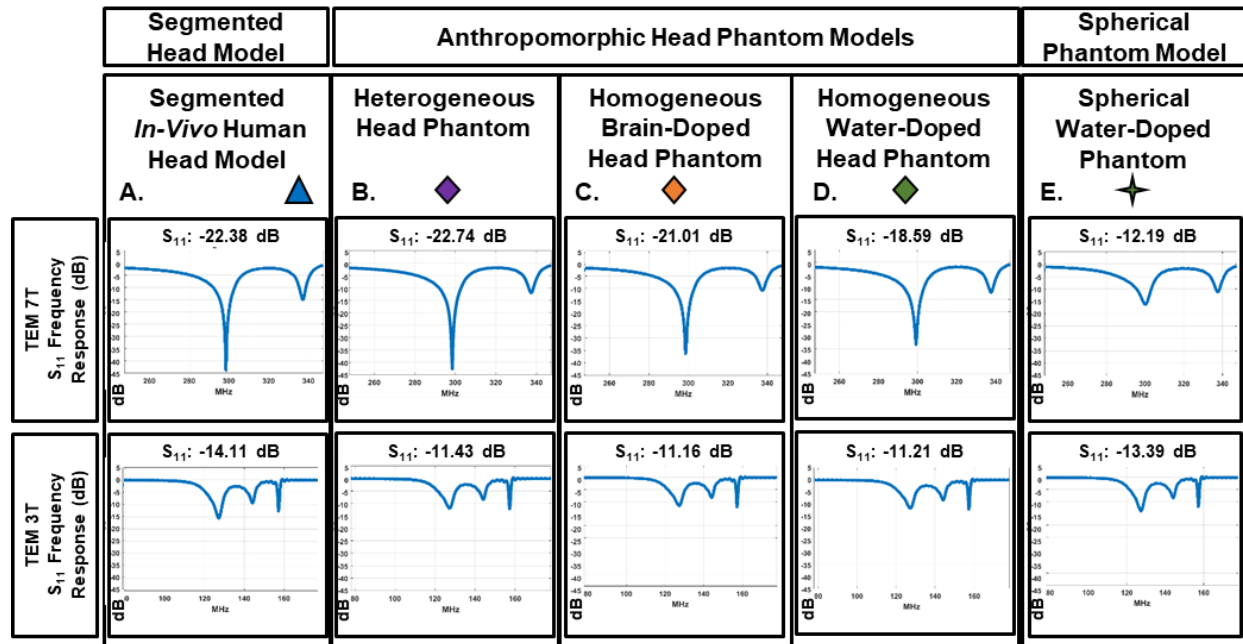


Figure 4.15. S-Parameters Measurements of Five Numerical Models Loaded in the 16-strut/4-port TEM Resonator at 3T and 7T. The frequency response is modeled for the segmented *in-vivo* human head model (A) and each phantom (B-E) model. A demo of the frequency response of one channel, S_{11} , is shown.

All models are appropriately tuned to the respective field strength. The TEM resonator at 3T is appropriately tuned but not matched as well as 7T. The difference in matching is shown visually in Figure 4.15. The impedance values are not entirely matched to 50Ω for each load within the TEM resonator at both field strengths. At 7T, the models were matched better because an experimental validation was conducted with the actual TEM resonator at 7T. In addition, the differences in matching at 7T are also due to the model being matched to the Virtual Family v1.0 Duke model and not being retuned or matched for the five numerical models. At 3T, the matching is not nearly as close to 50Ω because the loading at 3T was only for illustration and comparison to 7T, not an experimental validation.

Figure 4.15 indicates the RF loading of the coil and the phantom preference at 3T and 7T. At 3T, any phantom media and geometry is a useful comparison to the RF loading in a human head. In contrast, realistic human RF loading cannot be achieved using a spherical water-doped phantom at 7T. It is most advantageous to use an anthropomorphic head phantom (heterogeneous or homogeneous) to offer comparable RF loading to a human head at 7T and to use any phantom media and geometry at 3T.

At 3T, any phantom media and geometry is a useful comparison to the RF loading in a human head. In contrast, realistic human RF loading cannot be achieved using a spherical water-doped phantom at 7T. It is most advantageous to use an anthropomorphic head phantom (heterogeneous or homogeneous) to offer comparable RF loading to a human head at 7T and to use any phantom media and geometry at 3T.

4.4.4.2 Numerical Analysis Comparison of B_1^+ Field Mapping at 3T and 7T.

Since the RF wavelength decreases as the operational frequency increases, the B_1^+ field maps are more homogeneous at 3T than 7T as shown in Figure 4.16. Table 4.1 and Table 4.5 supports this observation by comparing the wavelengths of the tissues. In Figure 4.16, the matching losses per load were accounted for in the comparison of the numerical B_1^+ field maps using the TEM resonator at both frequencies. All numerical B_1^+ field maps are scaled to the same magnitude scale (0 to $1.90 \mu\text{T}/\sqrt{W}$) and are scaled to the maximum B_1^+ for 1 Watt of transmitted power in all models. At 3T, there does not appear to be considerable quantitative difference in the B_1^+ homogeneity of the anthropomorphic models. By accounting for the losses and using the transmitted power, a better qualitative comparison of the B_1^+ field distribution is observed. This observation indicates that changes in B_1^+ field distribution at 3T are subtle, but are more sensitive to the load's geometry and media at 7T.

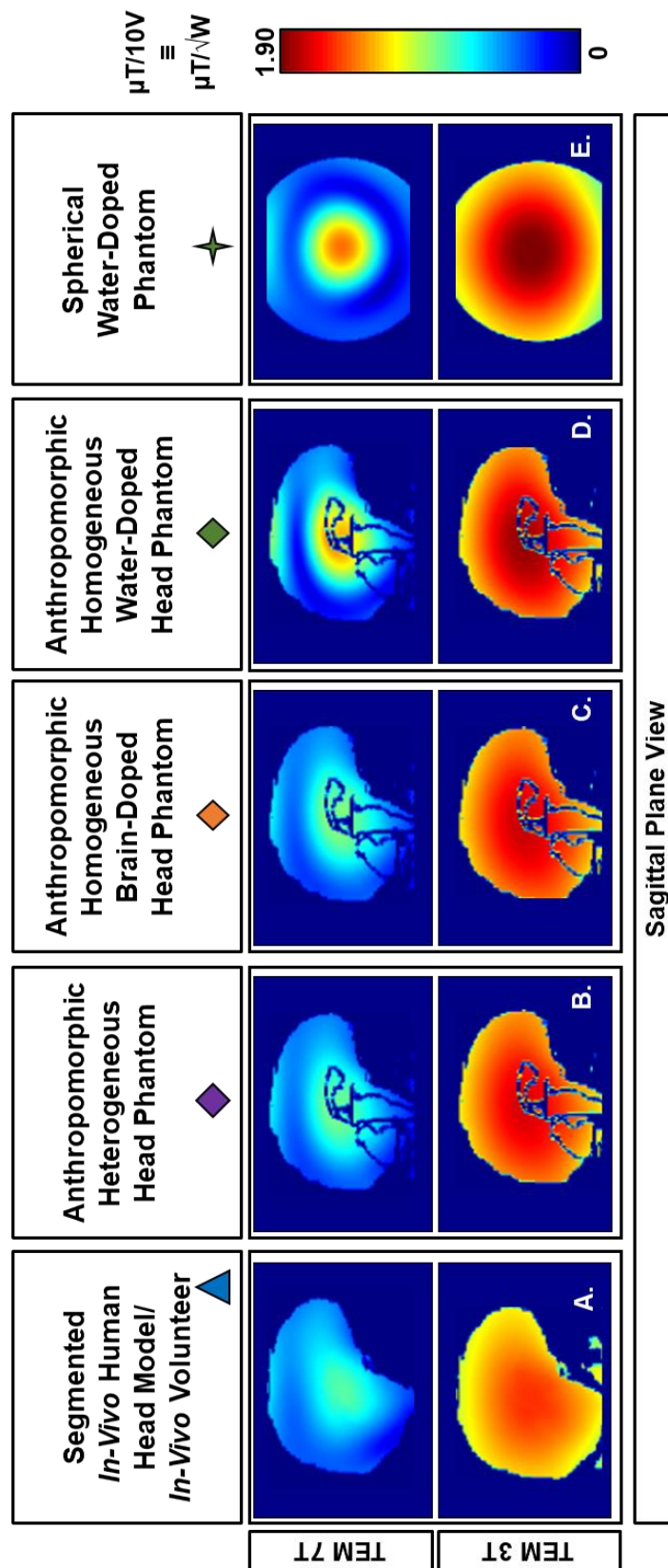


Figure 4.16. B_1^+ field Distributions within the 16-strut/4-port TEM Resonator at 3T and 7T. The B_1^+ field distribution for each numerical model is shown and compared to the model's numerical B_1^+ mapping measurements at 7T in the sagittal, axial, and coronal views (A-O). The numerical models are scaled to 1W accepted power supplied by the RF system. The color bar is scaled from 0 to the maximum numerical B_1^+ values.

Figure 4.16 (Continued)

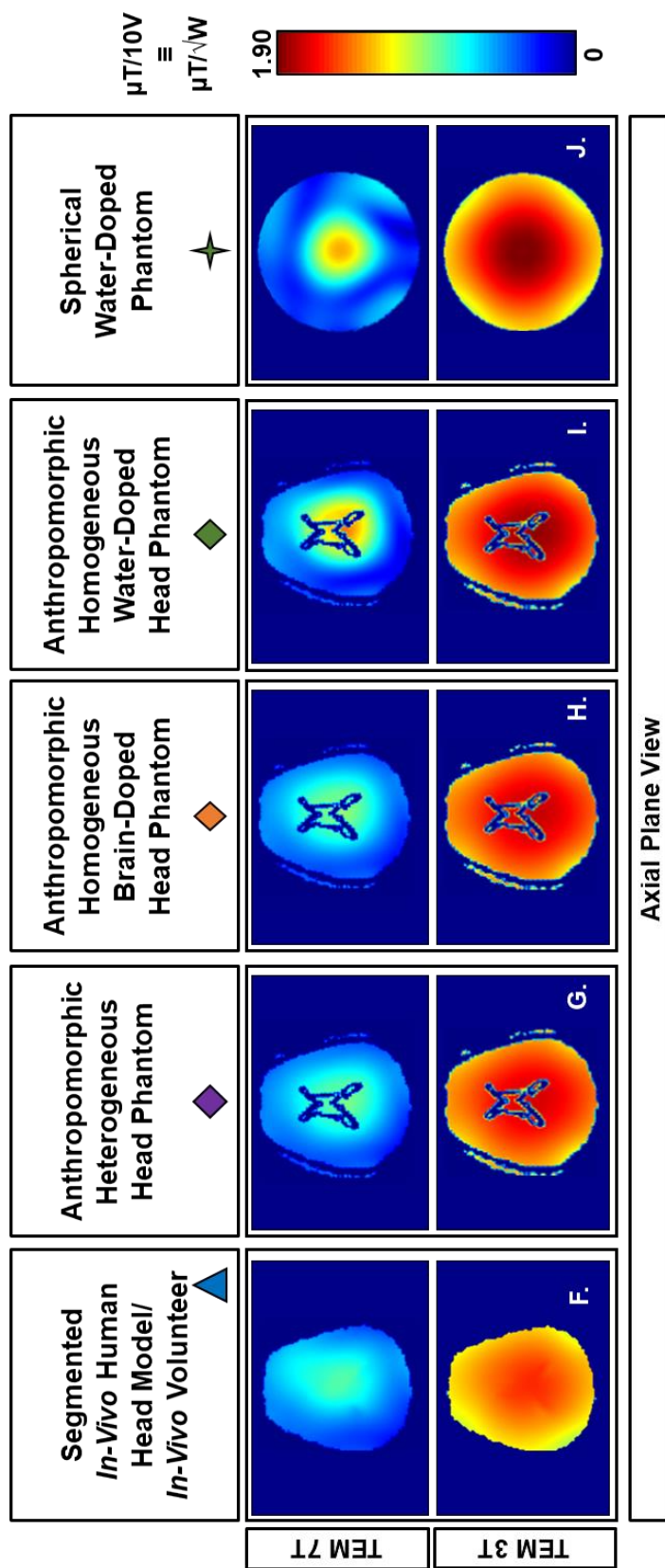


Figure 4.16 (Continued)

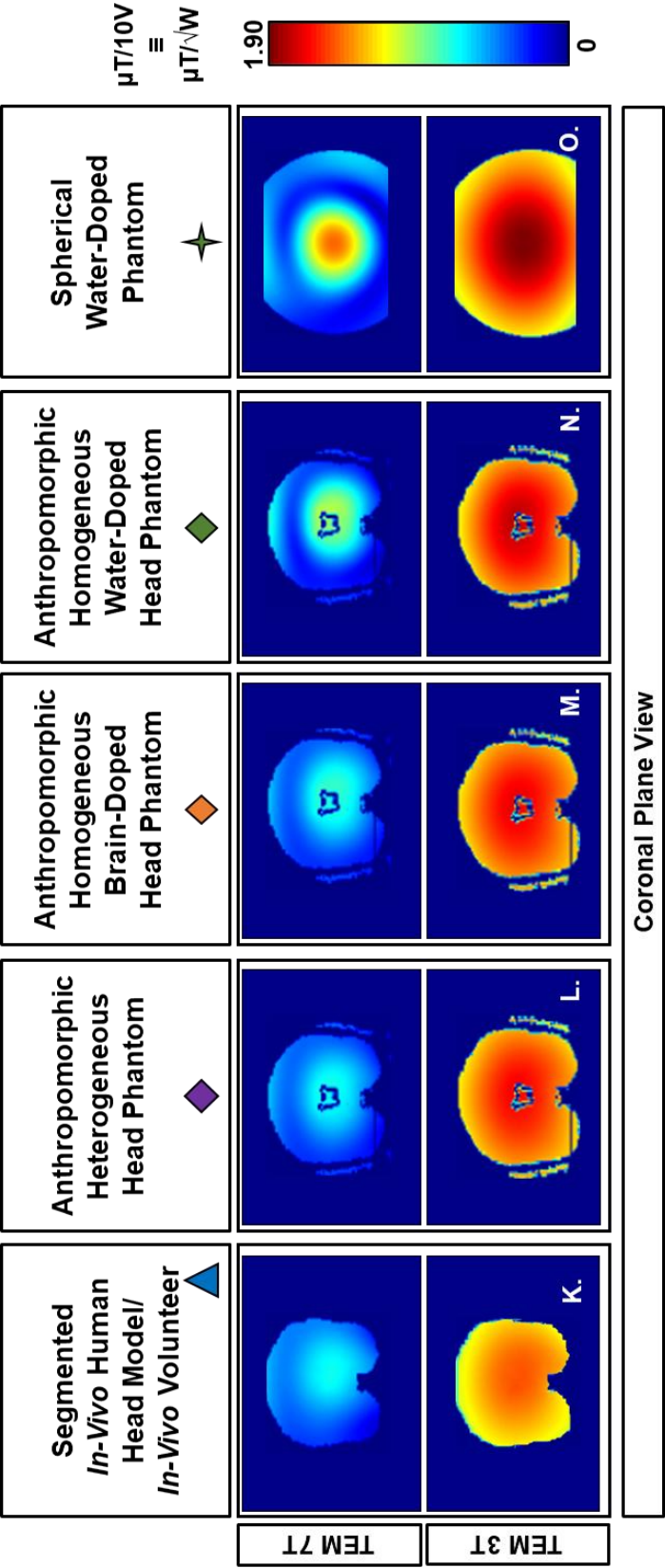


Table 4.9. Detailed Comparison of Mean B_1^+ Field Intensity Characteristics of Five Models through Numerical Studies at 3T and 7T. A comparison of numerical B_1^+ characteristics highlighting the mean B_1^+ field intensity for 1W of accepted power ($\mu T/\sqrt{W}$) in three brain regions on interest (all fillable compartments in the head phantom above and including the cerebellum), brain (excluding the Midbrain), and Midbrain).

Selected Regions of Interest in All Models	Head Models								Basic Phantom Model	
	Segmented <i>In-Vivo</i> Head Model/ In-Vivo Volunteer	Anthropomorphic Heterogeneous Phantom Model	Anthropomorphic Homogeneous (Brain-Doped) Phantom Model	Anthropomorphic Homogeneous (Water-Doped) Phantom Model					7T	3T
	7T	3T	7T	3T	7T	3T	7T	3T		
All Fillable Compartments in Head Phantom Above & Including the Cerebellum	0.501	1.304	0.511	1.452	0.517	1.475	0.523	1.502	0.695	1.328
Brain (excluding the Midbrain)	0.503	1.313	0.514	1.460	0.518	1.483	0.521	1.511	--	--
Midbrain	0.730	1.475	0.703	1.549	0.766	1.564	0.950	1.620	--	--

Table 4.9 highlights the numerical B_1^+ field statistics for each phantom in three different brain regions for each head phantom. The mean B_1^+ field intensity is highest in the Midbrain region given that the TEM resonator is driven in quadrature for all five models at both field strengths. Figure 4.16 and Table 4.9 highlights the mean B_1^+ field intensity is higher at 3T than 7T. A general observation for this specific coil on all the different loads, the quadrature excitation produces the highest B_1^+ field intensity in the middle region of the phantoms/models, but the B_1^+ field intensity considerably drops in the periphery in a semi-radial pattern away from the load's center at 7T. At 3T, a similar center-brightness is observed in the middle region, and the B_1^+ field intensity considerably drops at a slower rate in the periphery. Upon excluding the Midbrain region for the anthropomorphic homogeneous water-doped head phantom model and the full spherical water-doped phantom, Table 4.9 illustrates that the quantitative average B_1^+ field intensity values of various anthropomorphic head phantom models are comparable to that of the segmented *in-vivo* human head model at both field strengths.

Table 4.10. Detailed CV B_1^+ Characteristics of Five Models through Numerical Studies at 3T and 7T. A comparison of numerical B_1^+ characteristics highlighting the coefficient of variation (std/ mean) in three brain regions (all fillable compartments in the head phantom above and including the cerebellum), brain (excluding the Midbrain), and Midbrain).

Selected Regions of Interest in All Models	Head Models								Basic Phantom Model	
	Segmented <i>In-Vivo</i> Head Model/ <i>In-Vivo</i> Volunteer		Anthropomorphic Heterogeneous Phantom Model		Anthropomorphic Homogeneous (Brain-Doped) Phantom Model		Anthropomorphic Homogeneous (Water-Doped) Phantom Model		Spherical (Water-Doped) Phantom Model	
	7T	3T	7T	3T	7T	3T	7T	3T	7T	3T
All Fillable Compartments in Head Phantom Above & Including the Cerebellum	0.287	0.101	0.276	0.087	0.303	0.087	0.501	0.104	0.474	0.189
	0.268	0.090	0.267	0.083	0.296	0.083	0.494	0.100	--	--
Brain (excluding the Midbrain)	0.156	0.041	0.181	0.047	0.131	0.049	0.193	0.055	--	--

Table 4.10 tabulates a comparison of the numerical CV of the B_1^+ field distributions of three brain regions for each head phantom. In all models, the B_1^+ field map is most uniform at each frequency in the Midbrain region (smaller in volume). Figure 4.16 qualitatively demonstrates that the anthropomorphic heterogeneous phantom model's B_1^+ distribution is most comparable to the segmented *in-vivo* human head model at both field strengths. Table 4.10, however, illustrates that the quantitative CV values of the B_1^+ field distribution of the anthropomorphic heterogeneous phantom model and the anthropomorphic homogeneous brain-doped head phantom model are comparable to that of the segmented *in-vivo* human head model. A significant divergence in CV values is observed for the anthropomorphic homogeneous water-doped head phantom model and the spherical water-doped phantom model at 7T. There is not much of a significant difference in CV values from the segmented *in-vivo* human head model at 3T; however, the anthropomorphic heterogeneous phantom model and the anthropomorphic homogeneous brain-doped head phantom model are most comparable in CV value within all brain regions.

In summary, the results indicate that an anthropomorphic (heterogeneous or homogeneous) head phantom models are useful for accurate magnetic field comparisons to that of the segmented *in-vivo* human head model at both field strengths. Although the various models have similar CV values at 3T, the mean B_1^+ field intensity of the anthropomorphic (heterogeneous or homogeneous) head phantom models and spherical water-doped phantom are most accurate to that of the segmented *in-vivo* human head model.

4.4.4.3 Numerical Absolute Electric Field Analysis and Comparison at 3T and 7T.

As mentioned, EM numerical modeling is a resource to assess the MR safety of each phantom model in this study. Part I-B determined that assessing MR safety was the greatest advantage of using an anthropomorphic head phantom model at 3T. The coil's losses in each load were

accounted for to make an adequate comparison of the absolute electric field. Figure 4.17 and Figure 4.18 shows the absolute electric field in all phantom models and segmented *in-vivo* human head model are scaled from a minimum of 0 V/m to the maximum absolute electric field among all models being the anthropomorphic water-doped head. Figure 4.17 and Figure 4.18 demonstrates that the behavior of the absolute electric field is not uniform at different field strengths. The summation of the absolute electric field per model is unique to the coil and field strength.

As observed in Part I-A and Part I-B, the resin material within each anthropomorphic head phantom model has the highest absolute electric field, much higher than the segmented *in-vivo* human head model (baseline). Thus, when determining the absolute electric field range, the SLA resin regions (fat/bone/skin) is excluded and the peak absolute electric field value is positioned 3.00 cm above the ventricles in the anthropomorphic homogeneous water-doped head model at 7T. At 3T, the absolute electric field is highest in the middle of the head (periphery of the brain and middle muscle). The absolute electric field is highest in the anthropomorphic homogeneous water-doped head phantom model at both field strengths in what appears to be inverse peak regions.

When assessing the baseline absolute electric field distribution, the absolute electric field is greater in the segmented *in-vivo* human head model at 7T than at 3T. The absolute electric field has high peaks in the right shoulder at 7T; yet, the high absolute electric field peaks are not observed in the shoulders of the segmented *in-vivo* human head model at 3T. This observation is similar and seen in all anthropomorphic head models (Figure 4.17.B-D). At 3T, the absolute electric field is far greater around the nasal cavities and ear canal than its respective absolute electric field at 7T.

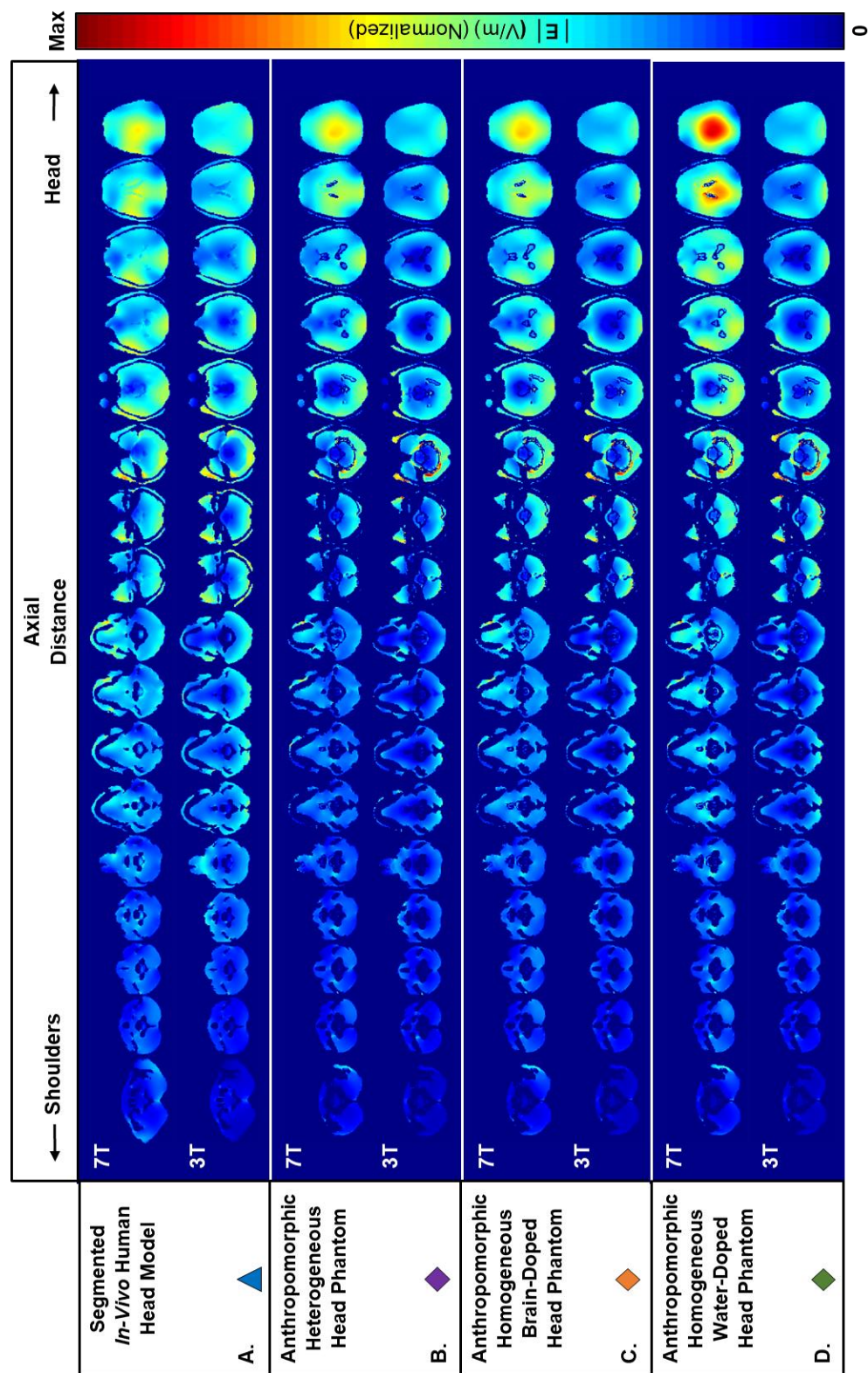


Figure 4.17. Comparison of the Absolute Electric Field in Four Models for 1-Watt of Accepted Power at 7T and 3T. The numerical absolute electric field is shown for each model in the head to upper shoulders to the 16-strut/4-port TEM resonator based on a scale to the highest peak in the midbrain region of the anthropomorphic homogeneous water-doped head phantom model at 7T

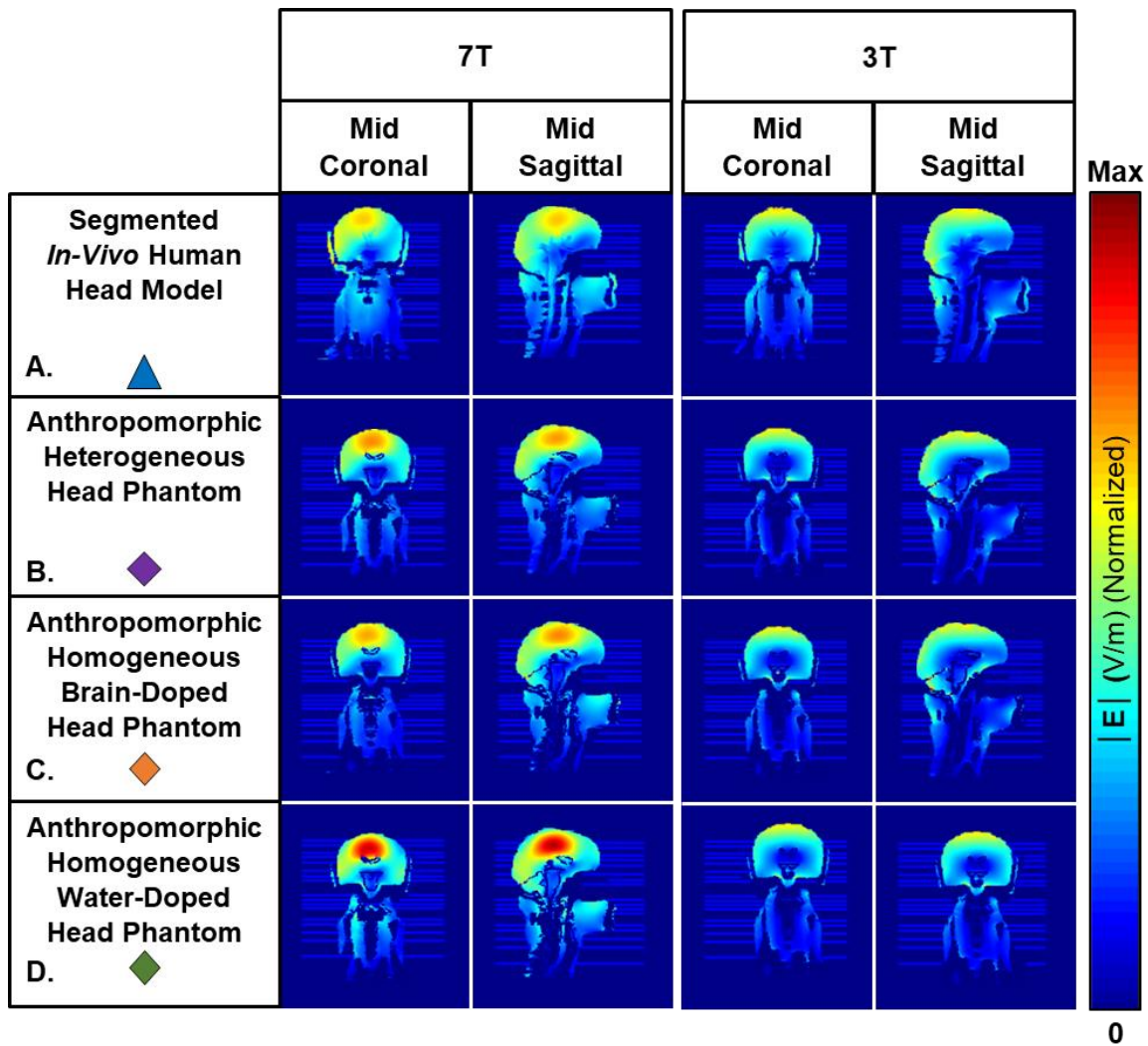


Figure 4.18. Comparison of Absolute Electric Field in Four Models in the Coronal and Sagittal Views for 1-Watt of Accepted Power at 7T and 3T. The numerical absolute electric field is shown for each model in the head and upper shoulders to the 16-strut/4-port TEM resonator based on a scale to the highest peak in the midbrain region of the anthropomorphic homogeneous water-doped head phantom model at 7T.

Figure 4.19 indicates the percent volume change in each phantom model's absolute electric field distribution/intensity in comparison to that of the segmented *in-vivo* human head model and indicates it is the more preferable model to predict *in-vivo* absolute electric field behavior. The overestimation and underestimation of the absolute electric field are shown to visualize

physiological regions where the absolute electric field is most or least overestimation or underestimated. The anthropomorphic head phantom model appears useful for analyzing unknown deviations in absolute electric field regions at 3T. When this coil is driven in quadrature, the peak absolute electric field is in a deep location of the Midbrain region and mouth at 3T.

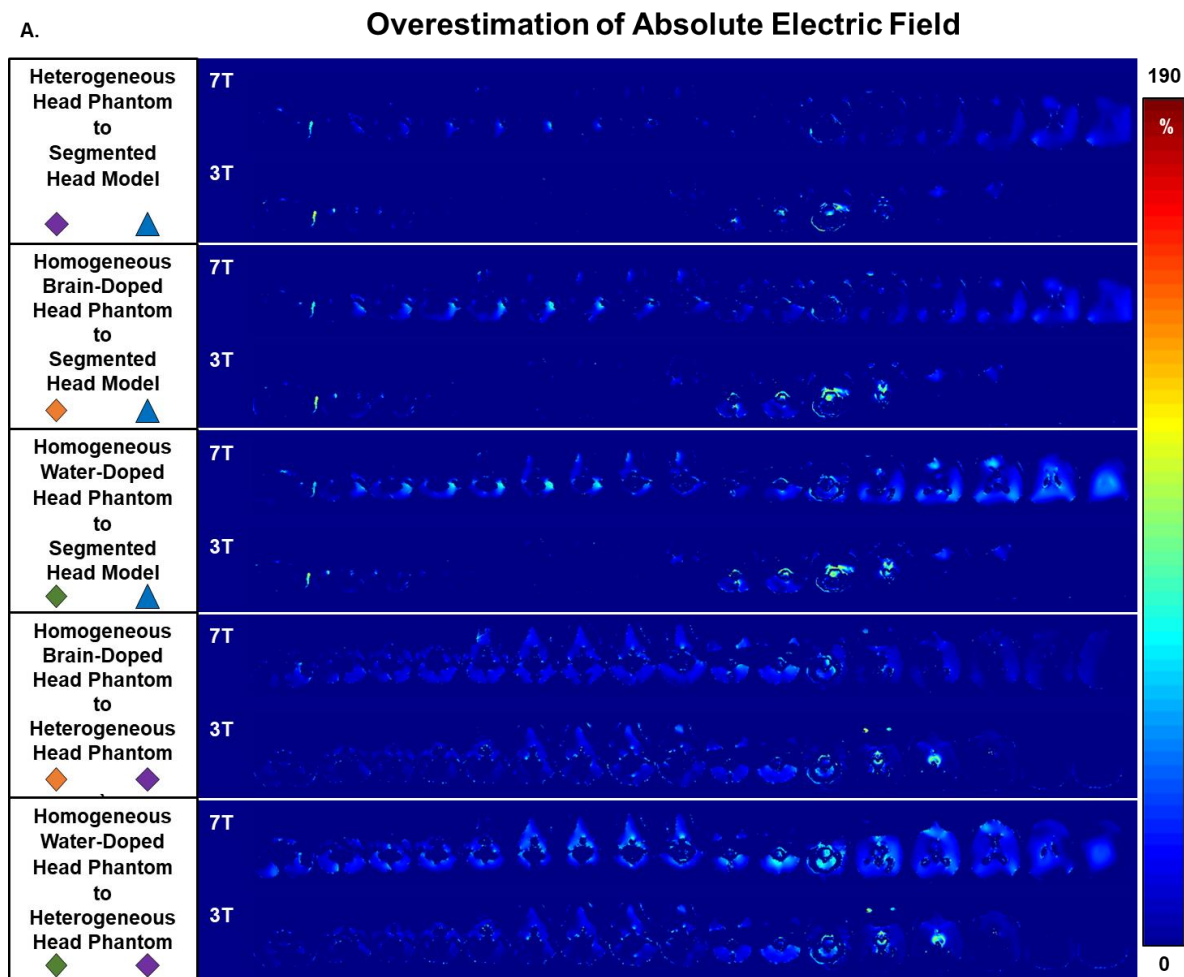
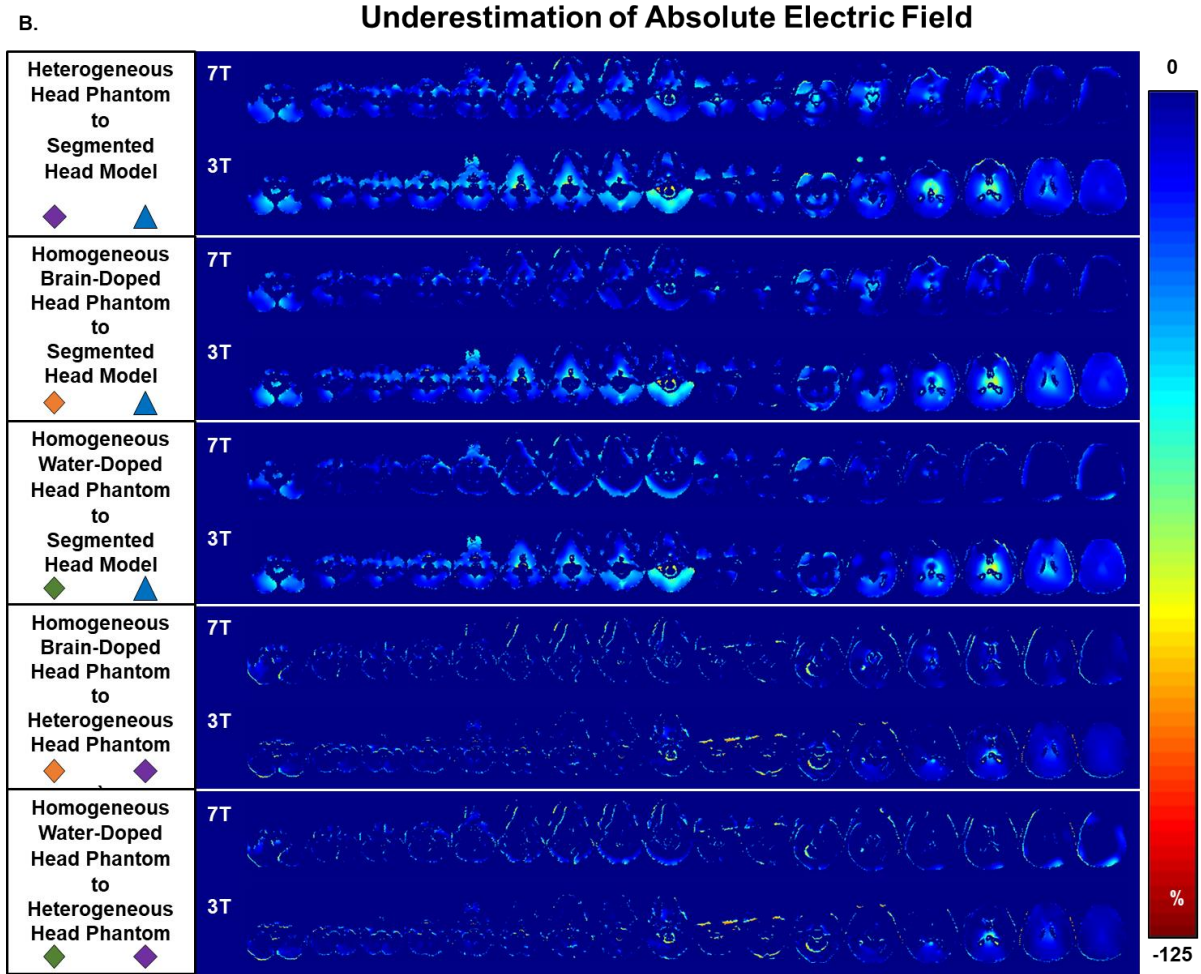


Figure 4.19. Percent Change Comparison of Absolute Electric Fields in Four Models for 1-Watt of Accepted Power at 7T and 3T. The percent change of each phantom model in Figure 4.17.B-D and Figure 4.18.B-D is compared to the segmented *in-vivo* human head model in Figure 4.17.A and Figure 4.18.A. The images are scaled to a maximum of 190% based on the anthropomorphic water-doped head phantom model. The SLA resin material is removed to focus on the absolute electric field distribution in the fillable compartments. The overestimation of the absolute electric field distribution based on each phantom is shown in (A). The underestimation of the absolute electric field distribution based on each phantom is shown in (B).

Figure 4.19 (Continued)



In contrast, the greatest errors in the absolute electric field changes at 7T appears to cover more physiological brain regions, neck, and shoulder in the head. Table 4.11 shows the corresponding calculations to Figure 4.19 for specified threshold percentages. Table 4.11 is organized to show the comparison of phantom models in rows and the threshold percentages in columns. The threshold percentages range from 25% to 100% in intervals of 25% and the threshold percentages represents the percentage of absolute electric field intensities within the model comparison that are above the threshold percentage. The threshold percentage correspond to the values 0 to $\pm 100\%$ along the colorbar in Figure 4.19. Table 4.11 shows the percentage volume change per model at

3T and 7T for each corresponding threshold percentage and accuracy deviation from the baseline model.

Table 4.11. Percent Volume Change in the Absolute Electric Field Models Beyond the Percent Threshold at 7T and 3T. Calculations compare the percent volume change of each phantom model in Figure 4.17.B-D and Figure 4.18.B-D to the segmented *in-vivo* human head model in Figure 4.17.A and Figure 4.18.A. The percentage volume change represents the deviation in accuracy from the segmented *in-vivo* human head model.







	Threshold							
	25		50		75		100	
Head/ Phantom Model	7T	3T	7T	3T	7T	3T	7T	3T
Heterogeneous Head Phantom  to  Segmented Head Model	9.66%	19.31%	0.88%	2.78%	0.07%	0.49%	0.00%	0.15%
Homogeneous Brain-Doped Head Phantom  to  Segmented Head Model	7.37%	16.89%	1.04%	2.54%	0.21%	0.74%	0.04%	0.36%
Homogeneous Water-Doped Head Phantom  to  Segmented Head Model	19.80%	16.49%	2.17%	2.82%	0.41%	0.85%	0.09%	0.46%

Figure 4.19.B demonstrates that the anthropomorphic head model is still an estimation of the segmented *in-vivo* human head model, even though, the anthropomorphic heterogeneous or homogeneous brain-doped head phantom model are more desirable than other models. Table 4.11 supports this finding at both frequencies, yet the table provides a clear indication of how great

these differences quantitatively are per model comparison based on the field strength and percent volume change above the threshold percentage. For instance, the first row in Table 4.11 shows the percentage volume change in the absolute electric field between the anthropomorphic heterogeneous head phantom model and the segmented *in-vivo* human head model at 3T and 7T with corresponding thresholds. The comparison volume is beyond the 25% threshold by 19.31% and 9.66% at 3T and 7T, respectively. This comparison indicates that the percent volume change is greater at 3T as oppose to 7T. While exploring the table, the values indicate that 99.12%, at 7T, and 97.22%, at 3T, of the volume change in the absolute electric field intensities, are less than a 50% error of the baseline absolute electric field intensity. The anthropomorphic heterogeneous head phantom model has the least amount of volume change with a significant error in the absolute electric field intensities in the segmented *in-vivo* human head model at both frequencies. A significant error is defined as 100% of the baseline model or less. The anthropomorphic homogeneous brain-doped head phantom model offers a lesser percent volume change in absolute electric field intensities of 50% or less than the anthropomorphic homogeneous water-doped head phantom model. In an assessment of the anthropomorphic homogeneous brain-doped head phantom model, 16.89%, at 3T, and 7.37%, at 7T, of the total volume change has an error of 25% or less and this comparison is lower than the anthropomorphic heterogeneous head phantom model at both field strengths. However, the anthropomorphic heterogeneous head phantom model has a better indication beyond 75%, which indicates the error in accuracy. The anthropomorphic homogeneous brain-doped head phantom model can be chosen if a lack of resources are available and a desire to reduce the complexity of the phantom's fabrication. However, the absolute electric field can result in peak SAR or peak temperature rise in these regions.

In summary, the anthropomorphic heterogeneous head phantom model is most useful to conduct MR safety analysis and produces the least amount of percent volume change with a significant error from the baseline model's absolute electric field intensities at 3T and 7T.

4.5 PART II: THERMAL AND SAR CHARACTERIZATION OF THE ANTHROPOMORPHIC HETEROGENEOUS HEAD PHANTOM USING A TEM RESONATOR AT 3T AND 7T

4.5.1 Introduction

Radiofrequency (RF) exposure and RF heating are a challenge for ultrahigh field (UHF) imaging applications (140-142) in humans and has become a widely researched topic in MR safety at UHF fields (68). RF power deposition is quantified by the specific absorption rate (SAR) and is used as one method to quantify MR safety. In MR safety, RF heating becomes an issue at 3T and the issue is enhanced at field strengths of 7T and higher. This observation is supported by the results of Part I-C (4.4) where the electric fields are heterogeneous at 3T and 7T despite the phantom's geometry and media. At higher field strengths, the tissues' dielectric properties increase at higher frequencies (98), and tissues with high conductivity may yield higher quantified SAR.

In MR experiments, RF exposure is monitored by government regulated SAR limits (64, 65) and temperature rise in specified human body regions through MR scanners. SAR limits are regulated through the Food and Drug Administration (FDA) and IEC. The FDA recommends that any averaged SAR within the head ≥ 3.2 W/kg per any gram is considered a significant risk when quantified beyond 10 minutes at any static magnetic field strength (65). The IEC limits local SAR

≤ 10 W/kg over any 10g within the human head. The IEC limits local temperature rise to $\leq 1^\circ\text{C}$. The scanner computes these values as a function of the scanner's power hardware, the RF coil, and subject-specific information. However, scanners are not currently equipped to have subject-specific physiological information or fast solvers to compute subject-specific SAR (68). As a result, patient-specific SAR is model-based and computed offline. The current methods to predict and monitor SAR are through the MR scanner and are based on the power transmitted into the body.

Thermal simulations are resourceful in monitoring subject-specific RF exposure through various bioheat equations and have been widely used at 3T and higher fields strengths to assess and model RF heating. RF heating is measured numerically and simulated through various bioheat equation methods, i.e., Penne's bioheat transfer equation (BHTE) (74). Penne's bioheat equation correlates temperature rise based on the power deposited into the human body and the physiological parameters (i.e., specific heat, thermal conductivity, basal metabolic rate, density, perfusion, etc.) of the human body. While works (44, 143-148) have proven that bioheat models are resourceful, thermal simulations are too time-consuming to conduct during experimental MR scans and the results are rarely compared in real-time to *in-vivo* studies.

Various studies have offered varying techniques to monitor RF safety during human scans by using animal models (143, 149, 150), phantoms (14), and thermal simulations. Limited studies compare the phantom temperature rise at UHF MR safety applications. While Graedel *et al.* (14) attempted to monitor experimental RF safety through a realistic head phantom, the realistic head phantom offered limited compartments and did not offer comparable thermal simulations to their designed head phantom. Since the field of MRI is moving further towards making 7T clinical, there is a stronger need to evolve technical resources that determine safe and predictable RF safety

and temperature rise in human tissue. Our studies (18, 151, 152) and Part I of this chapter have shown our designed experimental anthropomorphic heterogeneous head phantom to be a useful tool for UHF MR applications, and there is a need to explore its thermal characteristics through MR safety assessments further by expanding on Part I.

The purpose of Part II is to make a realistic numerical RF safety assessment of the numerical perfusionless anthropomorphic heterogeneous head phantom model and compare its results to a numerical perfused segmented *in-vivo* human head model. Two numerical thermal models are developed and compared using only numerical thermal simulations to offer a thermal characterization of the numerical anthropomorphic heterogeneous head phantom model at 7T MRI. Since the experimental anthropomorphic heterogeneous head phantom does not have perfusion, the numerical anthropomorphic heterogeneous head phantom (153) does not have perfusion in its model. However, the numerical segmented *in-vivo* human head model (from Part I) has perfusion because the human body has perfusion. The numerical thermal heating within both models is compared to assess the impact of the performance of the phantom at both field strengths, 3T and 7T. The numerical perfused segmented *in-vivo* human head model determines how similar or different the thermal heating of the experimental anthropomorphic head phantom might be to an actual human subject.

4.5.2 Materials and Methods

4.5.2.1 Numerical Studies

4.5.2.1.1 *Constitutive and Thermal Properties of Phantom Models at 3T and 7T*

Two numerical thermal models were developed for the numerical temperature calculations: 1) a perfused segmented *in-vivo* head model (baseline) and 2) a perfusionless anthropomorphic heterogeneous head phantom model. The perfused segmented *in-vivo* head model is the thermal model of the segmented *in-vivo* head model in Part I of this chapter. This model offers 10 different tissue types. The perfusionless anthropomorphic heterogeneous head phantom model is the thermal model of the numerical anthropomorphic heterogeneous head phantom model in Part I of this chapter. This model has six fillable tissues, air, and SLA resin, which represents the combination of fat, bone, and skin. Both models have an isotropic spatial resolution of $\sim 1.59 \text{ mm}^3$ as mentioned in subsection 4.2.2.1.1 of Chapter 4.0. Wolf *et al.* (154) and other works (155-158) indicated that modeling the head only developed unreal SAR elevations localized in the neck region. It was determined that modeling the head to shoulders was enough; thus, our perfused segmented *in-vivo* human head model and head phantom model include the head to shoulders and exclude the remainder of the body as shown in Figure 4.20 to Figure 4.22. The thermal properties of the models were based on thermal and constitutive properties provided in works ((31, 98, 153, 159-164) including the Virtual Family v1.0 Duke (31, 165)) and are reflected in Table 4.12 and Table 4.13 for 3T and 7T.

Table 4.12. Segmented *In-Vivo* Human Head Model and Anthropomorphic Heterogeneous Head Phantom Model's Constitutive Properties (Permittivity, Conductivity) and Thermal Properties (Basal Metabolic Rate, Specific Heat, Blood Perfusion Coefficient, Thermal Conductivity) at 297.2MHz. Derived from the Cited Literature (31, 98, 159-164).

Phantom Tissue Classification/Models	General Biological Tissue Classification	Basal Metabolic Rate A_0	Specific Heat C	Blood Perfusion Coefficient B	Thermal Conductivity K	Conductivity		Relative Permittivity ϵ	Density ρ
						σ	(S/m)		
Air ▲ ◆	Sinuses, Esophagus	0.0000	1003.6700	0.0000	0.0274	0.0000	0.0000	1.0000	1.2500
		7100.0000	3643.4718	30645.3022	0.5164	0.5500	0.5500	51.9800	1040.0000
Brain (WM/GM) ▲ ◆	White Matter, Gray Matter, External CSF, Dura	0.0000	4200.0000	0.0000	0.49800	0.4200	0.4200	36.9700	1039.0000
		7100.0000	3630.0000	33674.6498	0.5133	0.5060	0.5060	59.8600	1040.0000
Brainstem ▲ ◆	Midbrain, Pons, Medulla Oblongata, Spinal Cord	0.0000	4200.0000	0.0000	0.49800	0.9700	0.9700	72.8000	1007.0000
		7100.0000	3653.0000	46418.1667	0.5733	2.2200	2.2200	72.8000	1007.0000
Cerebellum ▲ ◆	Cerebellum	0.0000	4095.5000	0.0000	0.49800	0.9700	0.9700	59.8600	1040.0000
		7100.0000	3653.0000	46418.1667	0.5060	0.5060	0.5060	59.8600	1040.0000
Cerebrospinal Fluid (CSF) ▲ ◆	Internal CSF near lateral horns and around spinal cord	0.0000	4095.5000	0.0000	0.5733	2.2200	2.2200	72.8000	1007.0000
		0.0000	4200.0000	0.0000	0.49800	0.9700	0.9700	59.8600	1040.0000

Table 4.12 (Continued)

Eyes	▲	Cornea, Vitreous	0.0000	4052.6400	6439.8752	0.5848	0.9200	56.4600	1020.0700
	◆	Humor, Eyes Sclera	0.0000	4200.0000	0.0000	0.49800			
Muscle	▲	Tendons, Tongue, Muscle	116.9574	3422.5740	4385.6381	0.4917	0.7700	58.2400	1049.7800
	◆		0.0000	4200.0000	0.0000	0.49800			
Fat/ Bone/ Skin (3D SLA Material)	◆	Fat, Bone, Cartilage, Skin Dry	0.0000	1050.0000	0.0000	0.1700	0.1080	2.7900	1120.0000
Fat	▲	Fat	300.0000	2348.3300	1971.8274	0.2115	0.0395	5.6360	916.0000
Bone	▲	Cortical Bone/ Skull Cortical	610.0000	1312.8300	602.8333	0.3200	0.0824	13.4490	1990.0000
Skin	▲	Skin Dry	1620.0000	3390.5000	6413.0194	0.3722	0.6400	49.9340	1100.0000

Legend: ▲ Perfused Segmented *In-Vivo* Human Head Model ◆ Perfusionless Anthropomorphic Heterogeneous Head Model

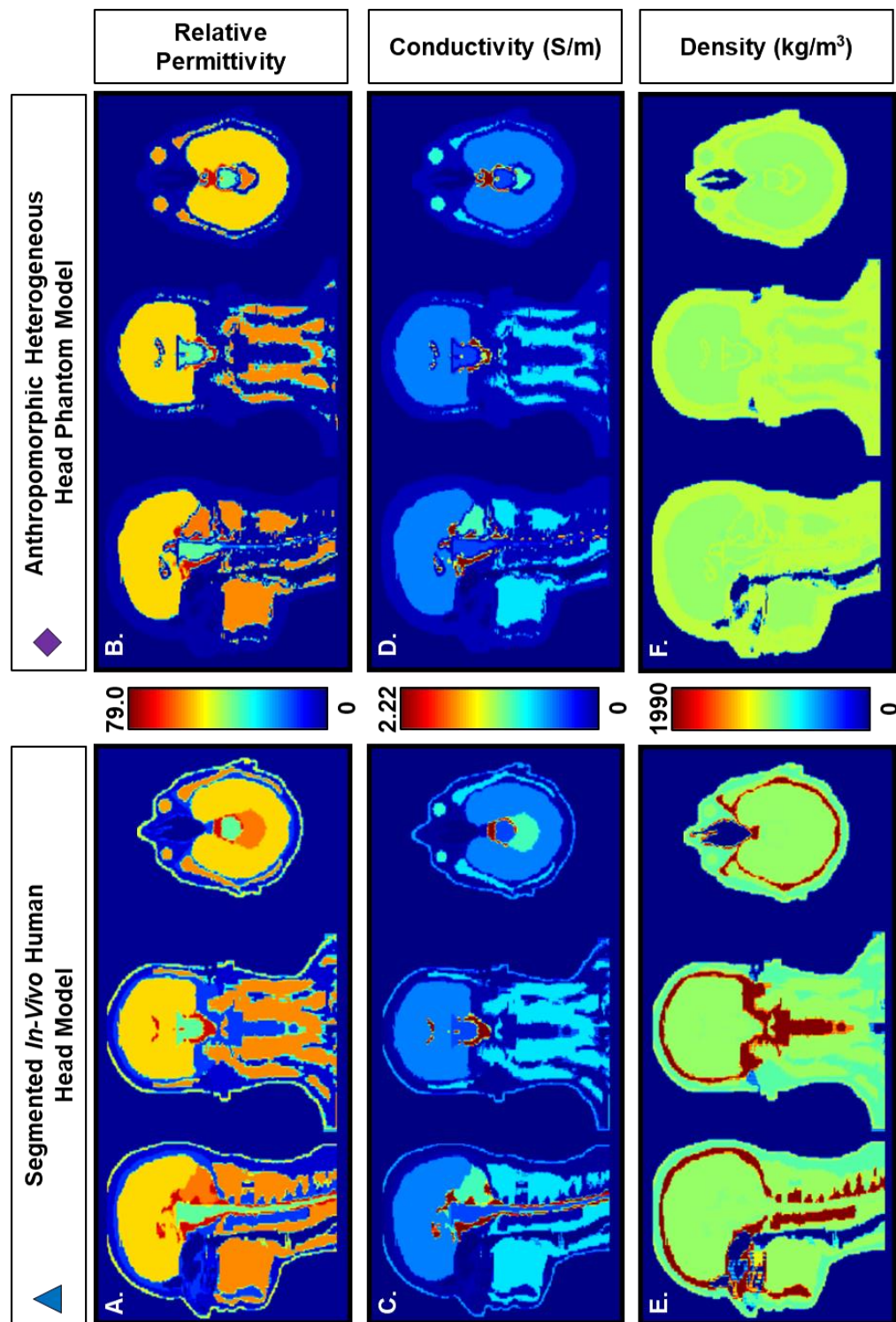


Figure 4.20. Visual Representation of the Constitutive Parameters in Each Head Model at 297.2 MHz. The segmented *in-vivo* human head model's properties are A.) Relative Permittivity, C.) Conductivity, and E.) Density. The anthropomorphic heterogeneous head phantom model's properties are B.) Relative Permittivity, D.) Conductivity, and F.) Density.

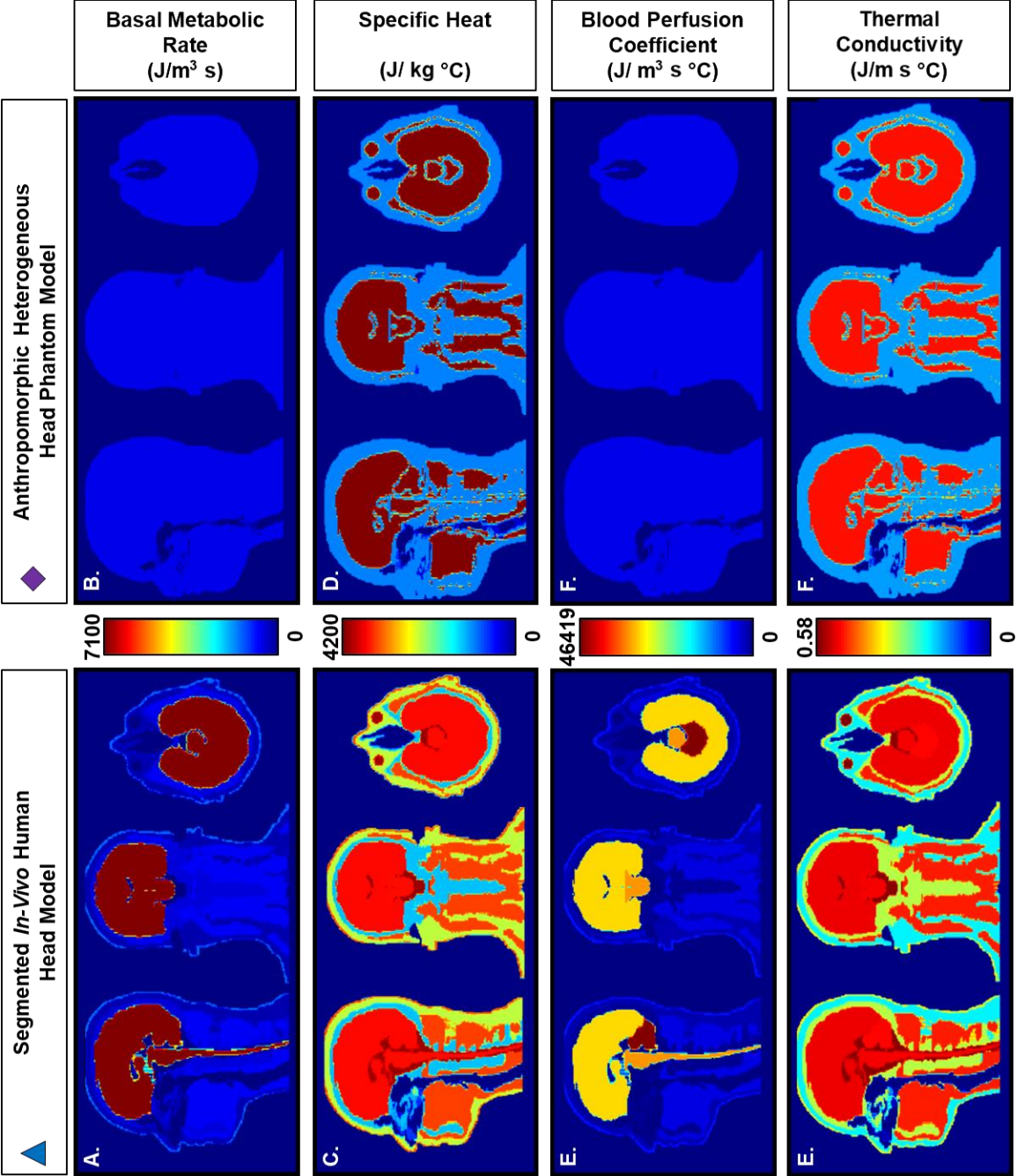


Figure 4.21. Visual Representation of the Thermal Parameters at 128.0 MHz and 297.2 MHz

Table 4.13. Segmented *In-Vivo* Head Model and Anthropomorphic Heterogeneous Head Phantom

Model's Constitutive Properties (Permittivity, conductivity) and Thermal Properties (Basal Metabolic Rate,

Specific Heat, Blood Perfusion Coefficient, Thermal Conductivity) at 128.0 MHz. Cited from the Literature

(31, 98, 159-164)

Phantom Tissue Classification/ Models	General Biological Tissue Classification	Basal Metabolic Rate A_0	Specific Heat C	Blood Perfusion Coefficient B	Thermal Conductivity K	Conductivity σ	Relative Permittivity ϵ	Density ρ
Air	Sinuses, Esophagus	0.0000	1003.6700	0.0000	0.0274	0.0000	1.0000	1.2500
Brain (WM/GM)	White Matter, Gray Matter, External CSF, Dura	7100.0000	3643.4718	30645.3022	0.5164	0.4735	63.8018	1040.0000
Brainstem	Midbrain, Pons, Medulla Oblongata, Spinal Cord	7100.0000	3630.0000	33674.6498	0.5133	0.3538	44.0650	1039.0000
Cerebellum	Cerebellum	7100.0000	3653.0000	46418.1667	0.5060	0.8294	79.7380	1040.0000
Cerebrospinal Fluid (CSF)	Internal CSF near lateral horns and around spinal cord	0.0000	4095.5000	0.0000	0.5733	2.1430	84.0410	1007.0000

Table 4.13 (Continued)

Eyes	▲	Cornea, Vitreous	0.0000	4052.6400	6439.8752	0.5848	1.3025	67.7137	1020.0700
	◆	Humor, Eyes Sclera	0.0000	4200.0000	0.0000	0.49800			
Muscle	▲	Tendons, Tongue, Muscle	116.9574	3422.5740	4385.6381	0.4917	0.7192	63.4950	1049.7800
	◆		0.0000	4200.0000	0.0000	0.49800			
Fat/ Bone/ Skin (3D SLA Material)	◆	Fat, Bone, Cartilage, Skin Dry	0.0000	1050.0000	0.0000	0.1700	0.0063	4.5600	1120.0000
Fat	▲	Fat	300.0000	2348.3300	1971.8274	0.2115	0.0369	5.9215	916.0000
Bone	▲	Cortical Bone/ Skull Cortical	610.0000	1312.8300	602.8333	0.3200	0.0674	14.7170	1990.0000
Skin		Skin Dry	1620.0000	3390.5000	6413.0194	0.3722	0.5227	65.4370	1100.0000
Legend: ▲ Perfused Segmented <i>In-Vivo</i> Human Head Model ◆ Perfusionless Anthropomorphic Heterogeneous Head Model									

The key legend in Table 4.12 and Table 4.13 indicates which tissues are represented in the various models. The perfusionless anthropomorphic heterogeneous head phantom model's tissue classification is based on the assumption that the averaged tissue classification is comparable to the percentage of the biological tissue in the Virtual Family v1.0 Duke head model. The thermal tissue parameters in Table 4.12 and Table 4.13 are not dependent on the frequency nor a specific temperature condition. The thermal properties

are averaged based on the weighted average of the tissues, which has only been seen for constitutive parameters and not thermal properties (68).

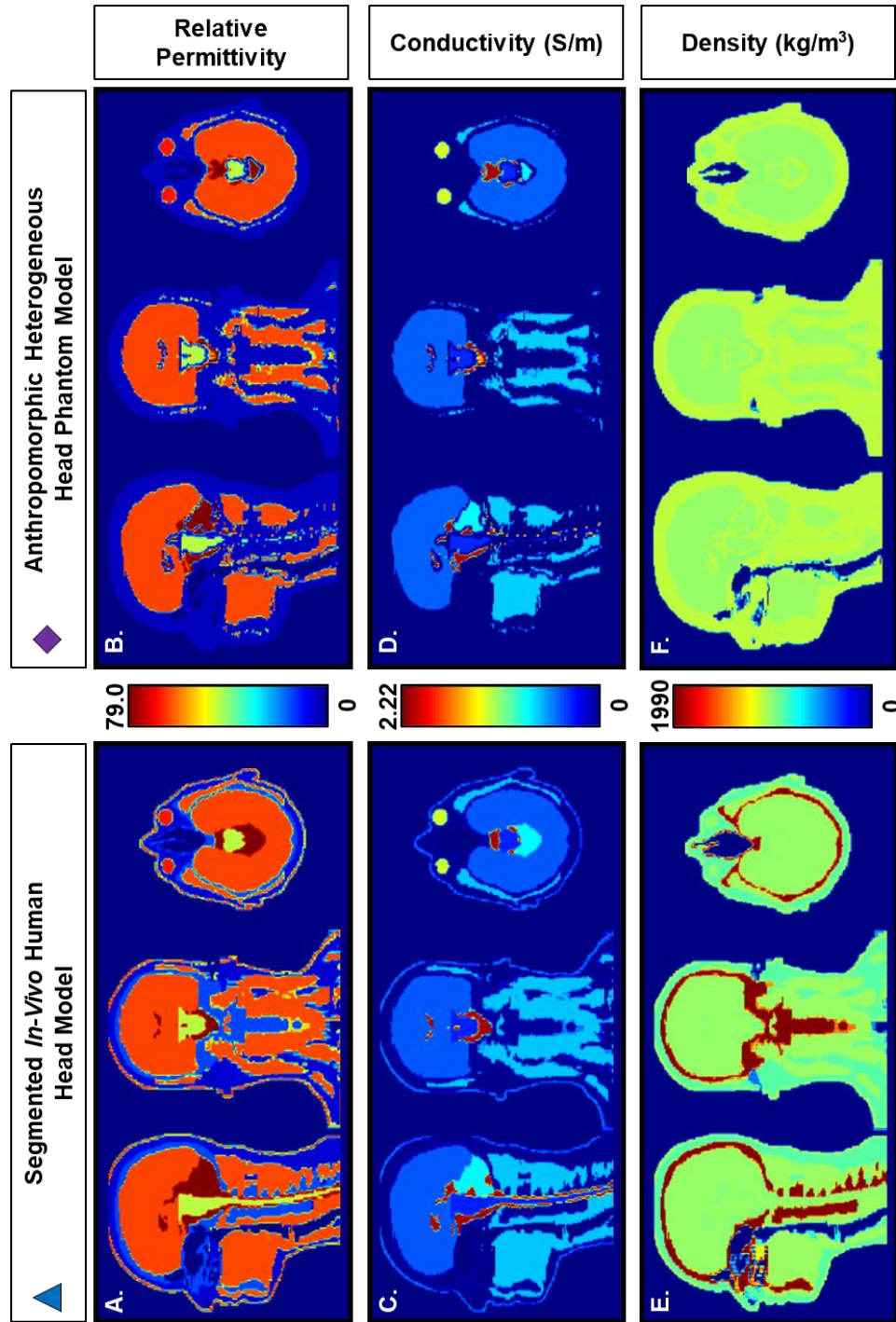


Figure 4.22. Visual Representation of the Constitutive Parameters in Each Head Model at 128.0 MHz.

Work (166) indicates that numerical thermophysiological models include two systems: a passive system and an active system (167). The active system includes the human body's regulatory responses such as sweating, shivering, vasoconstriction, and vasodilation (168). The passive system includes the heat transfer between the human body and its environment (the radiation, convection, radiation). Wang *et al.* (169) proved that it is not imperative to incorporate physiological responses to temperature in the simulation; thus, physiological responses are not incorporated in the numerical thermal simulations and calculations within this study. Since it is assumed that the rate of perfusion is independent of temperature and time to simplify the solution, the initial temperature of the blood is set to a constant of 37.00°C in models with perfusion. The thermal properties for the numerical segmented *in-vivo* human head model has perfusion. The experimental anthropomorphic heterogeneous head phantom is perfusionless (discussed in Chapter 5.0) and the constant (T_b) temperature of blood was set to a constant of 18.00°C – the MR scanner room temperature.

4.5.2.1.2 Numerical SAR Analysis at 3T and 7T.

The SAR is computed using the following SAR equation:

$$SAR_{(i,j,k)} = \frac{1}{2} \frac{\sigma_{(i,j,k)} (E_{x(i,j,k)}^2 + E_{y(i,j,k)}^2 + E_{z(i,j,k)}^2)}{\rho_{(i,j,k)}} \quad (4.2)$$

where i, j, k are the indices in a voxel of data on the 3D rectangular coordinate plane, σ (S/m) is the conductivity, ρ (kg/m³) is the density, and E (V/m) is the electric field (direct output from FDTD code). The SAR is computed using equation 4.2, scaled per 1-Watt of input power shown in Figure 4.24 and Figure 4.27. The SAR is derived from the electric fields that were generated using thermal models loaded within the numerical 16-strut/ 4-port TEM resonator as shown in Part I of this chapter at both field strengths. The SAR was used as the input power to Penne's BHTE

and was normalized to induce 3.2 W/kg over the entire head model, the current FDA standard, which is regulated by a time-average of 10 minutes.

4.5.2.1.3 Numerical Temperature Calculations at 3T and 7T

4.5.2.1.3.1 Bioheat Equation and Boundary Conditions

To adequately assess the numerical RF safety and robustness of the numerical phantom temperature models, temperature measurements are measured using a finite-difference implementation of Penne's BHTE (74):

$$\rho C_p \frac{dT}{dt} = \nabla \cdot (k \nabla T) + A_0 - B(T - T_b) + \rho \text{SAR} \quad (4.3)$$

where C_p (J/kg °C) denotes the specific heat (the amount of heat per unit mass required to raise the temperature by one degree Celsius), k (J/m s °C) denotes the thermal conductivity (the property of a material that indicates its ability to conduct heat), A_0 (J/m³ s) denotes the basal metabolic rate (the minimum calorific requirement needed to sustain life in a resting individual), B (J/m³ s °C) denotes the blood perfusion coefficient (162), T (°C) denotes the temperature, T_b (°C) denotes the constant blood temperature, and ρ (kg/m³) denotes the density. The Cartesian discretization of the bio-heat equation is covered in full in Chapter 2.0 within Subsection 2.6.4. The numerical stability is met by satisfying the equation in Subsection 2.6.4.

Convection based boundary conditions are the only mechanisms of heat transfer considered in this study. As mentioned, physiological responses are ignored, and the temperature calculations are more conservative in this study than real-life applications. The temperature change between

the tissue surface and the environment is proportional to heat transfer from the computational domain and environment. The boundary condition applied is:

$$k \frac{dT}{dt}(x, y, z) = -H_a(T_{x,y,z} - T_a) \quad (4.4)$$

where H_a ($\text{J/m}^2 \text{ s } ^\circ\text{C}$) denotes the convection transfer coefficient (a constant with a value of $20 \text{ J/m}^2 \text{ s } ^\circ\text{C}$ (75)), T_a ($^\circ\text{C}$) denotes the ambient temperature (162) (the property of a material that indicates its ability to conduct heat), $T_{x,y,z}$ ($^\circ\text{C}$) denotes the temperature as a function of Cartesian space, x,y,z denotes the Cartesian space, and k ($\text{J/m s } ^\circ\text{C}$) denotes the thermal conductivity. T_a is set to 18.00°C in each thermal simulation, which is the measured ambient temperature in the MR scanner for experiments with the perfusionless phantoms.

The in-house PBHE algorithm (13) was altered to incorporate GPU implementation for faster computations. The numerical thermal simulations were performed on a computer workstation with a GPU (4-6GB of memory) to include equilibrium and numerical RF heating. All algorithms were written in MATLAB (The MathWorks, Inc., Natick, MA, USA).

4.5.2.1.3.2 Stability of Boundary Conditions and Steady-State Temperature Calculations

The numerical perfusionless anthropomorphic heterogeneous phantom head model is placed in the MR system at the MR room temperature, an ambient temperature T_a of 18.00°C , with no applied SAR ($\text{SAR} = 0 \text{ W/kg}$) until an equilibrium is met. The duration to reach the thermal equilibrium is calculated for each model. To measure the correct numerical temperature rise, each model must reach steady-state while loaded inside of the RF coil.

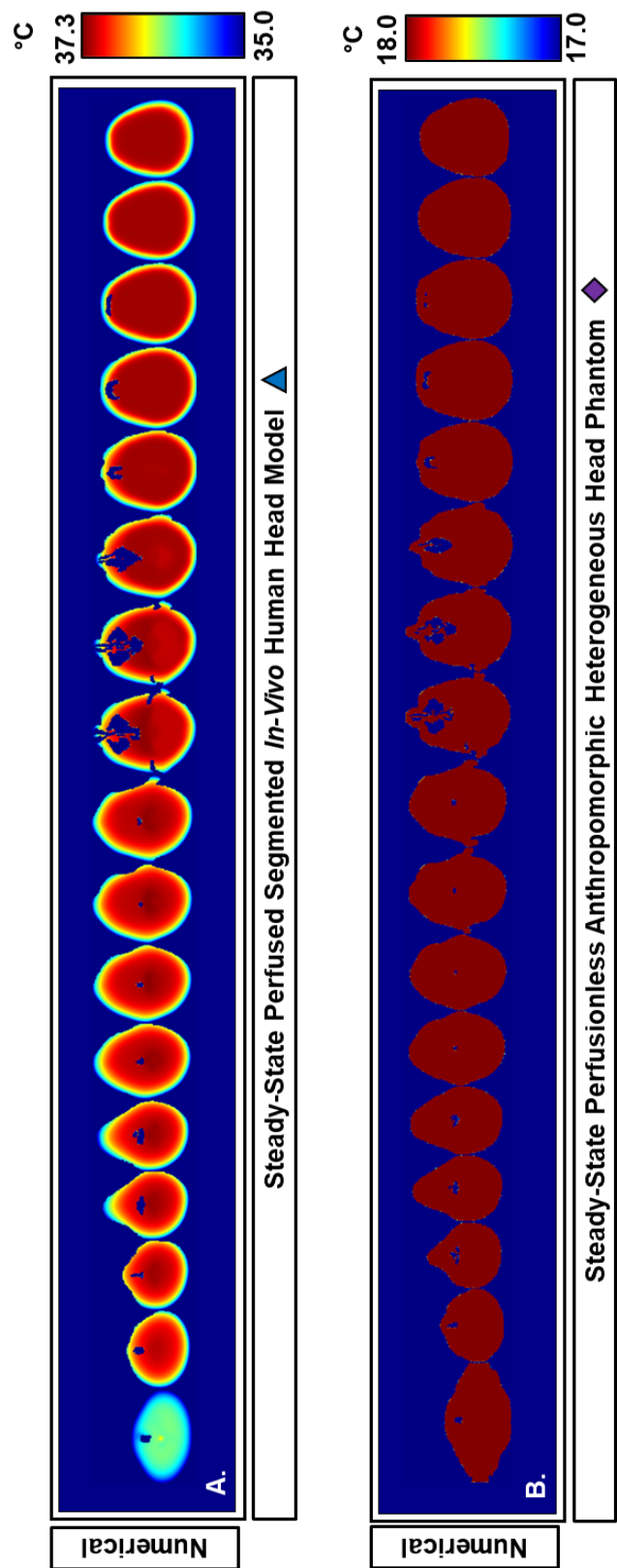


Figure 4.23. Steady-State in Segmented *In-Vivo* Human Head Model at 3T and 7T. The temperature in the A.) perfused segmented *in-vivo* human head model and B.) perfusionless Anthropomorphic Heterogeneous Head Phantom are shown upon reaching a steady-state

Using the stability constant in Subsection 2.6.4, the Δt was set to 1.924 ms. Steady-state was reached in the numerical perfused segmented *in-vivo* human head model after 56.00 minutes as illustrated in Figure 4.23.A and immediately in perfusionless anthropomorphic heterogeneous head phantom as illustrated in Figure 4.23.B. The perfusionless anthropomorphic heterogeneous head phantom reached steady state immediately because experimentally it is at the same temperature as the ambient temperature.

4.5.2.1.3.3 Temperature Elevation Calculations

All post-processing, analysis, and SAR and thermal calculations were performed in MATLAB. The SAR operates as the heat source in the PBHE. To reach steady-state, no input power (SAR) is applied; in contrast, an input power (SAR) must be applied to experience RF heating. Using the in-house PBHE algorithm (13), an input power is applied to reach the FDA limits with a 10-minute continuous input power that yields a 3.2 W/kg average SAR within the respective thermal head model (170). The numerical temperature change, ΔT , is computed and the results in the two numerical models are shown in Figure 4.25 and Figure 4.26.

4.5.3 Results and Discussion

4.5.3.1 Results

4.5.3.1.1 Numerical SAR Modeling and Analysis at 7T

The numerical SAR distribution is shown for the numerical perfused segmented *in-vivo* human head model and the numerical perfusionless anthropomorphic heterogeneous head phantom model

in Figure 4.24. Figure 4.24 is scaled by the maximum allowable peak SAR per 1-Watt of input power. The applied input power was normalized to an average SAR of 3.2 W/kg which is the current regulated FDA average SAR for a time average of 10 minutes. In both models, the peak SAR is observed at the highest point of the white matter and gray matter within the brain region.

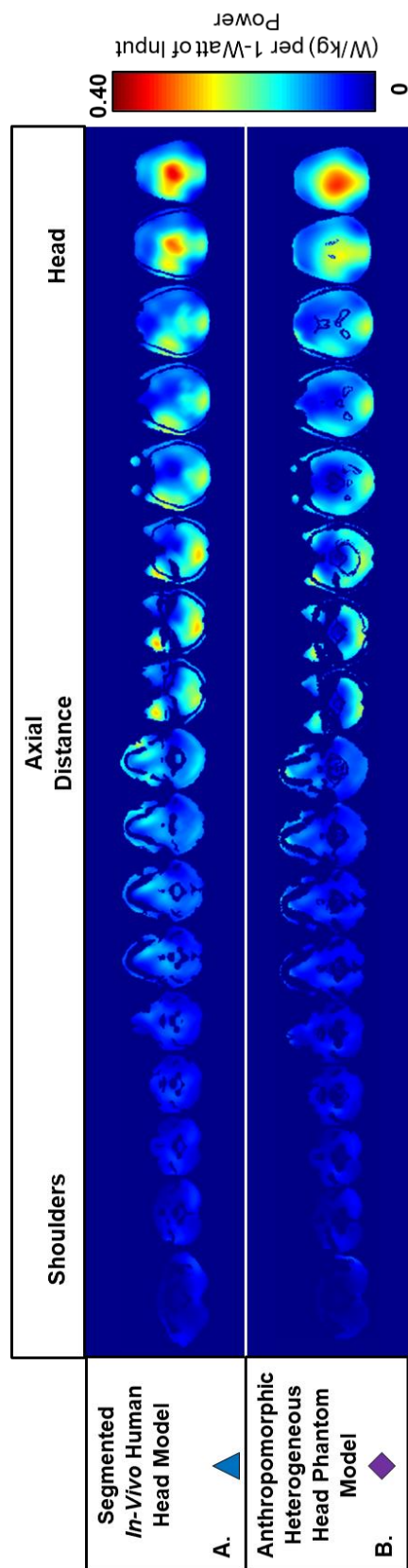


Figure 4.24. Numerical SAR Distribution in Two Numerical Thermal Head Models at 7T. The numerical SAR distribution per 1-Watt of Input Power is shown for each model loaded within the numerical 16-strut/4-port TEM resonator. The numerical SAR distribution is scaled from 0 to the highest peak SAR per 1-Watt of input power.

4.5.3.1.2 *Numerical Temperature Modeling and Analysis at 7T*

Once the steady-state was reached, numerical RF heating was applied for 10-minutes with the power required to achieve the FDA's maximum limit on the regulated average SAR at 3.2 W/kg. In Figure 4.25, the numerical temperature elevation is shown for the numerical perfused segmented *in-vivo* human head model from $T_b = 37.00^\circ\text{C}$ to the temperature at the completion of a 10-minute thermal heating and masked to the fillable compartments.

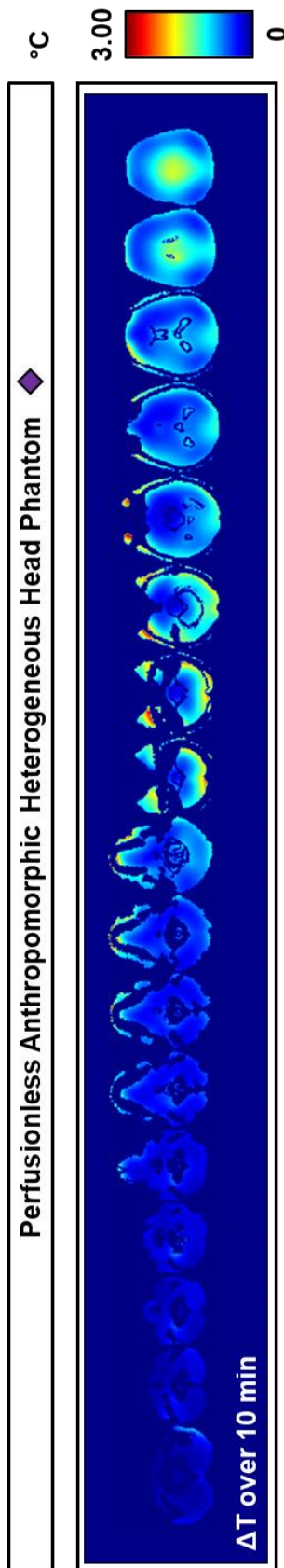


Figure 4.25. Temperature Elevation over time in the Numerical Perfusionless Anthropomorphic Head Model at 7T. The minimum to maximum temperature elevation is shown from steady-state (Figure 4.23.B) to a 10-minute thermal heating for a continuous FDA regulated average SAR of 3.2W/kg.

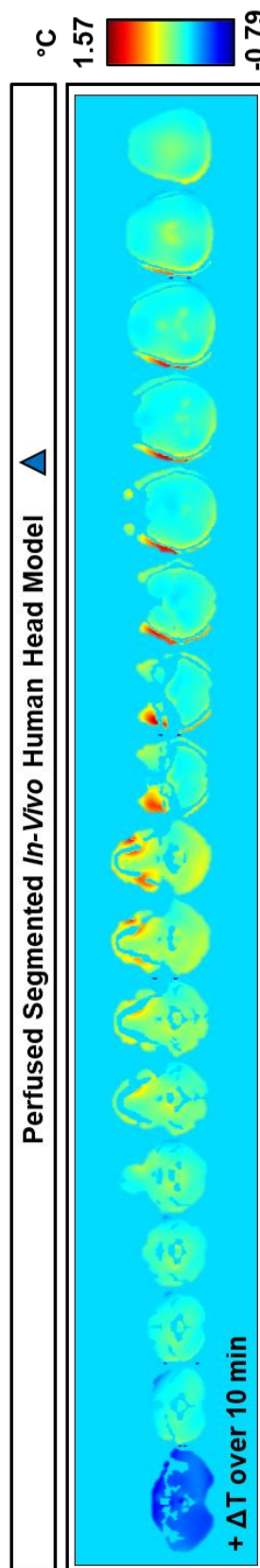


Figure 4.26. Temperature Elevation over time in the Perfused Segmented *In-Vivo* Human Head Model at 7T. The minimum to maximum temperature elevation is shown from steady-state (Figure 4.23.A) to a 10-minute thermal heating for a continuous FDA regulated average SAR of 3.2W/kg.

In Figure 4.26, the temperature elevation is shown for the numerical perfusionless anthropomorphic heterogeneous head phantom model from the ambient temperature to the temperature at the completion of a 10-minute thermal heating and masked to the fillable compartments. The results in Figure 4.26 and Figure 4.25 show the temperature elevation masked to the fillable compartments within each respective head model.

Although Figure 4.24 reveals similarities in the location of some SAR hot-spots to the local thermal rise in both thermal models, the numerical temperature rise is different in the numerical perfusionless anthropomorphic heterogeneous head phantom model. The highest temperature rise appears to correlate to high local SAR regions in the numerical perfusionless anthropomorphic heterogeneous head phantom model. Figure 4.26 shows the highest temperature rise in the numerical perfusionless anthropomorphic heterogeneous head phantom model's left tendon near the zygomatic bone (cheekbone). These locations are similar locations to the local SAR hot-spot regions in Figure 4.24. However, high SAR hot-spot regions do not necessarily correlate to high temperature rise. The SLA resin and areas with low permittivity in the tissue are producing high SAR and temperature.

4.5.3.1.3 *Numerical SAR Modeling and Analysis at 3T*

Figure 4.27 shows the numerical SAR distribution for the perfused segmented *in-vivo* human head model and the perfusionless anthropomorphic heterogeneous head phantom model at 3T. The local SAR hot-spot regions are in the periphery of the brain and the left tendon in both thermal models.

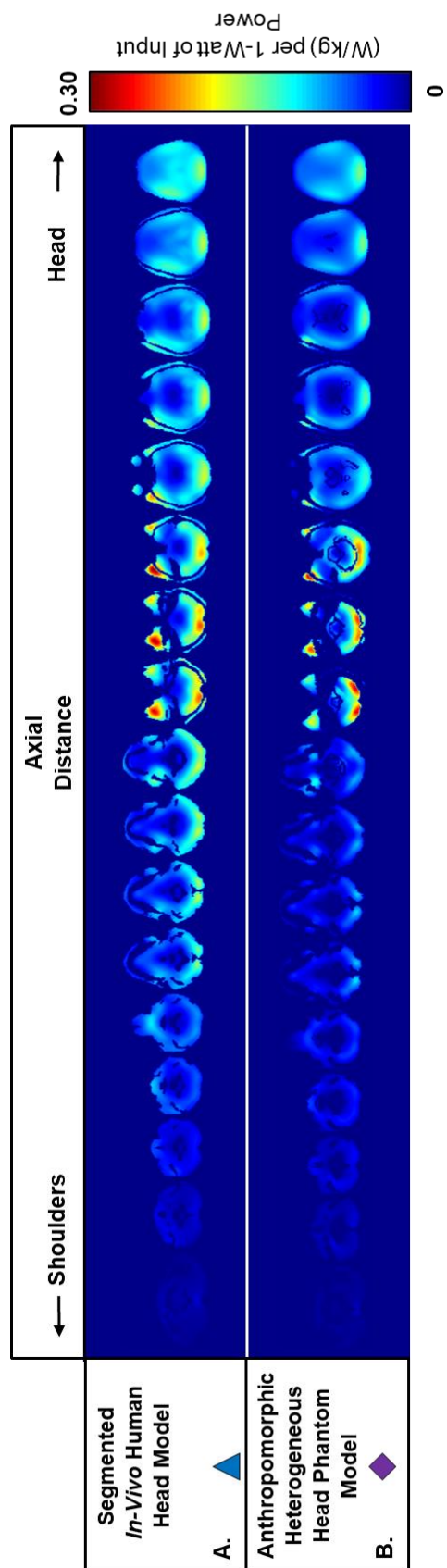


Figure 4.27. Numerical SAR Distribution in Two Numerical Thermal Head Models at 3T. The numerical SAR distribution per 1-Watt of Input Power is shown for each model loaded within the numerical 16-strut/4-port TEM resonator. The numerical SAR distribution is scaled from 0 to the highest peak SAR per 1-Watt of input power.

4.5.3.1.4 *Numerical Temperature Modeling and Analysis at 3T*

The temperature is elevated the most in the left temporal lobe and left tendon near the zygomatic bone (cheekbone) in Figure 4.28. This elevation is due to an elevated SAR in this region and the heat transferring from other nearby tissues. In general, the temperature elevates above the ambient temperature in the perfused tissues. The perfusionless tissues operate as a heat sink and lose their heat to the MR room environment. The temperature elevation reached a 7.00°C peak in the posterior right of the cerebellum in Figure 4.29. In general, the numerical perfusionless anthropomorphic heterogeneous head phantom model heats in the cerebellum and the anterior right and left tendons. These localized regions are the classified tissue regions where the FDA regulated average SAR is the greatest in the phantom model. These peak temperature regions correspond to the peak temperature regions in the perfused segmented *in-vivo* human head model.

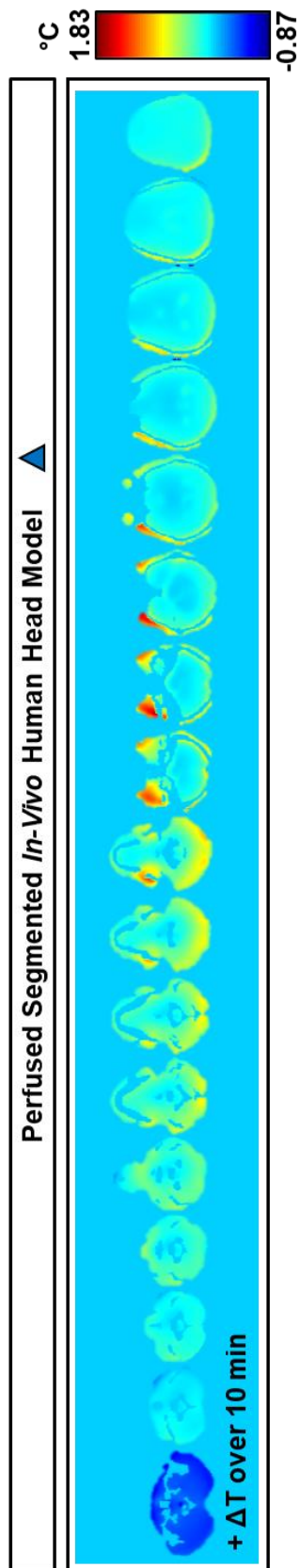


Figure 4.28. Temperature Elevation over time in the Perfused Segmented *In-Vivo* Human Head Model at 3T. The minimum to maximum temperature elevation is shown from steady-state (Figure 4.23.A) to a 10-minute thermal heating for a continuous FDA regulated average SAR of 3.2W/kg.

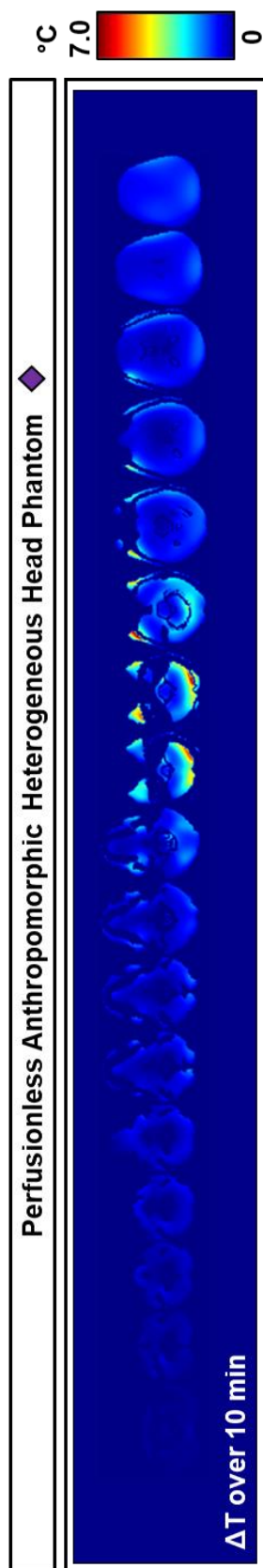


Figure 4.29. Temperature Elevation over time in the Perfusionless Anthropomorphic Head Model at 3T. The minimum to maximum temperature elevation is shown from steady-state (Figure 4.23.B) to a 10-minute thermal heating for a continuous FDA regulated average SAR of 3.2W/kg.

4.5.3.2 Discussion and Recommendation

Part II of this chapter builds on the EM characterization of the numerical perfusionless anthropomorphic heterogeneous head phantom model that is provided in Part I for 3T and 7T. Part II aims to provide the thermal characterization of the numerical perfusionless anthropomorphic head phantom model. Although the EM characterization results are coil-specific, the results offered a visual representation of the difference in the performance of the numerical anthropomorphic heterogeneous head phantom model to other numerical phantom models. Part I concluded that the anthropomorphic heterogeneous head phantom model was the most useful to conduct MR safety analysis at 3T and 7T because it had the least amount of percent volume change with a significant error. The absolute electric field analysis of this specific phantom model was the most comparable to the numerical segmented *in-vivo* human head model. Thus, Part II explores an MR safety comparison of the SAR and temperature performance of the numerical perfusionless anthropomorphic head phantom at 3T and 7T. The results were compared to the numerical perfused segmented *in-vivo* human head model to project a potential comparison of the temperature rise in the experimental phantom to a human subject.

4.5.3.2.1 Numerical SAR and Numerical Temperature Modeling at 7T

A more in-depth analysis of Section 4.2.3.1.3 highlights that not only are the constitutive parameters indicative of the changes in the electromagnetic behavior in each model but also the thermal parameters are indicative of the changes in the thermal behavior in each model. Our study assesses the numerical SAR distribution per 1-Watt of input power in two thermal head models. SAR per 1-Watt was used because the SAR is scalable per input power. Figure 4.24 assess each model's measured average and peak SAR. It is essential to reference back to the absolute electric

field distribution comparison of Figure 4.4, Figure 4.5, and Table 4.11 to understand Figure 4.24 further.

The perfusionless anthropomorphic heterogeneous head phantom model has low SAR in the SLA resin material. As previously mentioned, the experimental anthropomorphic head phantom model utilizes a resin material with conductivity = 0.11 S/m at 7T, which is similar to the averaged conductivity (0.17 S/m) of the fat, bone, and skin. Thus, Figure 4.24 highlights subtle differences in the SAR distributions and emphasize that the perfusionless anthropomorphic heterogeneous head model still offers a subtle overestimation and underestimation of the global SAR distribution. However, it offers the most accurate representation of the peak SAR.

Alon *et al.* investigated the anatomical differences in a human head model and found a similar outcome that SAR underestimation could result in a safety risk via SAR and temperature rise. In contrast, the overestimation may lead to inadequate RF coil safety.

In this study, the thermal simulations validate whether the estimated numerical SAR is a safety risk. The temperature simulations were performed for a continuous 10-minute RF power generated by a continuous FDA regulated average SAR, 3.2W/kg, and this power does not represent the real power generated by a specific MR sequence. However, the results demonstrate the PBHE algorithm and the numerical perfusionless anthropomorphic heterogeneous head phantom model have the capability to predict the temperature rise through any power generated by a specific MR sequence. Using the thermal models, the generated results can help modify MR sequences at 7T to meet clinical standards and government regulations. This analysis is a significant resource in assessing MR safety in RF coil design.

Differences in numerical SAR are shown in the comparison of the perfusionless anthropomorphic heterogeneous head phantom model and perfused segmented *in-vivo* human head

model. The SAR distributions are comparable among the thermal models but differ in SAR intensity per voxel. The absolute electric field is relatively higher in the SLA resin compared to its neighboring classified tissues in Figure 4.7.B due to a low dielectric constant compared to the weighted average dielectric constant that corresponds to the combination of the fat/bone/skin. This similar observation appeared in Figure 4.7.A in the electric field; however, the electric field varies in the fat, bone, and skin tissues. Figure 4.7.B illustrates that the SLA resin boundaries create an artificial electric field between the classified tissues perfusionless anthropomorphic heterogeneous head phantom model. Based on electromagnetic theory, differences are expected to occur between the electric field of the thermal models. The tangential component of the electric field is continuous, yet the normal component is discontinuous. Thus, the differences are caused by the changes in the magnitude of the normal component of the electric field between the thermal models. The differences in the electric field result in the differences in the SAR between each thermal model.

Due to the difference in the electric field and SAR, differences are also shown in the temperature elevations at 7T and are illustrated in Figure 4.30. The perfused segmented *in-vivo* human head model offers a better predictor of the temperature rise in an *in-vivo* human head throughout this sequence. As mentioned, there are differences caused by the heat source in the PBHE, SAR; and also, there are differences caused by perfusion. While it is not important to explore the impact by perfusion on temperature; it is important to note that the temperature elevation in the perfused segmented *in-vivo* human head model is much less than the perfusionless anthropomorphic heterogeneous head phantom model. It was observed that each thermal model would have the same slope in temperature rise until perfusion causes the temperature to remain constant. As a result of this study, while there are differences between the thermal models, the

perfusionless anthropomorphic heterogeneous head phantom model offers realistic locations to localized temperature rise for the perfused segmented *in-vivo* human head model.

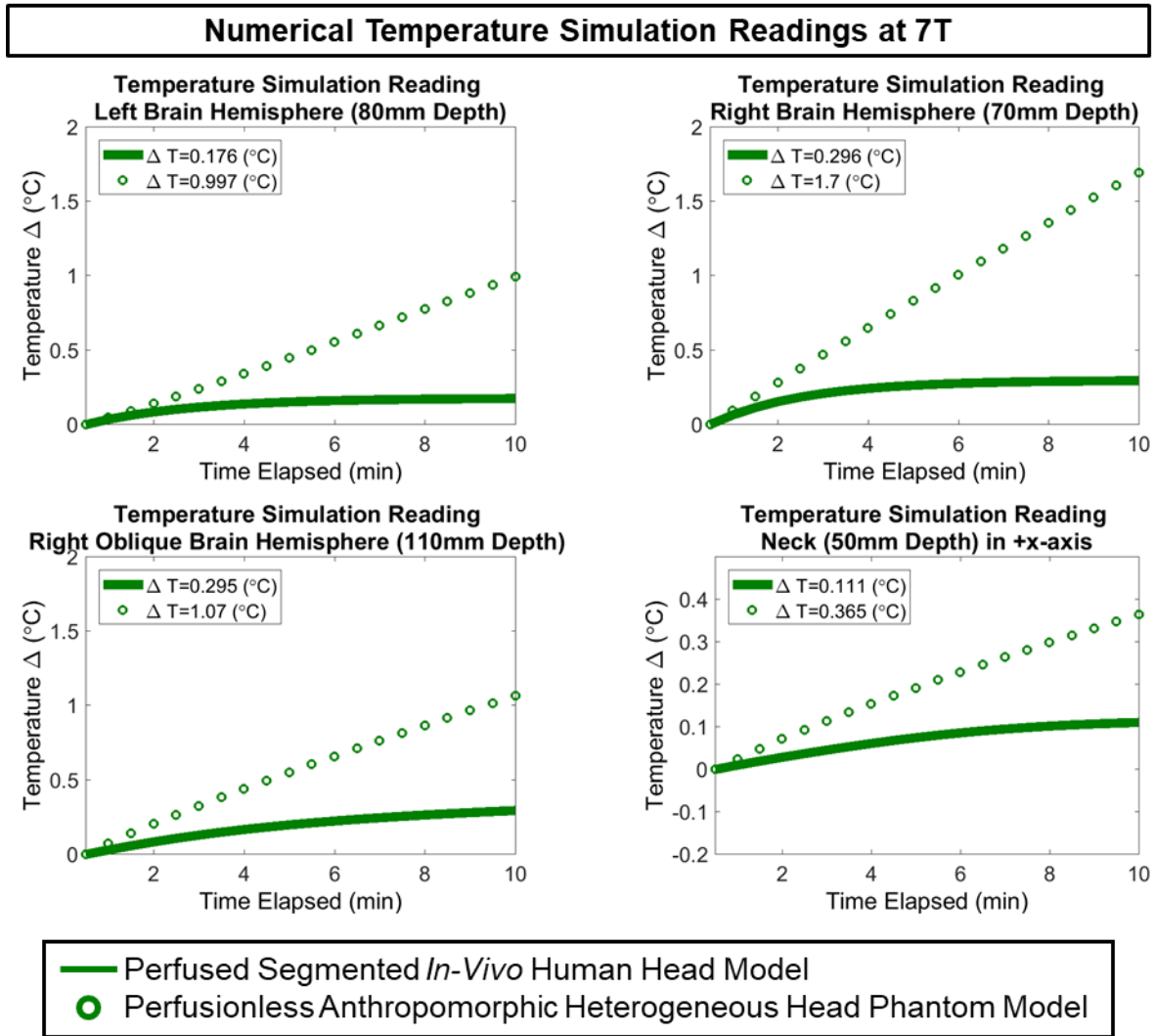


Figure 4.30. Temperature Elevation in Each Thermal Model at 7T. The temperature measurements in each model per temperature location for a duration of 10-minutes.

4.5.3.2.2 Numerical SAR and Numerical Temperature Modeling at 3T

At 3T, the numerical SAR distribution of each thermal model differs from 7T. The numerical SAR is higher in the periphery perfused segmented *in-vivo* human head model in comparison to the perfusionless anthropomorphic heterogeneous head phantom model. The numerical SAR

within the phantom underestimates the numerical SAR in the perfused segmented *in-vivo* human head model. This underestimation is supported by the illustration of the absolute electric field percent change between both models shown in Figure 4.19. The differences in SAR correlate to the differences in the absolute electric field.

There are differences in the numerical temperature rise in both numerical thermal models at 3T. An equivalent input power of an average SAR of 3.2 W/kg applied to each thermal model. The differences in localized temperature rise corresponds to the difference in localized SAR regions. Figure 4.31 illustrates the numerical temperature difference in both thermal models. The numerical thermal models have the same initial temperature rise slope. Over time, perfusion begins to bring the temperature rise to an equilibrium in the perfused segmented *in-vivo* human head models. The temperature elevation indicates that temperature rise in all shown regions is within the IEC guidelines.

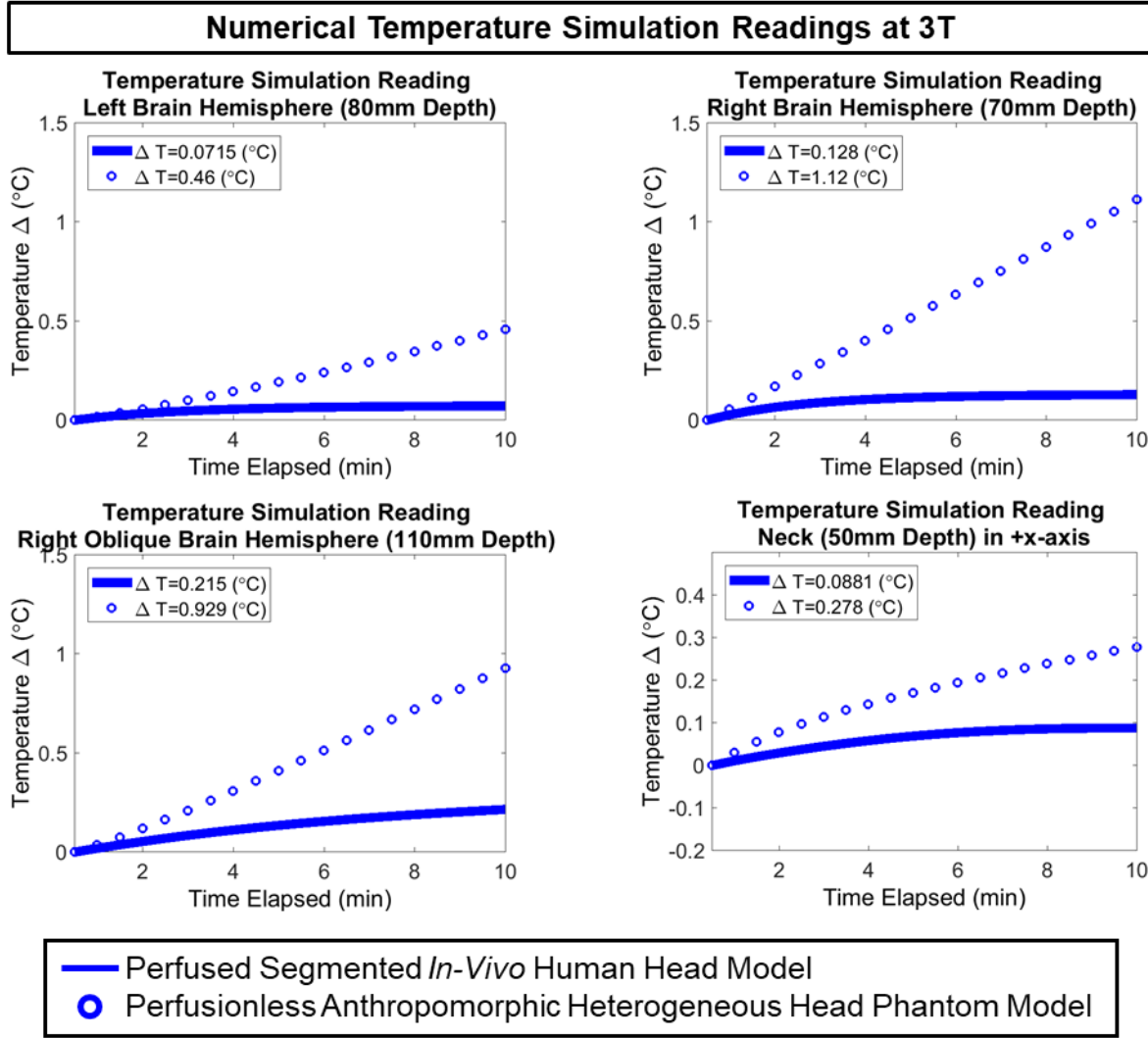


Figure 4.31. Temperature Elevation in Each Thermal Model at 3T. The temperature measurements in each model per temperature location for a duration of 10-minutes.

4.5.3.2.3 Thermal Characterization Comparison of the Thermal Head Models at 3T and 7T

A comparison of the temperature elevation is shown in both thermal models at 3T and 7T in Figure 4.32 and Figure 4.33.

Perfused Segmented *In-Vivo* Human Head Model ▲

A.

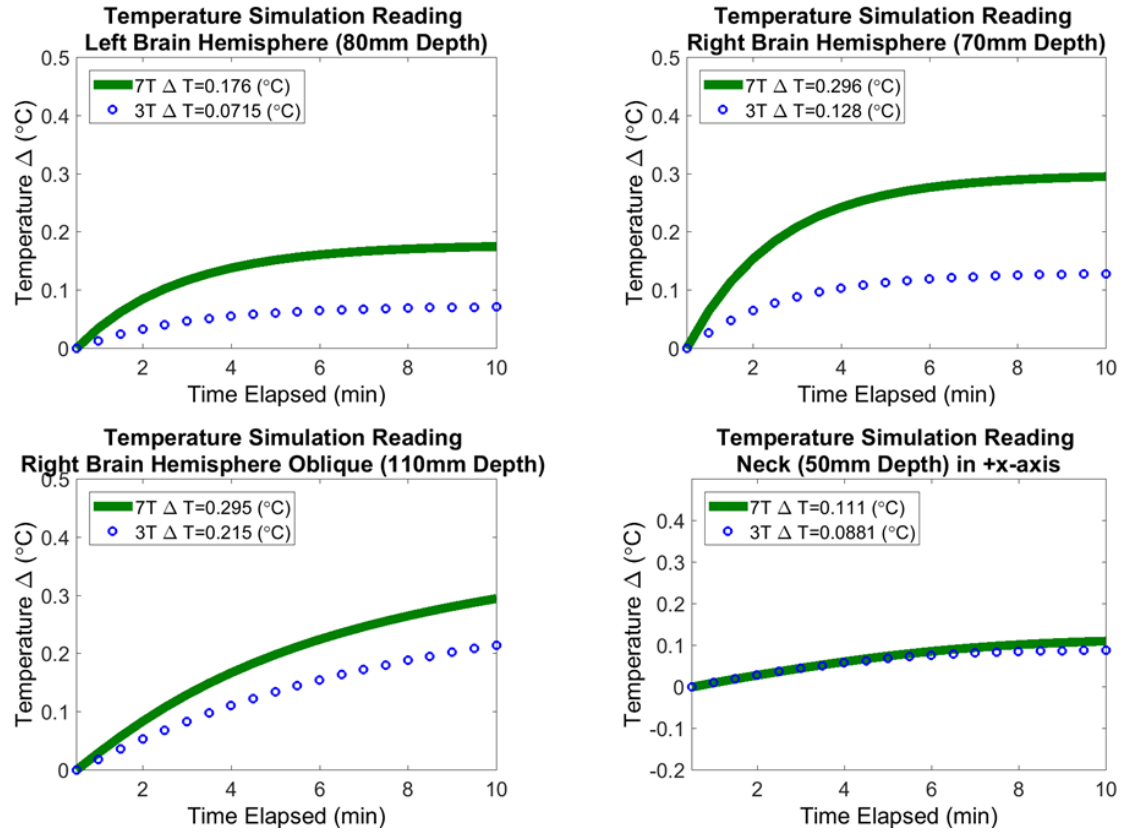
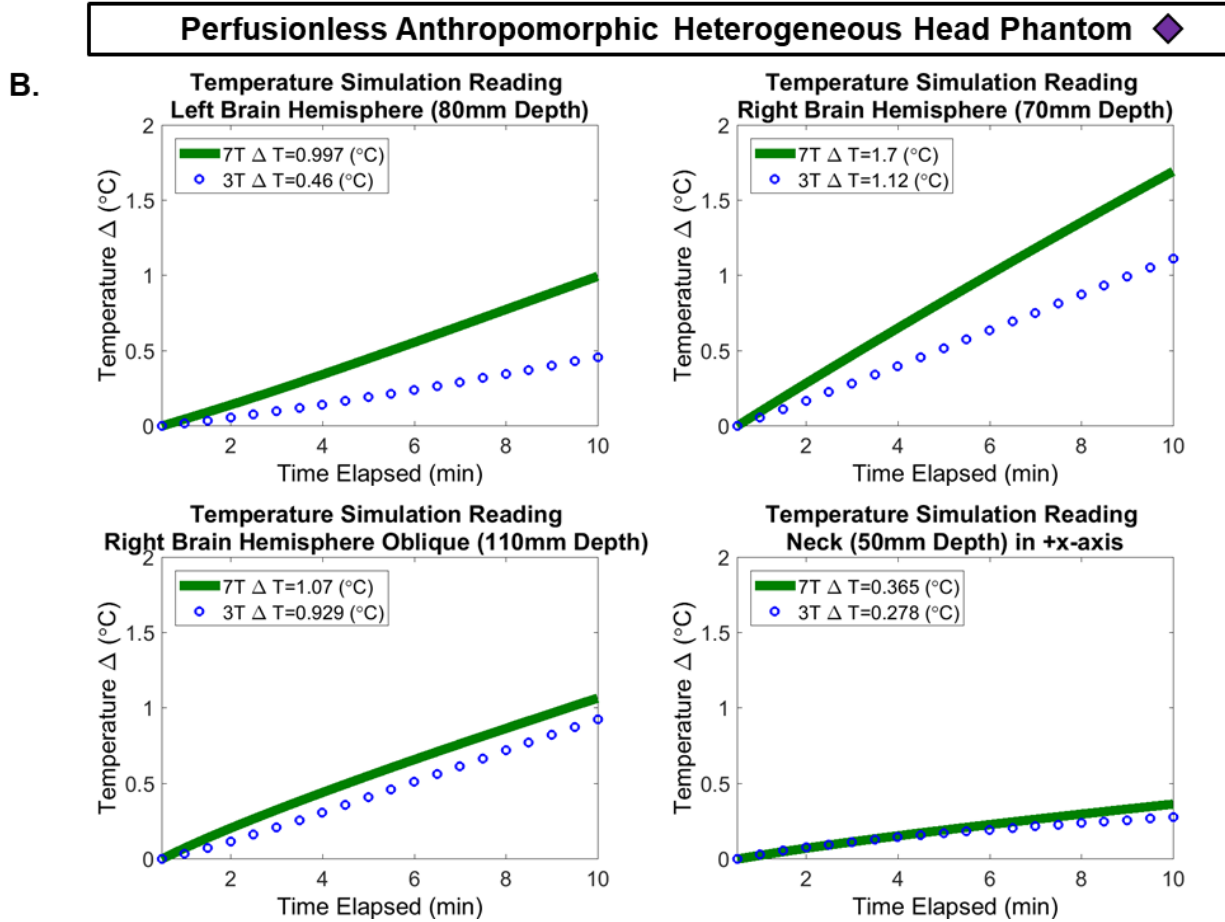


Figure 4.32. Comparison of the Temperature Rise in Two Thermal Head Models at 3T and 7T. A.) Perfused Segmented *In-Vivo* Human Head Model and B.) Perfusionless Anthropomorphic Heterogeneous Head Phantom Model loaded within the numerical 16-strut/4-port TEM Resonator.

Figure 4.32 (Continued)



The probe locations were arbitrarily chosen within the perfusionless anthropomorphic heterogeneous head phantom model to eliminate favorable locations based on field strengths. Studies have indicated that the electric field becomes inhomogeneous at 3T and higher field strengths. It was necessary to evaluate the numerical thermal heating in the perfusionless anthropomorphic heterogeneous phantom model at 3T and 7T. The numerical temperature heating at 3T is not uniform primarily due to the SAR not being uniform at 3T.

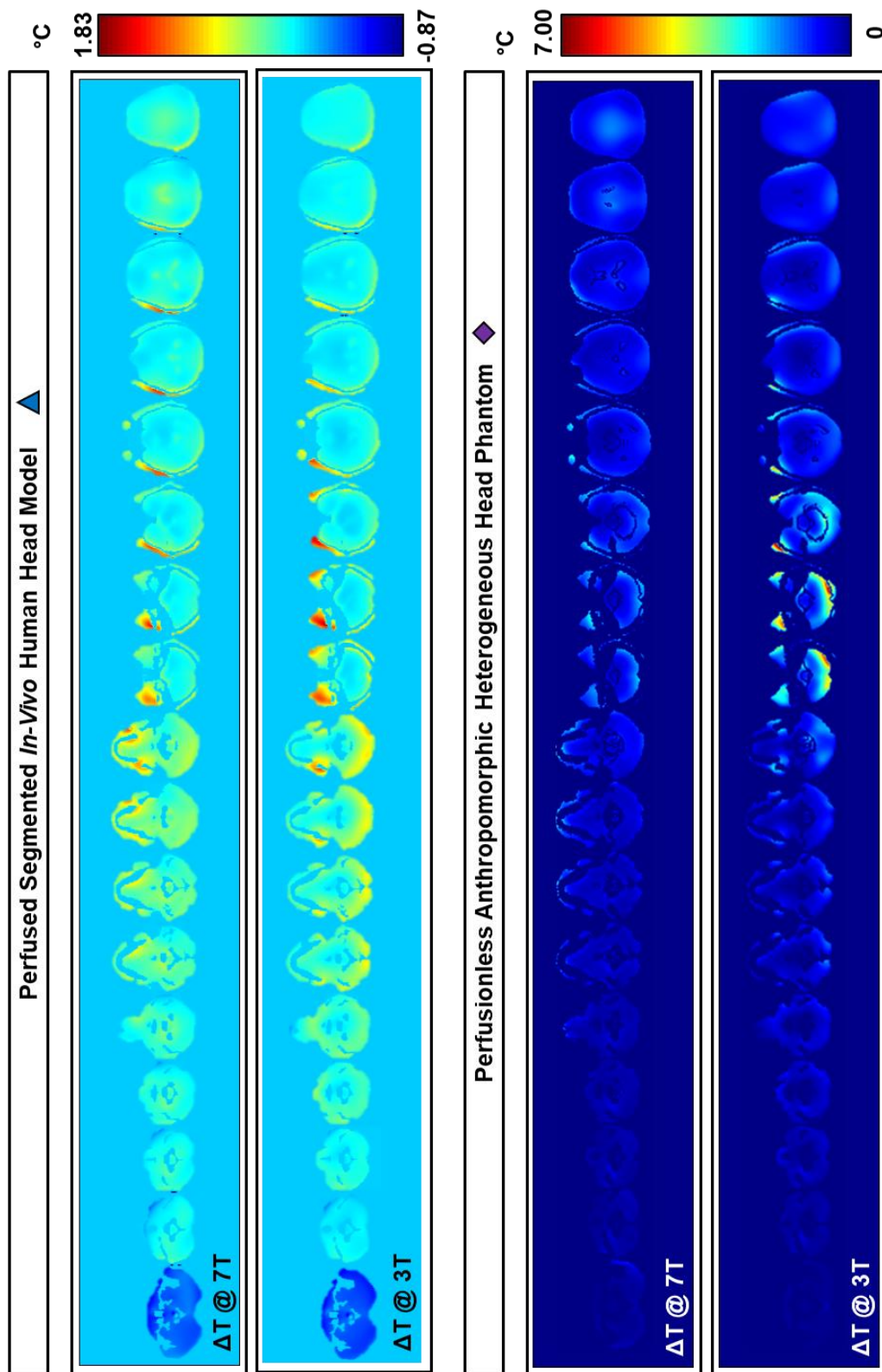


Figure 4.33. Comparison of Temperature Elevation Distribution in Each Thermal Model at 3T and 7T. The temperature elevation distributions are scaled from the minimum to the maximum temperature elevation from the ambient temperature.

Figure 4.33 indicates that using the power required to reach the FDA's average SAR limits, a peak of 3.2W/kg, causes higher peak temperature rise in some locations at 3T than 7T. Despite using the same continuous average SAR of 3.2W/kg, the power absorbed within the fillable compartments at 3T is much higher than 7T. This difference in RF power absorption is caused by the difference in the power absorption within the SLA resin material at respect to each field strength. A minimal power absorption in the SLA resin is experienced at 3T in comparison to 7T due to the differences in conductivity (3T: $\sigma = 0.006$ S/m; 7T: $\sigma = 0.108$ S/m).

4.5.4 Summary

In summary, the numerical perfusionless anthropomorphic head phantom model is a useful tool to assess MR safety at 3T and 7T. The numerical perfusionless anthropomorphic head phantom model has corresponding SAR hot-spots and localized temperature elevation as the numerical perfused segmented *in-vivo* human head model at 3T and 7T. The numerical temperature elevation over time differs in both thermal models at 3T and 7T because the perfusion stabilizes the temperature elevation after a designated duration in time.

4.6 CONCLUSION

This chapter was divided into two parts that discussed the EM and thermal characterization within a numerical perfusionless anthropomorphic head phantom using the TEM resonator at 3T and 7T. This chapter built on the work of Chapter 3.0 and further assessed the significance of the designed experimental anthropomorphic head phantom through numerical and experimental assessments.

Part I assessed the EM characterization of five numerical models at 3T and 7T by evaluating the S-parameters, B_1^+ field distributions/intensities, and absolute electric field distributions/intensities. This study determined that any model can be used to assess the S-parameters at 3T and 7T. Anthropomorphic head phantoms can be used to assess the B_1^+ field distributions/intensities regardless of the media. At 7T, homogeneous brain-doped or heterogeneous solutions should be used to be most comparable to the *in-vivo* volunteer. At 3T, any media can be used to compare to the segmented *in-vivo* human head model. However, the absolute electric field distribution/intensity is best assessed using the anthropomorphic heterogeneous head phantom to determine the least amount of volume change with a significant error, and it is most comparable to the segmented *in-vivo* human head model at both field strengths. The absolute electric field distribution/intensity is the bases for MR safety assessments. These results are frequently referenced in Part II.

Part II provided the thermal characterization of two thermal models at 3T and 7T by evaluating the SAR and the temperature elevation. The study determined that the perfusionless anthropomorphic head phantom model overestimates the SAR distribution at 7T and underestimates the SAR distribution at 3T. The overestimation and underestimation of SAR correlate to the absolute electric field distribution/intensity in Part I. The absolute electric field was higher in the stereolithography (SLA) resin than the individual fat, bone, and skin tissues at 7T; and in contrast, the absolute electric field was lower in the SLA resin than the individual fat, bone, and skin tissues at 3T. The thermal assessments showed that the perfusionless anthropomorphic head phantom model is a great predictor of the initial temperature rise quantity and temperature rise locations in the perfused segmented *in-vivo* human head model. At both field strengths, the perfusionless anthropomorphic head phantom model continues to rise in temperature

due to heat transfer, while the perfused segmented *in-vivo* human head model rises until it reaches an equilibrium due to the impact of perfusion. The thermal elevation is higher in some regions at 3T; however, the PBHE algorithm and the perfusionless anthropomorphic head phantom model are verified as helpful resources to validate the MR safety of an RF coil and MR sequence.

The results in Chapter 4.0 support Specific Aim 2. The results in Chapter 4.0 indicate that accurate numerical modeling is still an effective and efficient predictive resource for an EM and thermal analysis.

5.0 PRELIMINARY ELECTROMAGNETIC AND THERMAL CHARACTERIZATION OF THE ANTHROPOMORPHIC HETEROGENEOUS HEAD PHANTOM IN DIFFERENT 7T RF COILS

5.1 INTRODUCTION

Chapter 3.0 demonstrated through a few 7T MR measurements that the design of an anthropomorphic heterogeneous head phantom is a valuable tool for MR testing. Chapter 4.0 expands the work of Chapter 3.0 and determines the EM behavior of the anthropomorphic heterogeneous head phantom is the most comparable to the *in-vivo* volunteer in various MR measurements using the TEM resonator. In this chapter, various 7T MR experiments and numerical studies are conducted to further evaluate the anthropomorphic heterogeneous head phantom as a resourceful tool in MR testing at high fields. Several preliminary experiments were conducted to characterize various RF coil designs (RAPID coil (171-173), TEM resonator (62, 101, 174), and Tic-Tac-Toe (TTT) coil (55)) that have shown successful 7T neuroimaging.

The development of RF coils and arrays can be a challenge at 7T MRI. Before RF coils are used in human studies, several EM and thermal characterization must be performed to evaluate RF coil designs for performance and RF safety. Chapter 4.0 discussed EM and thermal measurements using the designed phantom and TEM resonator at 7T. Government limitations in RF coil designs regulate thermal measurements. Many works (14, 24, 107, 143, 175, 176) have

used fiber optic probes to monitor the temperature rise in various experimental thermal MR measurements to conduct a more accurate temperature rise measurements. While fiber optic probes have proven to be useful, they are only capable of reading the localized temperature rises. While global temperature measurement methods are available, preliminary RF heating measurements and assessments will be conducted in this chapter using fiber optic temperature probes.

In this chapter, the anthropomorphic heterogeneous head phantom is used to perform preliminary electromagnetic and thermal characterization in each RF coil by assessing the S-parameters, RF homogeneity, and thermal heating. Workbench analysis characterizes the S-parameters to assess the transmission and reflection between the various ports within each RF coil. RF and thermal simulations used discretized FDTD by applying Maxwell's equations in order to assess RF fields (electric and magnetic) and Pennes's Bioheat equation to assess thermal heating. The RF and thermal simulations are validated through an experimental B_1^+ mapping method and experimental temperature rise measurements using fiber optic probes (Subsection 5.3.2.1). Note that the experimental temperature rise measurements were conducted using the experimental anthropomorphic heterogeneous head phantom and TTT coil only. In addition, the thermal simulations (Subsection 5.3.3.1) compared temperature rise in two thermal models: 1) the perfusionless anthropomorphic heterogeneous head phantom model and 2) perfused segmented *in-vivo* human head model. The results of this chapter further assess the hypothesis of Specific Aim 2.

5.2 MATERIALS AND METHODS

The methodology covered within this chapter discusses methods used to assess the hypothesis of Specific Aim 2. This section outlines the organization of this chapter by detailing the experimental setup, MR and RF equipment, RF and thermal simulations, and experimental EM and thermal measurements.

5.2.1 Experimental Studies of Electromagnetic and Thermal Characterization

5.2.1.1 Experimental Setup

5.2.1.1.1 MR Magnet and RF Experimental Setup

Equipment at the RF Research and 7T Facilities at the University of Pittsburgh was used to perform RF and heating experiments. The UHF facility offered a passively shielded Siemens MAGNETOM® (Siemens Healthcare, Erlangen, Germany) 7T whole-body scanner. The machine offers 60.0-cm horizontal bore that is equipped with eight transmission channels. The scanner system operates on Siemens syngo MR VB17A.

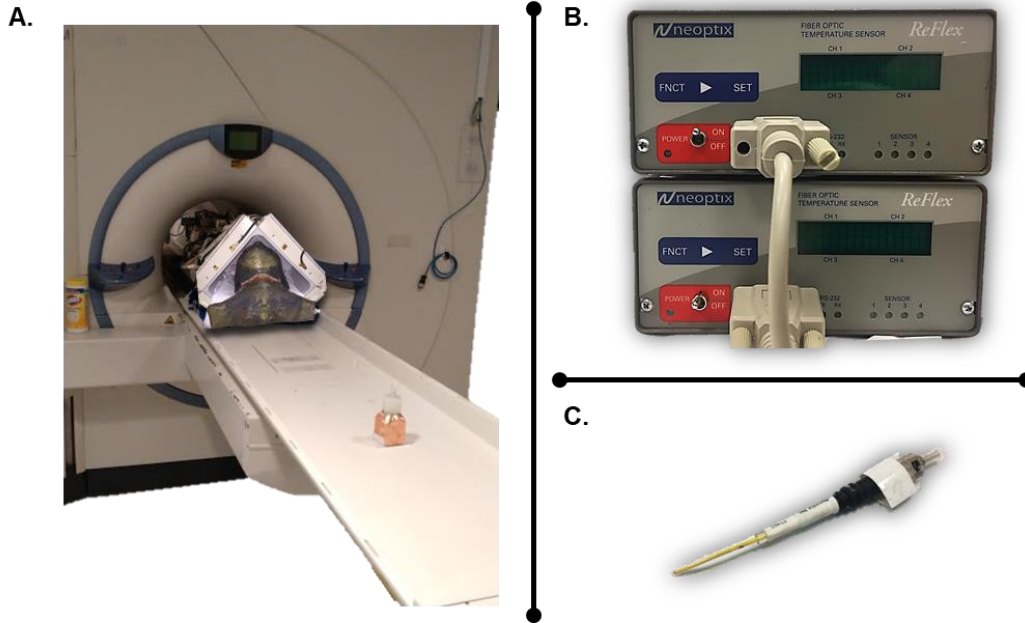


Figure 5.1. Experimental RF Heating Setup. A) RF coil, Anthropomorphic Head Phantom, and ambient control phantom setup on the MR scanner, B) two Neoptix™ ReFlex™ boxes with capabilities to read eight fiber optic probes, and C) example of Neoptix™ T₁ probes.

5.2.1.1.2 Experimental Network Analyzer

Scattering parameters were obtained to characterize the experimental anthropomorphic heterogeneous head phantom loaded in each experimental RF coil using an experimental network analyzer (Agilent E5602A, Keysight Technologies, Santa Rosa, California).

5.2.1.1.3 Neoptix™ Fiber Optic T₁ Probes and Reflex™

The experimental temperature was measured with fiber optic temperature probes (Neoptix™ (A Qualitrop Company)) (shown in Figure 5.1.C) with a 1s temporal resolution. The fiber optic temperature probes are attached to the Neoptix™ ReFlex™ (accuracy of $\pm 0.8^{\circ}\text{C}$) box (shown in Figure 5.1.B) which measures the temperature of each probe and is later visualized and recorded through Neoptix™ temperature software, Neoptix™ OptiLink Software.

5.2.1.1.4 *Experimental RF Coils*

This study provides electromagnetic and thermal characterization with the experimental anthropomorphic heterogeneous head phantom (18) loaded within various experimental 7T RF coils (TEM resonator, loop-based coil (RAPID), and TTT coil). Each experimental RF coil has a different design that is shown in Figure 5.2 and described below.

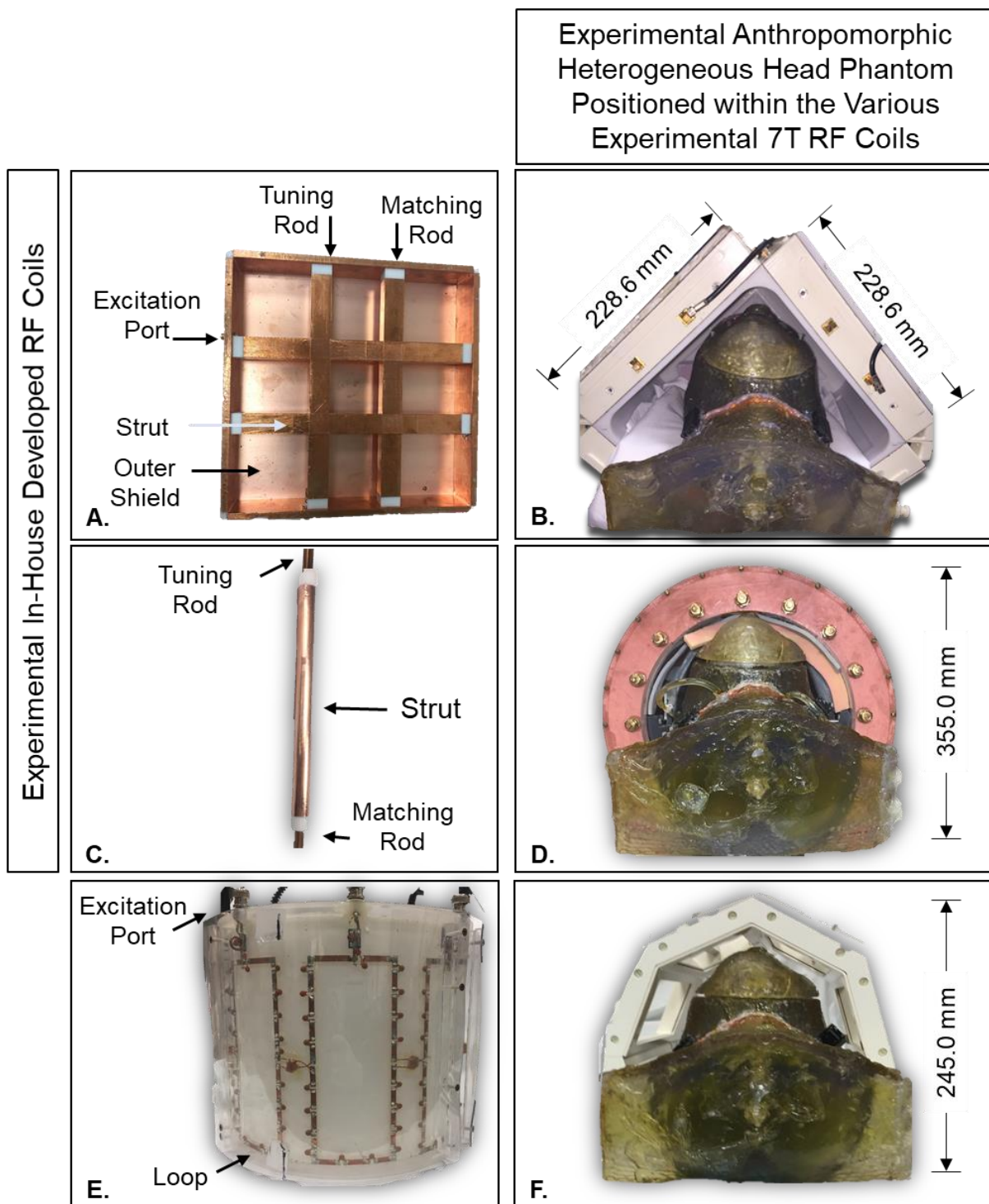


Figure 5.2. Dimensions and Placement of the Anthropomorphic Heterogeneous Head Phantom Positioned in Experimental Various 7T RF Coils.

5.2.1.1.4.1 Experimental 16ch–Tx/32ch-Rx TTT coil

An experimental in-house developed 16ch–Tx/32ch-Rx TTT coil (17, 55, 177-179) is the head coil in the TTT array and coil family (55, 59, 180, 181) and it comprises of four individual coil elements (shown in Figure 5.2.A) that yield a total of 16-channels (shown in Figure 5.2.B). The 16-channel transmit array is configured to use a combination of four-way (Werlatone® Inc., D11020-20, Patterson, New York, USA) and two-way (Werlatone® Inc., D11027-10, Patterson, New York, USA) splitters to produce one main channel that connects directly to the scanner's combined mode. Each channel is driven by customized RF shimming using pseudo modes (177) that generates the TTT's quadrature excitation.

The TTT coil (55) was designed on a 3D printed polycarbonate (PC) former using the Fused Deposition Modelling (FDM) (Redeye, Stratus USA) method to case the coil based on the design cross-pole antennas (55, 59, 180, 181). A picture of the entire coil (including the Tx/Rx arrays) is shown in Figure 5.2.B. The 2 x 2 cross-pole TTT coil (228.6 mm x 228.6 mm) has eight square-shaped copper (McMaster-Carr, USA) transmission lines (shown in Figure 5.2A). A PC support (dielectric constant = 2.4, $\sigma = 0.0$ S/m) is used as a support for the inner rods and outer struts. The struts are surrounded with an 8.0 μm thick single-layered copper sheet (Polyflon, Germany). The RF coil shielding (178) was designed with unique slits to minimize the eddy currents and ghosting (178) in the coil and was verified through echo planar imaging (EPI) applications. The RF excitation ports' center coaxial pin is connected to the strut and grounded by a connection to the RF shield. The 2 x 2 TTT array is tuned and matched by pushing the square-shaped copper rods in and out of the outer struts. Each coil was tuned to 297.2 MHz and matched to 50.0 Ω by adjusting the gap between the rods and validated through the scattering parameters

using a vector network analyzer (Agilent E5602A, Keysight Technologies, Santa Rosa, California). Four sets of the 2 x 2 TTT arrays are comprised together to generate the coil with a top shield. A 32-channel receive array was designed and is located within the center of the coil.

5.2.1.1.4.2 Experimental 16-strut/4-port TEM Resonator

An experimental in-house developed 16-strut/4-port TEM resonator (62) with a centered and fixed 14-channel receive (101) is used as shown in Figure 5.2.D. This RF coil was used in Section 4.2 to validate the numerical studies of the numerical phantom models loaded within the numerical TEM resonator. The experimental 16-strut/4-port TEM resonator was constructed using an acrylic cylinder with a 279.4 mm inner diameter, 355.6 mm outer diameter, and 228.6 mm length dimensions and two circular rungs. The 16-elements (Figure 5.2.C) are separated equally 22.5° apart around the inside of a thin copper shield and the acrylic cylinder. The inner rods have a 6.8 mm diameter and were used to tune and match the TEM resonator.

5.2.1.1.4.3 Experimental RAPID Biomed Coil

A commercially available experimental 8-element RAPID Biomed coil (RAPID Biomedical GmbH, Würzburg-Rimpar, Germany) (173) was used in the combined mode and shown in Figure 5.2.F. The dimensions of the coil are 235.0 mm for the inner diameter and 245.0 mm for the outer diameter. An 8-channel loop-based coil (Figure 5.2.E) was used to obtain the scattering parameters due to the RAPID coil being a commercial coil with the inability to obtain scattering parameters from individual channels.

5.2.1.1.5 *Experimental Phantoms*

5.2.1.1.5.1 Experimental Anthropomorphic Heterogeneous Head *Phantom Generation*

Chapter 3.0 and work (18) described the fabrication of the experimental anthropomorphic heterogeneous head phantom. However, the mimicked-tissues development was involved in creating gels for stable RF heating instead of using liquids that might offer incorrect readings to due diffusion. To achieve the desired constitutive parameters of Table 3.1, various concentrations of distilled water, polyvinylpyrrolidone (PVP) powder (ultra-high molecular weight, Sigma-Aldrich, St. Louis, Missouri, USA), sodium chloride (NaCl) (Fisher Scientific), copper sulfate (CuSO_4) (Fisher Scientific), sodium azide (NaN_3) (Sigma-Aldrich, St. Louis, Missouri, USA), and TMDOTMA⁻ (Sigma-Aldrich, St. Louis, Missouri, USA). PVP was used to lower the permittivity and preserves the signal instead of using sucrose (182). NaCl increased the conductivity and NaN_3 is used as a preservative within each compartment to prevent the gel from molding. CuSO_4 is used to adjust the relaxation time of water to an acceptable T1 for the given tissue. TMDOTMA⁻ is used as a temperature sensitive contrast agent.

5.2.1.1.5.2 Experimental Ambient Control Phantom

An ambient control phantom (dielectric constant = 79.0, $\sigma = 0.0 \text{ S/m}$) was placed 900.00mm from the experimental TTT coil within the bore (as shown in Figure 5.1.A), and RF shielding was placed on the experimental ambient phantom to deflect any possible RF inside of the bore during the MR scan.

5.2.1.2 Experimental Bench Measurements using an Experimental Network Analyzer

The experimental anthropomorphic heterogeneous head phantom was characterized by the reflection coefficient (S_{xx}) and neighboring coupling (S_{xy}) of the experimental 16-strut/4-port TEM resonator, 16ch–Tx/32ch–Rx TTT coil, and the 8-channel loop-based coil. Two channels were chosen for a demo analysis in each experimental RF coil to highlight the differences in loading between the RF coils that might occur using the experimental anthropomorphic heterogeneous head phantom.

5.2.1.3 Experimental B_1^+ Mapping Measurements in Each Experimental RF Coil

Before RF heating, experimental B_1^+ maps were acquired to compute the voltage required to produce a 180° . Experimental B_1^+ field mapping was acquired on the experimental perfusionless anthropomorphic heterogeneous head phantom on the experimental 16-strut/4-port TEM resonator, 16ch–Tx/32ch–Rx TTT coil, and RAPID coil. Experimental B_1^+ field mapping was performed using the saturated TurboFLASH (38) sequence with the following parameters: FOV: $64.0 \times 64.0 \text{ mm}^2$; TE: 1.16 ms; TR: 2000 ms; FA: 6° ; BW: 1502 MHz/px; Resolution: $3.1 \times 3.1 \times 2.0 \text{ mm}^3$; and 6 flip angles. Using ITK-Snap (134), the ROIs were determined and manually segmented for post-processing.

5.2.1.4 Experimental RF Heating Measurements Using the Experimental Anthropomorphic Heterogeneous Head Phantom Loaded within the TTT Coil at 7T (Preliminary Results)

5.2.1.4.1 RF Heating Experiment Setup

RF heating measurements were performed to quantify the temperature rise inside the experimental perfusionless anthropomorphic heterogeneous head phantom in the experimental 16ch–Tx/32ch–Rx TTT coil at 7T. The probe locations were chosen arbitrarily to not favor the SAR and temperature distribution within a specific experimental 7T RF coil. The temperature probes are listed in Table 5.1 and shown in Figure 5.3.

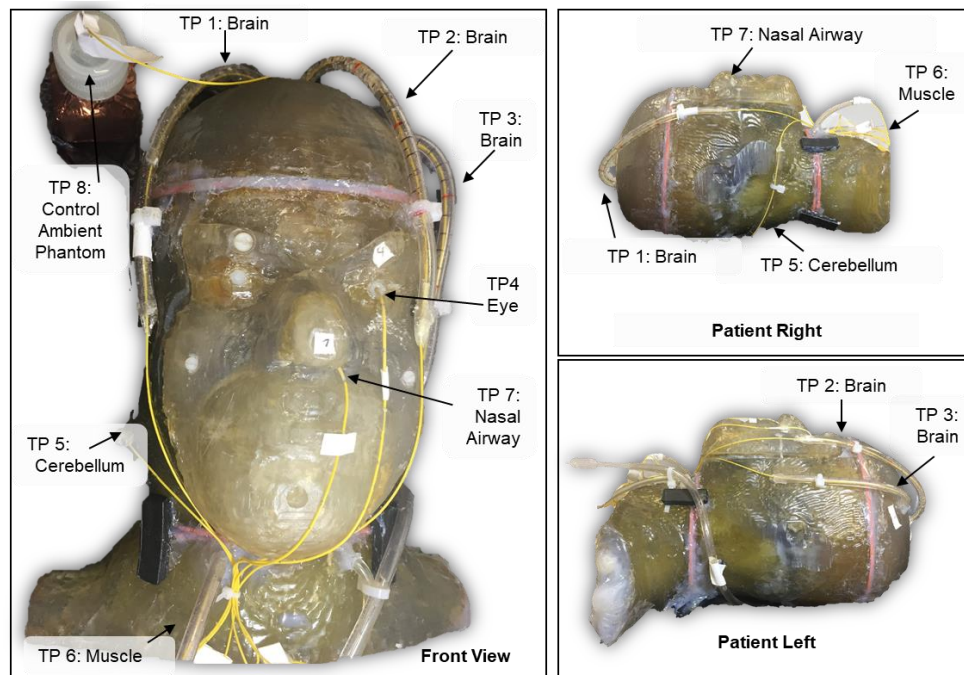


Figure 5.3. Eight Temperature probe locations in the Experimental Perfusionless Anthropomorphic Heterogeneous Head Phantom (shown on SLA Resin) and the ambient control phantom.

A total of eight probes were used for the experimental temperature measurements. Seven fiber optic probes were used in the experimental perfusionless anthropomorphic heterogeneous head phantom where three were in the brain, one in the left eye, one in the cerebellum, one in the neck, and one in nasal airway. One probe was placed in the ambient control phantom (TP 8 referenced in Figure 5.3) that was wrapped in RF shielding to measure the ambient temperature and reflect the radiated RF energy. The temperature probes were calibrated to have accurate temperature readings of the MR scanner room.

Table 5.1. Temperature Probe Locations within the Experimental Perfusionless Anthropomorphic Heterogeneous Head Phantom highlighting the location, tissue classification, and probe depth from the exterior locations in Figure 5.3.

Temperature Probe (TP) Label	Physiological Phantom Location	Depth of Probe (mm)
1	Brain (Left-Posterior)	80
2	Brain (Right-Anterior)	70
3	Brain (Oblique/ Right)	110
4	Eyes (Center-Left)	15
5	Cerebellum (Right)	90
6	Muscle (Right in Neck)	50
7	Nasal Airway (Phantom Left)	50
8	Ambient (Control Phantom)	N/A

The experimental perfusionless anthropomorphic heterogeneous head phantom was well insulated inside of the coil with blue foam (Ultra-Conformable Polyurethane Blue Foam Sheet, $\frac{3}{4}$ " thick, 12"x12", McMaster-Carr, Cleveland, OH, USA) while in the supine position as shown Figure 5.2.B.

5.2.1.4.2 *Experimental RF Heating Measurements*

Before RF heating, the experimental coil and the experimental perfusionless anthropomorphic heterogeneous head phantom were placed inside of the bore overnight to achieve equilibrium within the MR environment. 18.00°C was the ambient temperature reading inside of the bore.

While turning the gradient coils off, the experimental RF heating measurements are designed to measure the experimental temperature rise due to RF power absorption alone in the experimental perfusionless anthropomorphic heterogeneous head phantom. The reference voltage delivered (260.0 V) was based on achieving an 11.7 μ T mean B_1^+ field intensity in the experimental perfusionless anthropomorphic heterogeneous head phantom (experimental B_1^+ measurement shown in Figure 5.8). The experimental RF power is computed from acquiring the experimental mean B_1^+ field intensity and knowing the various parameters from the MR sequence.

A rectangular RF pulse is applied for an intense 30 minutes with an 11.1% duty cycle, 10 ms pulse width. Experimental RF heating is performed with the following MR sequence parameters: Sequence: FID Heating, TA: 30 min, BW: 10kHz/px, PW: 10ms, TR: 90ms, Voltage: 150V, FA: 836°, TE: 3.6ms, Averages: 4096. The MR system's power recordings were obtained through software and power logs.

During post-RF heating, the experimental TTT coil and the experimental perfusionless anthropomorphic heterogeneous head phantom were cooled. The experimental absolute temperature changes were computed against the ambient temperature measured in the ambient control phantom in comparison to the experimental temperature rise in various compartments of

the experimental perfusionless anthropomorphic heterogeneous head phantom. These results are shown in Figure 5.9.

5.2.2 Numerical Studies of Electromagnetic and Thermal Characterization

5.2.2.1 RF Simulations

This subsection describes the numerical RF coils and head models required to develop the RF models shown in Figure 5.4 via sub-subsections 5.2.2.1.1 to 5.2.2.1.2. The FDTD method (70) was used through a validated in-house numerical simulation software (13, 59, 71, 101, 132), with an accurate transmission line model for the excitation mechanism, generates output time-domain and frequency domain data. The in-house software implements the finite difference equation of Maxwell's equations. Each model uses an isotropic spatial resolution of $\sim 1.59 \text{ mm}^3$ and temporal resolution of $\sim 3.00 \text{ ps}$. Each numerical EM head model was placed in the supine position to correspond to the positioning of the experimental anthropomorphic heterogeneous head phantom model in Figure 5.2.B and D. The numerical EM head models were positioned such that the corpus callosum in the brain was asymmetrically centered along the z-direction as shown in Figure 5.4.B and D. Each numerical RF coil model was tuned and matched to 297.2 MHz. A first-order differentiated Gaussian pulse was used to excite the numerical RF coil model and head models. The pulse has a 5.8 ns period that ran until achieving a stable steady state solution - 100,000-time steps.

The output data is read by MATLAB (The MathWorks, Inc., Natick, MA, USA) in order to produce the electric and magnetic fields. The RF simulations are shown through the numerical

B_1^+ distribution and SAR distribution. The methodology to compute numerical B_1^+ and SAR calculations is covered in sub-subsection 5.2.2.1.3.

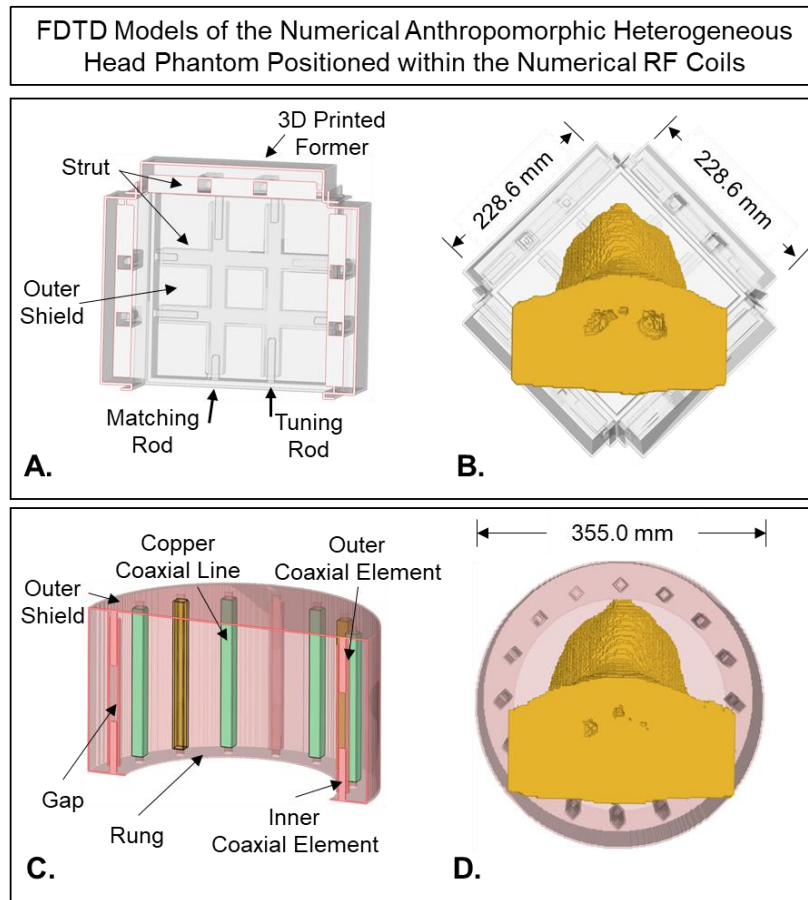


Figure 5.4. Numerical Coil Description and FDTD Models of the Anthropomorphic Heterogeneous Head Phantom model loaded in the in-house developed RF Coils. The 16ch–Tx/32ch–Rx TTT Coil model with the A) Schematic of the TTT Coil (without the Receive Array) model and B) loaded Anthropomorphic Heterogeneous Head Phantom model. The 16-strut/4-port TEM Resonator with the C) Schematic of the TEM Resonator (without the Receive Array) model and D) loaded Anthropomorphic Heterogeneous Head Phantom model.

5.2.2.1.1 Numerical RF Coils

5.2.2.1.1.1 Numerical 16-strut/4-port TEM Resonator Model

Sub-subsection 4.2.2.1 described the numerical modeling of the 16-strut/4-port TEM resonator model shown in Figure 5.4.C-D. The numerical modeling of this coil matches the design, construction, and dimensions of the experimental 16-strut/4-port TEM resonator detailed in sub-subsection 5.2.1.1.4.2.

5.2.2.1.1.2 Numerical 16ch–Tx/32ch–Rx TTT Coil Model

The numerical 16ch–Tx/32ch–Rx TTT coil modeling is shown in Figure 5.4.A-B. The numerical modeling of this coil matches the design, construction, and dimensions of the experimental 16ch–Tx/32ch–Rx TTT coil detailed in subsection 5.2.1.1.4.1. The coil is optimized by combining all 16-channels using the RF shimming tool (in Appendix C) to produce quadrature excitation and a bright center. The coil was tuned and matched by loading the coil with the Virtual Family v1.0 (31) Duke head to shoulder model. The coil was not retuned for each RF load.

5.2.2.1.1.3 Numerical RAPID Model

The RAPID coil was not modeled because it is a commercial RF coil and its RF configurations are not accessible.

5.2.2.1.2 Numerical Electromagnetic Head Models

Two numerical EM head models are used in this particular study namely: 1) a segmented *in-vivo* human head model and 2) an anthropomorphic heterogeneous head phantom model. The constitutive properties of the models were cited in works (31, 98, 153, 159-164) including the Virtual Family v1.0 Duke (31, 165) and were reflected in the previous chapter in Table 4.12. The computational domain of all numerical EM head models includes the anatomy of the entire head, neck, and upper shoulders.

5.2.2.1.2.1 Numerical Segmented *In-Vivo* Human Head Model

The numerical segmented *in-vivo* human head model is the numerical EM model of the *in-vivo* volunteer in Chapters 3.0 and 4.0. The model was generated from the acquired 3T dataset shown in Figure 3.2 through automatic segmentation using iSeg (ZMT Zurich MedTech AG, Zurich, Switzerland). The numerical head model consists of 10 group classified tissues namely: air, bone, brain (WM/GM), brainstem, cerebellum, cerebrospinal fluid (CSF), eyes, fat, muscle, and skin. The constitutive parameters were weighted averages of the tissues in the respective physiological location from the head to the upper shoulders. These physiological tissues are listed in Table 4.12 in the general biological tissue classification column which corresponds to the phantom tissue classification column. The numerical segmented *in-vivo* human head model was scaled to $\sim 1.59\text{mm}^3$ isotropic spatial resolution containing $252*252*287$ Yee-cells in the respective x, y, and z-direction.

5.2.2.1.2.2 Numerical Anthropomorphic Heterogeneous Head Phantom Model

The numerical anthropomorphic heterogeneous head phantom model is the numerical EM model of the experimental anthropomorphic heterogeneous head phantom. The numerical head phantom model was made in two steps. The first step involved its generation from the acquired 3T dataset shown in Figure 3.2 through automatic segmentation using iSeg. Next, the numerical head phantom model was merged with the STL file that contains the SLA resin boundaries between the tissues. The merging of the model components involved the alignment of anatomical landmarks. This numerical head phantom model consists of eight group classified tissues namely: air, brain (WM/GM), brainstem, cerebellum, CSF, eyes, muscle, and the remainder volume being a combination of the fat, bone, and skin (SLA Resin). The model comprises of the head to upper shoulders. All tissues except the SLA Resin have the same constitutive properties of the numerical segmented *in-vivo* human head model and these properties are listed in Table 4.12. The numerical anthropomorphic heterogeneous head phantom was scaled to $\sim 1.59 \text{ mm}^3$ isotropic spatial resolution containing $252 \times 252 \times 287$ Yee-cells in the respective x, y, and z-direction.

5.2.2.1.3 *FDTD Calculations of the B_1^+ Field and SAR*

The numerical EM calculations were performed primarily in the TTT coil. The TEM coil was only used to validate the SLA resin conductivity.

5.2.2.1.3.1 FDTD Calculations of the B_1^+ Field

The B_1^+ field intensity per volt is obtained using the simulated input pulse amplitude, which is determined by the Fast Fourier transform (FFT) of the Gaussian pulse in the time domain at ~ 297.2

MHz. The numerical B_1^+ distribution was scaled for 1-Watt of input power and was calculated with the same calculations referenced in sub-subsection 4.2.2.1.3. The numerical B_1^+ calculation and distribution were performed only on the TTT coil to validate the measured B_1^+ within the experimental anthropomorphic heterogeneous head phantom. The numerical B_1^+ calculations were not performed using the TEM resonator.

5.2.2.1.3.2 FDTD Calculations of the SAR

The numerical SAR is computed using equation (4.2). The numerical SAR was normalized per a continuous mean B_1^+ field intensity of $2\mu\text{T}$ to produce a 180° flip angle for a 1ms rectangular RF pulse. The numerical SAR calculations performed with the TEM resonator were used only to validate the SLA resin shown in Figure 5.5.B-C. The numerical SAR was calculated for the numerical TTT coil using the anthropomorphic heterogeneous head phantom model only. The numerical SAR distribution was scaled to the peak SAR in the model.

5.2.2.2 Thermal Simulations

This section describes the thermal simulation methods and the RF coils and head models required to develop the numerical thermal models shown in Figure 5.4.

5.2.2.2.1 *RF Coils*

5.2.2.2.1.1 Numerical 16-strut/4-port TEM resonator Model

Numerical thermal modeling was not performed using the 16-strut/4-port TEM resonator.

5.2.2.2.1.2 Numerical 16ch–Tx/32ch-Rx TTT coil model

Numerical thermal modeling was performed with the numerical 16ch–Tx/32ch-Rx TTT coil model loaded with both head models. The computational domain of both head models includes the anatomy of the entire head to shoulders. The coil is driven as described in Subsection 5.2.2.1.1.2 to perform the thermal simulations.

5.2.2.2.1.3 Numerical RAPID Coil

Numerical thermal modeling was not performed using the RAPID coil due to it being a commercial RF coil with unavailable design configurations.

5.2.2.2.2 *Numerical Thermal Head Models*

Two numerical thermal models are used in this particular study namely: 1) a perfused 10-tissue segmented *in-vivo* human head model and 2) a perfusionless anthropomorphic heterogeneous head phantom model. The thermal properties were based on the thermal and constitutive properties cited in works (31, 98, 153, 159-164) including the Virtual Family v1.0 Duke (31, 165) and were reflected in the previous chapter in Table 4.12. Numerical thermal simulations were conducted

using two of the three RF coils (TEM and TTT). The numerical thermal models are loaded within the RF coils as shown in Figure 5.4.B and D.

5.2.2.2.2.1 Numerical Segmented *In-Vivo* Human Head Model

The perfused segmented *in-vivo* human head model is composed of thermal parameters and constitutive parameters. All 10 classified tissues have a corresponding thermal parameter listed in Table 4.12. The thermal parameters were weighted averages of the tissues in the respective physiological location from the head to the upper shoulders and are visualized.

5.2.2.2.2.2 Numerical Anthropomorphic Heterogeneous Head Phantom Model

The numerical perfusionless anthropomorphic heterogeneous head phantom model is composed of thermal parameters and constitutive parameters. All eight classified tissues have a corresponding thermal parameter listed in Table 4.12. The thermal parameters were weighted averages of the tissues in the respective physiological location from the head to the upper shoulders and are visualized in Figure 4.21.B

Since the experimental perfusionless anthropomorphic heterogeneous head phantom tissues were fabricated with agar for thermal testing, the following thermal parameters were used for all fillable tissues. The specific heat capacity was set to 4200.00 J/ kg °C, which is the specific heat of the distilled water mixed with agar. The thermal conductivity was set to 0.498 J/m s °C. Due to there being no perfusion and basal metabolic rate in the experimental perfusionless

anthropomorphic heterogeneous head phantom, these parameters were set to for all specified fillable tissues. The thermal parameters of the SLA resin were only known for the thermal conductivity $0.17 \text{ J/m s } ^\circ\text{C}$. The specific heat was not known for the SLA resin and was set to the specific heat of Teflon, $1050.00 \text{ J/ kg } ^\circ\text{C}$.

5.2.2.2.2.3 Numerical Thermal Simulations Method

The numerical thermal simulations were performed using PBHE implemented with the FDTD method. The numerical thermal simulations used the PBHE with the T_b set to 37.00°C in the numerical perfused segmented *in-vivo* human head model and the numerical perfusionless anthropomorphic heterogeneous head phantom model set to 18.00°C . The thermal boundary conditions were set to $20 \text{ J/m}^2 \text{ s } ^\circ\text{C}$ (75). The numerical perfused segmented *in-vivo* human head model is used to determine how similar the thermal characterization of this model is to the numerical perfusionless anthropomorphic heterogeneous head phantom and to demonstrate the impact of perfusion on the temperature measurements.

Initially, the numerical TTT coil and the numerical thermal head models were run to reach steady-state as shown in Figure 4.23. The numerical perfused segmented *in-vivo* human head model's steady-state was reached in 56 minutes, and the numerical perfusionless anthropomorphic heterogeneous head phantom model was at steady-state since its temperature was the same as the MR room temperature – 18.00°C . Next, RF heating was applied with a specified power for an intensive 30 minutes to the numerical perfusionless anthropomorphic heterogeneous head phantom model and the numerical segmented *in-vivo* human head model loaded within the numerical TTT coil. The power is equivalent to the product of the scaled net input power and 11.1% duty cycle.

The net input power at the RF coil's plug was extracted from the scanner's RF power log. The numerical thermal heating calculations are described in sub-subsection 5.2.2.2.3.

5.2.2.2.3 *FDTD Calculations of Temperature Elevation*

The numerical thermal calculations were performed to obtain the temperature elevations (see sub-subsection 4.5.2.1.3) within both models using TTT coil for a preliminary comparison. The numerical SAR (see sub-subsection 5.2.2.1.3.2) was used as the input heat source for each model. The numerical and experimental temperature measurements are compared and shown in Figure 5.9 for the numerical and experimental perfusionless anthropomorphic heterogeneous head phantom. A numerical comparison between both thermal head models is shown in Figure 5.11 to offer a prediction of how similar the numerical thermal characterization in the perfusionless anthropomorphic heterogeneous head phantom model is to the perfused segmented *in-vivo* human head model.

5.3 RESULTS

5.3.1 Validation of Conductive SLA Resin

Figure 5.5.C shows the experimental temperature rise on the SLA resin material of the experimental anthropomorphic heterogeneous head phantom (151) and proves its conduction. To reach equilibrium, the experimental perfusionless anthropomorphic heterogeneous head phantom, and the experimental 16-strut/4-port TEM resonator remained inside the magnet bore overnight.

The temperature probes were strategically chosen (Figure 5.5.A, D) and placed on predicted hot-spots, localized areas of high RF energy, from the numerical modeling (Figure 5.5.B).

A less power intensive RF heating sequence was used to determine a simple conduction assessment of the SLA resin using the experimental 16-strut/4-port TEM resonator. The experimental RF heating parameters are as follows: Sequence: FID Heating; TR: 3500ms; FA: 3600°; Averages: 4096; Reference Voltage: 300V; TA: ~5.5 hours.

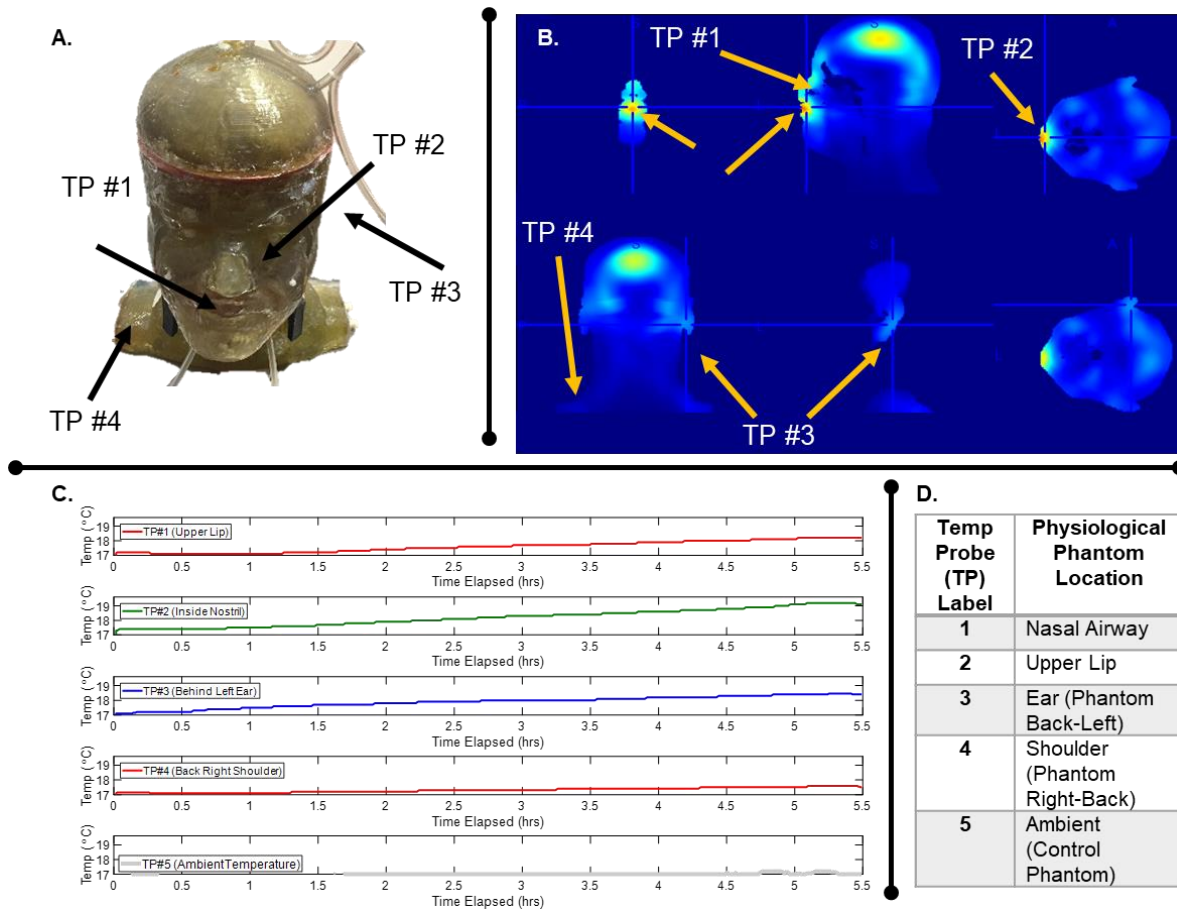


Figure 5.5. The SLA Resin by DSM Somos® is used to show the experimental anthropomorphic head phantom in (A), and the yellow arrows indicate the location of the probes. Various views of the numerical SAR model for the phantom are chosen to highlight local SAR points in (B). C.) The temperature rise of the SLA Resin that is indicated for 5.5 hours. The ambient temperature is captured in the last plot. D.) Temperature probe locations.

Figure 5.5.C illustrates the results of the experimental temperature rises in all probes located in Figure 5.5.A. The SLA resin material is heating considerably, and thus, we can conclude that the phantom material is conductive. The experimental temperature change is highest in the nasal passage with a rise of 2.00°C. There is an equal temperature rise on the upper lip of 1.10°C and behind the ear 1.30°C. There was minimal temperature rise in the shoulders. The averaged tissue in the fat, bone, and skin offer conductivity of 0.1663 S/m and density of 1223.49 kg/m³. While it would be ideal to have a conductive skin layer, the SLA resin shows promise in being a useful tool for MR purposes.

5.3.2 Verification of Experimental Bench Measurements

A workbench analysis is shown in Figure 5.6 to highlight the loading of the experimental anthropomorphic heterogeneous head phantom inside of the different experimental RF coils designs.

Chapter 4.0 summarized that the reflection coefficient varies in value based on the loaded experimental phantom's geometry and media within the experimental 16-strut/4-port TEM resonator. These results are also shown in Figure 5.6.A. In addition, these results demonstrated that the reflection coefficient and coupling of the experimental anthropomorphic heterogeneous head phantom were relatively similar to the *in-vivo* volunteer's bench results in Chapter 3.0.

Anthropomorphic Heterogeneous Head Phantom S-parameters and S-Matrix

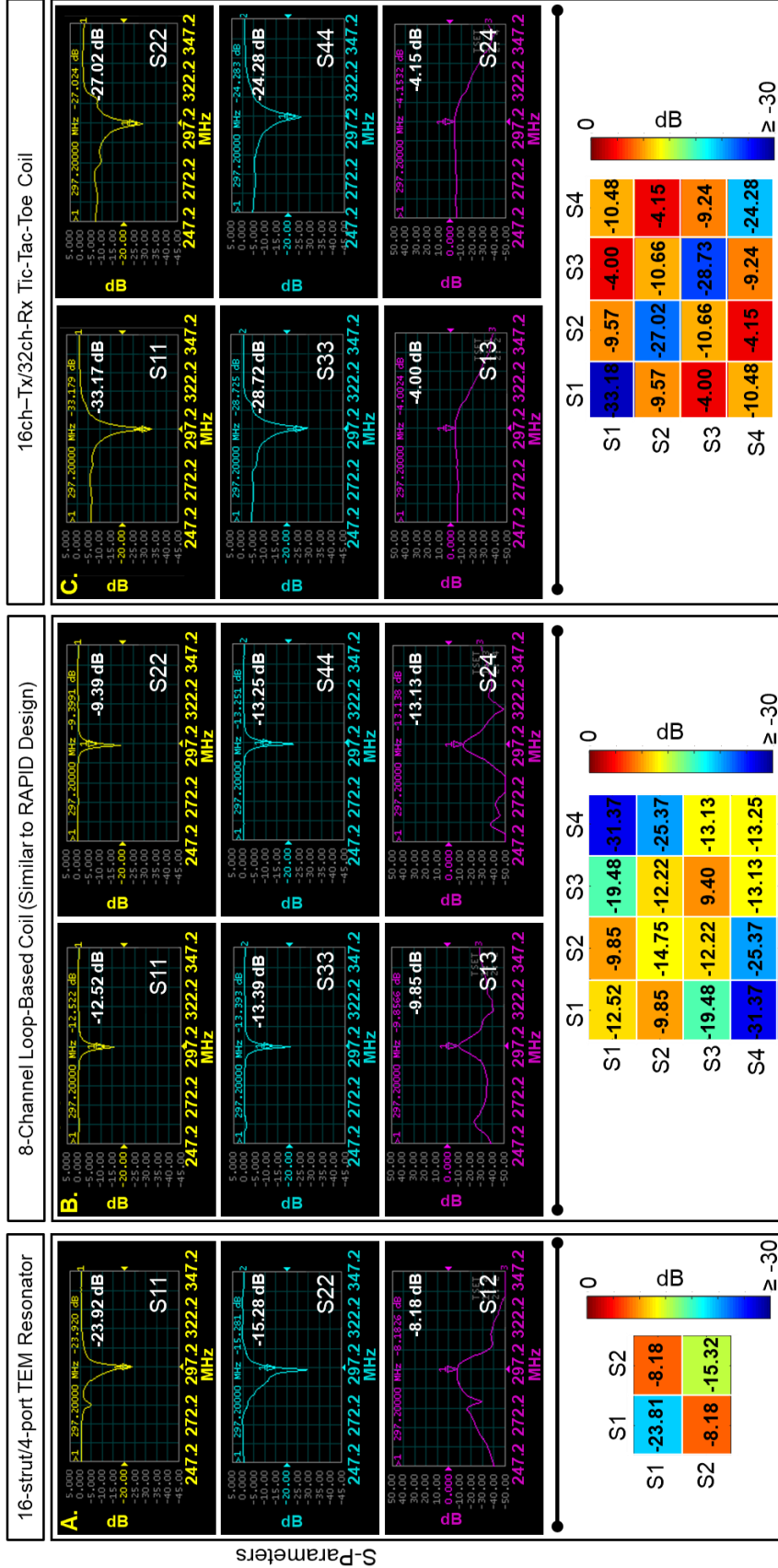


Figure 5.6. Comparison of Experimental Anthropomorphic Heterogeneous Head Phantom loading using the Scattering Parameters of three Experimental RF Coils. The anthropomorphic heterogeneous head phantom loaded within A.) an experimental 16-strut/4-port TEM resonator, B.) an experimental 8-channel loop-based coil (similar to the RAPID commercial coil's design), and C.) an experimental 16ch-Tx/32ch-Rx TTT coil.

The experimental 8-channel loop-based coil (Figure 5.2E) is used to observe the S-parameters of the RAPID coil since the RAPID coil is a commercial coil that was not opened. The 8-channel loop-based coil has a high coupling for the experimental anthropomorphic head phantom (Figure 5.6B) in comparison to the other two coils, while the TEM resonator and TTT have a much lower coupling for neighboring channels. In contrast, the reflection coefficient and matching of each channel are lower in amplitude (dB) in the 8-channel loop-based coil for each load in comparison to the TEM resonator and TTT coil.

While all the coils were tuned to *in-vivo* subjects, Figure 5.6 shows that the coupling and reflection coefficient amplitudes of the TTT coil is still optimal using the experimental anthropomorphic heterogeneous head phantom. Due to its high coupling nature, the TTT coil is load insensitive to any of anthropomorphic human head loads.

5.3.1 Experimental B_1^+ Field Comparison Using the Experimental Anthropomorphic Heterogeneous Head Phantom Centered in Various Experimental RF Coils

RF field homogeneity is a part of an RF coil's design consideration. The experimental B_1^+ field comparison was verified using each experimental RF coil. The results shown in Figure 5.7 demonstrates the RF homogeneity qualitatively that different coil geometries produce. The TTT coil is the most homogeneous experimental RF coil presented and is supported through detailed experimental B_1^+ field profiles in Figure 5.7. The experimental 16-strut/4-port TEM resonator and experimental RAPID coil often have low B_1^+ field intensities in certain spots which are shown in Figure 5.7. The low field values produce either low or no MR signal. The low fields are located in the temporal lobe, cerebellum, and upper parietal brain of the head phantom. In contrast, the

loss in these physiological brain regions is present with MR signal in the RAPID coil and TEM Resonator.

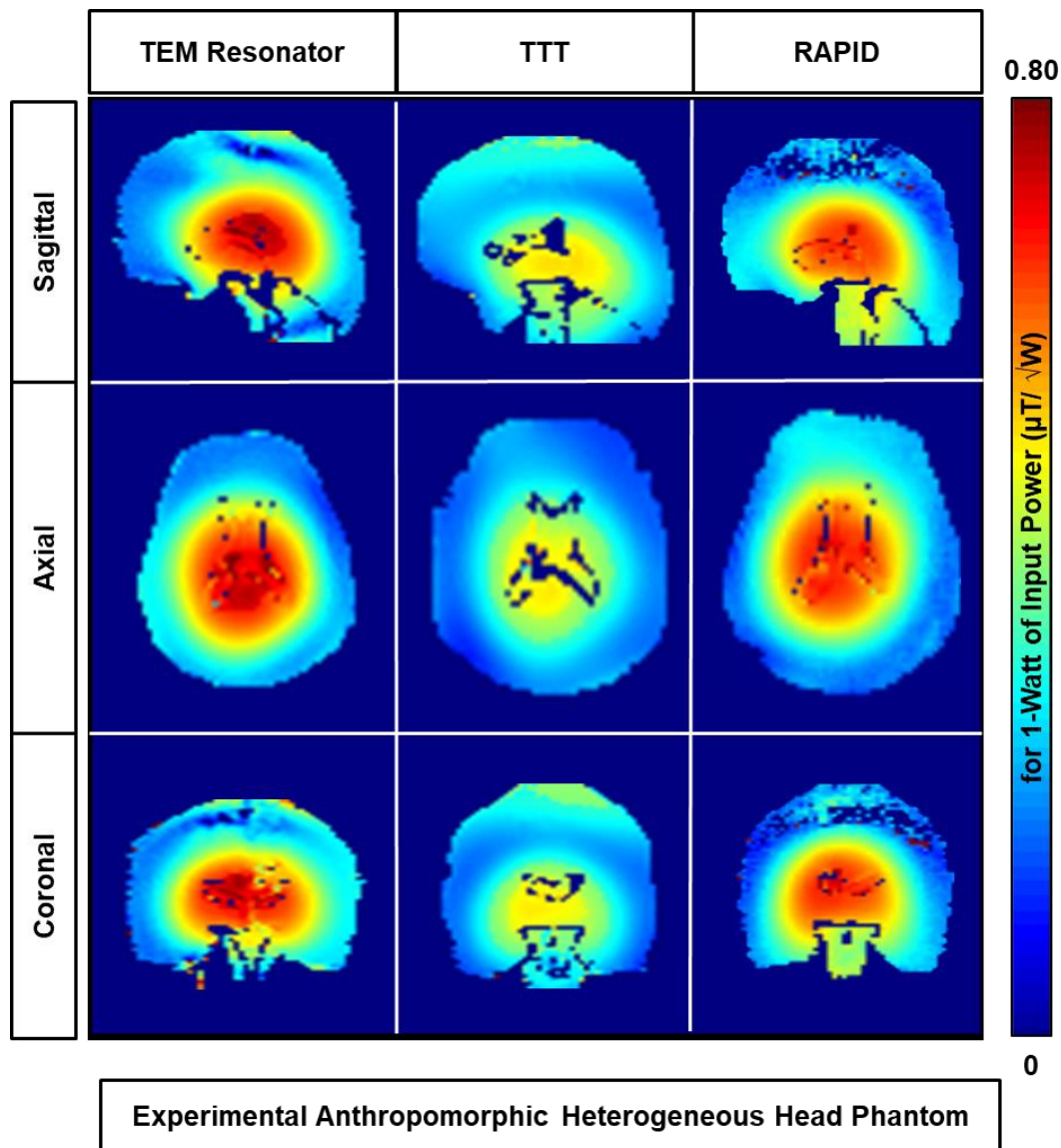
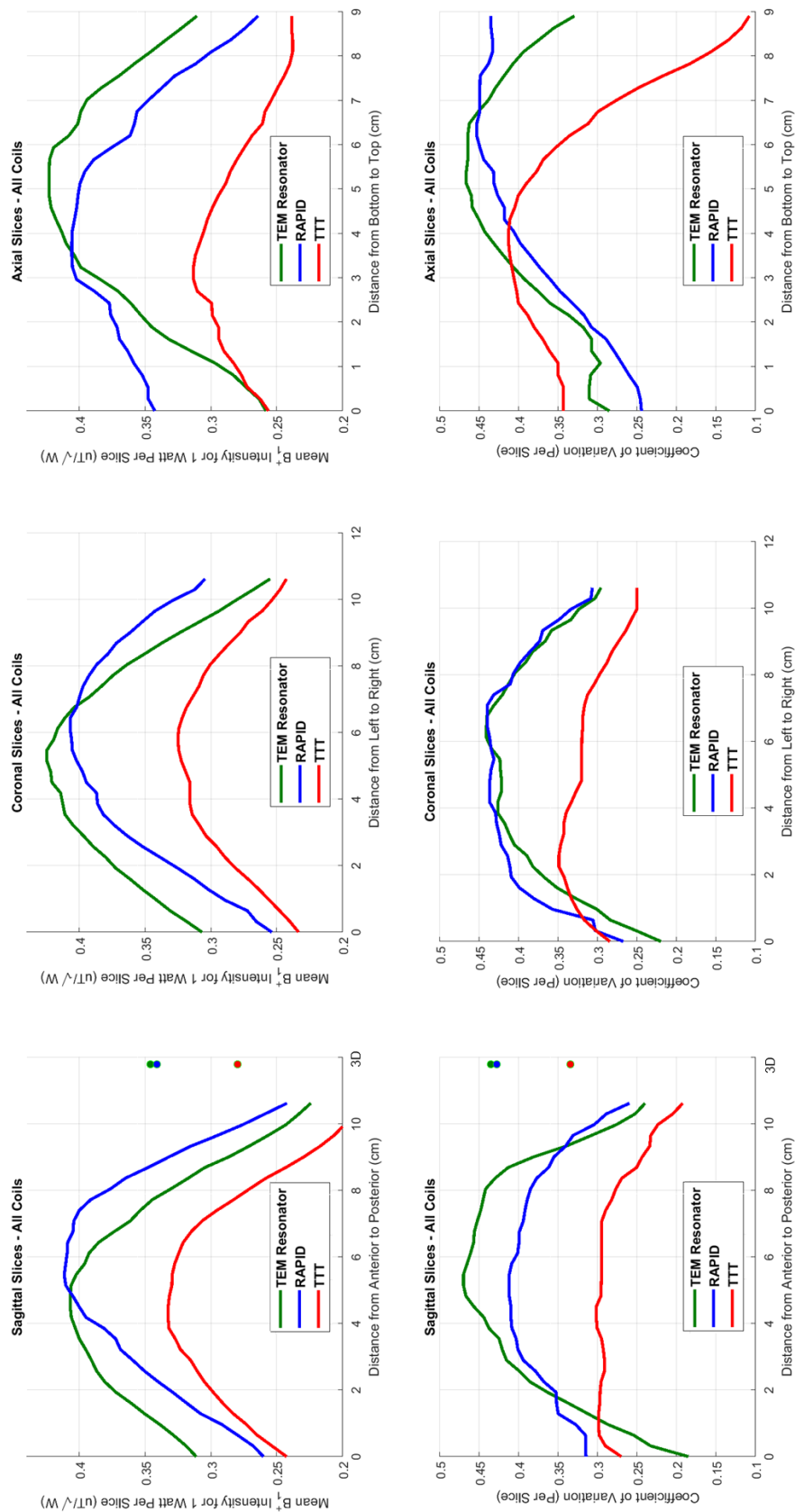


Figure 5.7. Experimental B_1^+ Field Comparison of the Anthropomorphic Heterogeneous Head Phantom loaded in Each Experimental 7T RF Coil. Single slices are shown in all planar views. The magnitude was scaled to a maximum B_1^+ intensity of $0.80 \mu\text{T}/\sqrt{\text{W}}$ for 1-Watt of input power.

The experimental mean B_1^+ field intensity and CV were assessed in various compartments of the brain in the experimental perfusionless anthropomorphic heterogeneous head phantom. In the brain compartment, the experimental mean B_1^+ field intensity is highest in the RAPID and 16-strut/4-port TEM resonator. For the 16-strut/4-port TEM resonator and RAPID coil, the mean B_1^+ field intensity is highest in the ventricles of the cerebrospinal fluid due to its quadrature excitation. The mean B_1^+ field intensity is highest next in the midbrain, and this observation is supported by the magnitude of the B_1^+ distribution illustrated in Figure 5.7. The mean B_1^+ field intensity is highest in the midbrain of the 16-strut/4-port TEM resonator. The experimental anthropomorphic heterogeneous head phantom demonstrates that the TTT coil has the lowest mean B_1^+ field intensity per input power and CV in all compartments and therefore the most homogeneous RF distribution. Note that while the TTT design possesses low B_1^+ per input power efficiency, it possesses higher B_1^+ per SAR efficiency when compared to the TEM design (183).



Experimental Anthropomorphic Heterogeneous Head Phantom

Figure 5.8. A representation of the Experimental Anthropomorphic Heterogeneous Head Phantom's Experimental B_1^+ profiles shown in all planar views. The distance is shown along the respective planar axis for the values of CV and mean B_1^+ field intensity (per slice measured in cm).

5.3.2 Experimental RF Heating Using the Experimental Perfusionless Anthropomorphic Heterogeneous Head Phantom Loaded within the TTT Coil (Preliminary Results)

Two RF heating experiments were conducted to perform RF heating in the perfusionless anthropomorphic heterogeneous head phantom for experimental temperature measurements: 1) validating thermal simulations with experimental thermal measurements and 2) comparing numerical RF heating of the numerical perfusionless anthropomorphic heterogeneous head phantom model to the numerical perfused segmented *in-vivo* human head model.

5.3.2.1 Validation of Numerical Temperature Rise to Experimental Temperature Measurements

The numerical ambient temperature was set to 18.00°C within and outside of the numerical perfusionless anthropomorphic head phantom model to match the experimental ambient temperature. The numerical and experimental temperature measurements are close in temperature change and slope in Probes 1 and 2 in Figure 5.9. The numerical input SAR was converted to the SAR per 1-Watt of input power and scaled by an average net coil input power of 34.88W. The net power is the average power delivered to the coil multiplied by the duty cycle and removes losses from the plug to the cables in the coil. The losses were measured with the network analyzer from the plug to the TTT's cables.

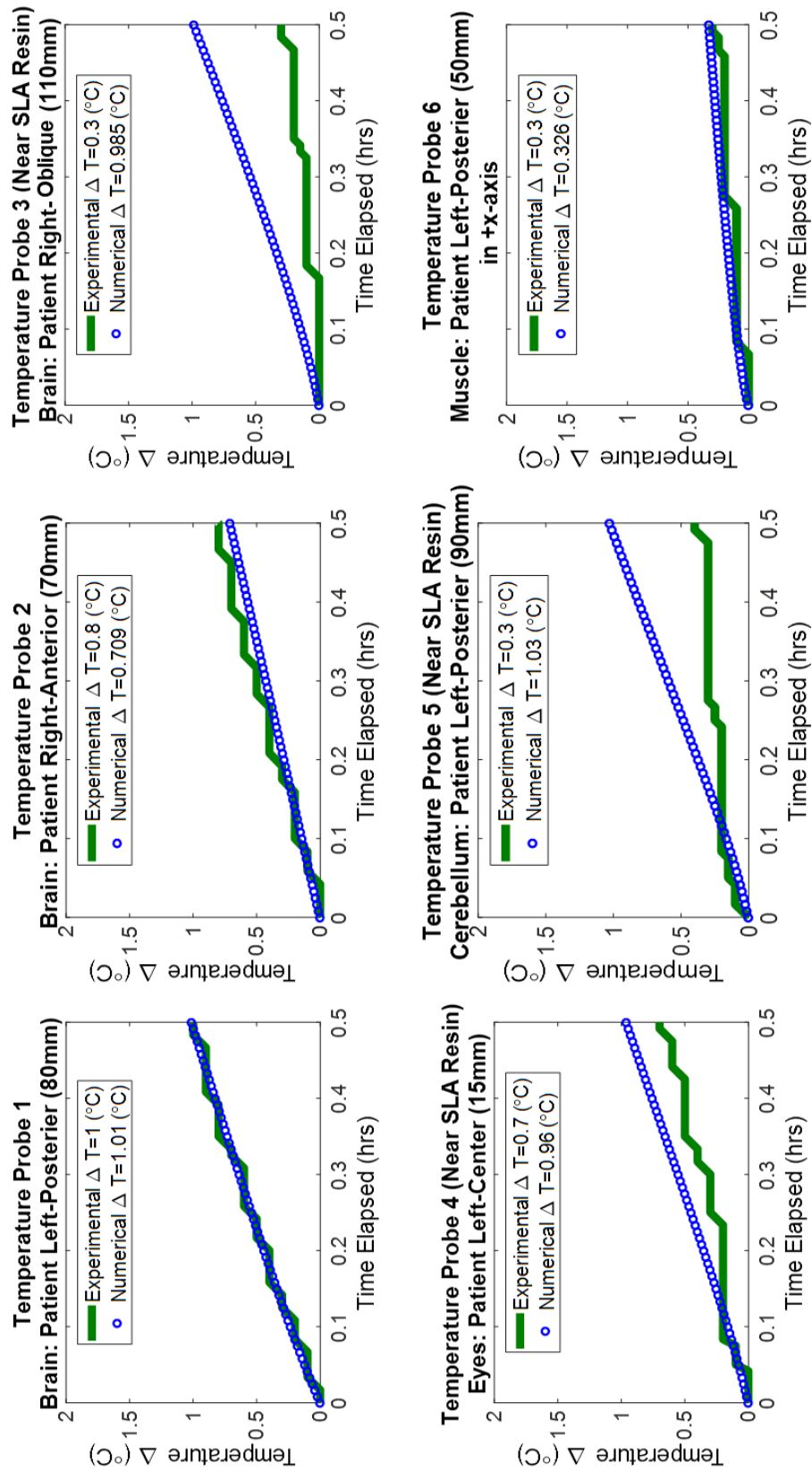


Figure 5.9. RF Heating Validation Per Probe using the TTT coil and comparison to Numerical Temperature Rise at 7T. The perfusionless anthropomorphic heterogeneous head phantom loaded within the experimental TTT coil uses the first six probes in the RF heating experiment and

The results of Figure 5.9 indicate that the numerical thermal model has the ability to predict the experimental thermal measurements. Despite its accuracy, the experimental and numerical models indicate that the temperature rise is linear because the phantom is perfusionless. Temperature probes 3 to 5 are close to the SLA resin that is between two compartments. The numerical simulations offer a better prediction for the temperature probes that are submerged around non-SLA resin media. The source of error should be further explored.

5.3.3 Numerical Studies of Electromagnetic and Thermal Characterization with the Anthropomorphic Heterogeneous Head Phantom using the TTT Coil

Figure 5.10.A and B shows the numerical and validated experimental B_1^+ distribution for 1-Watt of input power. The distributions are similar in B_1^+ distribution per slice. The B_1^+ field distribution is masked to all fillable compartments in the head phantom in order to eliminate the B_1^+ field in the SLA resin, which produces low MR signal. The ROI shown is based on the slice selection to acquire the experimental B_1^+ distribution. The numerical and experimental B_1^+ field distributions are scaled to the same magnitude scale (0 to $0.49 \mu\text{T}/\sqrt{W}$).

Figure 5.10.C shows the numerical SAR distribution per a continuous mean B_1^+ intensity of $2\mu\text{T}$ in the head phantom. The distribution is shown from 0 to 8.00 W/kg. The peak SAR is 7.89 W/kg. The peak SAR region is located in the left temporal lobe of the brain compartment and the left zygomaticus major muscle in the upper muscle compartment.

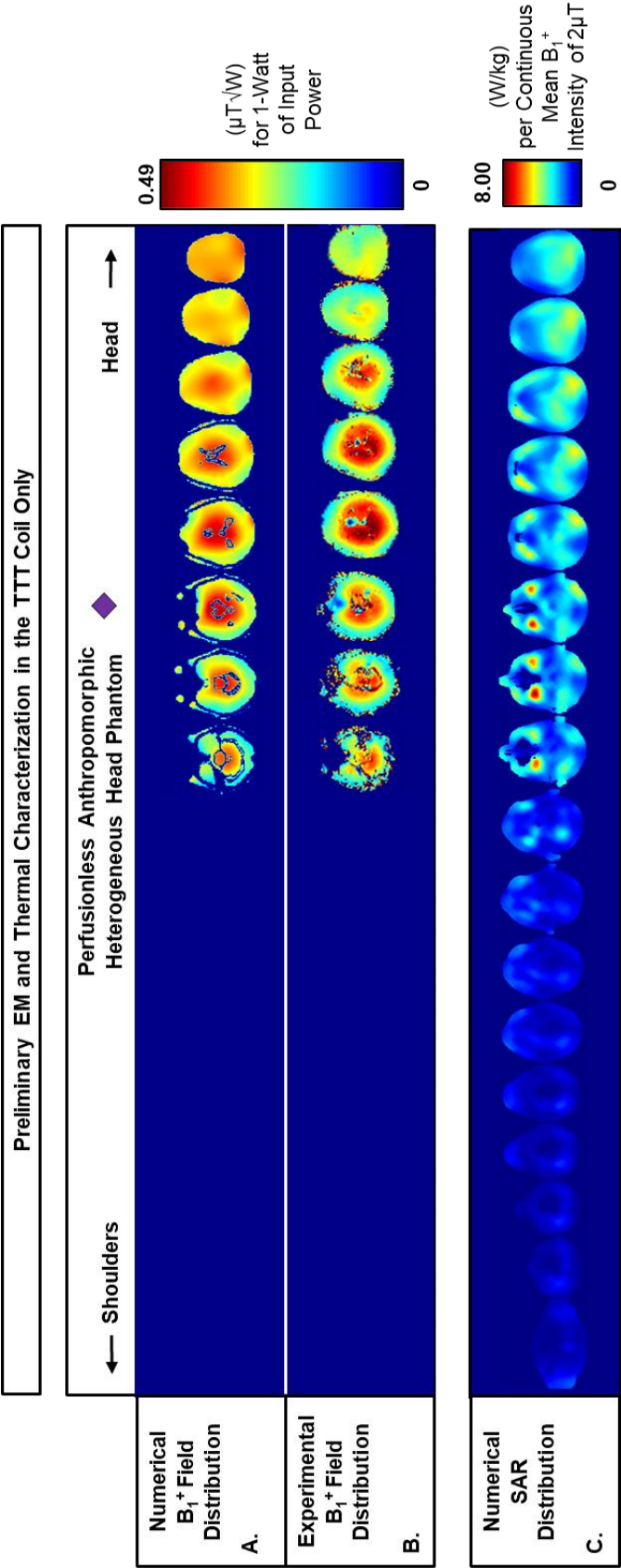


Figure 5.10. Electromagnetic and Thermal Characterization of the Perfusionless Anthropomorphic Heterogeneous Head Phantom using the TTT coil. A.) Numerical B_1^+ Distribution and validated by the B.) Experimental B_1^+ Distribution for 1-Watt of Input Power. C.) Numerical SAR per

5.3.3.1 Numerical RF Heating Comparison of the Perfusionless Anthropomorphic Heterogeneous Head Phantom to the Perfused Segmented *In-vivo* Human Head Model

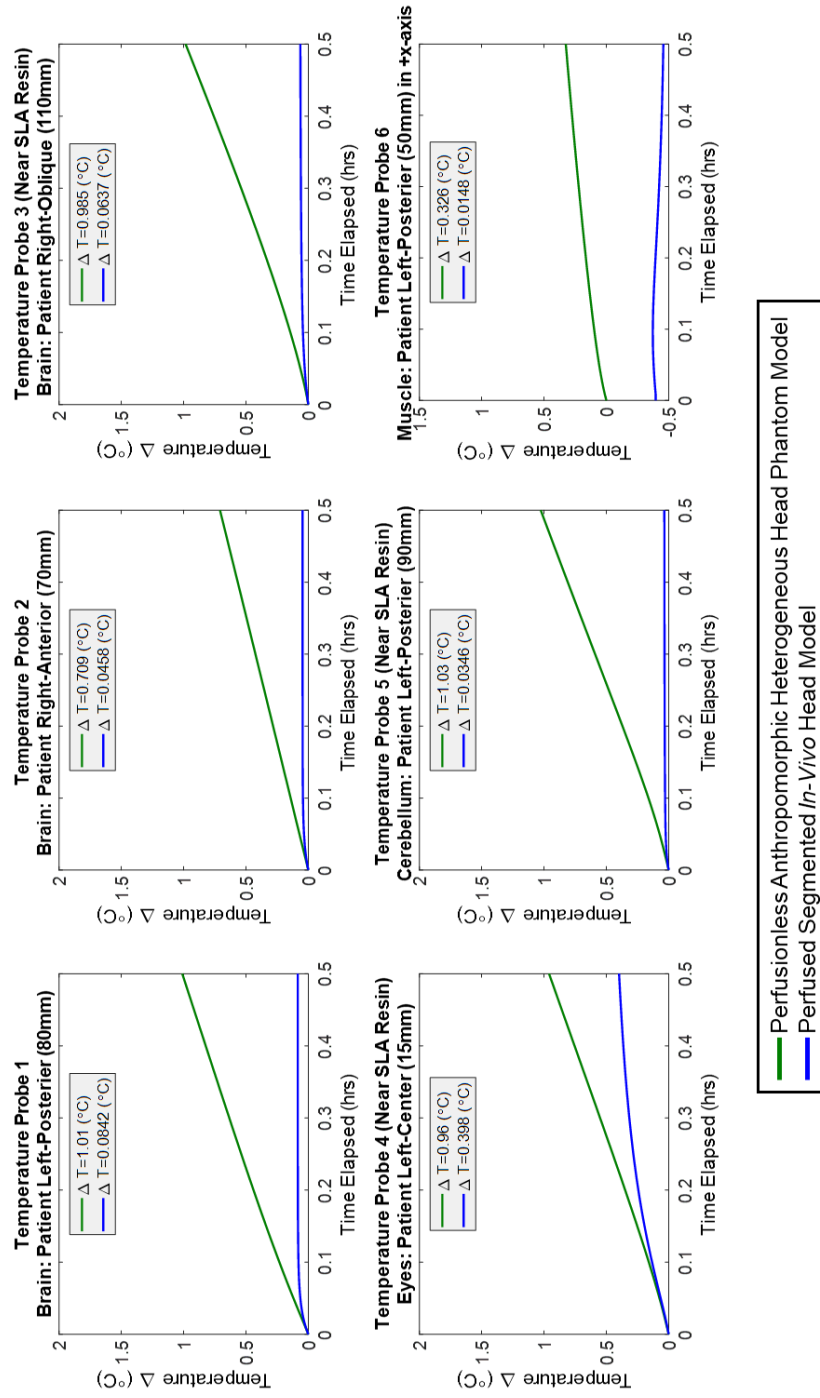


Figure 5.11. Numerical RF Heating Comparison of the Perfusionless Anthropomorphic Heterogeneous Head Phantom using the TTT coil at 7T. The temperature change is shown in both thermal models in six locations. These locations are the same locations as Figure 5.9.

A numerical RF heating experiment was conducted to perform RF heating in the anthropomorphic heterogeneous head phantom for experimental temperature measurements by comparing the numerical RF heating of the perfusionless anthropomorphic heterogeneous head phantom to the perfused segmented *in-vivo* human head model.

In the perfused segmented *in-vivo* human head model, the numerical temperature equilibrium was achieved by setting the body temperature to 37.00°C and bore temperature to 18.00°C. The numerical input SAR was scaled by an average net coil input power of 34.88W in both models. A 30-min RF exposure was applied to both models. Figure 5.11 indicates the results of the numerical RF heating comparison of both models for all probes. In this study, resources were not available to perform *in-vivo* RF heating on a volunteer. Thus, the perfused segmented *in-vivo* head model offers a prediction of the potential RF heating that this specific *in-vivo* volunteer may experience. Since the segmented *in-vivo* head model has perfusion, the temperature reaches an equilibrium state in most probe locations in the allotted time except for the temperature probe 6 (located in the neck).

5.4 DISCUSSION

This study provides several electromagnetic and thermal assessments of the perfusionless anthropomorphic heterogeneous head phantom using different RF coils. RF and thermal simulations validated experimental RF and thermal measurements using the anthropomorphic heterogeneous head phantom in different RF coil geometries. The thermal simulations compare the RF heating within each developed numerical thermal model.

Figure 5.5 validated that the SLA resin is conductive and a useful tool to assess the approximate temperature rise in mimicked human tissue. These measurements validate the SAR characterization of the head phantom shown in Chapter 4.0. Furthermore, the temperature measurements verify thermal parameters of the SLA resin not provided by the specification sheet. Future work will involve a more robust view of the temperature rise around the phantom and an analysis and distinction of the thermal and electrical losses in the phantom and environment.

Chapters 3.0 and 4.0 concluded that the experimental anthropomorphic heterogeneous head phantom is adequate for bench measurements. The work within this chapter further demonstrates through a demo-channel analysis that the experimental anthropomorphic heterogeneous head phantom is useful in determining bench measurements on different RF coil geometries. Chapters 3.0 and 4.0 summarized that the experimental anthropomorphic heterogeneous head phantom measurements are closest to the *in-vivo* measurements. Although this study does not offer *in-vivo* bench measurements, it offers a baseline for future *in-vivo* comparison.

Figure 5.7 and Figure 5.8 demonstrate the impact RF homogeneity using different experimental RF coil designs at 7T. Even though the experimental RF coils have different designs, Figure 5.7 and Figure 5.8 illustrate that the experimental anthropomorphic heterogeneous head phantom is a helpful tool for MR researchers that aim to improve RF homogeneity in RF coil design. Moreover, Figure 5.10.B demonstrates how the experimental B_1^+ distribution is in agreement with its numerical B_1^+ distribution results Figure 5.10.A.

Figure 5.10.C illustrates the SAR distribution throughout the numerical perfusionless anthropomorphic heterogeneous head phantom model. Figure 5.12.B and E aid in determining the physiological regions of the global SAR in the SAR distribution from Figure 5.10.C. The physiological regions of the numerical perfused segmented *in-vivo* human head model do not have

artificial boundaries between the tissues and the tissues within the numerical perfusionless anthropomorphic heterogeneous head phantom model are slightly smaller in volume due to these artificial boundaries. As mentioned, the peak SAR is located in the temporal lobe of the brain compartment and zygomaticus major muscle in the upper muscle compartment. It is important to note that the peak SAR region is not an accurate representation of the peak SAR region and intensity in the numerical perfused segmented *in-vivo* human head model and is supported by the comparison of the Figure 5.12.A and D. The peak SAR is 5.72 W/kg in the numerical perfused segmented *in-vivo* human head model. The temporal lobe and zygomaticus major muscle are small regions within the brain and muscle compartments that are surrounded by the SLA resin material.

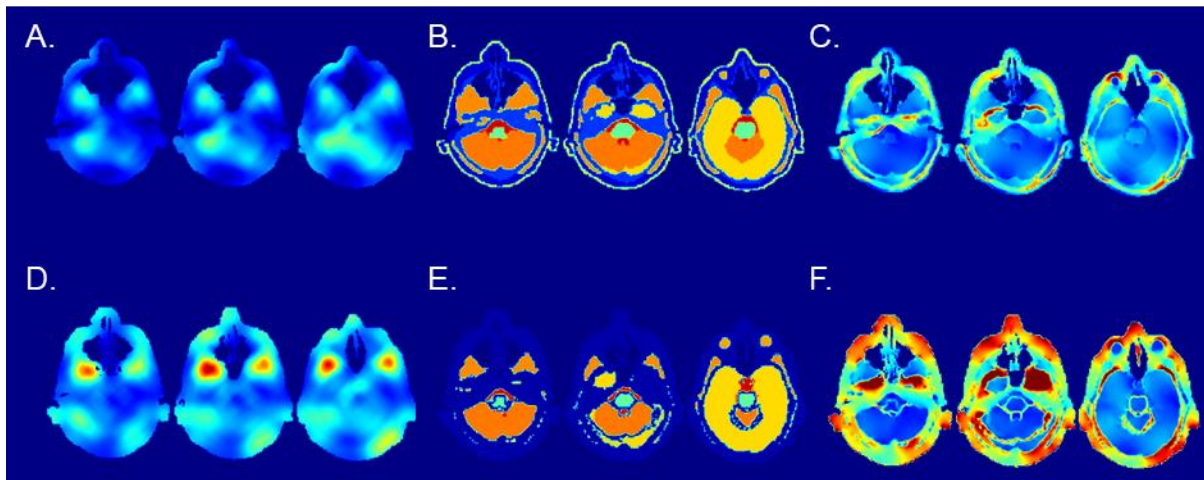


Figure 5.12. Numerical Comparison of the SAR, Permittivity and Absolute Electric Field Distribution in the Numerical Thermal Models within the Numerical TTT Coil. The numerical perfused segmented *in-vivo* human head model shows the A) SAR distribution in the region, B) permittivity in the region, C) the absolute electric field in the region, and the numerical perfusionless anthropomorphic heterogeneous head phantom model shows the D) SAR distribution in the region, E) permittivity in the region, F) the absolute electric field in the region.

The SLA resin has a much higher electric field intensity than the electric field in the individual fat, bone, and skin tissues due to the SLA resin having a lower permittivity that results in a higher electric field distribution. The absolute electric field is much higher in this region within the numerical perfusionless anthropomorphic heterogeneous head phantom model shown in Figure 5.12.C than with the numerical perfused segmented *in-vivo* human head model shown in Figure 5.12.F. Chapter 4.0 also demonstrates having similar differences between the absolute electric field behavior in each thermal model using the TEM resonator.

Preliminary thermal measurement results were conducted using the thermal simulations and experimental thermal probes in the TTT only shown in Figure 5.9. The results indicated that the numerical Penne's Bioheat equation was a good predictor of the numerical perfusionless anthropomorphic heterogeneous head phantom model's temperature rise based on the average net input power in the numerical TTT coil. The source of error for the locations closest to the SLA resin should be further explored. This thermal assessment was performed for an intensive 30 minutes of continuous power. The applied numerical RF heating does not present an MR sequence, but it shows the capability of presenting the thermal heating in a real MR sequence. While the results are preliminary, this analysis is essential because similar thermal simulations can be performed based on various MR protocols at 7T.

The last thermal characterization assessment suggests that the numerical perfused segmented *in-vivo* human head model will not have the same temperature rise as the numerical perfusionless anthropomorphic heterogeneous head phantom model. The numerical global SAR for a continuous mean B_1^+ intensity of $2\mu\text{T}$ indicated that the numerical perfusionless anthropomorphic heterogeneous head phantom model results would be higher than the numerical

perfused segmented *in-vivo* human head model. However, the impact of perfusion has a considerable influence on the difference in temperature rise. The perfusion in the numerical segmented *in-vivo* human head model allows the model to reach equilibrium, which is supported by the results. The thermal model was created with the best assumption of the most applicable electromagnetic and thermal properties; yet, there might be a need to further validate the thermal properties in a study (similar to the EM properties validated in Chapter 4.0).

A sub-goal in this chapter was to assess how accurate a predictor in thermal heating with the perfusionless anthropomorphic heterogeneous head phantom would be to an *in-vivo* comparison. Figure 5.11 shows that there are distinct differences in the temperature change between the two thermal models. However, the numerical perfusionless anthropomorphic heterogeneous head phantom offers an accurate comparison of temperature rise and slope before the numerical perfused segmented *in-vivo* human head model reaches equilibrium. The preliminary results are applicable only to the TTT coil, and further work should be done to compare the thermal characterization of the experimental perfusionless anthropomorphic heterogeneous head phantom in various RF coils.

5.5 CONCLUSION

In conclusion, various MR experiments conducted within this chapter highlight that the designed phantom is a valued resource for RF engineers and the MR community at 7T. In addition, the preliminary results indicate that the experimental perfusionless anthropomorphic heterogeneous head phantom offers promise in predicting thermal characterization of a phantom. This chapter

examines the hypothesis of Specific Aim 2. Future RF heating experiments can be conducted to validate the global, experimental temperature rise through MR thermometry.

6.0 CONCLUSIONS AND FUTURE WORK

6.1 SUMMARY AND FINDINGS

6.1.1 Development of an Anthropomorphic Heterogeneous Head Phantom to Evaluate and Characterize Experimental MRI Studies at 7T

An anthropomorphic heterogeneous head phantom was developed for MRI applications and can be used for other electromagnetic applications. The anthropomorphic head phantom was developed from a 3T MRI healthy male dataset to have eight classified tissue compartments. The anthropomorphic head phantom was successfully built and preliminarily evaluated through an application that involves electromagnetic-tissue interactions: MRI (due to it being an available resource). The anthropomorphic head phantom was filled with media possessing electromagnetic constitutive parameters that correspond to biological tissues at ~297 MHz. The anthropomorphic head phantom is unique in that it has more tissue compartments than previous works and its data is compared to the volunteer from whom the head phantom was prototyped.

A preliminary comparison between an *in-vivo* human volunteer (based on whom the anthropomorphic head phantom was created) and various phantoms types, one being the anthropomorphic heterogeneous head phantom, were performed using a 7T human MRI scanner.

The other phantom types were the same anthropomorphic head phantom filled with different media, which demonstrated its versatility). The comparison involved three assessments using EPI, B_1^+ field distributions, and the scattering parameters in Chapter 3.0. EPI acquisitions were performed, and minimal ghosting and fluctuations were observed using the proposed anthropomorphic phantom. The B_1^+ field distributions (during MRI experiments at 7T) and the scattering parameter (measured using a network analyzer) were most comparable between the anthropomorphic heterogeneous head phantom and an *in-vivo* human volunteer.

In conclusion, the developed anthropomorphic heterogeneous head phantom can be used as a resource to various researchers in applications that involve electromagnetic-biological tissue interactions such as MRI. The anthropomorphic heterogeneous head phantom's results prove the hypothesis as accurate determining that the anthropomorphic heterogeneous head phantom has a better comparison to the *in-vivo* human volunteer than the commercial homogeneous water-doped spherical phantom. Specific Aim 1 was completed and proved that those that use the anthropomorphic heterogeneous head phantom instead of a basic spherical phantom will find it easier to evaluate RF head coils.

6.1.2 Electromagnetic and Thermal Characterization of a Perfusionless

Anthropomorphic Heterogeneous Head Phantom using the TEM Resonator at 3T and 7T MRI

The anthropomorphic heterogeneous head phantom developed in Chapter 4.0 is further assessed in Chapter 4.0 through EM and thermal characterization using the TEM resonator at 3T and 7T. EM characterization was assessed through three quantitative studies in Section 4.2. The EM characterization was performed to accurately calculate the scattering parameters and the electric

and magnetic field distributions using B_1^+ field mapping methods on a 7T human MRI scanner and numerical full-wave electromagnetic simulations at 3T and 7T. In addition, future work could offer experimental validation to see if the same study can be validated through experiments at 3T.

All studies used the following:

1. a recently developed six-compartment refillable 3D-printed anthropomorphic head phantom (developed from MRI scans obtained *in-vivo*), where the phantom itself is filled in its entirety with either heterogeneous loading, or homogeneous brain-doped or water-doped loading,
2. *in-vivo* (the same volunteer on whom the phantom was based), and
3. a commercial homogeneous water-doped spherical phantom.

The results determined that the calculated S-parameters for all the anthropomorphic head phantoms were comparable to the *in-vivo* volunteer (within 17% difference of reflection coefficient value) and differed for the commercial homogeneous water-doped spherical phantom (within 45% difference of reflection coefficient value). The experimentally measured B_1^+ field maps of the anthropomorphic heterogeneous and homogeneous brain-doped head phantom results were most comparable to the *in-vivo* volunteer. The numerical simulations show that both the anthropomorphic homogeneous water-doped and brain-doped phantom models overestimate the absolute electric field intensities when compared to the originally segmented *in-vivo* human head model and anthropomorphic heterogeneous head phantom model. The results demonstrate the usefulness of 3D printing anthropomorphic phantoms for RF coils evaluation and testing applications.

The thermal characterization was assessed using the TEM resonator through the numerical full-wave thermal simulations at 3T and 7T. Penne's bioheat equation was applied using the SAR

input per a continuous power required to achieve the FDA regulated average SAR on the perfused segmented *in-vivo* human head model and perfusionless anthropomorphic heterogeneous head phantom model. The results determine that the perfusionless anthropomorphic heterogeneous head phantom does not have the exact temperature rise in the perfused segmented *in-vivo* human head model tissues beyond the perfused time constant. However, it does demonstrate that the numerical simulations and experimental thermal measurements are similar in locations far from the SLA resin boundary. This work is preliminary but shows promise in the anthropomorphic heterogeneous phantom being a useful tool in the RF heating assessment of RF coils and supports the hypothesis in Specific Aim 2.

6.1.3 Preliminary Electromagnetic and Thermal Performance Evaluation of the Perfusionless Anthropomorphic Heterogeneous Head Phantom using Various RF Coils at 7T MRI

In Chapter 5.0 anthropomorphic heterogeneous head phantom was assessed using various RF coils at 7T. Using the 7T human MRI scanner, the electromagnetic characterization of the designed anthropomorphic head phantom was assessed in the experimental TEM resonator, TTT 16-ch Tx/32-ch Rx coil, and the RAPID coil through a demo of the experimental scattering parameters and experimental B_1^+ mapping. The experimental mean B_1^+ is highest in the RAPID and TEM resonator at 7T. However, the experimental TTT coil provides the most uniform RF homogeneity with an extensive homogeneous coverage from the top of the head to the base of the cerebellum. The numerical temperature simulations are accurate in its comparison to the experimental results of RF heating in the experimental perfusionless anthropomorphic heterogeneous head phantom's compartments that are far from the interface of the SLA resin and a classified tissue. The

anthropomorphic heterogeneous head phantom is perfusionless and has a linear temperature rise through the thermal heating experiment. However, the perfused segmented *in-vivo* human head phantom has an exponential trend and reaches equilibrium upon achieving the perfused time constant. These results indicate that the experimental perfusionless anthropomorphic heterogeneous head phantom offers promise in predicting electrical and thermal characterization of a phantom.

6.2 FUTURE WORKS

As previously indicated, an anthropomorphic heterogeneous head phantom model with a realistic comparison to an *in-vivo* human head is limited. The applications of the designed anthropomorphic heterogeneous head phantom are a significant resource to the MR community and several entities that dedicate focused work to structural anatomies of the brain and neurological work.

The work within this dissertation suggests that the anthropomorphic heterogeneous head phantom is a helpful tool for RF engineers to predict an RF coil's electromagnetic and thermal characteristics and its similarities to an *in-vivo* human head. Work should continue to conduct a full analysis of well-known thermal and electromagnetic characterization methods on 7T RF coils used in the MRI community. The same work should be considered at various field strengths to be a useful tool to the MR community at various field strengths. The work within Chapter 5.0 suggests promising results for RF heating using the anthropomorphic heterogeneous head phantom. Further work should be explored at 7T to assess the RF temperature rise and safety through more detailed RF heating methods such as MR thermometry.

The designed anthropomorphic head phantom was designed with ease of access to the inner cavities of the brain; thus, the phantom could be a useful tool for implanted devices. Implanted devices can be placed inside of the brain with various brain-computer interface (BCI) applications. The anthropomorphic heterogeneous head phantom may become an additional resource for BCI applications within MRI studies.

In addition, the anthropomorphic heterogeneous head phantom could be used to model and mimic the anatomy of various diseases to implement anatomical neurological damage of the brain. Clinicians might be intrigued to use the anthropomorphic heterogeneous head phantom to simulate imaging predictive biomarkers and diagnosis in the human brain.

APPENDIX A

DEVELOPMENT AND MEASUREMENT OF MIMICKED BIOLOGICAL TISSUE PHANTOM RECIPES AT 7T

A.1 SUMMARY

Throughout this dissertation, the development of an anthropomorphic head phantom is mentioned. Chapter 3.0 describes the process to fabricate the rapid prototype of the designed anthropomorphic head phantom and its mimicked biological tissues. In Appendix A, the mimicked biological tissues process is elaborated further than in Chapter 4.0 and Chapter 5.0. Two different methods were applied to make the biological tissues. Section A.2 expresses one method involved creating the mimicked biological tissues for the EM measurements only, and Section A.3 details the other method involved creating the mimicked biological tissues for the thermal measurements using agar.

A.2 DEVELOPING PHANTOMS FOR ELECTROMAGNETIC MEASUREMENTS

Section 3.2.4 discusses the preparation to make the anthropomorphic head phantom's mimicked biological tissues and the process to fill the anthropomorphic head phantom to achieve electromagnetic measurements. It discusses the strategy for choosing the anthropomorphic head phantom tissue classification in Table 3.1. Different in-house mixtures were used to develop the mimicked biological tissues in Chapter 3.0 and Chapter 5.0. The in-house mixtures are composed of various concentrations of distilled water, NaCl, CuSO₄, and denatured C₂H₆O.

Before making the designated tissue, the constitutive parameters must be known to have target values to achieve. All containers are cleaned and deionized before making the tissues. Using the dielectric probe, the values are measured throughout developing the mixtures. The dielectric phantom recipe generator (<https://amri.ninds.nih.gov/cgi-bin/phantomrecipe>) is used to determine the amount of distilled H₂O and NaCl required to achieve the targeted permittivity and conductivity. These target values are repeatedly measured with the dielectric probe until the targeting value is achieved.

Next, if its desired to modify the T₁ relaxation, then CuSO₄ needs to be used. It needs to be added after the NaCl because it is more soluble in the H₂O mixture. The CuSO₄ concentration should be adapted to achieve the proper T₁ range. The T₁ must be measured using a T₁-weighted sequence and can be done by manipulating the TI parameter in the sequence.

Then, the permittivity is adjusted to the target value by adding various concentrations of denatured C₂H₆O. While monitoring the dielectric probe for the target permittivity value,

denatured $\text{C}_2\text{H}_6\text{O}$ is titrated. The titration of the NaCl and denatured $\text{C}_2\text{H}_6\text{O}$ are repeated until target values are reached.

The described process is used for the development of each in-house mixture to achieve the desired values reported in Table 3.1. Measurements are conducted several times ($n=10$, $\sigma=0.01$) to ensure the stability of the mixture over time.

A.3 DEVELOPING PHANTOMS FOR THERMAL MEASUREMENTS USING AGAR

Chapter 5.0 discusses the preparation to make the anthropomorphic head phantom's mimicked biological tissues to conduct the thermal measurements. Agar eliminates thermal measurement errors caused by diffusion, and its accuracy is supported through work (15). Different in-house mixtures are created using various concentrations of distilled water, NaCl, CuSO_4 , sucrose, and polyvinylpyrrolidone (PVP, - average mol wt 40,000, Sigma-Aldrich®).

The Dielectric phantom recipe generator offers estimated concentrations to use the mixtures. These values are used and validated using the DAK probe. The Dielectric phantom recipe generator also predicts the density and heat capacity based on work (184). Either sucrose or PVP can be used with agar to modify the permittivity (in place for denatured $\text{C}_2\text{H}_6\text{O}$). Work (182) indicates that the difference in using PVP does not impact the permittivity. Instead, it impacts the signal intensity based on the MR protocol's echo time (TE) parameters.

Once the concentrations of all solvents are mixed, the solution is boiled inside of a beaker using a high-powered microwave and a stirrer. The solution is boiled in the microwave for about 3 minutes. It is then stirred and cooled for 2 minutes. This cycle is repeated until gelling occurs. It is important to allow the mixture to boil but not spill. Stop the heating cycle before the spilling

begins and increase the stirring and cooling. It is also necessary to not burn the gel. If the gel burns, it is not useable.

During the cooling period, the stirrer is continuously checked for gelling of the solution. Once the gelling is observed, the cooling and heating cycle is complete.

APPENDIX B

ELECTROMAGNETIC CHARACTERIZATION OF THE VIRTUAL FAMILY DUKE MODEL AT 3T AND 7T

B.1 SUMMARY

Chapters 4.0 and 5.0 reference the Virtual Family v1.0 Duke model in instances regarding the tuning and matching of the RF coil; yet, the results are not shown in detail. Thus, the results of the Duke model are presented within this appendix in Section B.2.

The purpose of Chapter 4.0 was to display the numerical electromagnetic and thermal characterization anthropomorphic heterogeneous head phantom to various models and see which results yield the closest comparison to the Duke model. Chapter 4.0 Part I-A led to a discussion of how the electromagnetic media influences the electromagnetic characterization and a methodology to determine which media delivers the best performance in evaluating an RF coil. Additional electromagnetic models were developed to further elaborate the impact and influence of the constitutive parameters despite a phantom's media and geometry. Section 4.2 uses various electromagnetic media and highlights the results of the anthropomorphic head phantom and spherical phantom filled with various electromagnetic media.

B.2 ELECTROMAGNETIC PROPERTIES TO THE VIRTUAL FAMILY V1.0 DUKE MODEL

The Virtual Family v1.0 (31) Duke model was used to tune and match the numerical RF coils mentioned in Chapters 3.0 to 5.0. The electromagnetic measurements of the Duke model were not mentioned but are referenced in many of our works (185, 186). In this section, the visualization is shown for the S-Parameters (Figure B.2.1), Bfield distribution (Figure B.2.2), and absolute electric field distributions (Figure B.2.3) at 3T and 7T. The thermal characterization is shown through the SAR distribution only (Figure B.2.3). Since the segmented *in-vivo* human head model is used as the baseline in Chapters 3.0 to 5.0, its results are compared to the Duke Model's results.

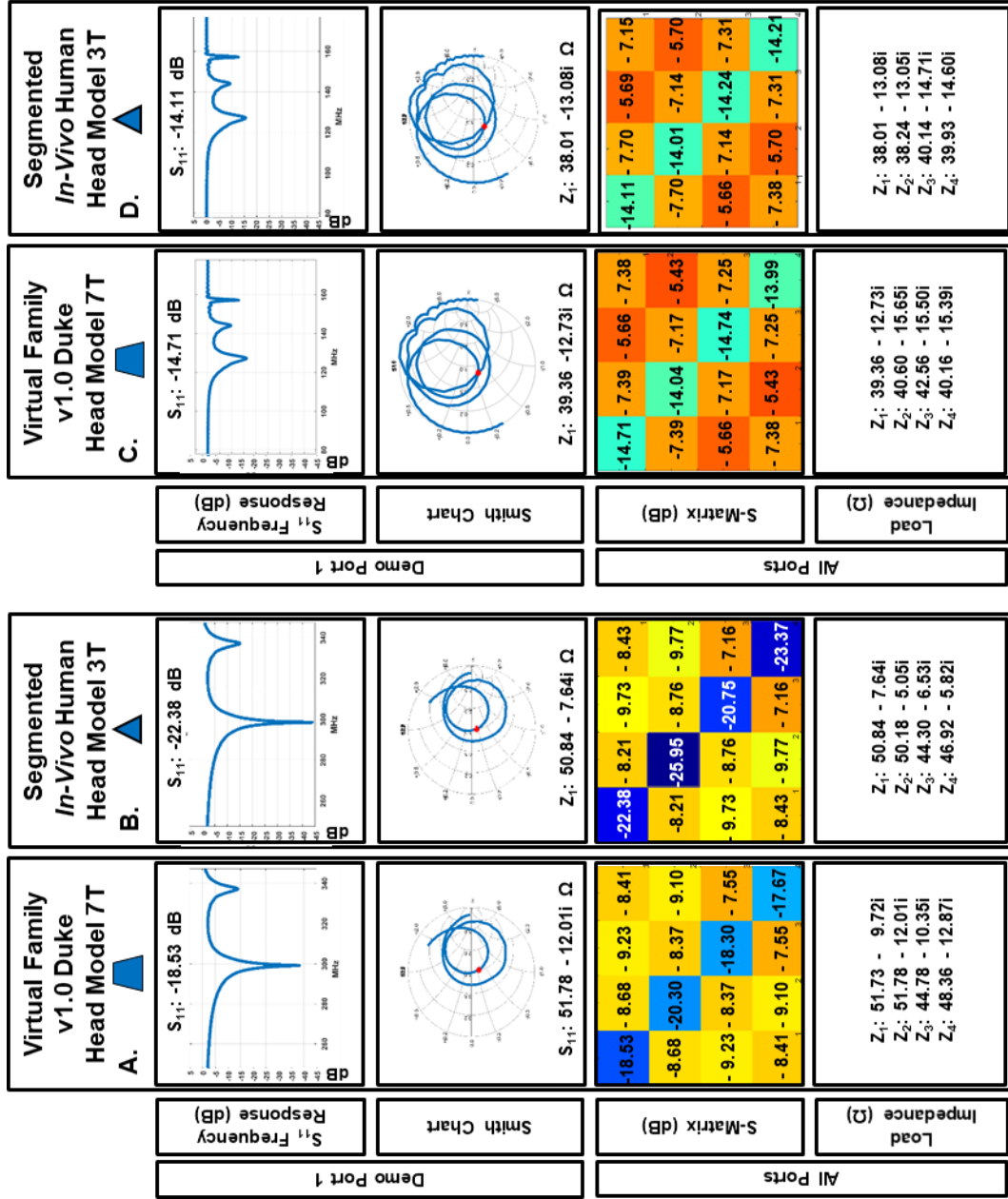


Figure B.2.1. FDTD calculated S-Parameters of the Duke Head Model (A & C) and Segmented *In-Vivo* Human Head Phantom (B & D) at 7T and 3T, respectively, using the TEM Resonator.

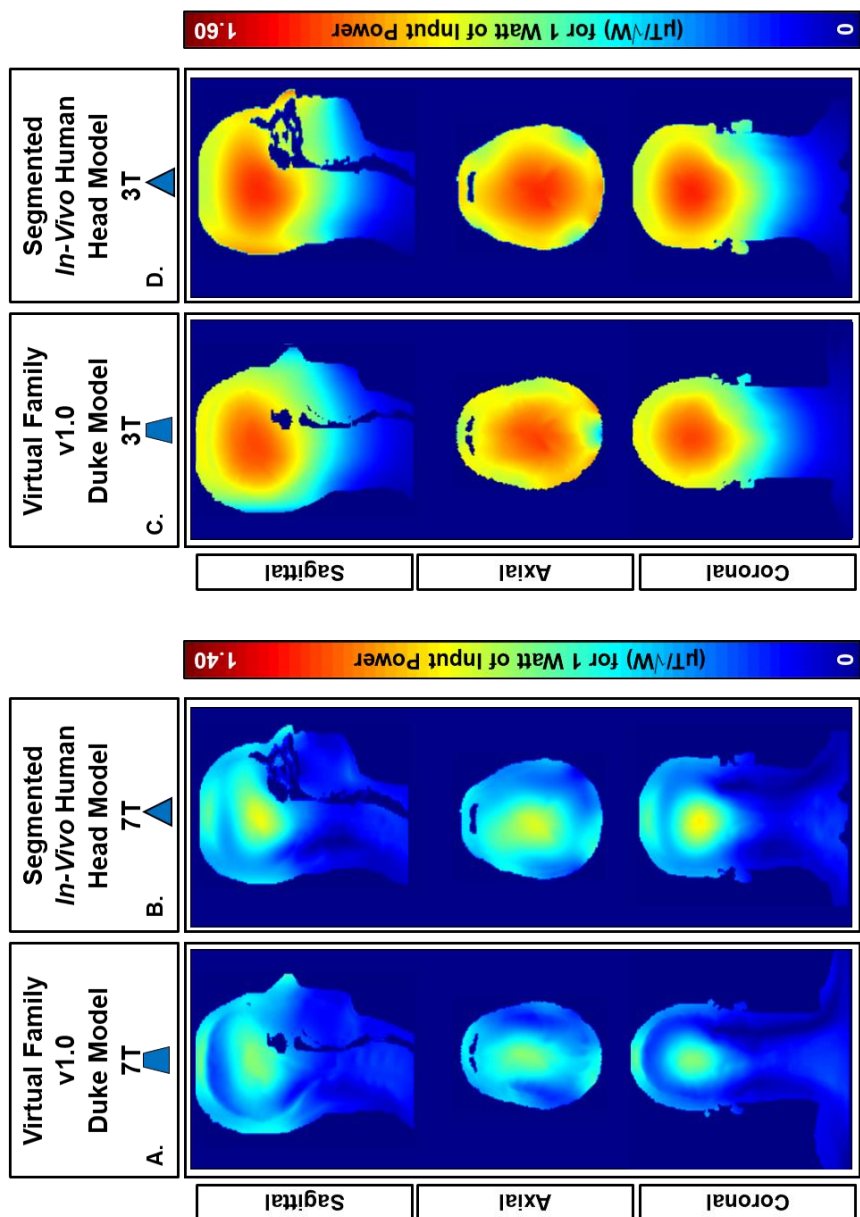


Figure B.2.2. BField Distribution for 1-Watt of Input Power of the Duke Head Model (A & C) and Segmented *In-Vivo* Human Head Phantom (B & D) at 7T and 3T, respectively, using the TEM Resonator.

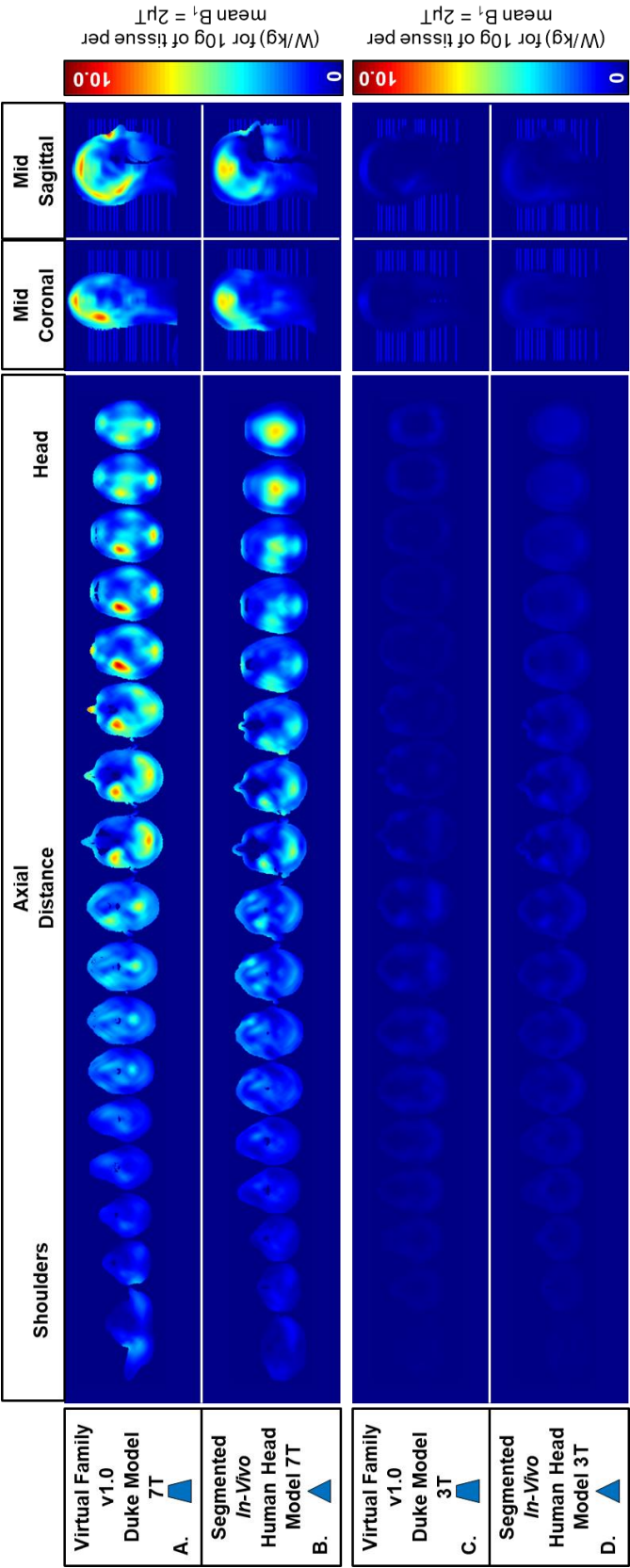


Figure B.2.3. SAR Distribution per continuous mean Bfield intensity of 2μT of the Duke Head Model (A & C) and Segmented In-Vivo Human Head Phantom (B & D) at 7T and 3T, respectively, using the TEM Resonator.

APPENDIX C

DESIGN, DEVELOP AND VALIDATE A NONLINEAR RF SHIMMING MRI OPTIMIZATION ALGORITHM AND GUI IN ORDER TO OPTIMIZE RF COIL PERFORMANCE AT 7T

C.1 INTRODUCTION

RF shimming (87, 147, 187-191) and transmit SENSE (191-195) are a few multi-transmission techniques used to achieve the RF homogeneity of a load within an RF coil while achieving government regulated SAR limits (64, 65). Works (71, 87, 147, 189) show optimizing the B_1^+ field through RF shimming leads to more homogeneous single slices to successfully achieve B_1^+ field homogeneity while achieving government regulated SAR limits. The current computational time is exhaustive (30), and although the current performance met the needs of recent findings (30, 101), our initial toolbox's performance was a concern.

Thus, the objective of Appendix C is to develop and validate a nonlinear algorithm that enhances the performance of our current nonlinear RF shimming MRI optimization algorithm to yield better numerical and experimental results at 7T. To test this objective, the results of the

nonlinear algorithm must be validated to generate novel RF excitations of each channel for different coil geometries.

Our rationale for Appendix C is that by determining the desired nonlinear algorithm and incorporating various parallel computing techniques, we will achieve the optimum performance in any RF coil (30). Upon completion, it is expected that Appendix C will strengthen and build upon the recent findings in works (30, 101); therefore, the improved performance of various RF coils may be achieved.

In Appendix C, the development and validation of a nonlinear RF shimming algorithm are studied to determine its ability to improve RF uniformity through simulation and experimental studies. All experimental studies were validated using the combined mode of the MR scanner at the Radiofrequency Research Facility at the University of Pittsburgh.

C.2 MATERIAL AND METHODS

C.2.1 Design and Development of an RF Shimming MRI Optimization Algorithm and Graphical User Interface

In order that the designed RF shimming algorithm is useful, a graphical user interface (GUI) is designed for the user to adjust the algorithm as desired. Several MR parameters directly impact the results of any load simulated within an RF coil. Researchers can shim numerical or measured fields of any load within an RF coil. Using MATLAB, a graphical user interface (GUI) was built

that is robust enough to compute MR characteristics to any coil and any load as shown in Figure C.2.1.

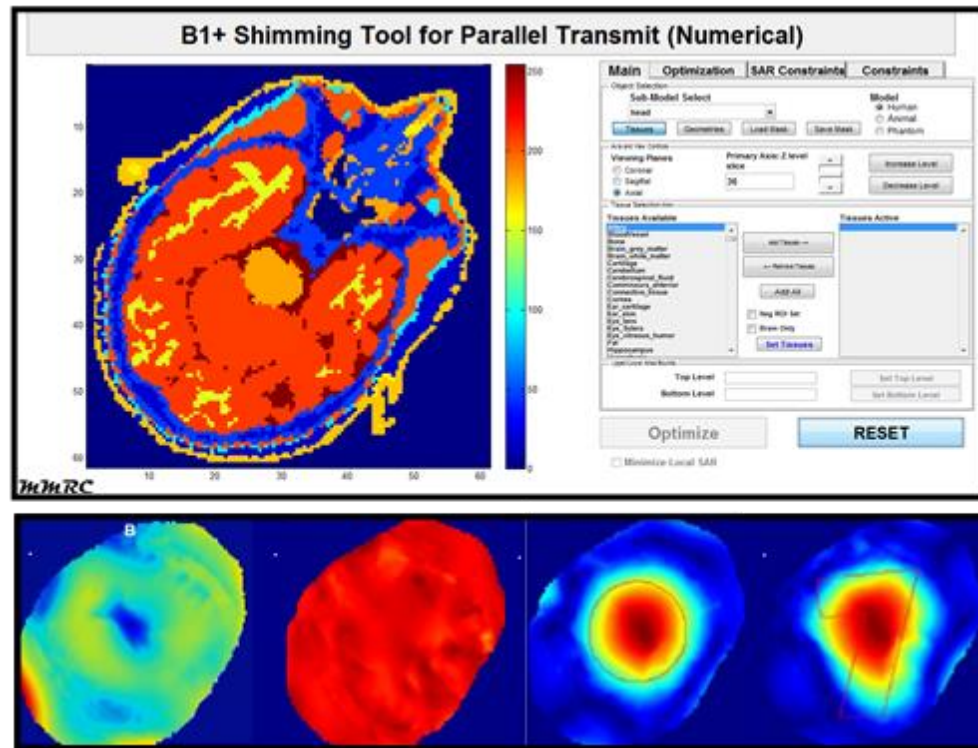


Figure C.2.1. RF Shimming MR Optimization Tool GUI and Shimmed RF Fields. An RF shimming toolbox GUI A) is used to find the optimal performance of any load within an RF coil. Results of a single slice axial views of a B) initial, non-optimized, C) optimized, D) circularly localized, and E) irregularly localized RF fields of a human within a TTT coil.

The graphical user interface allows the user to have versatility in selecting various physiological regions of the load in the left panel of Figure C.2.1.A. The user has the flexibility to select the entire tissue or specified portions of the tissue. If shapes or freehand are preferred to

acquire the load's ROI, the user can choose or make shapes as shown in Figure C.2.1.D and Figure C.2.1.E. For consistency, the same ROI can be used on different loads by loading previous masks.

The optimization tab offers parameters that constrain the optimization function. The number of channels can be selected or deselected. The optimization parameters indicate inputs that are necessary for the MATLAB Optimization algorithm 'fmincon' and other global optimization algorithms housed in MATLAB. The Optimization Parameters panel allows the maximum number of iterations, the maximum number of function calls, and the number of trials to be set. If you desire to alter a parameter, it is only recommended to increase the number of trials.

C.2.2 Verification of Various Nonlinear Algorithms using Experimental Studies

Several works (30, 185, 186, 196) have proved that the RF shimming technique incorporated within this in-house MATLAB optimization algorithm has been beneficial. However, these works have indicated that future work should be conducted to improve the uniformity of the magnetic field to find a global minimum to the desired objective function by utilizing various nonlinear algorithms that can allow various constraints to be set. Works (16, 30) indicates that more homogeneous slices (ultra-uniform slice selection) come at the cost of having increased SAR. However, this task's purpose is to seek ultra-uniform slices and achieving government regulated SAR limits by applying the optimal nonlinear algorithm for any given RF coil design.

Using a variety of computational resources such as an in-house 12 node cluster, clusters from the University of Pittsburgh's Supercomputing Center, or XSEDE, RF shimming of the magnetic fields and SAR calculations are performed on the electric and magnetic fields generated from the FDTD simulations. The MATLAB Optimization Toolbox™ and MATLAB Global

Optimization ToolboxTM was used to determine which nonlinear algorithm fits the criteria and yields the optimal RF coil performance. These algorithms were incorporated into the RF Shimming MRI Optimization tool. The baseline comparison consists of MR parameters selected from our preliminary data (177, 185, 186) using fmincon. The results of the B_1^+ field and SAR statistics using fmincon were compared to the results from other nonlinear algorithms within MATLAB (i.e. genetic, particle swarm).

Experimental Verification

To adequately measure the usability of the designed tool and whether it can be shared with the MR community, the designed tool was evaluated in various MR experimental studies.

The final package of the customized GUI and RF shimming MRI optimization algorithm was evaluated during experimental studies. Magnetic and electric fields that match the desired RF coil type and head dimensions were selected in the package. The desired parameters selected by the user were recorded.

C.3 RESULTS AND DISCUSSION

C.3.1 Design of Graphical User Interface (GUI)

The designed GUI and RF shimming algorithm were successfully designed. The tool has the versatility to be used regardless of the load. In our studies, we used the developed RF shimming algorithm to optimize the RF coil performance of various coils like the TTT head coil (185, 196),

TEM head coil (185), foot and ankle coil (181), knee coil, upper extremities such as the arm (197), and body coil (198, 199).

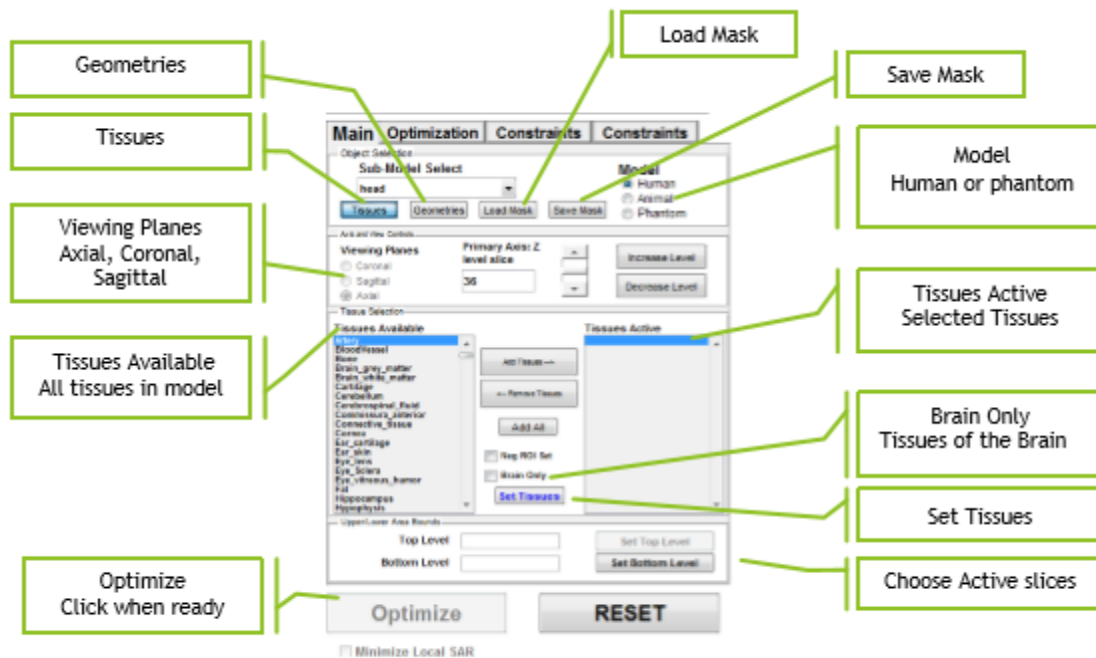


Figure C.2.2. Main Tab. The main tab of the GUI offers several parameters for the user to select the tissue, geometry, model type, and plane of view.

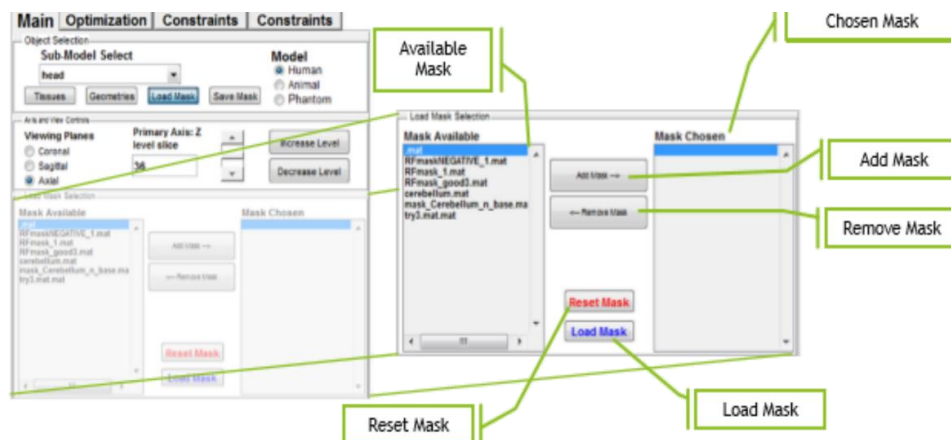


Figure C.2.3. Main Tab's Load Mask Subsection. The main tab of the GUI offers several parameters for the user to select the tissue, geometry, model type, and plane of view.

The toolbox is designed to give the user a large variation in selecting different regions of interest in the model. This variability spans to selecting different tissue types, geometries, loading mask, and saving mask. Once the user has chosen the desired region of interest, the user must also choose the desired optimization parameters, channel configuration, and constraints prior to selecting the Optimize button.

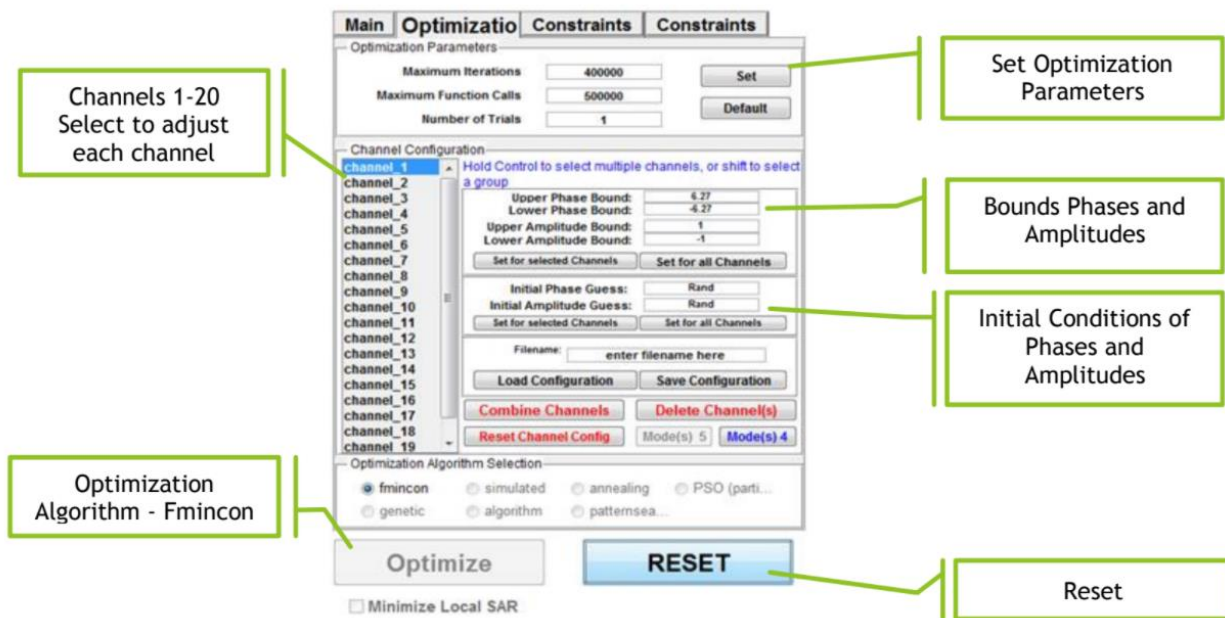


Figure C.2.4. Optimization Tab. Select optimization parameters for various excitation ports (channels) of the RF coil.

The Constraint Tab shown in Figure C.2.5 allows the user to set constraints to the nonlinear equation. The default objective function appears first, but the user can change the objective function to meet the needs.

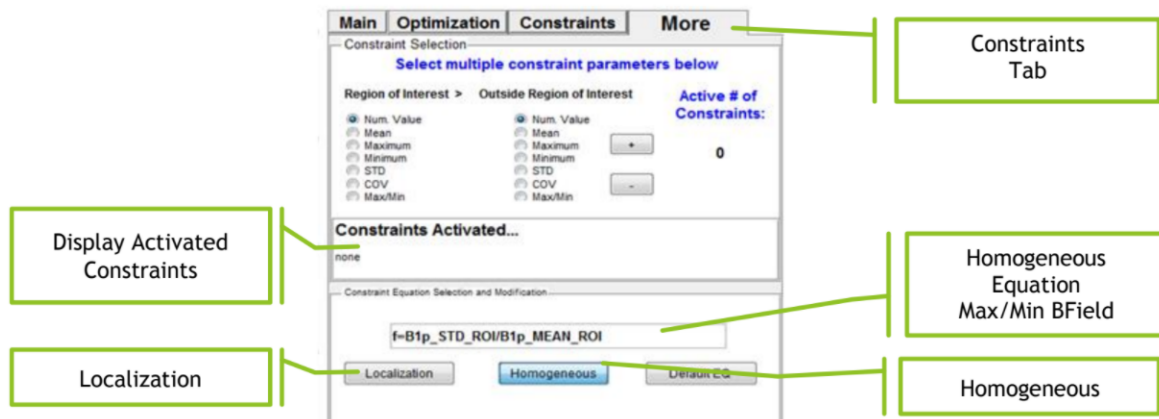


Figure C.2.5. Constraint Tab - Define optimization objective function to be minimizing the constraint

C.3.2 Verification of Nonlinear Algorithm using Experimental Studies

Our published studies (177, 181, 185, 186) utilize the nonlinear function ‘fmincon’. Desirable results were achieved and acceptable to be shared with the MR community. The RF shimming toolbox was shown in the morning categorical course at ISMRM in 2014 and 2015. For the scope of this work, the nonlinear comparison was only made for the anthropomorphic heterogeneous head phantom loaded within the 16ch-Tx/32ch-Rx TTT coil.

Below is an example of the initial trials run to determine the appropriate RF shimming case. Ten of the 2,000 cases were chosen to indicate the fmincon objective function output variables (iterations, funcCount and Trial Number) and indicate the SAR values (peak, average, STD, and CV). To achieve Table C.3.1, 2,000 cases were parsed through that fit the design criteria’s cost function and magnetic field constraints set to a mean magnetic field intensity above 9,000 H/m with CV below 0.23.

Table C.3.1. Example of Filtered Results using ‘Fmincon’ Algorithm

Ratio Max/Min	Mean	STD	COV	Iterations	funcCount	Trial Number	Peak SAR	Average SAR	STD SAR	COV SAR
3.362952871	9375.429755	2027.39185	0.216245218	1123	20002	643	0.52232	0.16533	0.082749	0.50052
3.145973606	9229.142558	2012.854193	0.218097638	319	5728	140	0.24835	0.074032	0.03631	0.49047
3.180667504	9018.428606	1955.740653	0.216860469	324	5894	1136	0.33029	0.094131	0.044947	0.4775
3.064408736	9160.233395	1947.341894	0.212586493	1152	20004	1054	0.35588	0.11383	0.053011	0.46571
3.767945095	9421.241378	1913.060286	0.203058197	128	2278	1363	0.65078	0.18855	0.1004	0.5325
3.195248504	9303.547956	1814.853185	0.195071084	419	7645	1905	0.49417	0.15114	0.076956	0.50918
3.310565863	9094.070325	1993.428913	0.219200956	506	9149	774	0.60587	0.16623	0.10204	0.61386
3.193969995	9056.868654	1760.717152	0.194406833	111	2014	682	0.65247	0.1453	0.087727	0.60375
3.197576351	9160.283902	1998.360275	0.218154841	968	17803	758	0.54386	0.16653	0.093472	0.5613
3.264677186	10086.98922	2236.61978	0.221733139	291	5310	923	0.33017	0.087253	0.043541	0.49901

In our recent studies (185, 186), the design criteria were set by RF field homogeneity with additional design criteria and constraints filtered by the relative B_1^+ efficiency and relative absorbed power efficiency. The best cases were taken and the results were tested. The validation of the results was acquired on the fabricated anthropomorphic heterogeneous head phantom. The results are shown in Figure 5.10.

Alternatives to the ‘fmincon’ algorithm were tested using the same initial conditions as the ten cases in Table C.3.1. The nonlinear algorithms ‘genetic’, ‘particle swarm’, and ‘fminbnd’ were used to optimize the magnetic field. The results did not determine better results but could be explored in the future.

C.4 CONCLUSION

In conclusion, an RF shimming toolbox was designed, developed, and validated through experimental MR studies. The objective of Appendix C is considered complete. Our studies indicated that the designed tool is useful for in-house related work. However, further strategies

need to be further developed in order to improve the performance of this preliminary optimization tool.

BIBLIOGRAPHY

1. Prince JL, Links JM. Medical Imaging Signals and Systems. 2013.
2. Blamire AM. The technology of MRI--the next 10 years? The British journal of radiology. 2008;81:601-17.
3. Hoult DI, Richards RE. The signal-to-noise ratio of the nuclear magnetic resonance experiment. Journal of Magnetic Resonance (1969). 1976;24(1):71-85.
4. Robitaille P-M, Berliner L. Ultra High Field Magnetic Resonance Imaging. 2006;26.
5. Opderbeck MT. New 7 Tesla MRI research system ready for future clinical use. 2015.
6. Noebauer-Huhmann I-M, Szomolanyi P, Kronnerwetter C, Widhalm G, Weber M, Nemec S, et al. Brain tumours at 7T MRI compared to 3T—contrast effect after half and full standard contrast agent dose: initial results. Eur Radiol. 2014;25:106-12.
7. Cho Z-H, Min H-K, Oh S-H, Han J-Y, Park C-W, Chi J-G, et al. Direct visualization of deep brain stimulation targets in Parkinson disease with the use of 7-tesla magnetic resonance imaging. J Neurosurg. 2010;113:639-47.
8. Hetherington HP, Hamid H, Kulas J, Ling G, Bandak F, de Lanerolle NC, et al. MRSI of the medial temporal lobe at 7 T in explosive blast mild traumatic brain injury. Magn Reson Med. 2014;71(4):1358-67.
9. Kerchner GA. Ultra-high field 7T MRI: a new tool for studying Alzheimer's disease. Journal of Alzheimer's disease : JAD. 2011;26 Suppl 3:91-5.

10. Moser E, Stahlberg F, Ladd ME, Trattnig S. 7-T MR--from research to clinical applications? *NMR Biomed.* 2012;25(5):695-716.
11. Kraff O, Fischer A, Nagel AM, Mönninghoff C, Ladd ME. MRI at 7 Tesla and above: demonstrated and potential capabilities. *Journal of magnetic resonance imaging : JMRI.* 2015;41(1):13-33.
12. Curtis AT, Gilbert KM, Klassen LM, Gati JS, Menon RS. Slice-by-slice B1+ shimming at 7 T. *Magn Reson Med.* 2012;68(4):1109-16.
13. Tang L, Hue YK, Ibrahim TS. Studies of RF Shimming Techniques with Minimization of RF Power Deposition and Their Associated Temperature Changes. *Concepts Magn Reson Part B Magn Reson Eng.* 2011;39B(1):11-25.
14. Graedel NN, Polimeni JR, Guerin B, Gagoski B, Wald LL. An Anatomically Realistic Temperature Phantom for Radiofrequency Heating Measurements. *Magn Reson Med.* 2015;73(1):442-50.
15. Wood S, Krishnamurthy N, Zhao Y, Raval S, Zhao T, Holmes JA, et al., editors. Anatomically Detailed Human Head Phantom for MR Testing Purposes. 22nd Annual Meeting of ISMRM; 2014; Milan, Italy.
16. Krishnamurthy N, Zhao Y, Raval S, Kim J, Wood S, Santini T, et al. 7T Multi-slab Whole-Head Homogeneous and Low SAR T2 Acquisitions with Limited RF Power Amplifiers Capabilities. Toronto, Canada, 2015.
17. Zhao Y, Krishnamurthy N, Wood S, Zhao T, Raval SB, Ibrahim TS, editors. 3D Eigenmodes Optimizations for 3D Imaging at 7T. 23rd Annual Meeting of ISMRM; 2015; Toronto, Canada.
18. Wood S, Krishnamurthy N, Santini T, Raval S, Farhat N, Holmes JA, et al. Design and fabrication of a realistic anthropomorphic heterogeneous head phantom for MR purposes. *PLoS One.* 2017;12(8).
19. Huber JS, Peng Q, Moses WW. Multi-Modality Phantom Development. *IEEE Trans Nucl Sci.* 2009;56(5):2722-7.

20. Kato H, Kuroda M, Yoshimura K, Yoshida A, Hanamoto K, Kawasaki S, et al. Composition of MRI phantom equivalent to human tissues. *Med Phys*. 2005;32:3199.
21. Keshvari J, Kivento M. Hand effect on head specific absorption rate (SAR) exposed by two realistic phone models. *IOP Conference Series: Materials Science and Engineering*. 2013;44:012017.
22. Shmueli K, Thomas DL, Ordidge RJ. Design, construction and evaluation of an anthropomorphic head phantom with realistic susceptibility artifacts. *J Magn Reson Imaging*. 2007;26(1):202-7.
23. Yang QX, Wang J, Collins CM, Smith MB, Zhang X, Ugurbil K, et al. Phantom design method for high-field MRI human systems. *Magn Reson Med*. 2004;52(5):1016-20.
24. Angelone LM, Vasios CE, Wiggins G, Purdon PL, Bonmassar G. On the effect of resistive EEG electrodes and leads during 7 T MRI: simulation and temperature measurement studies. *Magn Reson Imaging*. 2006;24(6):801-12.
25. Schick F. Whole-body MRI at high field: technical limits and clinical potential. *Eur Radiol*. 2005;15(5):946-59.
26. Gandhi OP, Gao B-Q, Chen J-Y. A Frequency-Dependent Finite-Difference Time-Domain Formulation for Induced Current Calculations in Human Beings. *Bioelectromagnetics*. 1992;13(6):543-55.
27. Ibrahim TS, Mitchell C, Abraham R, Schmalbrock P. In-depth study of the electromagnetics of ultrahigh-field MRI. *NMR Biomed*. 2007;20(1):58-68.
28. Ibrahim TS. A Perspective into Ultra High Field MRI RF Coils 2006. 163-208 p.
29. Hoult DI, Phil D. Sensitivity and power deposition in a high-field imaging experiment. *J Magn Reson Imaging*. 2000;12(1):46-67.
30. Zhao Y. Radio Frequency Antenna Designs and Methodologies for Human Brain Computer Interface and Ultrahigh Field Magnetic Resonance Imaging [Dissertation]: University of Pittsburgh; 2015.

31. Christ A, Kainz W, Hahn EG, Honegger K, Zefferer M, Neufeld E, et al. The Virtual Family--development of surface-based anatomical models of two adults and two children for dosimetric simulations. *Phys Med Biol*. 2010;55(2):N23-38.
32. Field and Wave Electromagnetics (2nd Edition): David K. Cheng: 9780201128192: Amazon.com: Books, 1993.
33. Hartwig V, Giovannetti G, Vanello N, Lombardi M, Landini L, Simi S. Biological effects and safety in magnetic resonance imaging: a review. *Int J Environ Res Public Health*. 2009;6:1778-98.
34. Sherar MD, Moriarty JA, Kolios MC, Chen JC, Peters RD, Ang LC, et al. Comparison of thermal damage calculated using magnetic resonance thermometry, with magnetic resonance imaging post-treatment and histology, after interstitial microwave thermal therapy of rabbit brain. *Phys Med Biol*. 2000;45(12):3563-76.
35. Cho Z-H, Jones JP, Singh M. Foundations of Medical Imaging. 1993.
36. Pohmann R. An Experimental Comparison of B1-Mapping Techniques at Two Field Strengths. *Proceedings 19th Scientific Meeting, International Society for Magnetic Resonance in Medicine*. 2011;57:4410.
37. Pohmann R, Scheffler K. A theoretical and experimental comparison of different techniques for B1 mapping at very high fields. *NMR Biomed*. 2013;26:265-75.
38. Fautz H-P, Gumbrecht R, Gross P, Schmitt F. Extending the sensitivity range for transmit array B1 mapping using relative B1 maps. *ISMRM*. 2012;1422:6307.
39. Oh S, Webb AG, Neuberger T, Park B, Collins CM. Experimental and numerical assessment of MRI-induced temperature change and SAR distributions in phantoms and in vivo. *Magn Reson Med*. 2010;63(1):218-23.
40. Zhang X, Liu J, Member S, Schmitter S, Moortele P-fVD, He B. Predicting Temperature Increase through Local SAR Estimation by B1 Mapping : A Phantom Validation at 7T. 2014:1107-10.
41. Hekmatyar SK, Babsky A, Pakin SK, Bansal N. TmDOTMA - : A sensitive MR thermometry probe for in vivo applications. 2004;11:2004.

42. Park SM, Nyenhuis Ja, Smith CD, Lim EJ, Foster KS, Baker KB, et al. Gelled versus nongelled phantom material for measurement of MRI-induced temperature increases with bioimplants. *IEEE Transactions on Magnetics*. 2003;39:3367-71.
43. Rieke V, Butts Pauly K. MR thermometry. *J Magn Reson Imaging*. 2008;27(2):376-90.
44. Leeor A, Murat DC, Ryan B, K. SD, Yudong Z. Method for in situ characterization of radiofrequency heating in parallel transmit MRI. *Magn Reson Med*. 2013;69(5):1457-65.
45. McRobbie DW, Moore EA, Graves MJ, Prince MR. *MRI: from picture to proton*, 2003. New York: Cambridge University Press ISBN. 2003;10:0-521.
46. Jin J. *Electromagnetic analysis and design in magnetic resonance imaging*: CRC press; 1998.
47. Vaughan JT, Griffiths JR. *RF coils for MRI*: John Wiley & Sons; 2012.
48. Cohen-Adad J, Wald LL. Array Coils. *Quantitative MRI of the Spinal Cord*. 2014:59-67.
49. Bloch F. Nuclear induction. *Physical review*. 1946;70(7-8):460.
50. Purcell EM, Torrey HC, Pound RV. Resonance absorption by nuclear magnetic moments in a solid. *Physical review*. 1946;69(1-2):37.
51. Jin J. *Electromagnetic Analysis and Design in Magnetic Resonance Imaging (Biomedical Engineering)*. 1999.
52. Ackerman JJ, Grove TH, Wong GG, Gadian DG, Radda GK. Mapping of metabolites in whole animals by ³¹P NMR using surface coils. *Nature*. 1980;283(5743):167.
53. Hayes CE, Edelstein WA, Schenck JF, Mueller OM, Eash M. An efficient, highly homogeneous radiofrequency coil for whole-body NMR imaging at 1.5 T. *Journal of Magnetic Resonance (1969)*. 1985;63(3):622-8.
54. Roschmann PK. High-frequency coil system for a magnetic resonance imaging apparatus. *Google Patents*; 1988.

55. Ibrahim T, Zhao T, Krishnamurthy N, Raval S, Zhao T, Wood S, et al., editors. 20-To-8 channel Tx array with 32-channel adjustable receive-only insert for 7T head imaging. The 21st International Society of Magnetic Resonance in Medicine Annual Meeting; 2013.
56. Kozlov M, Turner R, editors. Analysis of RF transmit performance for a 7T dual row multichannel MRI loop array. Engineering in Medicine and Biology Society, EMBC, 2011 Annual International Conference of the IEEE; 2011: IEEE.
57. Banerjee S, Krug R, Carballido-Gamio J, Kelley DA, Xu D, Vigneron DB, et al. Rapid in vivo musculoskeletal MR with parallel imaging at 7T. *Magnetic Resonance in Medicine: An Official Journal of the International Society for Magnetic Resonance in Medicine*. 2008;59(3):655-60.
58. Vaughan JT, Snyder CJ, DelaBarre LJ, Bolan PJ, Tian J, Bolinger L, et al. Whole-body imaging at 7T: preliminary results. *Magnetic Resonance in Medicine: An Official Journal of the International Society for Magnetic Resonance in Medicine*. 2009;61(1):244-8.
59. Kim J, Krishnamurthy N, Santini T, Zhao Y, Zhao T, Bae KT, et al. Experimental and numerical analysis of B1+ field and SAR with a new transmit array design for 7 T breast MRI. *J Magn Reson*. 2016;269:55-64.
60. Wright AC, Lemdiasov R, Connick TJ, Bhagat YA, Magland JF, Song HK, et al. Helmholtz-pair transmit coil with integrated receive array for high-resolution MRI of trabecular bone in the distal tibia at 7 T. *J Magn Reson*. 2011;210(1):113-22.
61. Wang C, Shen GX. B1 field, SAR, and SNR comparisons for birdcage, TEM, and microstrip coils at 7T. *Journal of Magnetic Resonance Imaging: An Official Journal of the International Society for Magnetic Resonance in Medicine*. 2006;24(2):439-43.
62. Vaughan JT, Hetherington HP, Otu JO, Pan JW, Pohost GM. High frequency volume coils for clinical NMR imaging and spectroscopy. *Magn Reson Med*. 1994;32:206-18.
63. WillisHRH. *Magnetic Resonance Imaging hazards and safety Guidelines*. Willis HRH. 2009.
64. Commission IE. *International Standard. Medical electrical equipment. . Part 2–33: Particular requirements for the safety of magnetic resonance equipment for medical diagnosis*: Geneva: International Electrotechnical Commission; 2008. p. 33–5.

65. Criteria for Significant Risk Investigations of Magnetic Resonance Diagnostic Devices. Guidance for Industry and Food and Drug Administration Staff. Rockville, MD, USA: Food and Drug Administration; 2014.
66. Bottomley PA. Turning up the heat on MRI. *Journal of the American College of Radiology : JACR*. 2008;5:853-5.
67. Baker KB, Tkach JA, Nyenhuis JA, Phillips M, Shellock FG, Gonzalez-Martinez J, et al. Evaluation of specific absorption rate as a dosimeter of MRI-related implant heating. *J Magn Reson Imaging*. 2004;20(2):315-20.
68. Fiedler TM, Ladd ME, Bitz AK. SAR Simulations & Safety. *Neuroimage*. 2017(March).
69. Gurler N, Ider YZ. Numerical methods and software tools for simulation, design, and resonant mode analysis of radio frequency birdcage coils used in MRI. *Concepts in Magnetic Resonance Part B: Magnetic Resonance Engineering*. 2015:n/a-n/a.
70. Yee KS. Numerical solution of initial boundary value problems involving Maxwell's equations in isotropic media. *IEEE Transactions on antennas and propagation*. 1966;14(3):302-7.
71. Ibrahim TS, Tang L. Insight into RF power requirements and B1 field homogeneity for human MRI via rigorous FDTD approach. *J Magn Reson Imaging*. 2007;25(6):1235-47.
72. Ibrahim TS, Mitchell C, Schmalbrock P, Lee R, Chakeres DW. Electromagnetic perspective on the operation of RF coils at 1.5-11.7 Tesla. *Magnetic resonance in medicine : official journal of the Society of Magnetic Resonance in Medicine / Society of Magnetic Resonance in Medicine*. 2005;54(3):683-90.
73. Taflove AaSCH. *Computational Electrodynamics: The Finite-Difference Time-Domain Method*. 2005.
74. Pennes HH. Analysis of Tissue and Arterial Blood Temperatures in the Resting Human Forearm. *J Appl Physiol*. 1948;1(2):93-122.
75. Ibrahim TS, Abraham D, Rennaker RL. Electromagnetic Power Absorption and Temperature Changes due to Brain Machine Interface Operation. *Ann Biomed Eng*. 2007;35(5):825-34.

76. Wang J, Fujiwara O. FDTD computation of temperature rise in the human head for portable telephones. *IEEE Trans Microwave Theory Tech.* 1999;47(8):1528-34.
77. Alderson SW, Lanzl LH, Rollins M, Spira J. An instrumented phantom system for analog computation of treatment plans. *The American journal of roentgenology, radium therapy, and nuclear medicine.* 1962;87:185.
78. Stacey A, Bevan A, Dickens C. A new phantom material employing depolymerised natural rubber. *The British Journal of Radiology.* 1961;34(404):510-5.
79. Iida H, Hori Y, Ishida K, Imabayashi E, Matsuda H, Takahashi M, et al. Three-dimensional brain phantom containing bone and grey matter structures with a realistic head contour. *Ann Nucl Med.* 2013;27:25-36.
80. DeWerd LA, Kissick M. *The phantoms of medical and health physics*: Springer; 2014.
81. Caon M. Voxel-based computational models of real human anatomy: a review. *Radiat Environ Biophys.* 2004;42(4):229-35.
82. Chen CC, Wan YL, Wai YY, Liu HL. Quality assurance of clinical MRI scanners using ACR MRI phantom: preliminary results. *J Digit Imaging.* 2004;17(4):279-84.
83. Tofts PS. QA: Quality Assurance, Accuracy, Precision and Phantoms. *Quantitative MRI of the Brain.* 2003:55-81.
84. Radiology ACo. ACR White Paper on Magnetic Resonance (MR) Safety. *Radiology.* 2004:1-24.
85. Christ A, Chavannes N, Nikoloski N, Gerber HU, Pokovic K, Kuster N. A numerical and experimental comparison of human head phantoms for compliance testing of mobile telephone equipment. *Bioelectromagnetics.* 2005;26(2):125-37.
86. Mobashsher AT, Abbosh AM. Three-Dimensional Human Head Phantom With Realistic Electrical Properties and Anatomy. *IEEE Antennas and Wireless Propagation Letters.* 2014;13:1401-4.

87. Ibrahim TS, Hue YK, Tang L. Understanding and manipulating the RF fields at high field MRI. *NMR in Biomedicine: An International Journal Devoted to the Development and Application of Magnetic Resonance In vivo*. 2009;22(9):927-36.
88. Pang Y, Wong EW, Yu B, Zhang X. Design and numerical evaluation of a volume coil array for parallel MR imaging at ultrahigh fields. *Quant Imaging Med Surg*. 2014;4(1):50-6.
89. Zhang X, Schmitter S, Van de Moortele PF, Liu J, He B. From complex B(1) mapping to local SAR estimation for human brain MR imaging using multi-channel transceiver coil at 7T. *IEEE Trans Med Imaging*. 2013;32(6):1058-67.
90. Gandhi OP, Lazzi G, Furse CM. Electromagnetic absorption in the human head and neck for mobile telephones at 835 and 1900 MHz. *IEEE Trans Microwave Theory Tech*. 1996;44:1884-97.
91. Hoult DI. The principle of reciprocity in signal strength calculations—A mathematical guide. *Concepts in Magnetic Resonance*. 2000;12:173-87.
92. Committee ISC, editor *IEEE SA - 1528-2013 - IEEE Recommended Practice for Determining the Peak Spatial-Average Specific Absorption Rate (SAR) in the Human Head from Wireless Communications Devices: Measurement Techniques*. Institute of Electrical and Electronics Engineers; 2013.
93. Ikemoto Y, Takao W, Yoshitomi K, Ohno S, Harimoto T, Kanazawa S, et al. Development of a human-tissue-like phantom for 3.0-T MRI. *Med Phys*. 2011;38:6336-42.
94. Murphy SV, Atala A. 3D bioprinting of tissues and organs. *Nat Biotechnol*. 2014;32:773-85.
95. Mironov V, Trusk T, Kasyanov V, Little S, Swaja R, Markwald R. Biofabrication: a 21st century manufacturing paradigm. *Biofabrication*. 2009;1:022001.
96. Kim GB, Lee S, Kim H, Yang DH, Kim YH, Kyung YS, et al. Three-Dimensional Printing: Basic Principles and Applications in Medicine and Radiology. *Korean J Radiol*. 2016;17(2):182-97.

97. Jürgen K. Mai TV, G. Paxinos. The Human Brain Atlas of the Human Brain. Elsevier. 2010.
98. Gabriel C, Gabriel S, H. Grant E, H. Grant E, S. J. Halstead B, Michael P. Mings D. Dielectric parameters relevant to microwave dielectric heating. Chem Soc Rev. 1998;27(3):213.
99. Fukunaga K, Watanabe S, Yamanaka Y, Dependence T, Properties D, Dielectric OFT-e, et al. Time dependence of dielectric properties of tissue-equivalent dielectric liquid materials: IEEE; 2002.
100. Chou CK, Chen GW, Guy aW, Luk KH. Formulas for preparing phantom muscle tissue at various radiofrequencies. Bioelectromagnetics. 1984;5:435-41.
101. Krishnamurthy N, Zhao T, Ibrahim TS. Effects of receive-only inserts on specific absorption rate, B1 (+) field, and Tx coil performance. Journal of magnetic resonance imaging : JMRI. 2014;39:475-84.
102. Weisskoff RM, MGH-NMR Center DoR, Massachusetts General Hospital and Harvard Medical School, Charlestown, Massachusetts, MGH-NMR Center tS, Rm. 2301, Charlestown, MA 02129. Simple measurement of scanner stability for functional NMR imaging of activation in the brain. Magn Reson Med. 1996 36(4):643-5.
103. Friedman L, Glover GH, Consortium TF. Reducing interscanner variability of activation in a multicenter fMRI study: Controlling for signal-to-fluctuation-noise-ratio (SFNR) differences. Neuroimage. 2006;33:471-81.
104. Friedman L, Glover GH, Krenz D, Magnotta V, BIRN F. Reducing inter-scanner variability of activation in a multicenter fMRI study: Role of smoothness equalization. Neuroimage. 2006;32:1656-68.
105. Simmons A, Moore E, Williams S. Quality control for functional magnetic resonance imaging using automated data analysis and Shewhart charting. Magn Reson Med. 1999.
106. Ibrahim TS. A Numerical Analysis of Radio-Frequency Power Requirements in Magnetic Resonance Imaging Experiment. IEEE Trans Microwave Theory Tech. 2004;52:1999-2003.

107. Kangarlu A, Ibrahim TS, Shellock FG. Effects of coil dimensions and field polarization on RF heating inside a head phantom. *Magn Reson Imaging*. 2005;23(1):53-60.
108. Collins CM, Wang Z. Calculation of radiofrequency electromagnetic fields and their effects in MRI of human subjects. *Magn Reson Med*. 2011;65(5):1470-82.
109. Van de Moortele P-F, Akgun C, Adriany G, Moeller S, Ritter J, Collins CM, et al. B1 destructive interferences and spatial phase patterns at 7 T with a head transceiver array coil. *Magn Reson Med*. 2005;54:1503-18.
110. Chen X, Lin CXI. *Computational Analysis and Methods for Electromagnetic Exposure Limits , Antenna Optimization and Cell Phone Design* PAR. 2013.
111. Pizarro YAA. Specific Absorption Rate (SAR) in the head of Google glasses and Bluetooth user's. 2014.
112. Alon L, Cho GY, Yang X, Sodickson DK, Deniz CM. A method for safety testing of radiofrequency/microwave-emitting devices using MRI. *Magn Reson Med*. 2015;74(5):1397-405.
113. Wood S, Santini T, Krishnamurthy N, Raval S, Ibrahim TS, editors. Evaluation of an Anthropomorphic Phantom with In-Vivo Using Quantitative MRI. 25th Annual Meeting of ISMRM; 2017; Honolulu, HI, USA.
114. FDA clears first 7T magnetic resonance imaging device [press release]. www.fda.gov/: U.S. Food and Drug Administration, October 12, 2017 2017.
115. Hand JW. Modelling the interaction of electromagnetic fields (10 MHz-10 GHz) with the human body: methods and applications. *Phys Med Biol*. 2008;53(16):R243-86.
116. Liu F, Crozier S. Electromagnetic fields inside a lossy, multilayered spherical head phantom excited by MRI coils: models and methods. *Phys Med Biol*. 2004;49(10):1835-51.
117. Taylor HC, Burl M, Hand JW. Experimental verification of numerically predicted electric field distributions produced by a radiofrequency coil. *Phys Med Biol*. 1997;42(7):1395-402.

118. Ihalainen TM, Lonnroth NT, Peltonen JJ, Uusi-Simola JK, Timonen MH, Kuusela LJ, et al. MRI quality assurance using the ACR phantom in a multi-unit imaging center. *Acta Oncol.* 2011;50(6):966-72.
119. The Phantoms of Medical and Health Physics: Devices for Research and Development. In: DeWerd LA, Kissick M, editors. *Med Phys: Biological and Medical Physics, Biomedical Engineering*; 2013. p. 285.
120. Brink WM, Wu Z, Webb AG. A simple head-sized phantom for realistic static and radiofrequency characterization at high fields. *Magn Reson Med.* 2018.
121. Hetherington HP, Avdievich NI, Kuznetsov AM, Pan JW. RF shimming for spectroscopic localization in the human brain at 7 T. *Magn Reson Med.* 2010;63:9-19.
122. Voigt T, Homann H, Katscher U, Doessel O. Patient-individual local SAR determination: In vivo measurements and numerical validation. *Magn Reson Med.* 2012;68:1117-26.
123. van den Bergen B, Van den Berg CAT, Bartels LW, Lagendijk JJW. 7 T body MRI: B1 shimming with simultaneous SAR reduction. *Phys Med Biol.* 2007;52:5429-41.
124. van den Bergen B, van den Berg CaT, Klomp DWJ, Lagendijk JJW. SAR and power implications of different RF shimming strategies in the pelvis for 7T MRI. *Journal of magnetic resonance imaging : JMRI.* 2009;30:194-202.
125. Liu F, Beck BL, Xu B, Fitzsimmons JR, Blackband SJ, Crozier S. Numerical modeling of 11.1T MRI of a human head using a MoM/FDTD method. *Concepts in Magnetic Resonance Part B: Magnetic Resonance Engineering.* 2005;24B:28-38.
126. Cloos MA, Bonmassar G. Towards Direct B1 Based Local SAR Estimation. *International Society for Magnetic Resonance in Medicine; Honolulu, HI, USA* 2009. p. 3037.
127. Dimbylow PJ. FDTD Calculations of the Whole-Body Averaged SAR in an Anatomically Realistic Voxel Model of the Human Body from 1 MHz to 1 GHz. *Phys Med Biol.* 1997;42:479-90.
128. Wang H, Trakic A, Xia L, Liu F, Crozier S. An MRI-dedicated parallel FDTD scheme. *Concepts in Magnetic Resonance Part B: Magnetic Resonance Engineering.* 2007;31B(3):147-61.

129. Onishi T, Uebayashi S. Biological Tissue-Equivalent Phantoms Usable in Broadband Frequency Range. NTT DoCoMo Tech. 2006;7:61-5.
130. Christ A, Chavannes N, Nikoloski N, Gerber H-U, Poković K, Kuster N. A numerical and experimental comparison of human head phantoms for compliance testing of mobile telephone equipment. Bioelectromagnetics. 2005;26(2):125-37.
131. Ibrahim TS. Analytical approach to the MR signal. Magn Reson Med. 2005;54(3):677-82.
132. Zhao Y, Tang L, Rennaker R, Hutchens C, Ibrahim TS. Studies in RF power communication, SAR, and temperature elevation in wireless implantable neural interfaces. PLoS One. 2013;8:e77759.
133. Krishnamurthy N, Zhao T, Ibrahim TS. Effects of Receive-Only Inserts on SAR, B(1)(+) Field and Tx Coil Performance. Journal of magnetic resonance imaging : JMRI. 2014;39(2):475-84.
134. Yushkevich PA, Piven J, Hazlett HC, Smith RG, Ho S, Gee JC, et al. User-guided 3D active contour segmentation of anatomical structures: Significantly improved efficiency and reliability. Neuroimage. 2006;31(3):1116-28.
135. Zhang X, Schmitter S, Van De Moortel P-F, Liu J. From Complex B 1 Mapping to Local SAR Estimation for Human Brain MR Imaging Using Multi-channel Transceiver Coil at 7T. IEEE Trans Med Imaging. 2013;32:1058-67.
136. Nguyen UD, Brown JS, Chang IA, Krycia J, Mirotznik MS. Numerical evaluation of heating of the human head due to magnetic resonance imaging. IEEE Trans Biomed Eng. 2004;51(8):1301-9.
137. K.W. YD, Kwan-Ying F, C.C. CQ, D. KA. Chemical shift imaging in the head and neck at 3T: Initial results. J Magn Reson Imaging. 2010;32(5):1248-54.
138. Boris K, N. BJ, Stephan B, Philipp H, Veneta T, Kawin S, et al. A 64-channel 3T array coil for accelerated brain MRI. Magn Reson Med. 2013;70(1):248-58.
139. F. KA, J. DJ, K. MR, M. TR, J. BM, Robert B. A novel MRI-compatible brain ventricle phantom for validation of segmentation and volumetry methods. J Magn Reson Imaging. 2012;36(2):476-82.

140. Protection ICoN-IR. Medical magnetic resonance (MR) procedures: protection of patients. Health Phys. 2004;87(2):197-216.
141. (IEC) IEC. Medical electrical equipment–Particular requirements for the safety of magnetic resonance equipment for medical diagnosis. IEC 60601-2-33, 30 2010–03 edn. Geneva, Switzerland: International Electrotechnical Commission; 2010.
142. G. SF. Radiofrequency Energy-Induced Heating During MR Procedures: A Review. J Magn Reson Imaging. 2000;12(1):30-6.
143. Shrivastava D, Utecht L, Tian J, Hughes J, Thomas Vaughan J. In vivo radiofrequency heating in swine in a 3T (123.2-MHz) birdcage whole body coil. Magn Reson Med. 2014;72(4):1141-50.
144. Collins CM, Liu W, Wang J, Gruetter R, Vaughan JT, Ugurbil K, et al. Temperature and SAR calculations for a human head within volume and surface coils at 64 and 300 MHz. Journal of magnetic resonance imaging : JMRI. 2004;19(5):650-6.
145. Murbach M, Neufeld E, Cabot E, Zastrow E, Córcoles J, Kainz W, et al. Virtual population-based assessment of the impact of 3 Tesla radiofrequency shimming and thermoregulation on safety and B1+ uniformity. Magn Reson Med. 2015:n/a-n/a.
146. Murbach M, Neufeld E, Capstick M, Kainz W, Brunner DO, Samaras T, et al. Thermal tissue damage model analyzed for different whole-body SAR and scan durations for standard MR body coils. Magn Reson Med. 2014;71(1):421-31.
147. Tang L, Hue Y-K, Ibrahim TS, Manuscript A, Deposition P, Associated T, et al. Studies of RF Shimming Techniques with Minimization of RF Power Deposition and Their Associated Temperature Changes. Concepts in magnetic resonance Part B, Magnetic resonance engineering. 2011;39B(1):11-25.
148. van Lier ALHMW, Kotte ANTJ, Raaymakers BW, Lagendijk JJW, van den Berg CAT. Radiofrequency heating induced by 7T head MRI: thermal assessment using discrete vasculature or Pennes' bioheat equation. Journal of magnetic resonance imaging : JMRI. 2012;35(4):795-803.

149. Shuman WP, Haynor DR, Guy AW, Wesbey GE, Schaefer DJ, Moss AA. Superficial- and deep-tissue temperature increases in anesthetized dogs during exposure to high specific absorption rates in a 1.5-T MR imager. *Radiology*. 1988;167(2):551-4.
150. Barber BJ, Schaefer DJ, Gordon CJ, Zawieja DC, Hecker J. Thermal effects of MR imaging: worst-case studies on sheep. *AJR Am J Roentgenol*. 1990;155(5):1105-10.
151. Wood S, Martins T, Santini T, Ibrahim TS, editors. An Electrically Conductive SLA Resin used for the Design of Anthropomorphic Phantoms. Joint Annual Meeting ISMRM-ESMRMB; 2018 June 1, 2018; Paris, France: International Society for Magnetic Resonance in Medicine
152. Wood S, Krishnamurthy N, Santini T, Raval SB, Ibrahim TS, editors. Evaluation of an Anthropomorphic Phantom with *In-Vivo* Using Quantitative MRI. International Society of Magnetic Resonance in Medicine Annual Meeting; 2017; Honolulu, Hawaii, USA: International Society of Magnetic Resonance.
153. Sossena Wood NK, Tales Santini, Shailesh Raval, Nadim Farhat, John Andy Holmes, Tamer S. Ibrahim. Design and fabrication of a realistic anthropomorphic heterogeneous head phantom for MR purposes. 2017.
154. Wolf S, Diehl D, Gebhardt M, Mallow J, Speck O. SAR simulations for high-field MRI: How much detail, effort, and accuracy is needed? *Magn Reson Med*. 2013;69.
155. Jin JM, Chen J, Chew WC, Gan H, Magin RL, Dimbylow PJ. Computation of electromagnetic fields for high-frequency magnetic resonance imaging applications. *Phys Med Biol*. 1996;41(12):2719.
156. Makris N, Angelone L, Tulloch S, Sorg S, Kaiser J, Kennedy D, et al. MRI-based anatomical model of the human head for specific absorption rate mapping. *Med Biol Eng Comput*. 2008;46(12):1239-51.
157. Collins CM, Yang B, Yang QX, Smith MB. Numerical calculations of the static magnetic field in three-dimensional multi-tissue models of the human head. *Magn Reson Imaging*. 2002;20(5):413-24.
158. Ibrahim TS, Lee R, Baertlein BA, Robitaille PML. B 1 field homogeneity and SAR calculations for the birdcage coil. *Phys Med Biol*. 2001;46(2):609.

159. Bernardi P, Cavagnaro M, Pisa S, Piuze E. Specific absorption rate and temperature elevation in a subject exposed in the far-field of radio-frequency sources operating in the 10-900-MHz range. *IEEE Trans Biomed Eng.* 2003;50(3):295-304.
160. Bernardi P, Cavagnaro M, Pisa S, Piuze E. SAR distribution and temperature increase in an anatomical model of the human eye exposed to the field radiated by the user antenna in a wireless LAN. *IEEE Trans Microwave Theory Tech.* 1998;46(12):2074-82.
161. Buccella C, Santis VD, Feliziani M, editors. Numerical Prediction of SAR and Thermal Elevation in a 0.25-mm 3-D Model of the Human Eye Exposed to Handheld Transmitters. 2007 IEEE International Symposium on Electromagnetic Compatibility; 2007 9-13 July 2007.
162. DeMarco SC, Lazzi G, Wentai L, Weiland JD, Humayun MS. Computed SAR and thermal elevation in a 0.25-mm 2-D model of the human eye and head in response to an implanted retinal stimulator - part I: models and methods. *IEEE Transactions on Antennas and Propagation.* 2003;51(9):2274-85.
163. Duck FA. Chapter 2 - Thermal Properties of Tissue. In: Duck FA, editor. *Physical Properties of Tissues.* London: Academic Press; 1990. p. 9-42.
164. Schaumburg F, Guarnieri FA. Assessment of thermal effects in a model of the human head implanted with a wireless active microvalve for the treatment of glaucoma creating a filtering bleb. *Phys Med Biol.* 2017;62(9):N191.
165. Hasgall PA DGF, Baumgartner C, Neufeld E, Lloyd B, Gosselin MC, Payne D, Klingensböck A, Kuster N. IT' IS Database for thermal and electromagnetic parameters of biological tissues. 4.0 ed2018.
166. Katić K, Li R, Zeiler W. Thermophysiological models and their applications: A review. *Build Environ.* 2016;106:286-300.
167. Fiala D, Lomas KJ, Stohrer M. A computer model of human thermoregulation for a wide range of environmental conditions: the passive system. *J Appl Physiol.* 1999;87(5):1957-72.

168. Fiala D, Lomas KJ, Stohrer M. Computer prediction of human thermoregulatory and temperature responses to a wide range of environmental conditions. *Int J Biometeorol.* 2001;45(3):143-59.
169. Zhangwei W, C. LJ, Thomas VJ, M. CC. Consideration of physiological response in numerical models of temperature during MRI of the human head. *J Magn Reson Imaging.* 2008;28(5):1303-8.
170. Nadobny J, Szimtenings M, Diehl D, Stetter E, Brinker G, Wust P. Evaluation of MR-induced hot spots for different temporal SAR modes using a time-dependent finite difference method with explicit temperature gradient treatment. *IEEE Trans Biomed Eng.* 2007;54(10):1837-50.
171. Kollia K, Maderwald S, Putzki N, Schlamann M, Theysohn JM, Kraff O, et al. First Clinical Study on Ultra-High-Field MR Imaging in Patients with Multiple Sclerosis: Comparison of 1.5T and 7T. *Am J Neuroradiol.* 2009;30(4):699-702.
172. Kozlov M, Turner R. Fast MRI coil analysis based on 3-D electromagnetic and RF circuit co-simulation. *J Magn Reson.* 2009;200(1):147-52.
173. Weisser A, Lanz T, editors. A volume head array with 8 transmit/Receive Channels for 7 T. *Proc Intl Soc Mag Reson Med*; 2006.
174. Ibrahim TS, Abduljalil AM, Baertlein BA, Lee R, Robitail PM. Analysis of B1 field profiles and SAR values for multi-strut transverse electromagnetic RF coils in high field MRI applications. *Phys Med Biol.* 2001;46(10):2545-55.
175. Shrivastava D, Hanson T, Kulesa J, DelaBarre L, Iaizzo P, Vaughan JT. Radio frequency heating at 9.4T (400.2 MHz): In vivo thermoregulatory temperature response in swine. *Magn Reson Med.* 2009;62(4):888-95.
176. Akca IB, Ferhanoglu O, Yeung CJ, Guney S, Tasci TO, Atalar E. Measuring local RF heating in MRI: Simulating perfusion in a perfusionless phantom. *J Magn Reson Imaging.* 2007;26(5):1228-35.
177. Zhao Y, Zhao T, Raval S, Ibrahim T, editors. 3D eigenmodes optimizations for 3D imaging at 7T. *The 23rd International Society of Magnetic Resonance in Medicine Annual Meeting*; 2015.

178. Zhao Y, Zhao T, Raval SB, Krishnamurthy N, Zheng H, Harris CT, et al. Dual optimization method of radiofrequency and quasistatic field simulations for reduction of eddy currents generated on 7T radiofrequency coil shielding. *Magn Reson Med*. 2015;74(5):1461-9.
179. Krishnamurthy N, Wood S, Kim J, Zhao Y, Raval S, Zhao T, et al., editors. Transmit Array Performance across Subjects at 7T MRI: Simulations and Experiments. ISMRM 23rd Annual Meeting & Exhibition 2015; Toronto, Canada: International Society for Magnetic Resonance in Medicine.
180. Kim J, Santini T, Bae KT, Krishnamurthy N, Zhao Y, Zhao T, et al. Development of a 7 T RF coil system for breast imaging. *NMR Biomed*. 2017;30(1):e3664.
181. Santini T, Kim J, Wood S, Krishnamurthy N, Farhat N, Maciel C, et al. A new RF transmit coil for foot and ankle imaging at 7T MRI. *Magn Reson Imaging*. 2018;45:1-6.
182. Ianniello C, Brown R, Cloos M, Duan Q, Walczyk J, Wiggins G, et al., editors. Sugar free tissue-mimicking MRI phantoms for improved signal-to-noise ratio. Proceedings of the 24th Annual Meeting of ISMRM, Singapore; 2016.
183. Tales Santini YZ, Sossena Wood, Narayanan Krishnamurthy, Junghwan Kim, Nadim Farhat, Salem Alkhateeb, Tiago Martins, Minseok Koo, Tiejun Zhao, Howard Aizenstein, Tamer S. Ibrahim. In-vivo and numerical analysis of the eigenmodes produced by a multi-level Tic-Tac-Toe head transmit array for 7 Tesla MRI. *PLoS One*. 2018.
184. Asadi M. Beet-sugar handbook: John Wiley & Sons; 2006.
185. Santini T, Wood S, Krishnamurthy N, Zhang Y, Farhat N, Vinjamuri N, et al., editors. New optimization strategies for RF shimming at UHF MRI. The 26th International Society of Magnetic Resonance in Medicine Annual Meeting; 2018; Paris, France.
186. Santini T, Zhao Y, Wood S, Kim J-H, Farhat N, Krishnamurthy N, et al., editors. Experimental and numerical evaluations of simultaneously excitable Eigenmodes in a 20-channel transmit RF array for 7 Tesla human MRI. The 26th International Society of Magnetic Resonance in Medicine Annual Meeting; 2018; Paris, France.
187. van den Bergen B, Van den Berg CA, Bartels LW, Lagendijk JJ. 7 T body MRI: B1 shimming with simultaneous SAR reduction. *Phys Med Biol*. 2007;52(17):5429.

188. Flöser M, Bitz A, Jost S, Orzada S, Gratz M, Kraff O, et al. Hybrids of Static and Dynamic RF Shimming for Body Imaging at 7T. Toronto, Canada2015.
189. Tang L, Ibrahim T. SAR and Temperature Evaluations for B1 Shimming at 7 tesla2009.
190. Park B, Sung K, McGarrity J, Oh S-h, Cao Z, Wang Z, et al. Slice-Selective Transmit Array Pulses for Improvement in Excitation Uniformity and Reduction of SAR. *Journal of Electromagnetic Analysis and Applications*. 2013;05:205-12.
191. Kaneko Y, Soutome Y, Ito K, Takizawa M, Habara H, Seki Y, et al. Transmit Power Reduction and B₁+ Homogenization Using 4-channel Regional RF Shimming for Shoulder Imaging at 3T. Toronto, Canada, 2015.
192. Katscher U, Börnert P, Leussler C, Van Den Brink JS. Transmit sense. *Magnetic Resonance in Medicine: An Official Journal of the International Society for Magnetic Resonance in Medicine*. 2003;49(1):144-50.
193. Orzada S, Maderwald S, Poser BA, Bitz AK, Quick HH, Ladd ME. RF excitation using time interleaved acquisition of modes (TIAMO) to address B1 inhomogeneity in high-field MRI. *Magnetic resonance in medicine : official journal of the Society of Magnetic Resonance in Medicine / Society of Magnetic Resonance in Medicine*. 2010;64:327-33.
194. Stenger VA, Saekho S, Zhang Z, Yu S, Fernando E. B1 Inhomogeneity Reduction with Transmit SENSE.
195. Thesis A, Engineering E. Novel SAR Reduction Methods for Magnetic Resonance Imaging, 2011.
196. Stough DK, Ibrahim TS. Optimization and Validation of a Highly-coupled , 20-Channel Transmit UHFMRI Head Coil Design.
197. Raval SB, Britton CA, Zhao TJ, Krishnamurthy N, Santini T, Gorantla VS, et al. Ultra-high field upper extremity peripheral nerve and non-contrast enhanced vascular imaging. *PLoS One*. 2017;12(6).
198. Raval SB, Zhao T, Krishnamurthy N, Zhao Y, Wood S, Bae K, et al. Initial Results: Ultra-High Field 32-ch Tx Body Array with Bright Centers. Toronto, Canada2015.

199. Raval SB, Zhao, Y, Zhao, T, Krishnamurthy, N, Wood, S, and Ibrahim, TS. 7T Tx Body Coil with Rx-Only Insert: Primarily Results. Proc Intl Soc Mag Reson Med. 2013;21:4368.